THERMAL PROPERTIES OF ABLATIVE CHARS

W. A. Clayton, P. B. Kennedy
R. J. Evans, J. E. Cotton
A. C. Francisco

THE BOEING COMPANY

T. J. Fabish, E. A. Eldridge
J. F. Lagedrost

BATTELLE MEMORIAL INSTITUTE

This document has been approved for public release and sale; its distribution is unlimited.

FOREWORD

This report was prepared by the Aerospace Group of The Boeing Company under USAF Contract Number AF 33(615)-3804. The contract was initiated under Project Number 7381. The work was administered under the direction of the Air Force Materials Laboratory, Materials Application Division, Task 738106, "Design Information Development", with Dr. Merrill L. Minges and Gary L. Denman acting as Project Engineers.

The Boeing Company Program Manager was W. A. Clayton. The program was conducted in the Plastics and Ablation Research Group under the management of P. B. Kennedy and W. M. Sterry, Chief, Materials Research and Development. R. W. Evans and Dr. J. E. Cotton were the principal investigators for char charaterization. A. C. Francisco developed the methods for furnace char production. The contributions of G. W. Way in photomicrography, I. L. Brower in X-ray diffraction analysis, K. Vannier in X-ray transmission analysis, and Dr. M.E. Taylor, H.M. Goldberg, S. S. Cannaday, and A. D. VonVolkli in other measurements is greatly appreciated. K. W. Irwin, S. D. Kyte, and D. J. Ottestad assisted in preparation of the final report.

All thermophysical property measurements were conducted at the Battelle Memorial Institute Columbus Laboratories by T. J. Fabish, thermal conductivity, E. A. Eldridge, specific heat and thermal expansion, and J. F. Lagedrost, Project Manager. These gentlemen provided the written discussion of the measurements in Sections IX, X, and XI and the appendices in this report. Battelle acknowledges the assistance of the following staff members: R. McCann, J. Childers, D. Hackney, A. Noe, L. Porter, W. Schmitt, and Gerry Trivello.

The authors wish to acknowledge the contributions to this program by NASA in releasing the Aerotherm computer predictions and in releasing the original MX-4926 nozzle prepreg material, by Aerotherm in performing additional computer predictions; and by the material suppliers, Thompson-Ramo-Wooldridge and Fiberite, in reproducing the original material.

This report covers work conducted from March 1, 1966 through September 15, 1967.

This technical report has been reviewed and is approved.

Albert Olevitch

ALBERT OLEVITCH, Chief
Materials Engineering Branch
Materials Applications Division
Air Force Materials Laboratory

ABSTRACT

Thermal conductivity, specific heat, thermal expansion, and a complete microstructural and chemical compositional characterization were established from room temperature to 4500°F for MX-4926 phenolic-carbon and FM-5014 phenolic-graphite nozzle throat chars recovered from fired 120-inch solid boosters. Characterization of FM-5055A ablative chars from plasma tests simulating reentry was also completed. Characterization, versus depth from the char surface, included determination of apparent and solid density, total porosity, open porosity size distribution, microstructural characteristics, elemental composition, thermal stability, and extent and nature of char "graphitization". Computer predicted internal density and temperature histories related post-test ablative char characteristics to temperature during prior ablation. Thermophysical properties were measured as a function of layup angle on virgin material and on furnace charred samples duplicating three distinct char zones found in the nozzle chars. Thermophysical properties were correlated with sample characterization and heat transport theory to predict properties applicable during ablation. Thermal conductivity, obtained by the steady state, unidirectional comparative disk method, depended on the rate controlled pyrolysis generation of porosity and on temperature dependent "graphitization" so that data for any application must be extrapolated from values measured on after-test chars. Low lamination angles relative to the heat flow path gave substantially lower conductivity for all states of ablating material. Specific heat, obtained from Bunsen ice calorimeter enthalpy measurements, was established as a function of temperature in third order equations for all states of ablating material. Linear thermal expansion did not behave systematically and permanent dimensional changes were obtained on all samples. Permanent crossply shrinkage during pyrolysis offset thermal expansion and was the largest dimensional change resulting from ablation heating.

CONTENTS

CONTENTS (cont)

CONTENTS (cont)

ILLUSTRATIONS

ILLUSTRATIONS (CONT.)

ILLUSTRATIONS(CONT.)

ILLUSTRATIONS (CONT.)

ILLUSTRATIONS (CONT.)

ILLUSTRATIONS (CONT.)

ILLUSTRATIONS (CONT.)

ILLUSTRATIONS(CONT.)

ILLUSTRATIONS (CONT.)

TABLES

TABLES (CONT.)

NOMENCLATURE

Letter Symbols

A	=	Area, Ft^2
C_p	=	Specific heat, $Btu\text{-}lb^{-1}\cdot R^{-1}$
D	=	Characteristic x-ray diffraction crystal spacing value in Å
ΔH	=	Heat of reaction for DTA exothermic event, microvolts-°C
I	=	Intensity of x-ray diffraction, counts - $second^{-1}$
K	=	Thermal conductivity, Btu-Inch, $Hr.^{-1}\ Ft.^{2-1}\cdot R^{-1}$
P	=	Percent deviation, dimensionless, P equals one
PC	=	Phenolic carbon
PG	=	Phenolic graphite
Q	=	Heat flux, Btu, $Ft^{2-1} - Hr^{-1}$
R	=	Radocon x-ray transmission intensity, Roentgens per minute
T	=	Temperature
t	=	Distance, inches or cm
V	=	Volume, cm^3
μV	=	Measure of DTA exothermic reactions, microvolts
W	=	Weight, grams
w	=	Weight for DTA tests, milligrams
x,y,z	=	Axes of ellipsoidal pores
X_p	=	Pyrolyzed resin fraction

Greek Letter Symbols

β	=	Pore shape factor, Appendix B
ξ	=	Porosity fraction, dimensionless
μ	=	X-ray mass absorption coefficient, $cm^2/gram$
ρ	=	Density, $grams/cm^3$
θ	=	Angle, degrees

Subscripts

c	=	apparent
a	=	initial characteristic for DTA data
c	=	closed
c	=	end characteristic for DTA data
c	=	mature char value
d	=	dry condition for density
g	=	portion convertible to pyrolysis gas
l	=	a single solid phase, single zone
n	=	normal to isotherms, Appendix C
o	=	open to gas
p	=	penetrated by mercury for porosity

NOMENCLATURE (cont.)

Subscripts (cont.)

p	=	peak characteristic for DTA data
s	=	solid material or solid phase for density
t	=	total
v	=	virgin value

Superscripts

1	=	single zone
r	=	radiation component conductivity, Btu-inch, $Hr.^{-1}$ $Ft.^{2-1}{}_{R}{}^{-1}$
t	=	based on linear K(T)

SECTION I

INTRODUCTION

Analytical predictions of ablation performance require accurate values for thermophysical properties of ablators at the temperatures and states of decomposition encountered during ablation. Although data for the virgin state of commonly used ablators have been available, thermophysical properties for the highly unstable pyrolysis zone and high temperature char layers have not. Design of refractory reinforced ablation systems for large rocket motors and reentry vehicles has been uncertain because of lack of data on ablators for over 80 percent of the ablation temperature range. Most previous attempts to obtain these data have utilized transient or steady state measurements on "charred" samples. However, a wide range of values were obtained and those applicable to active ablation could not be identified due to lack of suitable characterization of the thermophysical property samples and their correlation with actual chars.

The objective of this program was to determine thermal conductivity, specific heat, thermal expansion and density to 4500°F on well-defined samples of charred phenolic-carbon and phenolic-graphite ablators. Methods were to be established for characterizing chars of three phenolic carbon or phenolic graphite ablators from tested full scale hardware. Then methods for producing stable duplicates of three zones between 1200 and 4500°F in each char were to be developed. Samples of each of these zones and the virgin ablator were to be produced for measurement of thermal conductivity, specific heat and thermal expansion by Battelle Memorial Institute. Properties parallel to and perpendicular to the laminate were to be determined from room temperature to 700°F on virgin material and between 1200 and 4500°F on chars. Properties for the unstable pyrolysis zone were to be derived by extrapolation guided by characterization and heat transport theory.

The accomplishment of the program objectives presented in this report provides accurate phenolic-carbon and phenolic-graphite thermophysical property data to 4500°F for all ablation applications.

SECTION II

SUMMARY

This final report to the Materials Application Division summarized work on Contract No. AF33(615)-3804. Under this contract, thermal conductivity, specific heat and thermal expansion were measured between room temperature and 4500°F on laboratory produced samples representing four stages of ablation in MX-4926 phenolic-carbon and FM-5014 phenolic-graphite ablators. The Boeing Company prepared and characterized all chars while Battelle Memorial Institute performed all thermophysical property measurements under contract to Boeing. The four zones for which properties were measured were as follows:

Char Zone I - Stable surface char that has experienced temperatures from 4600°F on the outer hot face to 2900°F at the inner boundary. It is characterized by significant "graphitization", high porosity, high residual carbon content and absence of phenolic resin. Property specimens representing this zone were produced at 4000°F.

Char Zone II - Stable char that has experienced temperatures from 2900°F down to 1900°F at the lower boundary. It is characterized as fully charred material similar to Zone I except that it is not "graphitized." Property specimens representing this zone were produced at 2500°F.

Char Zone III - Unstable char including the outer portion of the pyrolysis zone that has experienced temperatures from 1900°F to 1200°F. It is similar to Zone II except that it contains some unpyrolyzed phenolic and less residual carbon. Property specimens representing this zone were produced at 1200°F.

Virgin Zone - Ablation material unaffected by heating except for volatilization losses not exceeding four percent by weight with a total porosity less than 3 percent. The maximum temperatures to maintain these characteristics are 500°F for MX-4926 and 700°F for FM-5014.

Characterization of ablative chars from full scale tested hardware delineated the distinct zones in an ablative char for which properties were required. The Air Force provided charred nozzle throats recovered from test firings of 120-inch solid propellant boosters for both of the materials on which properties were measured. The first was Fiberite MX-4926 phenolic-carbon from a Thompson-Ramo-Wooldridge

oblique tape wrapped nozzle for the Aerojet-General Corporation 120-SS-1 motor. The second was U.S. Polymeric FM-5014 phenolic-graphite from an H.I. Thompson rosette-molded nozzle for the United Technology Corporation Titan 3C-10 solid strap-on. The Air Force also provided, for characterization only, a plasma-test specimen of U.S. Polymeric FM-5055A phenolic-carbon typical of reentry applications.

Complete characterization of the post-ablation chars yielded a microstructural and chemical compositional description as a function of depth in the char. Density, total porosity and pore size distribution measurements were used to delineate char microstructure and provide porosity data for correlation of thermal conductivity results. Elemental and thermal analyses were used to determine amounts of unpyrolized resin and establish the presence of hydrocarbon material deposited in the mature char during cooling from the ablation exposure. Polarized light photomicrography and X-ray diffraction analyses established the nature and extent of "graphitization" in the char and enabled correlating the effects of "graphitization" on thermal conductivity. In this report "graphitization" is referred to parenthetically as the accepted description of increased crystallinity in the char with the characteristic crystal spacing of graphite but unknown crystal structure. Internal temperature and density versus time during the ablation exposure and cooldown period were established by computer predictions, and identified the maximum temperature requirement for thermophysical properties in each distinct char zone.

Thermally stable furnace char analogues of nozzle char zones I, II and III were produced in an induction heated graphite retort. Characterization of the furnace chars showed that they reproduced all characteristics of active ablation chars except apparent density, which was higher due to pyrolysis shrinkage on unrestrained material in the furnace.

The thermal conductivities of the virgin material and three char zones of both materials were measured parallel to the laminations, representing ablators with laminations perpendicular to the char surface (hereafter called 90° layup angle material) and perpendicular to the laminations representing ablators laid up parallel to the char surface (hereafter called 0° layup angle material). Data were also obtained at 20° and 45° to the laminations. In MX-4926 the layup angle was defined along the bias direction in the uniformly oriented carbon cloth reinforcement to provide properties applicable to tape-wrapped construction. In FM-5014 the graphite cloth reinforcement layers were randomly oriented. Thermal conductivity was determined by the steady state, unidirectional comparative disk method. Estimated precision of the measurements was best, ±8%, on low temperature 0° layup material and decreased with increasing temperature and layup angle to ±25% on 90° layup Zone I material.

The thermal conductivity versus temperature of both FM-5014 and MX-4926 char zone specimens was correlated to enable extrapolation within the accuracy of the measurements to all states of ablation up to 4500°F. The correlations were established for both the laminate direction and the crossply direction in each material so conductivity in any other direction can be obtained by a layup angle relationship to these two principal conductivities. The correlations were developed by separating the radiation and the solid conduction components of apparent (measured) conductivity versus temperature and establishing the effects of pyrolysis and high temperature char "graphitization" on the solid component. The effect of pyrolysis was shown to be due to the pyrolysis rate dependent generation of porosity which lowers the solid component of conductivity and is essentially complete at temperatures below the onset of the radiation component. The pyrolysis rate (hence heating rate) dependent lowering of conductivity by generation of porosity must be separately superimposed for each different ablation application. Therefore, the rate independent solid conductivity component versus temperature correlations were established for theoretical zero-porosity or "dense" charred material by calculating out the effect of porosity included in apparent solid conductivity using the porosity effect equation given below. "Graphitization" depended only on the maximum temperatures reached so its effects could be combined in the "dense" material solid conductivity versus temperature correlations. The final "dense" material solid conductivities and the separate radiation components of conductivity versus temperature are given in Figures 86 and 88 for FM-5014 and MX-4926 respectively.

The conductivity data applicable to any ablation problem are extrapolated from the data of Figures 86 and 88 by correcting the "dense" material solid conductivity, K^{θ}_{s}, for pyrolysis generated porosity and adding the radiation component, K'_{θ} at each temperature point desired. The equation used for 0 and 90 degree layup angle, θ, material is:

$$K_{\theta} = \left[\frac{1 - X_p \xi_{tc}}{1 + X_p \beta \xi_{tc}}\right] K^{\theta}_{s} + K^{r}_{\theta} \qquad \text{(7, page 149)}$$

where:

β = Pore shape factor;
4/5 for θ = 0° layup angle,
1/8 for θ = 90° layup angle

ξ_{tc} = Final char porosity;
0.31 for FM-5014
0.45 for MX-4926

X_p = Pyrolyzed resin fraction

Values of the pyrolyzed resin fraction term, X_p, versus temperature for typical applications of these materials are given in Figure 83. They may also be obtained from applicable computer results. Ideally, this entire data correlation would be incorporated directly into in-depth ablation computer programs to insure that values of conductivity corresponding to the instantaneous state of the material were used. The desired K versus T curve in the pyrolysis zone is different for each different heating rate encountered as illustrated in Figure 84. Due to irreversible temperature dependent pyrolysis and graphitization, conductivity values versus temperature applicable to cooling or reheating in the char are different than for initial heating; each level of permanent change gives an individual curve applicable to these periods as illustrated in Figure 84, 86, and 88. The above equation must also be applied to the cooling curve data.

To obtain conductivity data for intermediate layup angles, θ, the results for both 0 and 90 degree layup angles obtained from the above equation are combined in the following relationship:

$$K_\theta = K_0 \left[1 + \left(\frac{K_{90}}{K_0} - 1 \right) \sin^2 \theta \right] \qquad \text{(8, page 150)}$$

The results obtained are assumed to apply for all cloth orientations within the laminate plane. This layup angle correlation applied for all cases except for layup angles above 45 degrees in the virgin or pyrolysis zones, where substitution of $\sin \theta$ for $\sin^2 \theta$ will give better fit to the experimental data.

The thermal conductivity results show that low layup angles relative to the char surface gave substantially lower conductivity versus temperature due to the lower virgin thermal conductivity, more conductivity decrease due to pyrolysis generation of porosity and little conductivity increase (a decrease in MX-4926) from internal "graphitization." The effect of "graphitization" was the greatest in MX-4926, substantially increasing the conductivity at high temperatures in the laminate direction.

Specific heat was obtained on virgin and Zone I furnace char samples of both materials and on corresponding samples from the MX-4926 nozzle char. Specific heat was determined from enthalpy measurements in a Bunsen ice calorimeter to better than ±5% accuracy and results on furnace chars and nozzle chars agreed well. Virgin material specific heats were higher than the low temperature specific heats of "graphitized" mature char as shown in Figures 93 and 94. High temperature char specific heats were near those for graphite. Third order equations for enthalpy and specific heat as a function of temperature for both virgin and charred material were established for use

in ablation computer programs. Values for the pyrolysis zone may be considered as intermediate between the average of char values and virgin values with corrections for the amount of pyrolysis.

Linear thermal expansion was measured in the laminate and crossply directions of the virgin zone and Zone III and I furnace chars of both materials and on corresponding samples from the MX-4926 nozzle char. Permanent dimensional changes were obtained in all expansion cycles on both nozzle and furnace chars regardless of the maximum test temperature. Thermal expansion did not behave systematically so no general correlation was possible. Comparison of measured thermal expansion and the pyrolysis shrinkage occurring in furnace char production showed crossply shrinkage to be the largest thermally induced dimensional change.

SECTION III

MATERIALS

COMPONENT DESCRIPTION

All ablative materials studied on this program were high density carbon or graphite reinforced phenolic laminates provided by the Air Force after component test firing. Two were charred throat sections taken from 120-inch solid propellant boosters, specifically: Fiberite MX-4926 phenolic-carbon from a 120-SS-1 motor, Figure 1, and U.S. Polymeric FM-5014 phenolic-graphite from a Titan 3C-10 motor, Figure 2. The third ablator, U.S. Polymeric FM-5055A phenolic-graphite, represented material for reentry vehicle applications. Details of these samples are furnished in Table I.

The FM-5014 phenolic-graphite charred nozzle sections were large enough to provide all of the virgin material needed for thermal property test specimens but additional virgin MX-4926 phenolic-carbon material was required. This additional material was obtained from Thompson-Ramo-Wooldridge and from Fiberite.

MANUFACTURER'S DESCRIPTION - PREPREGS

All prepregs consisted of woven cloth reinforcement impregnated with a carbon filled phenolic resin per MIL-R-9299. Table II lists the range of values for the lots used to manufacture all of the items used in the program.

MATERIAL SPECIFICATION - FABRICATOR

Table III lists the material specifications used by the original fabricators of the charred ablators provided by the USAF.

FABRICATION PROCEDURES

MX-4926

Nozzle Component

The prepreg tape was bias-wrapped on a cylindrical mandrel with a starting-ring surface inclined 75 degrees to the nozzle centerline, minimum tape tension (less than 10 lbs.), and a roller pressure of 100-300 pounds per inch of tape width.

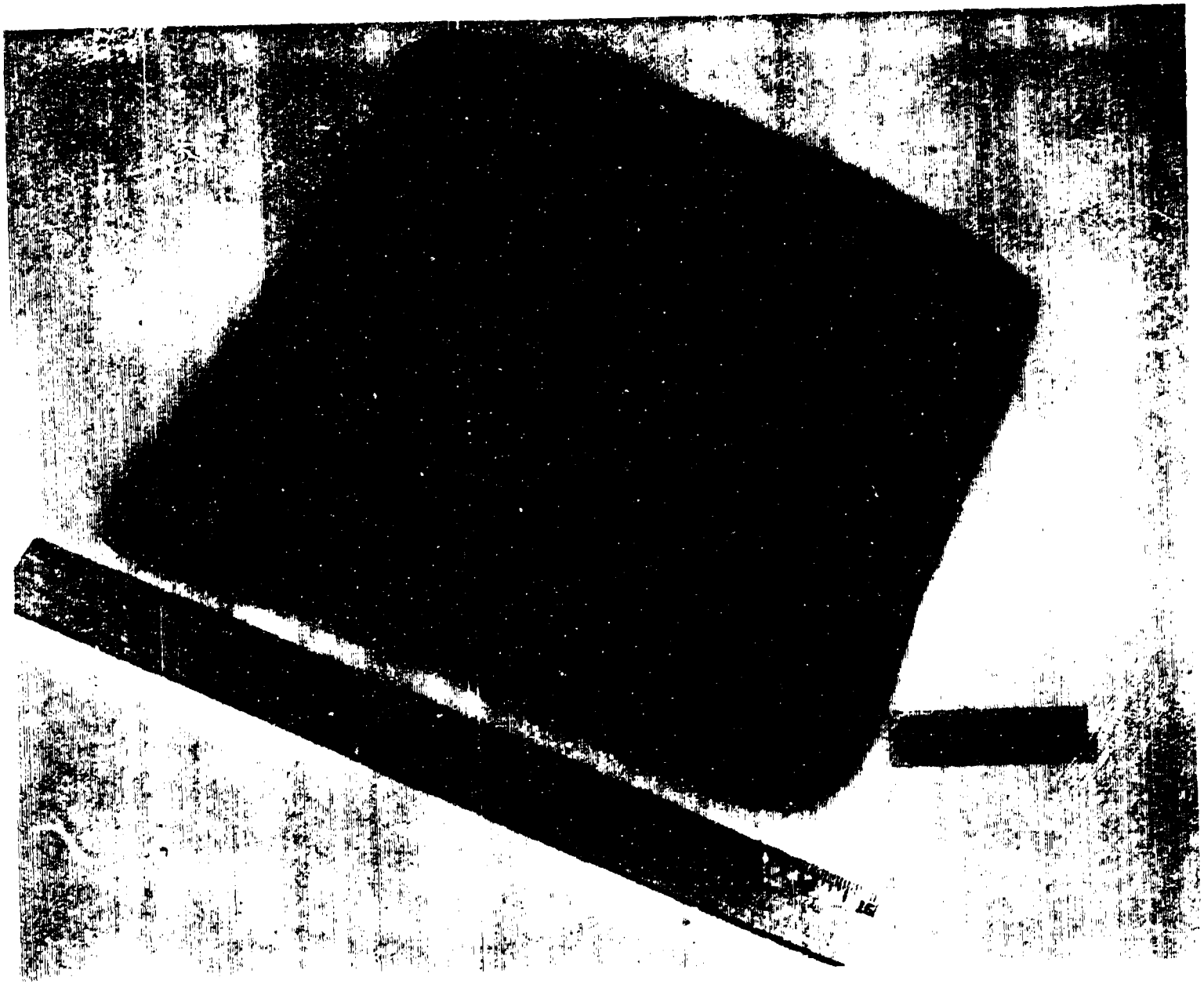

FIGURE 1 MX-4926 PHENOLIC CARBON TAPE WRAPPED 120-SS-1 THROAT SEGMENT CHAR SAMPLE

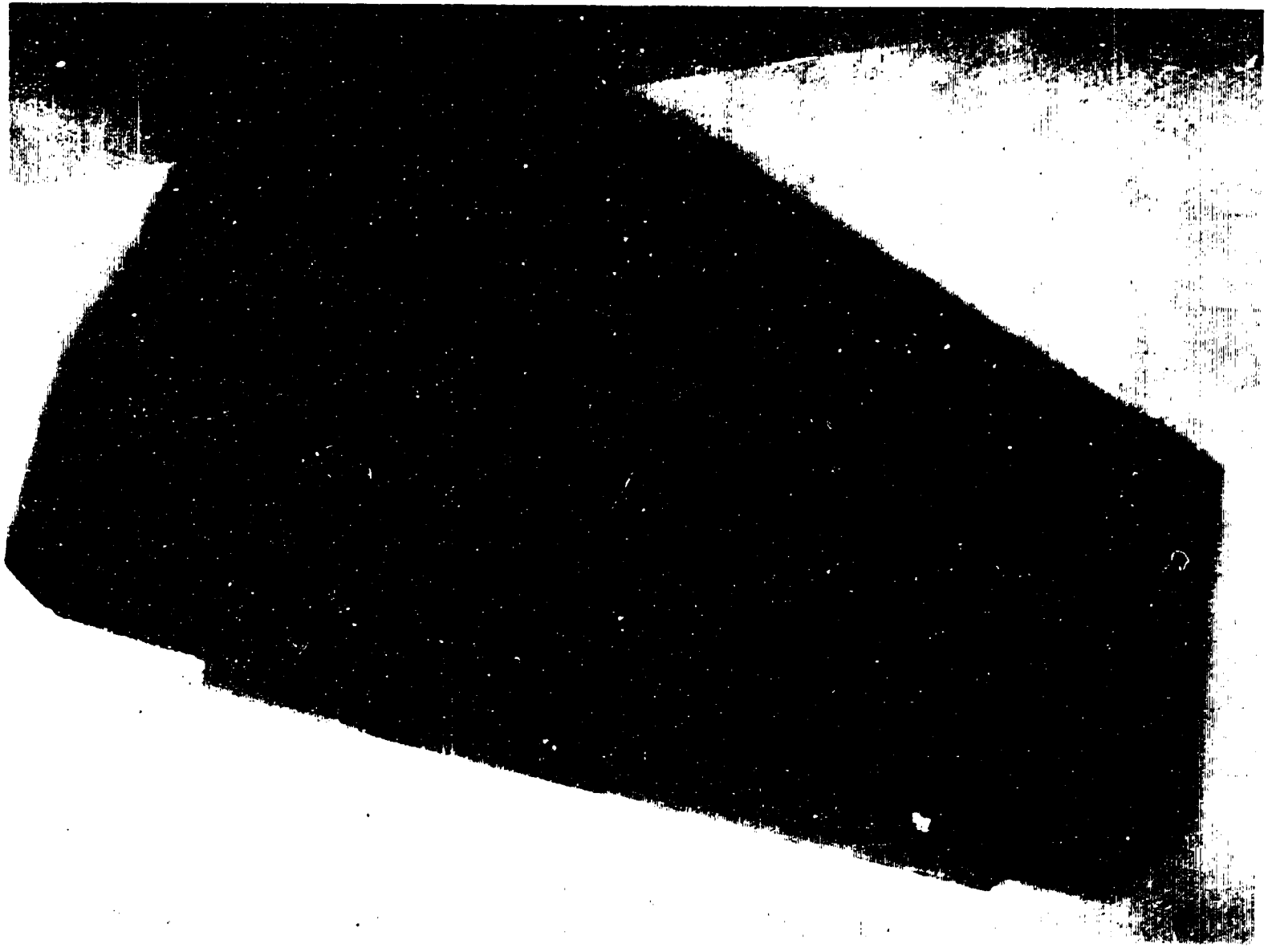

FIGURE 2 FM-5014 PHENOLIC-GRAPHITE ROSETTE LAYUP TITAN 3-C THROAT SEGMENT CHAR SAMPLE

TABLE I COMPONENT DESCRIPTION

MATERIAL	FABRICATOR	COMPONENT	ABLATIVE EXPOSURE	PROPERTIES			ABLATIVE CHAR CHARACTERIZATION
				K	C_p	α	
Fiberite Corp. MX-4926 Phenolic-Carbon	Thompson-Ramo-Wooldridge	Oblique tape wrapped nozzle segment	Aerojet-General 120-SS-1 Motor 120" Nozzle Throat		X	X	X
	Thompson-Ramo-Wooldridge	Molded Block	None	X	X	X	
	Fiberite Corp.	Molded Block	None	(Charred sample production trials)			
U.S. Polymeric FM-5014 Phenolic-Graphite	H.I. Thompson Co.	Rosette layup nozzle segment	United Technology Corp. Titan 3C-10 120" Nozzle Throat	X	X	X	X
U.S. Polymeric FM-5055A Phenolic-Graphite	General Electric Missile & Space Division	2" diameter plasma test models.	Arc-Plasma Test Space-General Corp.				X

TABLE II

MANUFACTURERS' DESCRIPTIONS OF PREPREGS

	Fiberite MX-4926	U. S. Polymeric FM-5014	U. S. Polymeric FM-5055A
Resin:			
Trade Name	Monsanto SC 1008	CTL 91LD	CTL 91LD
Generic Name	Phenolic	Phenolic	Phenolic
Curing Agent	None	Proprietary	Proprietary
Resin Mix	--	F-014	F-014
Resin Solids	31.5-36.5%	30 - 35.2%	31 - 37%
Filler or Resin Reinforcement:			
Trade Name	Sterling R	USP-6 (Carb. Powder)	USP-6 (Carb. Powder)
Chemical Comp:			
Carbon	99%	99.5% min.	99.5% min.
Ash	--	0.10% max.	0.10% max.
Solid Density g/cm^3	1.9	--	--
Size Range, Microns	0.080	0.01-0.05 7% 0.10-0.40 85% 0.40-0.70 8%	0.01-0.05 7% 0.10-0.40 85% 0.40-0.70 8%
Concentration	6-10%	12-14%	12-14%
Reinforcement:			
Trade Name	HITCO-CCA-1	Union Carbide-WCA	HITCO-CCA-1 (1641)
Generic Name	Carbon fabric	Graphite cloth	Pure carbon fabric
Weave Type	8-Harness Satin	Square	8-harness satin
Weight, oz/sq.yd.	7.0 - 9.0	7.6	7.0-9.0
Thickness, inches	0.016 - 0.020	0.025	0.017-0.023
Yarn Count	-		
Warp	52 - 58	26.9	50-60
Fill	47 - 53	22.7	45-55
Yarn Construction	Continuous Fil.	--	---
Filament/yarn	720	1440	720
Fil. size, in.	0.00035 - 0.00045	0.0003	0.00035-0.00045
Fiber Density, g/cm^3	--	1.5 (ASTM-C-135-61)	1.8 - 1.9

TABLE III - PREPREG MATERIAL SPECIFICATIONS

		MX-4926 Phenolic Carbon	FM-5014 Phenolic Graphite	FM-5055A Phenolic-Carbon
Resin Solids	Weight Loss on Pyrolysis to 1200°C	31.5-36.5%	30.4-35.2%	35.6%
Volatile Content	Weight Loss 20 Min. @320°F	4 - 8%	3.2-3.5%	4.5%
Resin Flow	150 psi	2 - 7%	1.1-8.0%	17.4%
Specific Gravity	ASTM D-792-50	1.40 Min.	1.41 Min.	-
Viscosity Index		1.8-2.8	-	-
Infrared Polymerization Index		-	1.49-1.70%	-
Prepreg Breaking Strength	lbs/in	-	45 Min.	-
Flexural Strength	ASTM D-790-61T psi	30,000 Min.	17,000 Min.	-
Tensile Strength	psi	-	9,500 Min.	-
Interlaminar Shear Strength	psi	-	1,700 Min.	-
Procurement Specification		Thompson-Ramo-Wooldridge WS-1048A, Type I, Class 2	H. I. Thompson ECO-5224 UTC-4MDS-40721A, Class I Infrared per 4MDS-91605, para. 4.4.1	-

Tape temperature was controlled to optimize tack characteristics during wrapping. An overwrap of U.S. Polymeric FM-5131 phenolic-silica was applied for additional structural support. Processing sequences follow:

1. Wrap bias tape onto mandrel.
2. Seal in rubber bag.
3. Preform in hydroclave; pressure 1000 psi, hold temperature at 185°F for six hours, then reduce to room temperature at a rate of 100°F per hour.
4. Machine outer surface to interface dimensions.
5. Apply FM-5131 phenolic-silica overwrap. Use two-inch wide tape parallel to outer surface and same wrap technique as phenolic-carbon.
6. Seal in rubber bag.
7. Cure in hydroclave; pressure 1000 psi and temperature 185°F for nine hours, then temperature 320°F for 13 hours, then reduce to room temperature at a rate of 100°F per hour.
8. Finish machine to outside diameter.
9. Inspect radiographically for flaws.
10. Bond nozzle to steel shell with epoxy adhesive Epon 913.
11. Remove mandrel.
12. Machine interior contour of throat.

The carbon component showed the following test properties on sections taken from end test rings:

Characteristic	Standard	Average Test Value
Specific Gravity	1.38 min.	1.45
Volatiles	3.0% max.	2.18%
Acetone Extractables	1.0 max.	0.14%
Interlaminar Shear Strength	1000 psi min.	1,030 psi
Edgewise Compression Strength	No standard	36,200 psi

Radiographic inspection by radial shots along the angle of the plies showed no indications of unsound sections.

Virgin Material Blocks

TRW Blocks

Thompson-Ramo-Wooldridge determined that the MX-4926 prepreg remaining from the nozzle program still met the material specification, WS 1048A Type I Class 2. NASA released the prepreg for use in this program and TRW molded

two blocks, duplicating the original nozzle cure cycle as closely as possible. The blocks were molded from MX-4926 lot A-430 roll No. 4 which had the following properties:

Resin Solids	33.3%
Volotile Content	4.9%
Laminate Flow	4.9%
Infrared Polymerization Index	1.0%

These blocks were used to produce virgin and furnace charred thermophysical property specimens, since they best reproduced the nozzle material in both prepreg characteristics and final cured density.

The cure cycle for the TRW blocks follows:

1. Place laminate in press (vacuum bag maintained at 26.6 inches Hg).
2. Apply 200 psi pressure.
3. Raise temperature to 185°F (approximately 20 minutes).
4. Hold for 90 minutes.
5. Raise pressure to 780 psi.
6. Raise temperature to 320°F (approximately 1 hour).
7. Hold for 19 hours.
8. Reduce temperature to 85°F in 3.5 hours under 780 psi pressure.
9. Remove laminate from press.

The TRW laminated blocks possessed the following properties:

Property	Block A	Block B
Nominal Minimum Size, in.	9 x 8 x 4	12 x 8 x 3
Cloth Warp Direction	Long Dimension	Long Dimension
Specific Gravity	1.45	1.46
Acetone Extractables	0.32%	0.15%
Alcohol Penetrant Inspection	No Indication	No Indication

Fib rite Blocks

Since insufficient virgin material molded from the original prepreg was available for all laboratory char production trials, additional laminate blocks of virgin MX-4926 reproducing the nozzle material as closely as possible were purchased from Fiberite Corporation. The two Fiberite laminate blocks were 8.5 x 9 x 4

inches with average densities of 1.51 g/cm^3. Since this density was higher than the nozzle material, these blocks were used only for laboratory char production trials. The blocks were molded from MX-4926 lot C-412, roll No. 1 which had the following properties:

Resin Solids	35.1%
Volatile Content	5.3%
Laminate Flow at 150 psi	4.7%

The cure cycle for the Fiberite blocks follows:

1. Vacuum bag 56,000 grams of precut 10.5 x 11 inch plies of MX-4926.
2. Place in hydroclave and draw full vacuum.
3. Increase hydroclave pressure to 1000 psi.
4. Increase temperature 100°F per hour to 185°F.
5. Hold at 185°F for 15 hours.
6. Increase temperature 100°F per hour to 320°F.
7. Hold at 320°F for 13 hours.
8. Cool down 100°F per hour under pressure.
9. Remove part and vacuum bag.

FM-5014 Nozzle Component

U. S. Polymeric FM-5014 phenolic-graphite fabric was molded in nozzle ring sections by H. I. Thompson Company (HITCO), Gardena, California.

The throat section of the nozzle was produced by hand rosette layup of ring sections, each with a final thickness of 4 inches in the nozzle axial direction. The hand layup was done in a female mold using prepreg segments cut to a pattern that resulted in each ply extending for approximately 90 degrees around the nozzle ring segment in a plane extending from edge to edge in the nozzle axial direction and intersecting both the inside and outside surface of the ring. Viewed with the nozzle cross section in a horizontal plane, the edge-to-edge slope of the laminate plane was 5 to 10 degrees, extending clockwise from top to bottom. Initial patterns were laid on a sloped block which was removed and replaced with prepreg plys when the layup sequence around the ring section returned to the starting point. The finished hand layup extends above the mold surface. The prepreg patterns were cut randomly from the broadgoods for maximum utilization of material, so that yarn orientations in the final part are random. The processing sequence is described by HITCO as follows:

1. Cut layup patterns from broadgoods, package in moisture resistant film with identifying pattern number and store until used.

2. Clean mold and apply release agent.
3. Layup precut patterns in a clockwise direction (mold horizontal), maintaining a consistent layup density throughout that will insure a 5° to 10° face-to-face orientation of the cured ring.
4. Vacuum bag layup assembly and preheat in circulating air oven for a maximum of 95 minutes, depending on temperature, at 160 to 200°F.
5. Mechanically compress (debulk) the preheated layup assembly in a cold press by alternately opening and closing the press followed by holding under pressure until the surface temperature is below 110°F.
6. Preheat the assembly in a vacuum bag at 26 inches Hg vacuum to over 170°F in 2 1/2 hours, then apply 300 psi autoclave pressure and maintain both pressure and vacuum during a 30 minute hold at temperature followed by a 3-hour cool down to below 100°F.
7. Hydroclave cure the debulked assembly in vacuum bag held at more than 24 inches Hg initial vacuum and no more than 12 inches Hg above initial value throughout the cure. Raise temperature to 170 to 210°F at 200 psi maximum and maintain for 130 minutes maximum. Raise pressure to 1000 ±50 psi and then raise temperature to 290 to 340°F; maintain temperature for 150 to 240 minutes, and cool to 125°F maximum before increasing pressure.
8. Remove cured billet from layup mold and postcure in circulating air oven at 275 ± 20°F for 18 ± 2 hours, followed by cooling to 200°F maximum before removal from oven.
9. Package billet to protect from moisture and dirt until machining.
10. Machine billet in following sequence:
    a. Machine diameters.
    b. Cut 24 core specimens and 12 dust samples for quality inspection.
    c. Machine billet top surface.
    d. Machine billet bottom surface.

The phenolic graphite ring section for which records were provided showed the following properties on six core specimens:

Characteristic	Test Method	Standard	Test Values
Density	ASTM D-792	88 lb/ft^3 min.	89.7-90.3 lb/ft^3
Volatiles	4 MDS 91605 44.8	3% max.	2.8-2.9%
Interlaminar Shear Strength	FTMS 406-1041	1500 psi min.	3,599-4,935 psi
Degree of Cure	ASTM D-494	99.5% min.	99.9%

Final inspection of the ring segments determined that billet density was above 88 lbs/ft^3 and that dimensional, radial and flat radiographic, and alcohol penetration tests were passed.

FM -5055A Plasma Test Specimens

The U. S. Polymeric FM-5055A phenolic carbon plasma test samples provided by the Air Force had been machined by Aerospace Corporation from a block provided by General Electric Company, MSD, Philadelphia, Pennsylvania. Seven right cylinder models, with the circular test face parallel to the laminates, were exposed to a simulated reentry environment at Space General Corporation, El Monte, California, to produce the chars for characterization. Pictures of the models before and after test and a discussion of the plasma tests are given in Reference 22 .

The 7 1/4" x 6 5/8" x 2 5/8" block from which all plasma test samples were obtained was molded from FM-5055A prepreg lot C-6845, roll No. 17 with the following properties:

Resin Solids	35.6%
Volatile Content	4.5%
Flow	17.4%

The molding cycle was as follows:

1. 500 psi at 300°F for 5 minutes
2. Reduce to zero pressure at 300°F for 30 minutes
3. Raise pressure to 1000 psi at 300°F for 60 minutes
4. Post cure material at 250°F for 16 hours

The plasma test models were machined from the block by conventional methods, except that all cutting was done dry to avoid contamination of the material.

SECTION IV

CHAR CHARACTERIZATION METHODS

Methods of char characterization were developed for defining microstructural and chemical compositional features of charred ablators as a function of depth and prior thermal history. These methods enabled correlating furnace-produced chars, used in thermophysical property measurements, to real chars. An X-ray density measurement technique provided a continuous, nondestructive measurement of the variation of density with depth in ablation chars and nondestructively verified the uniformity of furnace chars. Photomicrography, X-ray diffraction, density and porosity techniques delineated microstructure and areas of graphitization. Thermogravimetric (TGA) and elemental chemical analyses were used to determine the amounts of residual resin while differential thermal analyses (DTA) indicated the thermal stability of the chars. Computer predictions of density and temperature throughout the ablator, including the cooldown period, were transformed to functions of depth in the final ablation chars to relate observed characteristics to temperature history. These predictions showed that the major density and resin content gradients in chars from ablated specimens were formed during cooling but also identified the char characteristics resulting only from the period of heat up and steady state ablation.

Characterization as a function of depth in the post-test chars enabled delineation of the major ablation zones in each char as follows:

1. The virgin zone, where no pyrolysis has occurred.
2. The pyrolysis zone, where phenolic resin pyrolysis occurs leaving the major density and resin content gradients.
3. The mature char zone, where resin pyrolysis is complete but redeposited hydrocarbon material may exist.

The mature char zone is further subdivided into:

Zone I, A "graphitized" mature char zone at the surface
Zone II, An "ungraphitized" intermediate mature char zone
Zone III, A zone of nearly complete pyrolysis at the boundary between the mature char and pyrolysis zones,

which are reproduced by charring virgin material in a furnace to yield the specimens for thermophysical property measurements. These subdivisions are described below and in Section VIII. Both characterization and thermophysical property results are discussed in terms of char zones I, II, and III.

CHAR SAMPLING

The sampling sequence for each post-test ablation char was established to insure maximum utilization of material and good resolution of property variation with depth. Sampling of 120-inch nozzle sections was based on char columns approximately one inch square which provided sufficient surface size and bulk quantities when increments were taken at 0.1-inch depths. The 0.1-inch increment was based on photomicrographic observations on the post-test nozzle chars, but after the Radocon X-ray density survey technique was developed, increments were varied to obtain maximum resolution of property variations in areas exhibiting a steep density gradient such as the pyrolysis zone. This approach enabled obtaining all required characterization samples with good depth resolution on a single column of material from the small plasma test sample of the FM-5055A material.

Sampling of each post-test char is described below. Samples are coded to provide location references for all data. Rough sample cuts were made with a carbide saw and fine cuts, with a diamond saw. All cuts were made dry to avoid contamination of the samples.

MX-4926 Char Sampling

Figures 3 through 5 illustrate the specimen locations in the MX-4926 nozzle material. Radial columns on upstream faces of segments are designated by a W series of numbers and char-layer depths, by an H series.

The one-inch thick segment, II-C between axial stations L5 and L6, was selected as the throat sample for the analyses because it was located at the crown of the char surface and represented the location of minimum throat area in the nozzle.

The char surfaces and char zone layers were found to be parallel to the silica-phenolic base in segment II-C; therefore, char layer depth specimens (H series) were cut parallel with the base for machining accuracy on columns W-2 and W-3, as shown in Figure 5.

Radial plane photographic analyses were made of the D-radial plane from excess material adjacent to W-1. Column W-4 was used for initial X-ray transmission analyses, ultra-thin section photographic analyses, and electron microprobe elemental analyses. Subsequently, column W-1 and a downstream segment from half II between stations L6 and L7 were used for Radocon X-ray transmission analyses.

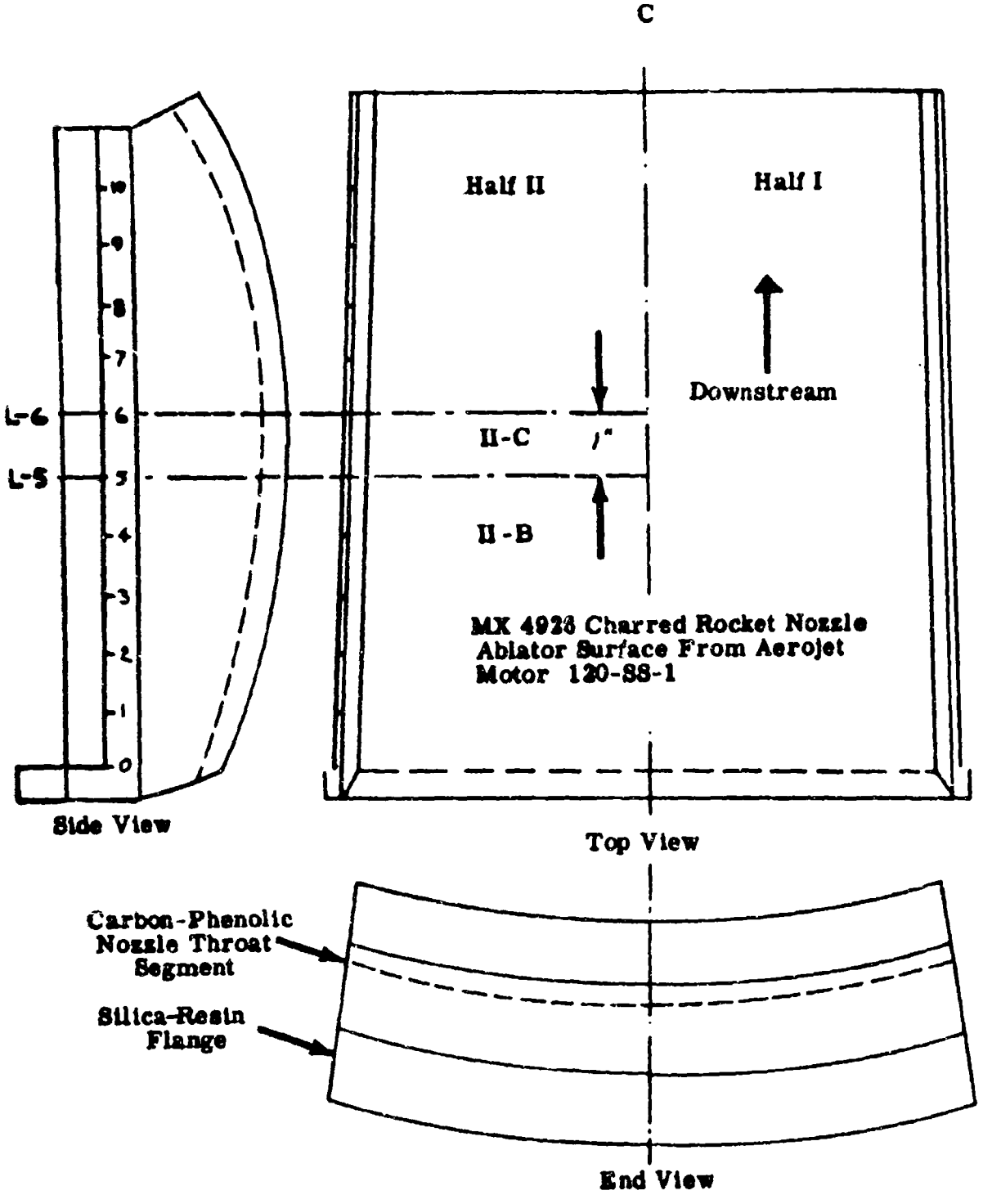

FIGURE 3 MX-4926 CHAR THROAT SAMPLING LOCATION

MX 4926 Charred Rocket Nozzle
Ablator Surface From Aerojet
Motor 120-SS-1, Throat Specimen
II-C At Length Stations L-5 to L-6

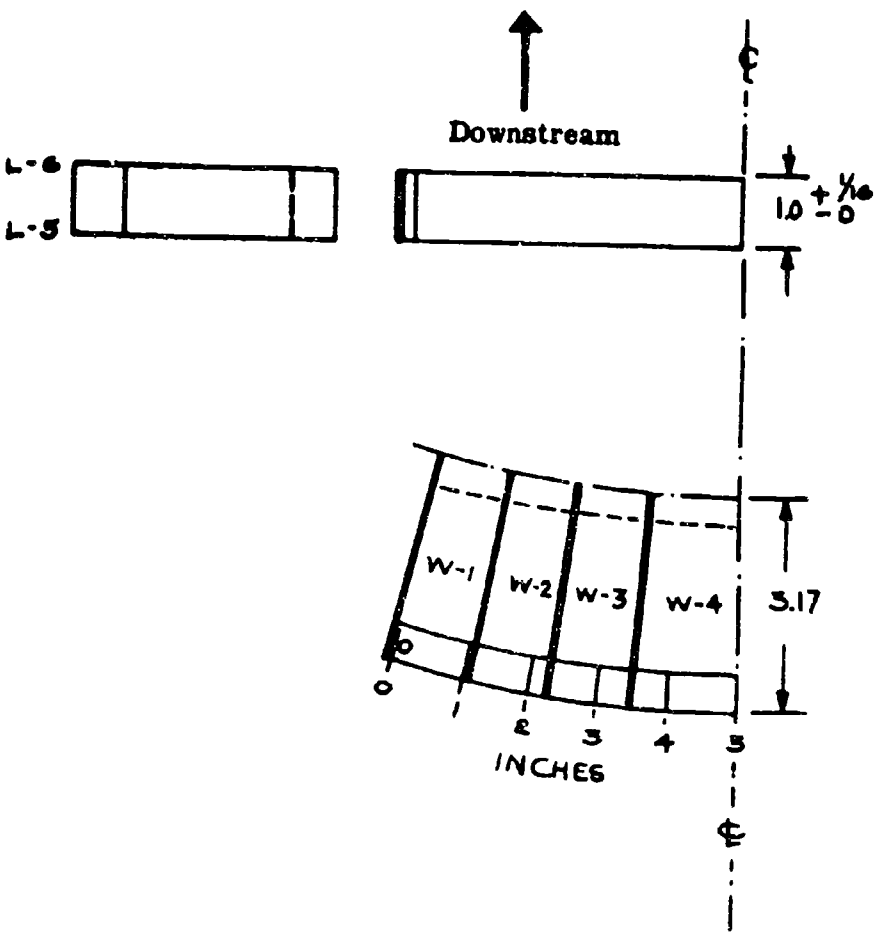

FIGURE 4 MX-4926 CHAR THROAT SAMPLE LOCATIONS OF RADIAL SEGMENTS

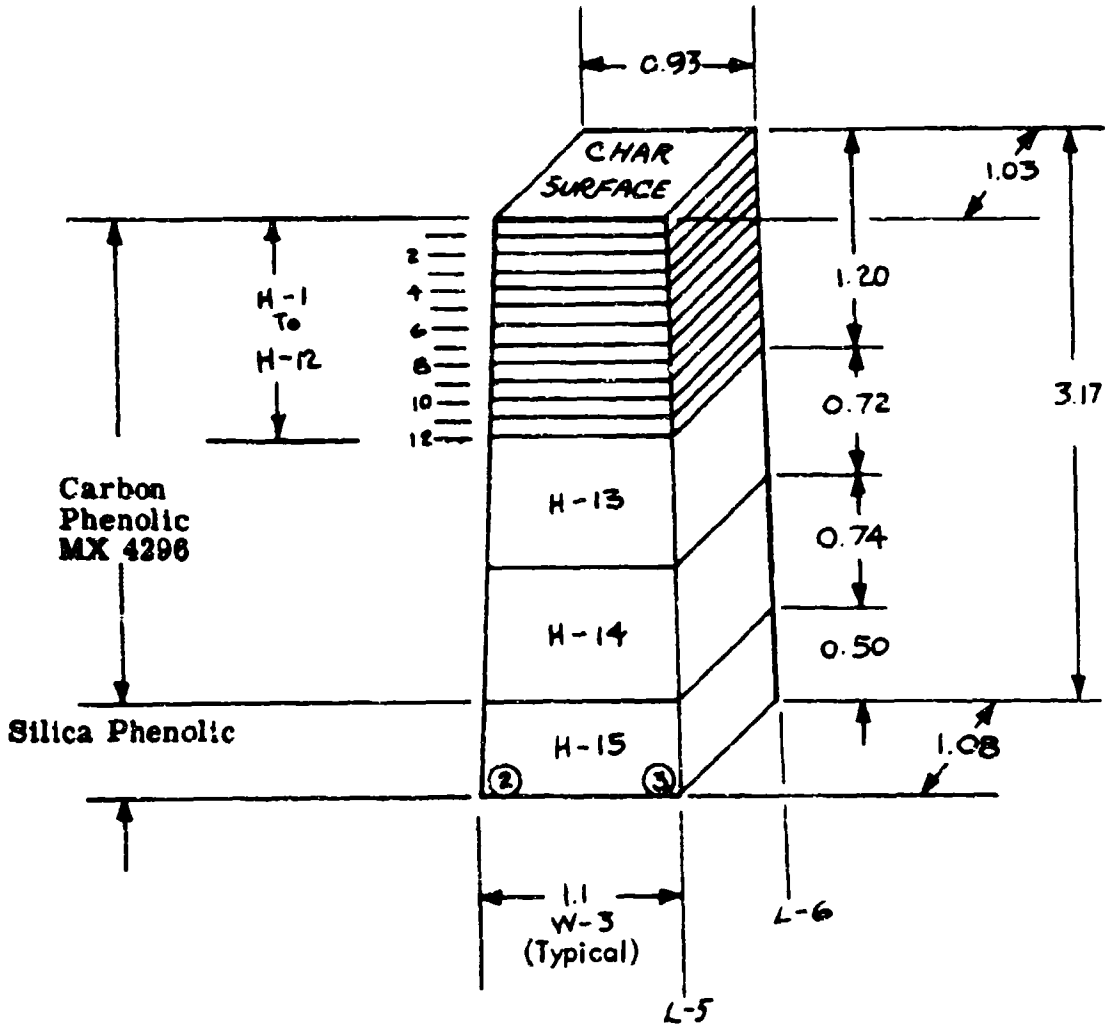

FIGURE 5 MX-4926 CHAR THROAT DEPTH SPECIMEN LOCATIONS

FM-5055A Phenolic-Carbon

Only one of the plasma test models displayed reasonably flat laminations and uniform side-to-side density suitable for meaningful characterization. The characterization of this model required eliminating the mercury porosimeter tests, using minimum sample sizes, and proper sequencing of all other characterization tests.

Radocon X-ray determinations of the density profile on 0.75-inch wide slices from the center of the plasma test specimens provided the basis for selection of uniformly charred material for characterization. Radocon data for the most uniform plasma test model, Number 20, is shown in Figure 31. The X-ray density surveys showed significant side-to-side variation in final char density caused by two factors: uneven interlaminar dimensional changes and delaminations, and uneven fabrication of the original block. The laminations were so nonuniform, even in the virgin material, that a ply across the 2-inch diameter might curve up 0.25 inch at one end and down 0.25 inch at the other. Radocon testing identified only model Number 20 as suitable for characterization. The X-ray density profile also guided the sectioning illustrated in Figure 6.

The sections shown in Figure 6 were utilized to provide samples for all tests. Reflected light photomicrographs were obtained on the vertical face of the unsliced portion of the slab. X-ray diffraction measurements and electron beam microprobe analyses were made on the slice surfaces. Dry bulk density and helium pycnometer penetrated porosity were determined on the 0.75-inch square test portion of each slice. Each slice test portion was then ground and the powder was proportioned among the thermal and elemental analyses.

FM-5014 Phenolic-Graphite

Figures 7 and 8 illustrate the specimen sample locations on the FM-5014 nozzle material. Figure 7 shows the long nozzle-segment configuration comprised of successive canted blocks. The downstream portion of Block B was located at the crown of the char surface with respect to the outer cylindrical surface and represented the minimum diameter nozzle throat area location.

An outward warp on the downstream face of Block B was machined flat to make a reference surface. Throat sample section B-1 was cut to a uniform thickness of 1.10 inches. Radial plane lines were then established on the faces. Radial column widths between radial planes are denoted by a W series of numbers and char-layer depths by an H series, as in the MX-4926 material.

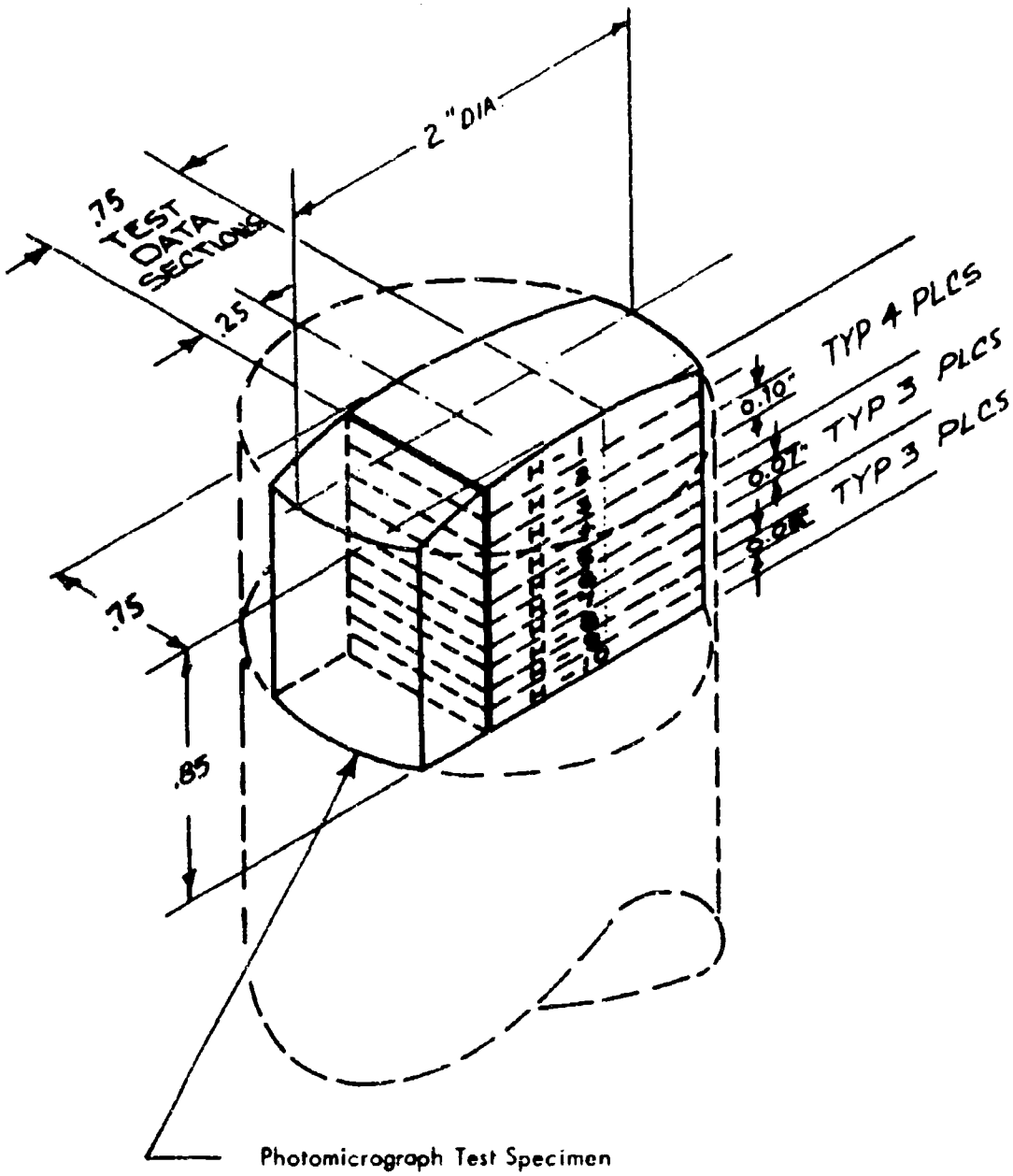

FIGURE 6 FM 5055A PLASMA CHAR DEPTH SPECIMEN LOCATIONS

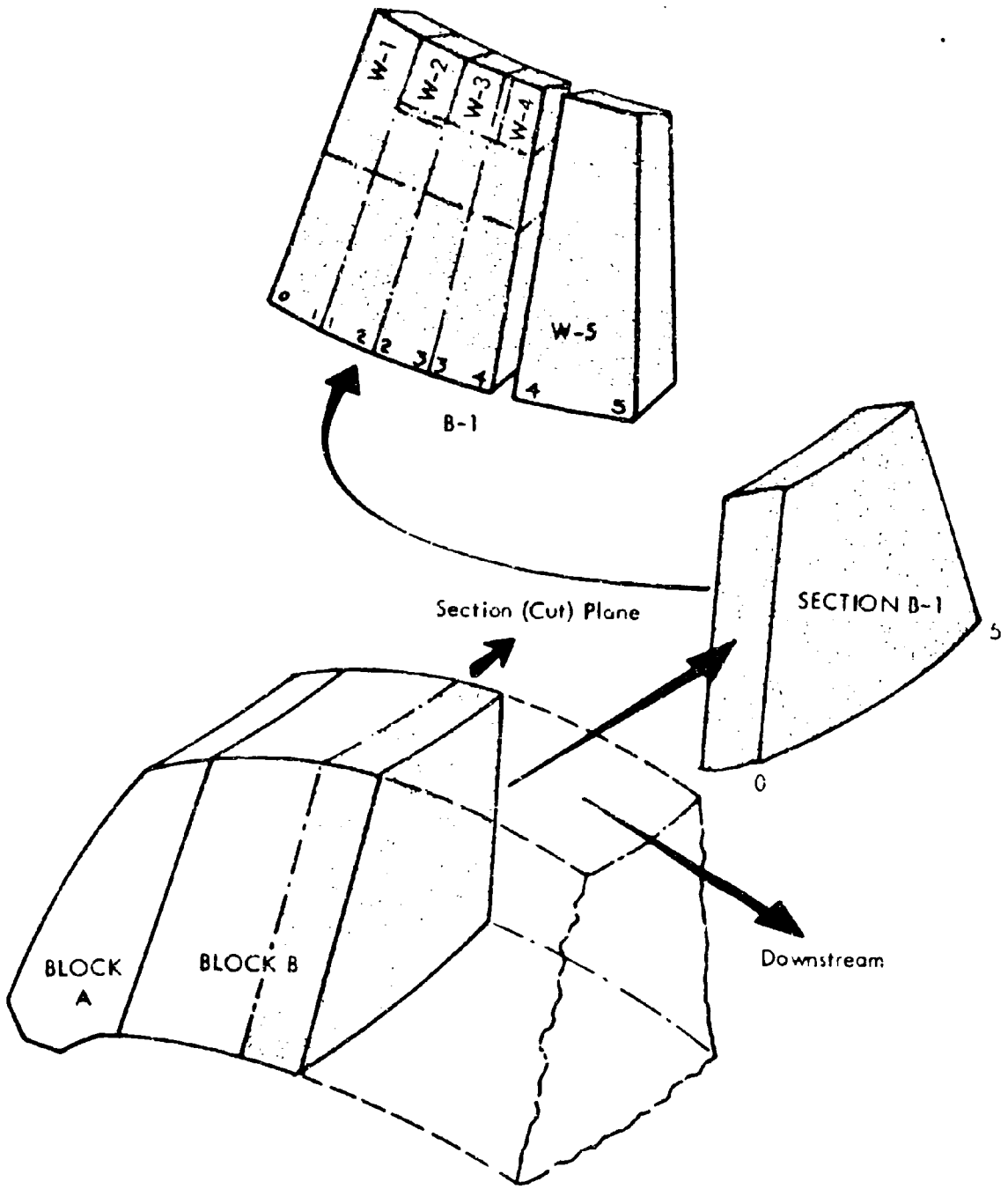

FIGURE 7 FM-5014 CHAR THROAT SAMPLE AND RADIAL SEGMENT LOCATIONS

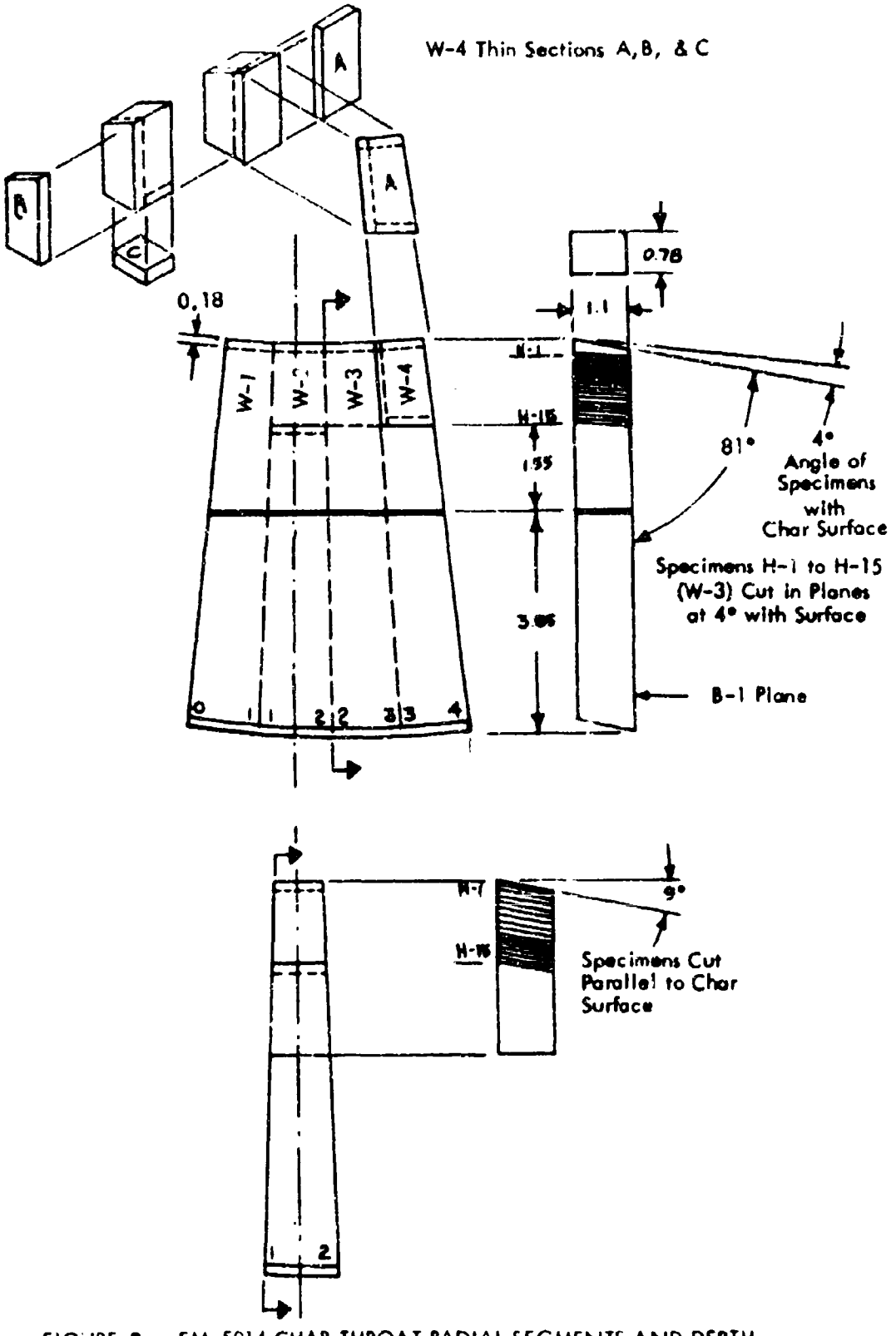

FIGURE 8 FM-5014 CHAR THROAT RADIAL SEGMENTS AND DEPTH SPECIMEN LOCATIONS

Column W-1 was used for photographic analysis of the 1-1 radial plane. Columns W-2 and W-3 were used for char-layer depth samples. Ultra-thin section photographic analyses and electron microprobe elemental analyses were conducted on Column W-4.

Segment W-5 of Section B-1 was used for Radocon X-ray transmission analyses.

The two radial columns W-2 and W-3 were sectioned differently for char-layer depth samples. Column W-2 char-layer specimens were cut parallel to the char surface and column W-3 char-layer specimens were cut parallel to visual char layer zones in order to obtain true char zone data. Measurements on section B-1 and on initial one-power photomacrograph of the 1-1 radial plane indicated that the char-surface plane sloped downward in the upstream direction at an 81° angle with the face planes. Visual char-zone layers were parallel with the char surface to only about a 0.3-inch depth; below a 0.4-inch depth char zones were parallel with the outer cylindrical surface at an 85° angle with face planes (4° angle with char surface).

PHOTOMICROGRAPHY

This method was used initially to estimate char zone depths, the thickness and depth requirements for char-zone samples, and the condition of material in char zones. In characterization, it was used to confirm the spatial arrangement, phases present, void dimensions, and general orientation of the various phases.

Photomacrographs, 1 to 2.5 power, were made under reflected light on planar polished surfaces of both unpotted and Marglas epoxy resin vacuum potted specimens. Photomicrographs with the Zeiss Ultraphot II Metallograph, 2.5 to 2500 power, utilized potted and polished planar views, with reflected light for conventional detail and polarized light for anisotropic effects such as internal graphitization. Thin sections were made by thinning potted planar sections to the thickness of the specimen component viewed (e.g., a cloth, yarn, or fiber thickness dimension). Reflected and transmitted light were used separately and in combination on thin section photomicrographs.

Special emphasis was placed on differentiating crystalline from amorphous material by reflection characteristics under polarized light. The high magnification obtained with the Ultraphot makes the primary zones of char graphitization discernable. Since crystalline particles can have dimensions much less than one micron, all crystalline carbon cannot be seen using optical techniques.

DENSITY AND POROSITY ANALYSIS

Density and porosity are considered as combined characteristics that affect both thermophysical and thermomechanical properties, and thermal conductivity proved to be very dependent on density/porosity characteristics. Direct measurements of densities and porosities provided the primary data and the calibration for the Radocon X-ray transmission analysis of density profile developed on this program.

The particular density obtained is a function of the method used to measure sample volume. The total sample volume, including all voids, gives the apparent ρ_a. Since both weight and volume data were usually obtained on dried samples, the term ρ_{ad}, apparent dry density, is used for dried samples. Solid densities, ρ_s, are based on the weight and the solid volume of dry powdered samples as determined in the gas pycnometer. Powdering the sample is assumed to eliminate all closed porosity. Gas pycnometer determinations of solid volume on dry bulk samples yield ρ_{as}, apparent solid volume, since the volume of closed porosity is included.

Porosity data was obtained as porosity fraction, ξ, from density data by the relationships;

$$\xi_t = 1 - \rho_{ad}/\rho_s \qquad (1)$$

$$\xi_o = 1 - \rho_{ad}/\rho_{as} \qquad (2)$$

ξ_t is total porosity based on true solid density, ρ_s, and ξ_o is open porosity consistent with its calculation based on apparent solid density, ρ_{as}, that includes closed pores. Closed porosity, ξ_c, is simply the difference between ξ_t and ξ_o. Porosity fractions measured directly by mercury penetration are designated as penetrated porosity, ξ_p.

Direct Density and Porosity Measurements

Apparent dry densities, ρ_{ad}, apparent solid densities, ρ_{as}, and open porosity fractions, ξ_o, were determined for sliced specimens and blocks before their usage in other tests.

Apparent dry densities,).3 percent precision were calculated from weight and dimensional n. .ents on the dried char depth slices. Most of the direct density measurements were made on oven dried (150°F) and vacuum outgassed samples. It was found early in the program that the charred materials were hygro-

scopic and had to be dried to obtain reproducible data. Before drying, a mass spectrographic survey of the entrained volatiles was run to establish that only water was being eliminated.

Solid volumes of both bulk and ground samples for the calculation of ρ_{as} and ρ_s were determined in a Beckman Model 930 gas pycnometer. Initial tests with air for MX-4926 char were unsuccessful due to absorption of moisture during the compression cycle. Outgassing, desiccator storage, and three helium purges were required to obtain reproducible results on all three charred materials. Accuracies of ρ_{as} and ρ_s were estimated at 3 percent, based on the solid volume determination.

Total penetrated porosity fractions, ξ_p, including all open porosity with openings between 0.01 and 100 microns in diameter were determined by mercury penetration with the Aminco-Winslow 15,000 psi porosimeter. Photomicrographic analysis had indicated that, except for complete delaminations, the pore/microcrack diameters were below the 100 micron upper limit of this technique. Determination of approximate pore size distribution by porosimetry provides data needed for detailed correlations of char thermal conductivity data and for use in analysis of internal gas flow and pressure build-up during ablation. When the data is used for these purposes, it should be correlated with the photomicrographs showing pore shapes and sizes relative to the sizes of pore openings. The amount of mercury penetration vs. pressure gives porosity fractions as a function of the size of pore openings, which may be smaller than the pores themselves.

X-Ray (Radocon) Transmission Analysis of Density Profile

The Radocon X-ray transmission test provided a sensitive and rapid nondestructive method for establishing the density gradient in carbon or graphite reinforced chars since density variations of 0.005 g/cm^3 can be resolved in a distance as small as 10 mils along any path in material up to 1-inch thick. This sensitivity was useful in establishing that important density changes were being resolved by the measurements on char slices. This nondestructive test also provided a method for establishing the uniformity of thermophysical property test samples.

The test facility shown in Figure 2 utilized a Norelco X-ray tube, 25 to 150 KVCP, with a beryllium window operated at 90 KV and 7.5 milliamperes. Samples were supported on a horizontal traversing mechanism operated at 2 inches per minute. The sensing system aperture was a 0.125-inch thick lead sheet containing a slot 0.012-inch wide (in the traverse direction) and 0.25-inch long (parallel with char surface) located 5 inches below the tube target. An unshielded

FIGURE 9 X-RAY TEST SETUP

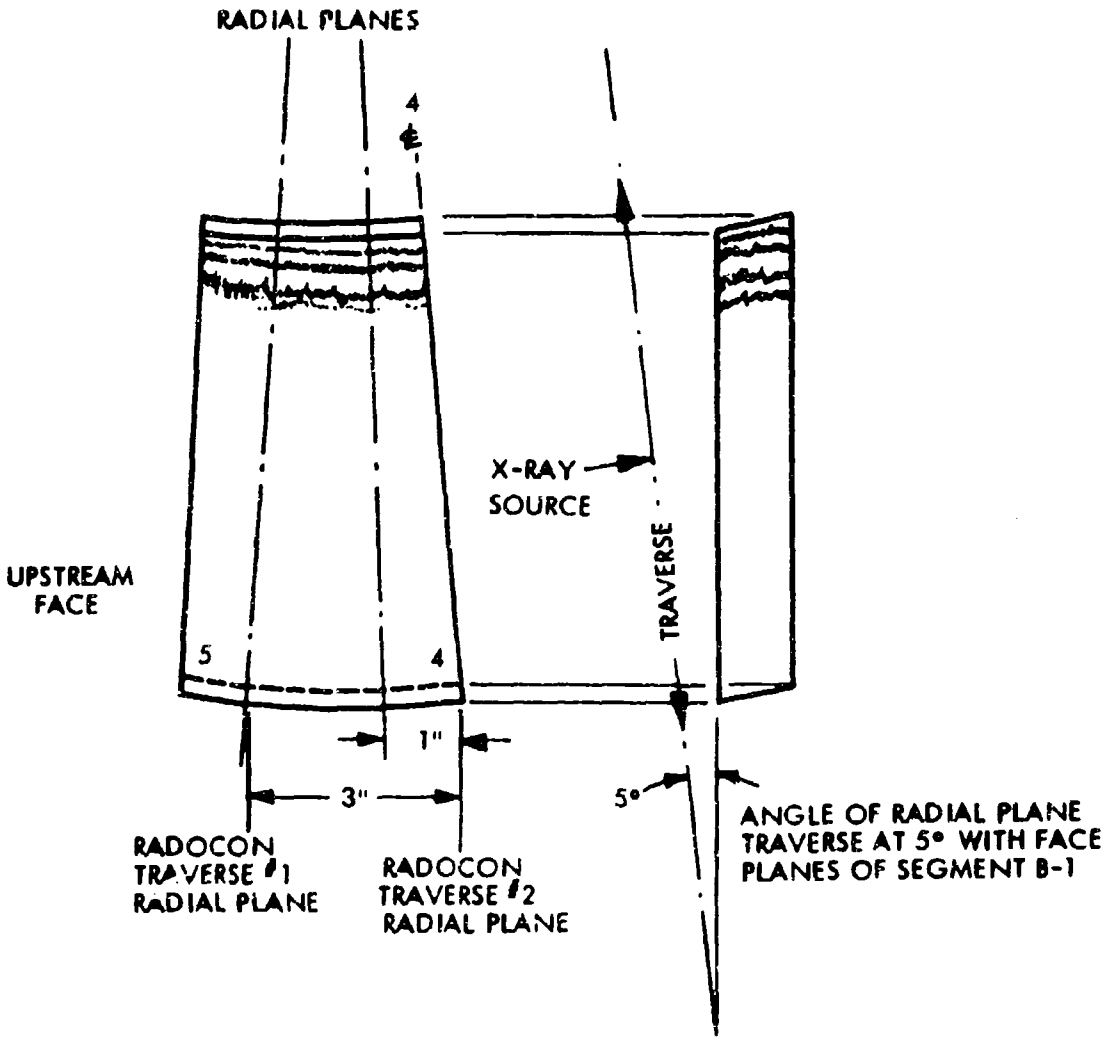

FIGURE 10 LOCATION OF RADOCON TRAVERSES,

FM-5014 CHAR SEGMENT B-1

Victoreen Model 601 ionization tube sensor was positioned directly below the slot. X-ray transmission from the tube sensor was received by a standard Radocon Model 575 ratemeter and transmitted to a Sanborn char recorder. Figure 10 shows the radial trace orientations for the FM-5014 char sample, where the sample faces were sloped to maintain X-ray penetration parallel to the char surface, and Figure 11, typical Radocon traces for MX-4926 and FM-5014.

An empirical calibration for obtaining apparent dry density, ρ_{ad}, based on curves of log Radocon readout R (Roentgens/minute) versus the product of apparent dry density and thickness, $\rho_{ad}t$ (g-inches/cm^3) was used for each material. This approach is similar to the theoretical exponential relationship

$$\log R = f\left(t \sum_{1}^{i} X_i \rho_{si} \mu_{mi}\right) \qquad (3)$$

but avoids the necessity of determining the parameter $X_i \rho_{si} \mu_{mi}$ (volume fraction · density · X-ray absorption coefficient) for very solid phase present in the char layer.

This calibration method utilized the apparent dry densities, ρ_{ad} (g/cm^3), determined directly on char depth slices. Densities at terminal (virgin and extreme char surface) and char zone inflection points (maximum and minimums within char layer) were obtained. Sample thickness t(inches) and Radocon readings R were then obtained from the radial traces for charred materials at corresponding terminal and inflection points regardless of char depth position. Plots of log R versus product $\rho_{ad}t$ for each material are shown in Figure 12 independent of char depth position. The calibration obtained for MX-4926 was assumed to hold for FM-5055A, since the two materials are similar.

Individual Radocon traces were analyzed at char depth intervals corresponding to density specimen centerlines. Products $\rho_{ad}t$, corresponding to each Radocon number, were obtained from the semi-log plots and divided by true thickness, t, at the char depth location in order to obtain Radocon predicted density. Predicted density profiles were then plotted versus char depth location from Radocon traces.

THERMAL ANALYSIS

Thermogravimetric (TGA) and differential thermal analyses (DTA) of char depth slices identified fully charred layers and characterized the char layer versus depth in terms of thermal stability. These tests, particularly TGA, give quantitative characterization in the pyrolysis zone since the measured responses are proportional to the amount of incompletely pyrolyzed resin remaining.

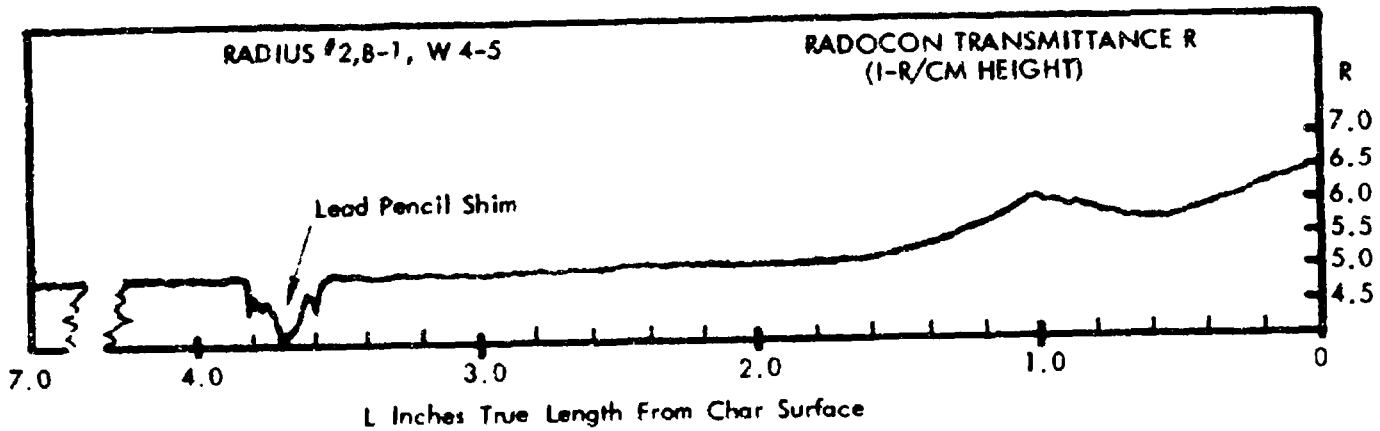

FM 5014 CHAR, TRUE LENGTH SCALE OVERLAY ON ONE TYPICAL SANBORN CHART TRACE

1. REFERENCE
   R = 97 FOR AIR ON RADOCON 100 SCALE
2. SANBORN SCALE SET FOR MAXIMUM SENSITIVITY WITH MAXIMUM RANGE BETWEEN VIRGIN AND CHAR LINEAR WITH THE RADOCON 10 SCALE.
   CHART SPEED 1 MM/SEC
3. RADOCON TRUE READING R MARKED ON EACH TRACE DURING OPERATION

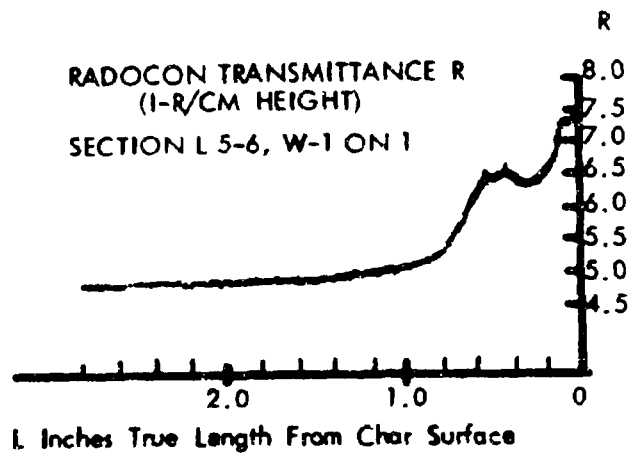

MX 4926 CHAR, TRUE LENGTH SCALE OVERLAY ON ONE TYPICAL SANBORN CHAR TRACE

FIGURE 11 TYPICAL RADOCON-SANBORN CHART TRACES OF CHAR DEPTH

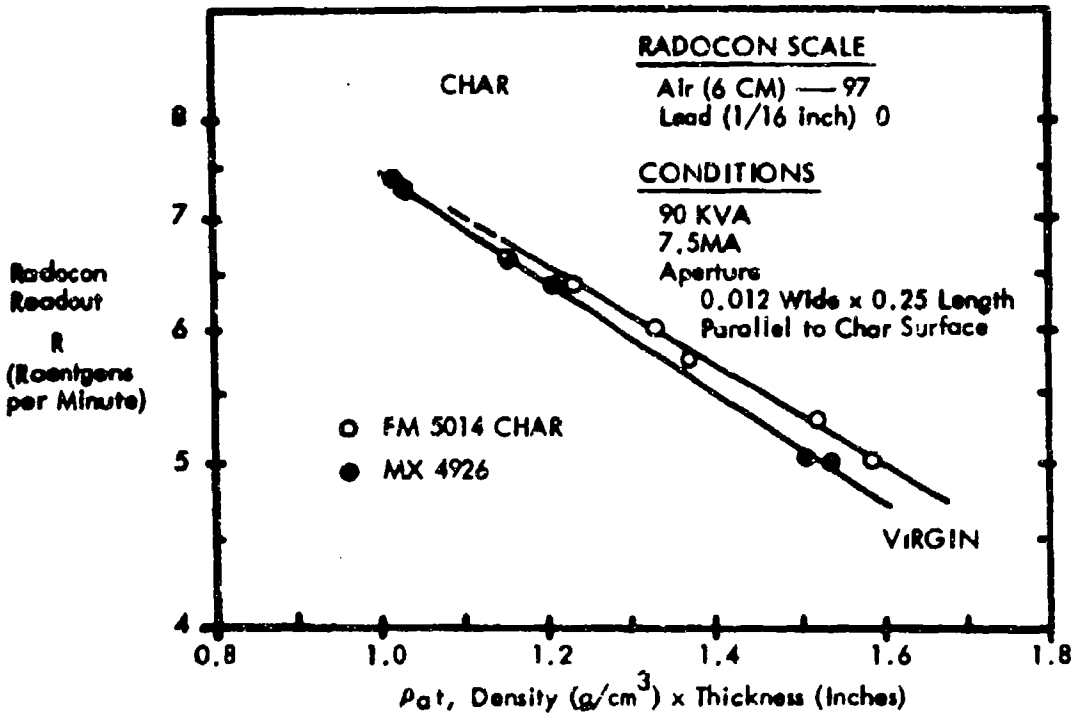

FIGURE 12 EMPIRICAL CORRELATION OF X-RAY TRANSMITTANCE, R, VERSUS THE CHAR DENSITY-THICKNESS PRODUCT, ρ_{at}

Dynamic TGA's of 0.5 gram samples were run in helium to 1900°F at a constant heating rate of 10°F/minute in a Stanton Thermobalance. The data is reduced to tabular form for concise presentation by tabulating the nodes or temperature points denoting changes in rate of weight loss. Relative thermal stabilities of char slices are indicated primarily by total weight loss and secondarily by the tabulated temperature nodes. Incremental weight losses between nodes are also related to the quantity and nature of residual resin or pyrolysis deposition products.

DTA tests on 5 to 15 milligram samples were run on a Stone Differential Thermal Analyzer in air and helium at a constant heating rate of 18°F/minute to 1800°F. Data in the usual form of microvolt output of the differential thermocouple versus temperature were obtained for the net exothermic events in air atmosphere. FM-5055A material was also run in helium, but the endothermic events expected were too small to give meaningful data. For each discernable exothermic event, the initial temperature, Ta, exotherm maximum temperature, Tp, and end temperature, Tc, were tabulated along with the heat of reaction for the event.

Heat of reaction, ΔH, for each net exothermic event is proportional to the area under the reaction curve. Areas under exotherms were graphically integrated by planimeter measurements and were converted to heats of reaction per unit weight of sample (microvolts °C/milligram) by the following relationship:

$$H/W = \frac{1}{w} \int_{Ta}^{Tc} (\mu V)\, dT \qquad (4)$$

This DTA parameter was calculated for MX-4926 and FM-5014 chars to determine its usefulness for characterization. The single DTA parameter most sensitive to specimen location in the char was the initial temperature of the first exothermic event in the air atmosphere measurements.

ELEMENTAL ANALYSIS

Quantitative elemental analysis of major constituents (C and H) confirmed results of other characterizations which depend on amounts of hydrocarbons, particularly thermal analysis, that defined zones of mature char, pyrolysis product deposition zones, and interior pyrolysis zones. Elemental analysis also provides a basis for partition of the char at any depth into the fraction of reinforcement and residual resin. A qualitative analysis for signficant impurities was conducted using an electron beam microprobe.

The primary analysis method was the microcombustion determination of carbon and hydrogen by the method of Pregl. The difference between the total mass and sum of carbon, hydrogen, and ash was assumed to be oxygen. Samples were first

thoroughly oven dried and vacuum degassed to remove absorbed water then burned in an oxygen atmosphere at 700°C, except for more stable layers near the char surface which required a temperature of 900°C. A standard of C_8H_9NO was run between specimen runs.

Electron beam microprobe analyses were used mainly to detect the more stable impurities such as metals and their oxides since the vacuum environment and heat of the electron beam tend to drive off less stable components. Analyses were conducted on an Applied Research Laboratories microprobe using oscillograph readout.

X-RAY DIFFRACTION ANALYSIS

X-ray diffraction analysis of the surfaces of char depth slices provided a quantitative measure of the relative concentrations of anisotropic or crystalline material. Most of this anisotropy was visible in polarized light photomicrographs. This anisotropy was arbitrarily referred to as "graphitization" in this report, through the crystal spacing intensities are far less than for bulk graphite, and there is no confirmation of the true graphite structure in the anisotropic material.

X-ray diffraction analysis of "graphitization" produced chart recordings of diffraction intensities, I, in counts per second versus diffraction angle. Maximum or peak intensities occurred at the angles corresponding to the two predominant crystal spacings for graphite and were used as a measure of graphitization. Figure 13 shows typical char data and corroborating Debye-Scherrer diffraction pattern photographs for an MX-4926 char. The graphic determination of intensity relative to the background is also illustrated. Diffraction pattern photographs are less sensitive measures of graphitization, but they verify the crystal spacings.

COMPUTER ABLATION ANALYSIS

Meaningful ablator char characterization must be related to the density and temperature history at that point during ablation since ablation processes and rates depend upon temperature and thermophysical properties of the ablator at any given time. In addition, the maximum temperature experienced establishes the maximum temperature at which thermal properties are required at that point in the char and gives the temperature limits for the three zones in the char selected for reproduction in the form of thermophysical property test specimens.

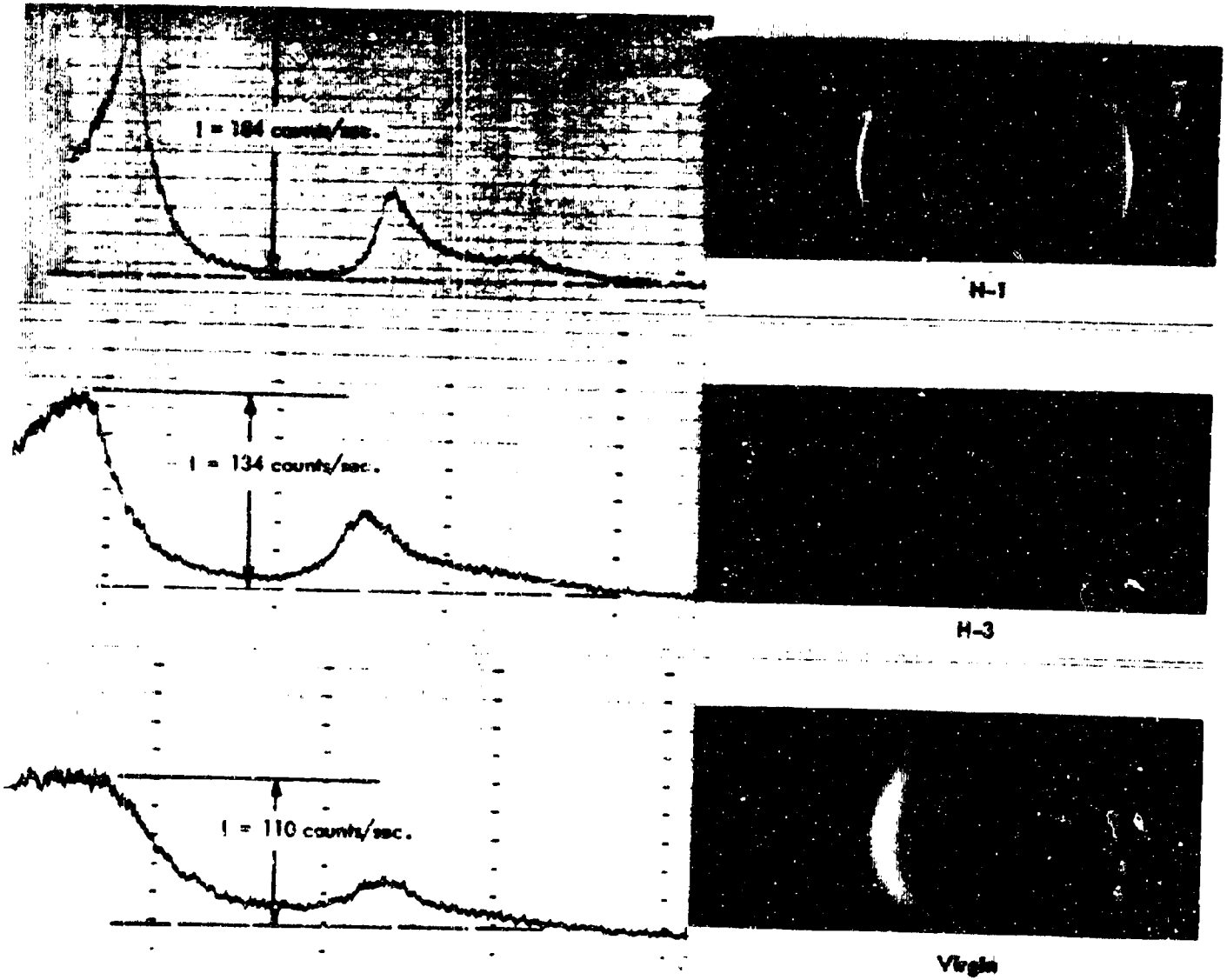

FIGURE 13: TYPICAL X-RAY DIFFRACTION DATA FOR MX4926 CHAR

SECTION V

MX-4926 PHENOLIC CARBON CHAR CHARACTERISTICS

Characterization of the char in the MX-4926 phenolic carbon nozzle throat from Aerojet-General Corporation's 120-SS-1 120-inch solid propellant booster provides a complete physical and chemical description of the post-test ablator as a function of depth. The results are discussed in terms of their variations within and between the major zones: virgin, pyrolysis, and mature char zones.

The data are also discussed in terms of their significance for the definition of the three subzones in the mature char zones I, II, and III, used as the basis for thermophysical properties.

VISIBLE CHARACTERISTICS

Major char zone, char depth, and cloth layer orientations were defined by the 1.25 power photomicrograph shown in Figure 14 . Analysis of this plane to a depth of 1.1 inches using a 63-power assembled strip photomicrograph (6 feet long) showed size and distribution of voids, char zone degradation effects, and spatial dimensions of the carbon cloth matrix.

Cloth-yarn spatial dimensions, cloth weave information, additional description of voids, extent of char degradation and polarized light observations of anisotropic "graphitized" portions of the char were obtained on potted and polished thin sections. Thin sections were made in both yarn directions in planes perpendicular to cloth as shown in Figure 15 . Because there was no distinguishable difference between the photomicrographs of the two yarn directions, only those of thin-section A are shown. In Figure 16 , large cracks and voids are apparent under transmitted light. Figure 17 shows the surface portion in a 25X magnification combined light view where voids are represented by the white (clear through the thin section) and dark areas. Successive 200X and 2000X magnifications of a void location shows light transmitted through a small portion of the dark void area as well as the size and undegraded condition of fill yarn fibers.

Successive magnifications under polarized light in Figures 18 through 21 show the high concentration of anisotropic "graphitized" material at pore surfaces and around fibers and the columnar deposition of anisotropic material at the surfaces of large pores. White areas indicate high concentrations of anisotropic material.

SECTION V

MX-4926 PHENOLIC CARBON CHAR CHARACTERISTICS

Characterization of the char in the MX-4926 phenolic carbon nozzle throat from Aerojet-General Corporation's 120-SS-1 120-inch solid propellant booster provides a complete physical and chemical description of the post-test ablator as a function of depth. The results are discussed in terms of their variation within and between the major zones: virgin, pyrolysis, and mature char zones.

The data are also discussed in terms of their significance for the definition of the three subzones in the mature char zones I, II, and III, used as the basis for thermophysical properties.

VISIBLE CHARACTERISTICS

Major char zone, char depth, and cloth layer orientations were defined by the 1.25 power photomicrograph shown in Figure 14 . Analysis of this plane to a depth of 1.1 inches using a 63-power assembled strip photomicrograph (6 feet long) showed size and distribution of voids, char zone degradation effects, and spatial dimensions of the carbon cloth matrix.

Cloth-yarn spatial dimensions, cloth weave information, additional description of voids, extent of char degradation and polarized light observations of anisotropic "graphitized" portions of the char were obtained on potted and polished thin sections. Thin sections were made in both yarn directions in planes perpendicular to cloth as shown in Figure 15 . Because there was no distinguishable difference between the photomicrographs of the two yarn directions, only those of thin-section A are shown. In Figure 16 , large cracks and voids are apparent under transmitted light. Figure 17 shows the surface portion in a 25X magnification combined light view where voids are represented by the white (clear through the thin section) and dark areas. Successive 200X and 2000X magnifications of a void location shows light transmitted through a small portion of the dark void area as well as the size and undegraded condition of fill yarn fibers.

Successive magnifications under polarized light in Figures 18 through 21 show the high concentration of anisotropic "graphitized" material at pore surfaces and around fibers and the columnar deposition of anisotropic material at the surfaces of large pores. White areas indicate high concentrations of anisotropic material.

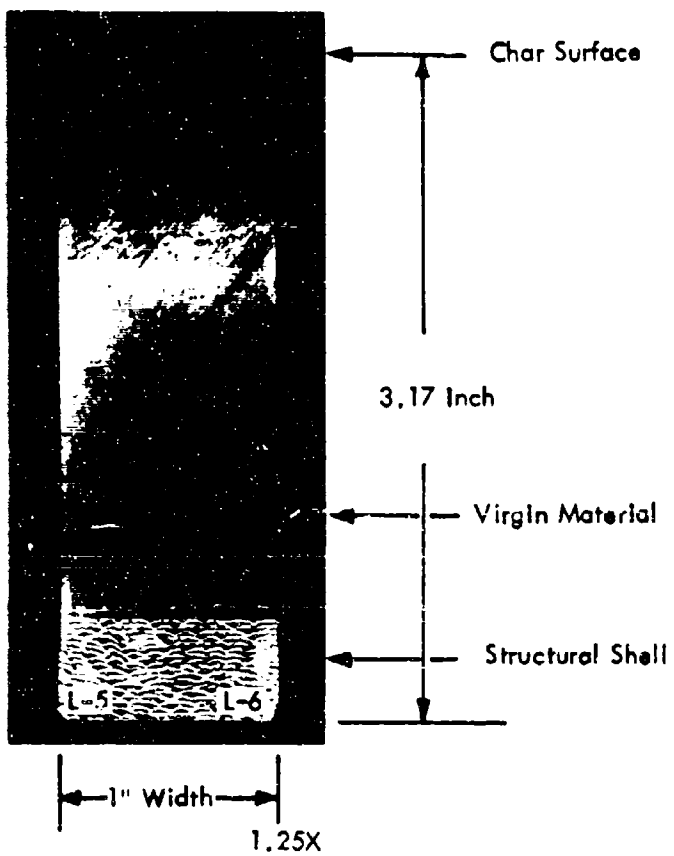

FIGURE 14 MX-4926 CHAR THROAT RADIAL PLANE VIEW

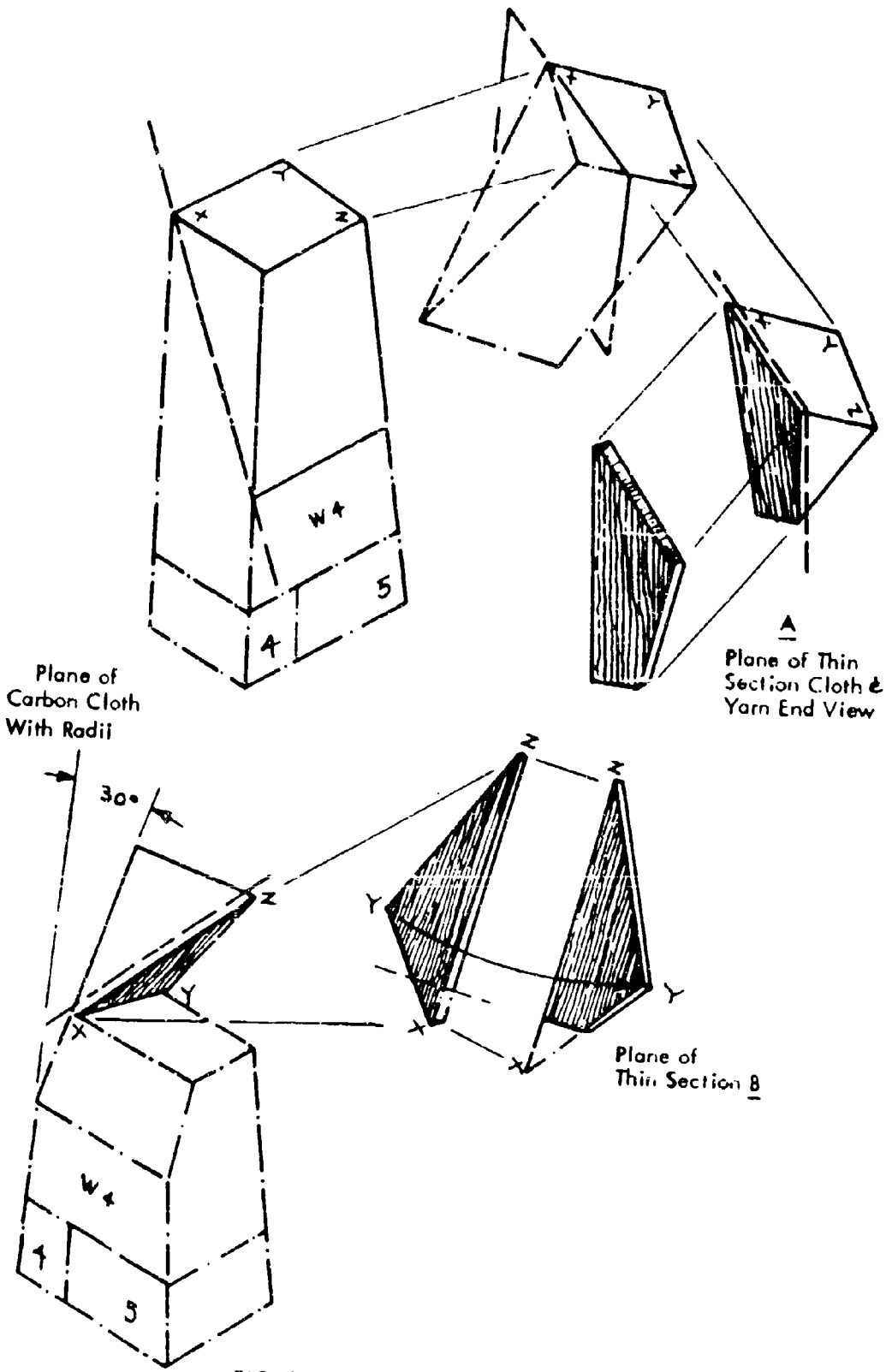

FIGURE 15 MX-4926 CHAR THIN SECTION LOCATIONS

REFLECTED LIGHT 2X

PERPENDICULAR TO CLOTH LAYERS
PARALLEL WITH YARN

TRANSMITTED LIGHT 2.5X

FIGURE 16 MX-4926 CHAR THIN SECTION A VIEWS

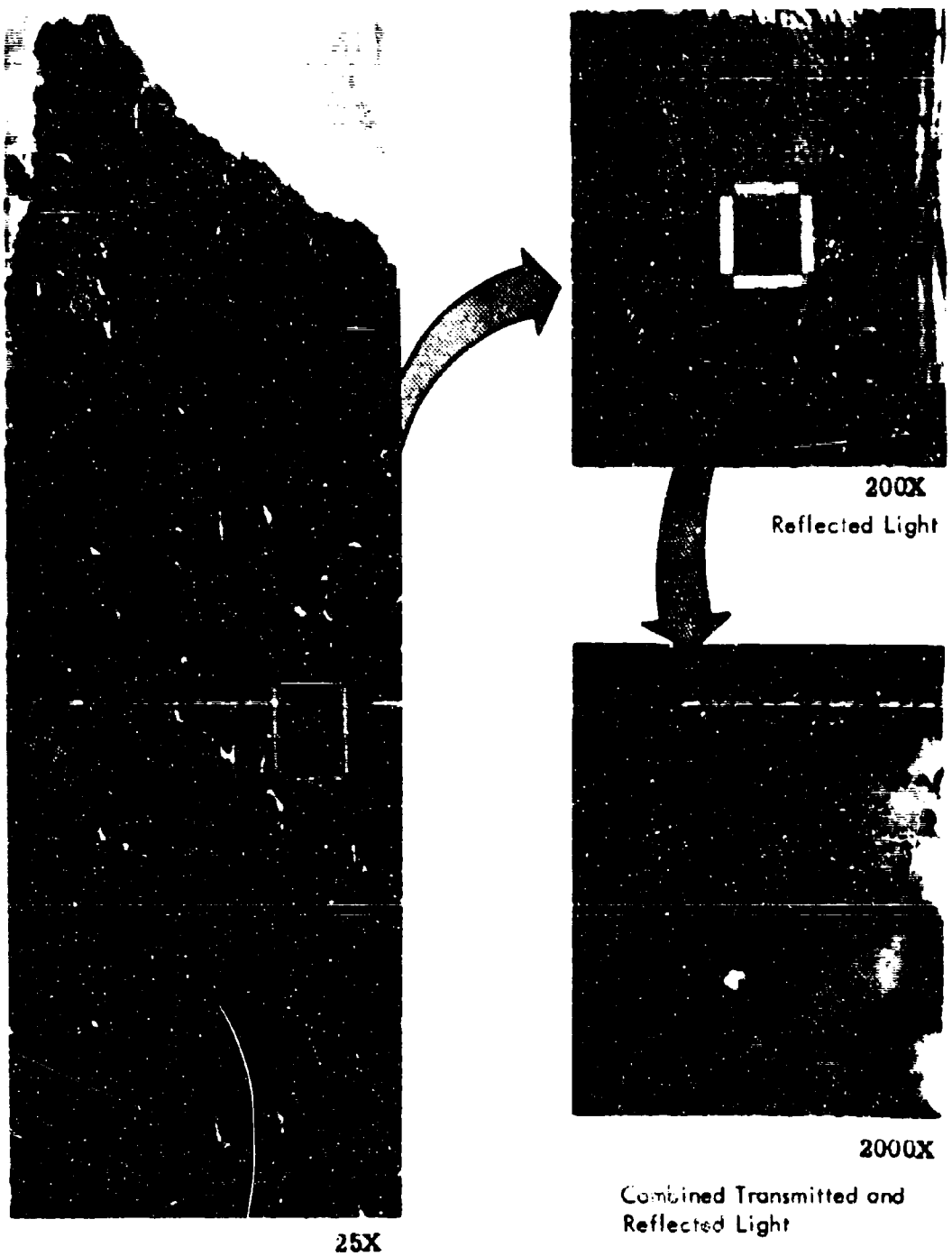

FIGURE 17 MX-4926 CHAR THIN SECTION A MAGNIFIED VIEWS OF CHAR SURFACE

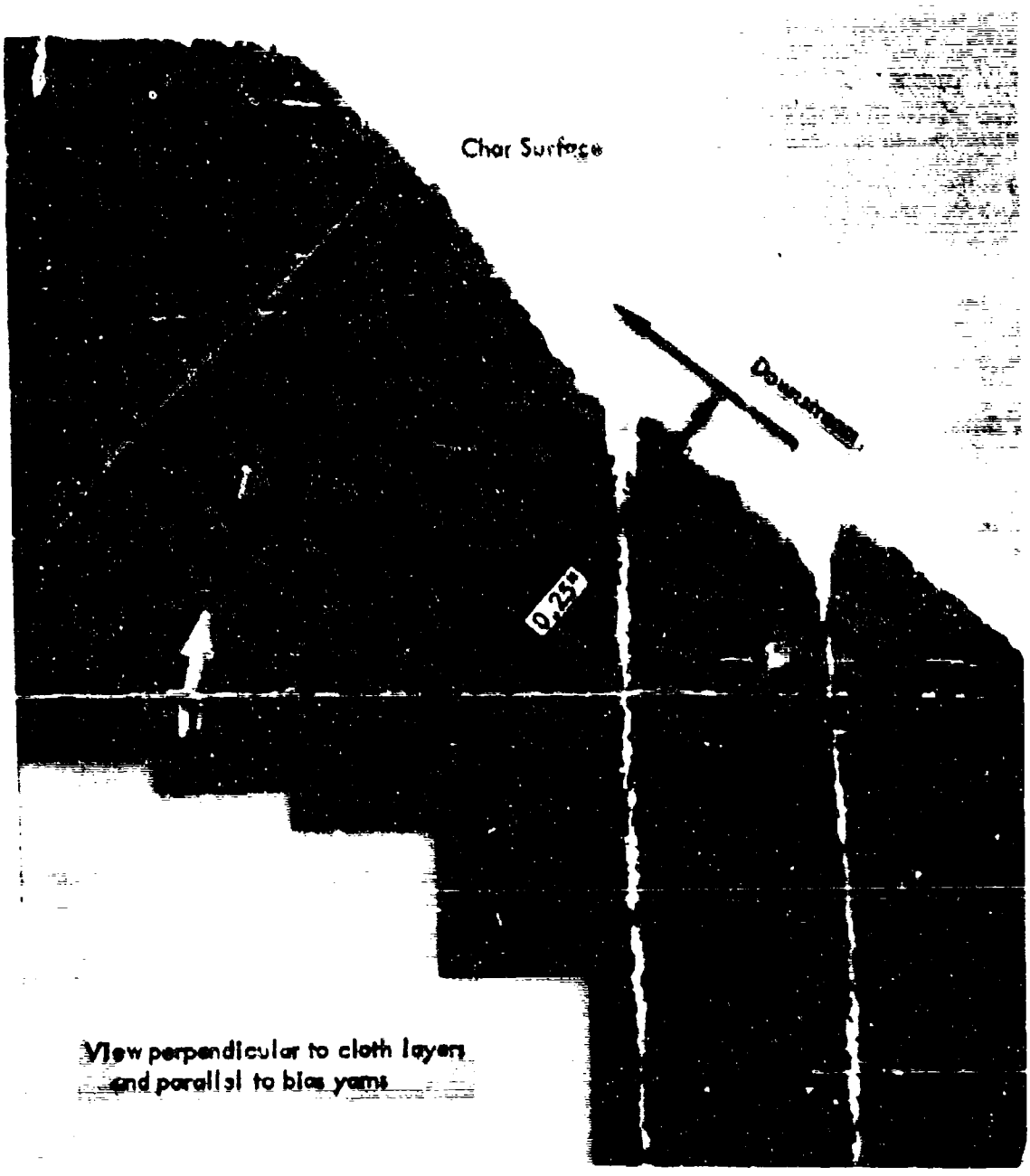

FIGURE 18 MX-4926 CHAR ANISOTROPY WITH POLARIZED-REFLECTED LIGHT

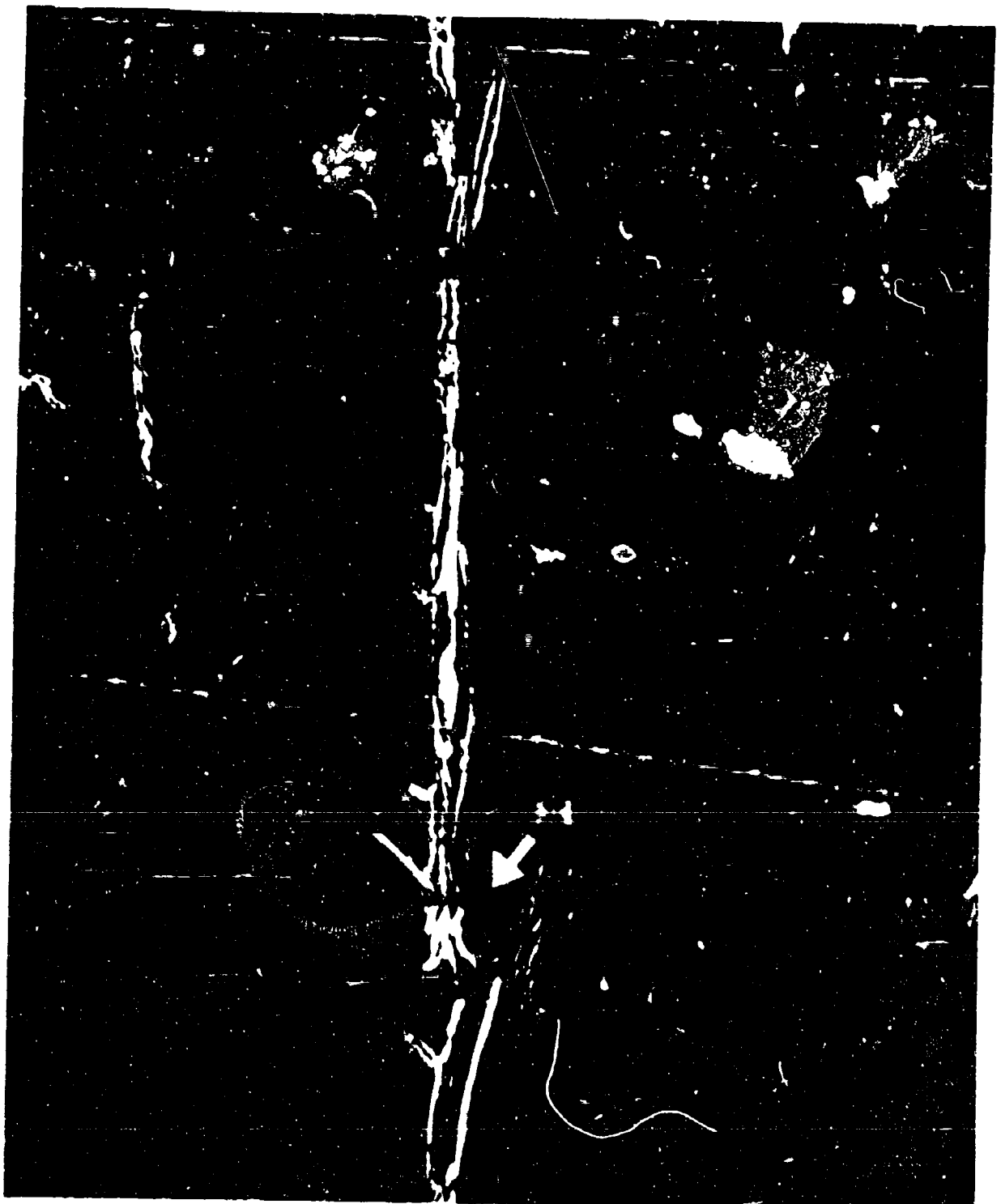

50X View made from One 25X Photomicrograph of the Mosaic (Arrow-I) for Thin Section "A" Showing Anisotropic Material Deposition in a Large Pore

FIGURE 19 MX-4926 CHAR ANISOTROPY WITH POLARIZED-REFLECTED LIGHT

1000X View Made on Thin Section "A", at One Location Indicated on the 50X View (Arrow-II), Showing Anisotropic Material Deposition at Pore Surfaces and Between Carbon Fibers

FIGURE 20 MX-4926 CHAR ANISOTROPY WITH POLARIZED-REFLECTED LIGHT

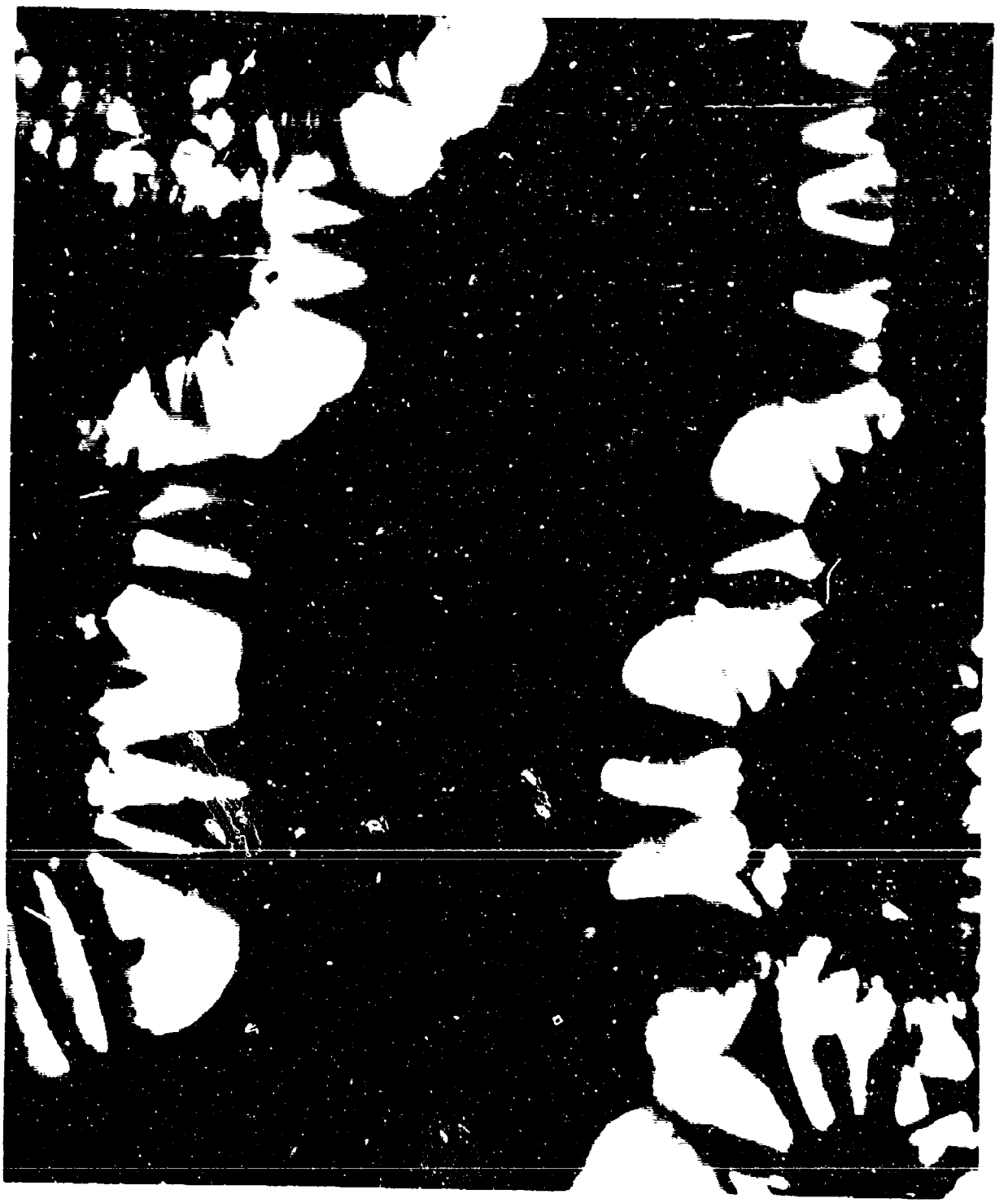

3800X View, Polarized-Reflected Light

FIGURE 21 MX-4926 CHAR COLUMNAR ANISOTROPY AT PORE SURFACES

"Graphitization", as evidenced by visible anisotropy, extended to 0.25 inch below the char surface, in good agreement with X-ray diffraction results. The depth of graphitized material was the major consideration in establishing the boundaries of char zone I.

"Graphitized" deposits are one of the most distinctive characteristics of the MX-4926 nozzle char. The concentration of "graphitized" material in fairly continuous paths along cracks and fibers is believed to be a major factor in the very high thermal conductivity of graphitized char measured parallel with laminare planes.

The following observations were made by correlating the photographic analyses with the other analyses described in Section IV.

Char Characteristics

Visible char zones, such as the pyrolysis zone/virgin zone interface, were parallel with the surface. Resin degradation indicated by porosity at 63X was visible to a depth of 0.8 inches, about the middle of the pyrolysis zone on the basis of density/porosity data. Heat-affected material, indicated by color change, was seen to a depth of 1.2 inches. This is approximately where density/porosity data indicates the beginning of the virgin zone.

Inter-yarn pores and microcracks were up to 100 microns (0.004 inches) wide near the surface and decreased in size with depth to 40 microns (0.0015 inches) at a depth of 1.03 inches. The maximum depth of visible inter-yarn cracks was below the visible resin degradation depth. The maximum limit of inter-fiber void size was about 10 microns. These pore size limits provided a basis for classification of penetrated porosity results in ranges representing inter-yarn and inter-fiber size porosity. The inter-yarn size porosity would be expected to vary the most as a function of the thermal cracking and delamination encountered in any ablation application.

Anisotropic or "graphitized" material coated pore surfaces and fibers in a sub-surface band from 0.06 inches to 0.25 inches depth. The highest concentration of visible anisotropic material was columnar deposits on the surfaces of gas-path pores.

Carbon Cloth, Matrix Characteristics

Spacings of cloth yarns and cloth layers were constant with char depth regardless of resin degradation of porosity changes. Volumetric concentrations of cloths,

yams, and fibers were therefore constant, but there was disiocation or cracking of the fibers in high porosity zones.

Cloth layers were oriented downstream at a 60° angle with the surface in the mature char, but appeared oriented at lesser angles down to 55° in the virgin zone. Yam directions were 45° to radial planes in the cloth layer as expected for bias tape wrapped construction. There were 42 fill yams per inch compared with an average of 50 in the prepreg, indicating the results of bias stretch and hydroclave compression. The carbon fibers had irregular surfaces and a mean diameter of 0.0003 inches. A count of 70 cloth layers per inch indicated that approximately 40 percent compression had occurred during the fabrication cycle.

DENSITY AND POROSITY PROFILE

Apparent dry densities obtained on vacuum-dried char-depth slices are plotted in Figure 22 along with computer predicted densities and open porosity calculated from helium pycnometer determinations of ρ_{as}. Figure 22 illustrates the following observations based on density/porosity data:

1. Most of the porosity increase and apparent dry density decrease occurs in the pyrolysis zone and these changes are inversely proportional.

2. The computer results are reasonably accurate based on post-test char density profiles. Agreement of predicted and measured post-test density profiles lends confidence to predicted density and temperature histories at any point in the char.

3. The apparent dry density in the pyrolysis zone of the post-test char represents the low heating rate cool-down period, not the motor firing period.

These observations, which also hold for FM-5014 phenolic-graphite, support the approach used in the presentation of thermophysical property data, particularly thermal conductivity; that is, a density/porosity correlation of properties is the proper basis for predicting properties in the unstable pyrolysis zone. This approach is discussed in detail in section IX.

The apparent density profile given by Radocon X-ray transmission measurements is shown in Figure 23. Agreement with direct measured values is good, and it is apparent that no significant density variations have been missed by the char sampling technique. The Radocon data does give somewhat better resolution of a density peak at the 0.3-inch depth.

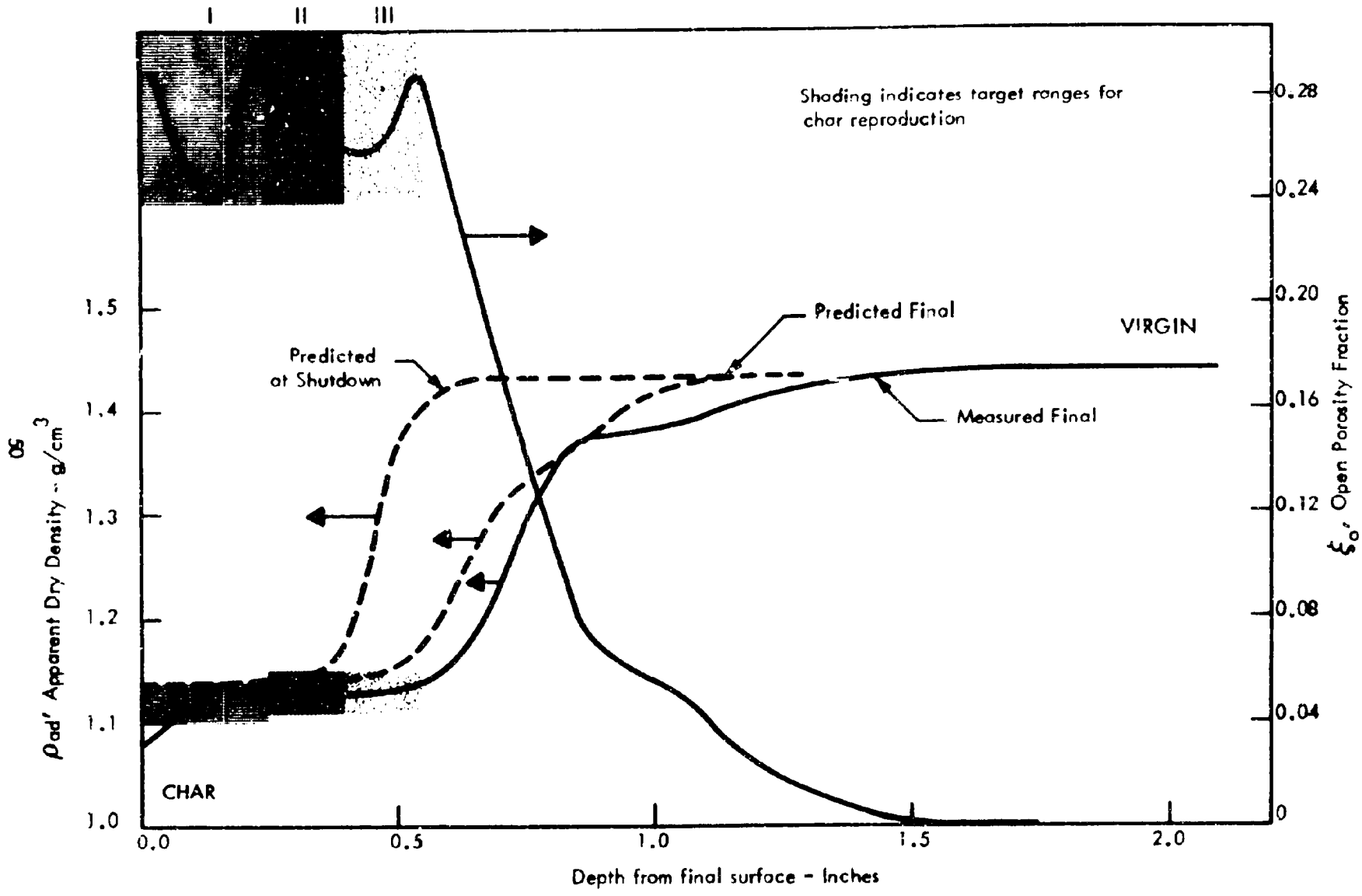

FIGURE 22 MX-4926 NOZZLE CHAR DENSITY AND POROSITY

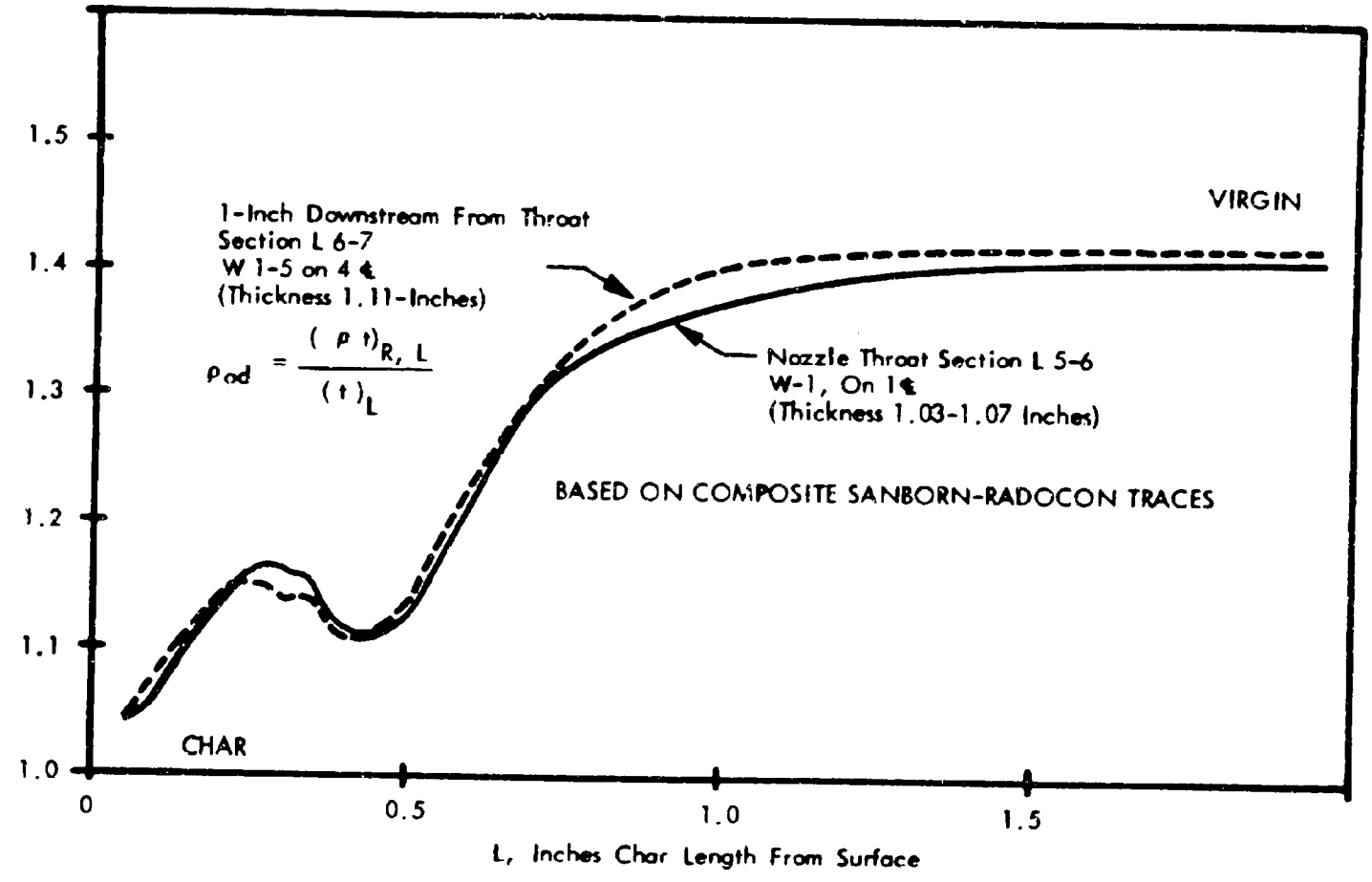

FIGURE 51 MX-4926 CHAR DENSITIES CALCULATED FROM X-RAY TRANSMITTANCE CORRELATIONS WITH DENSITY-THICKNESS PRODUCT

Since the effect on thermal properties of the density changes accompanying pyrolysis is most easily visualized in terms of porosity, all other density/porosity data is presented in terms of porosities in Figure 24 . All data was obtained on H-series depth slices, except the unconnected points, which were obtained on slices representing char zones I, II, and III after these zones were defined. These zone data are an average from three measurements on each of two sets of specimens and represent all values to within ±5 percent. In zones II and III the high total and trapped porosities, which are a result of high solid densities, are consistent with the results obtained on furnace char analogues of these zones. The "graphitization" in zone I apparently yields material of low solid density. Furnace chars "graphitized" after pyrolysis showed the same behavior.

The reason that open porosity measured on char zone samples was higher than that of small H-series char depth slices is probably related to the proportion of sample surface to sample volume. Smoothing the surfaces of a thin slice tends to eliminate some of the large size open porosity and give lower open porosity values. On this basis, the difference between open porosity values on zone specimens and char depth slices is attributed to large open porosity associated with partial delaminations. The difference between the open and penetrated porosity measurements on char depth slices is believed to be due to porosity larger than about 100 μ .

The density/porosity data indicates that the mature char layer ends at a 0.5-inch depth in agreement with thermal analysis results. Beginning at the surface, there is a rapid increase in apparent density and decrease in porosity to a depth of 0.15 inches, where apparent density levels off but solid density increases accompanied by an increase in both interlaminar and inter-yarn size porosity and in closed porosity. The decrease in inter-fiber and fine range void fractions into the pyrolysis zone to a depth of about 0.8 inches is due to the increase in undecomposed resin content indicated by thermal and elemental analysis. A peak in inter-fiber range voids at 0.8-inch depth followed by a decrease to a depth of 1.2 inches is attributable to thermal cracks rather than pyrolysis generated vents on the basis of photomicrographic observations.

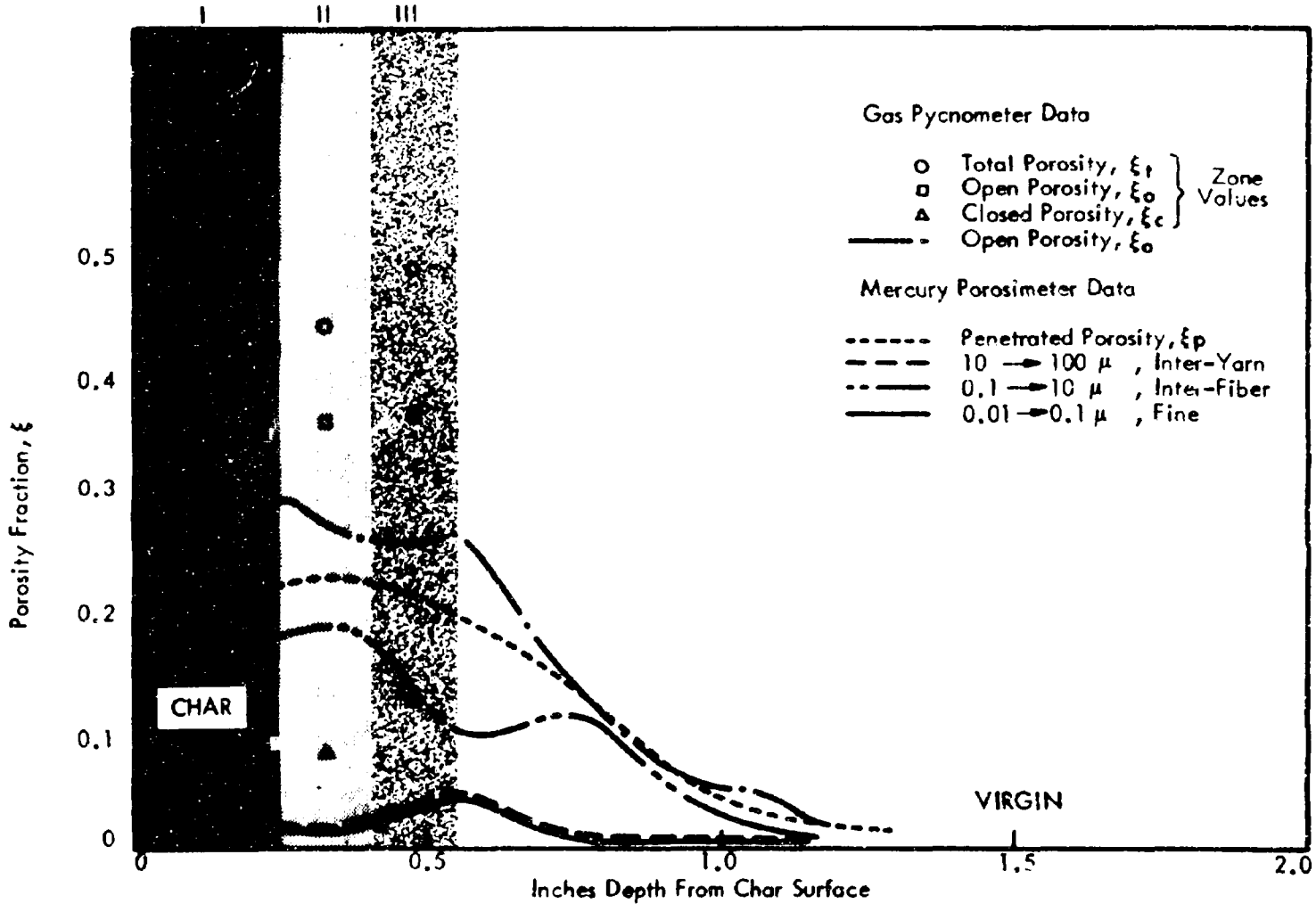

FIGURE 24 MX-4926 CHAR POROSITY FRACTION VS. DEPTH

THERMAL STABILITY PROFILE

All thermogravimetric (TGA) and differential thermal analysis (DTA) results are summarized in Tables IV and V . The total weight-loss to 1800°F in the helium TGA measurements and the initial temperature, Ta, of the first exotherm in the air DTA measurements were quantitatively sensitive to depth in the char and are plotted versus char depth in Figure 25 .

The total weight-loss to 1800°F in TGA measurements is considered the primary measure of the thermal stability of all material at any depth in the char. The data from node to node (inflection points) give confirmatory information on thermal stability. High thermal stability is indicated by the first node occurring at high temperatures and by few nodes. The increase in total weight-loss, and in weight-loss at the temperature of the first node in specimens taken near 0.5 inches depth indicates the end of the mature char zone, in agreement with other analyses. Within the mature char zone, however, specimen H-3 at a depth of 0.25 inches exhibits the highest weight loss, the lowest temperature initial node, and the most nodes in the mature char zone. This indicates deposition of hydrocarbon pyrolysis products as confirmed by elemental analysis. Thermal instability indicates that this deposition occurred during cooling at a depth having the maximum apparent density and low open porosity characteristics typical of pyrolysis product deposition zones. Specimen H-4 exhibits these same characteristics to a lesser degree consistent with the density/porosity data. Specimens H-1 and H-2 indicate stable mature char material in the region of high porosity, wherein apparent and solid density decreased and "graphitization" increased near the surface.

The initial temperature of the first DTA exotherm decreases sharply through the mature char zone to a depth of 0.45 inches. This same behavior was not noted on FM-5014,so no general interpretation of the DTA data is possible. Only the initial temperature of the first node was independent of sample size and the rate of oxygen transfer in the particular test setup. Since it could not be related to physical and chemical characteristics in the char, DTA offers little in the way of reproducible, quantitative characterization.

COMPOSITION PROFILE

Microcombustion analysis provided composition versus depth in the char. Electron-beam microprobe analysis indicated no significant amount of contaminants, but a supplementary spark analysis of ash from the carbon-hydrogen analysis indicated small amounts of Al, Fe, and Si and traces of Ca, Cu, and Mg.

TABLE IV MX-4926 CHAR DTA-IN-AIR CHARACTERIZATION RESULTS

Nozzle Throat Sample 11-C (Stations L-5 To L-6)
With H-Specimens Cut Parrallel To The Char Surface

CHAR SPECIMENS				NET EXOTHERMIC EVENTS Line 1: Heat $\Delta H_r/\omega$ or I/ω; $\int \rho V_{dt} = \sum \Delta H/\omega$ (microvolts °C/mg) Line 2: Temperatures at peak microvolts, T_p (°C) Line 3: Temperatures at start - T_a and end - T_c, (°C) Line 4: Peak microvolts, μV_p							Total Heats $\Delta H/\omega$ and Temp. Limits: Initial T_a Final T_c
Designation Code Depth	Radial Col.	Depth from Surface (inches)	Weight ω (m-gm)	Items	R-1	R-2	R-3	R-4	R-5	R-6	
H-1	(W-3)	0.05	8.7	$\Delta H_r/\omega$ T_p T_a/T_c μV_p		2040 805°C (575) (837) 195				820 837 (783) (882) 205	2860 T_a - 575°C T_c - 882°C
H-3	(W-3)	0.25	9.24	$\Delta H_r/\omega$ T_p T_a/T_c μV_p		2931 700°C (450) (737) 265			429 735°C (700) (778) 230		3360 T_a = 450°C T_c = 778°C
H-5	(W-3)	0.45	8.47	$\Delta H_r/\omega$ T_p T_a/T_c μV_p	2835 626°C (250) (645) 265		270 651°C (626) (658) 185				3100 T_a = 250°C T_c = 658°C
H-7	(W-3)	0.65	7.5	$\Delta H_r/\omega$ T_p T_a/T_c μV_p	1554 545°C (250) (590) 105	1816 622°C (545) (637) 268	290 637°C (622) (654) 230				3660 T_a = 250°C T_c = 654°C
H-9	(W-3)	0.85	10.3	$\Delta H_r/\omega$ T_p T_a/T_c μV_p	864 500°C (250) (567) 67	2416 636°C (476) (667) 278					3280 T_a = 250°C T_c = 667°C
H-11	(W-3)	1.05	11.0	$\Delta H_r/\omega$ T_p T_a/T_c μV_p	2552 637°C (200) (684) 230			348 684°C (650) (697) 175			2900 T_a = 200°C T_c = 697°C
Virgin (H-13)	(W-3)	1.82	9.65	$\Delta H_r/\omega$ T_p T_a/T_c μV_p	293 518°C (200) (551) 35	1689 615°C (476) (644) 215	562 644°C (600) (674) 200	516 674°C (630) (700) 213			3060 T_a = 200°C T_c = 700°C

TABLE V MX-4926 CHAR THERMOGRAVI[illegible]C ANALYSIS RESULTS, HELIUM ATMOSPHERE

Specimens	Char Depth (inches)	*Incremental Weight Loss % Between Temperature Nodes, Dry Basis												Cumulative Weight Loss % Dry Basis	
		0		1		2		3		4		Maximum		1800°F	Max T(°F)
		T(°F)	%	T(°F)	%	T(°F)	%	T(°F)	%	T(°F)	%	T(°F)	%	%	%
H-1	0.05	R.T.	0	1800	1.2							--	--	1.2	--
H-2	0.15	R.T.	0	1800	0.7							1850	0.0	0.7	0.7
H-3	0.25	R.T.	0	400	0.7	1090	1.6	1500	0.2	1800	0.7	1830	0.5	3.2	3.7
H-4	0.35	R.T.	0	1000	1.7	1450	0.5	1800	0.5			1830	0.1	2.7	2.8
H-5	0.45	R.T.	0	1000	1.1	1680	1.4	1800	2.4			1890	1.7	4.9	6.6
H-7	0.65	R.T.	0	1000	2.3	1350	4.4	1600	1.4	1800	1.2	1890	3.5	9.3	12.8
H-9	0.85	R.T.	0	800	3.5	1180	9.5	1360	2.5	1800	2.2	1840	0.6	17.7	18.3
H-11	1.05	R.T.	0	750	3.2	880	2.1	1200	8.7	1800	2.4	--	--	16.4	--
Block H-13	1.82 (Virgin)	R.T.	0	600	2.8	800	1.7	980	3.3	1800	9.7	1890	1.3	17.5	18.8

*Constant rate of temperature increase with time, 9.5 to 10°F/min. from R.T. to near 1800°F in helium atmosphere with nodes denoting apparent changes in rate of percent weight loss.

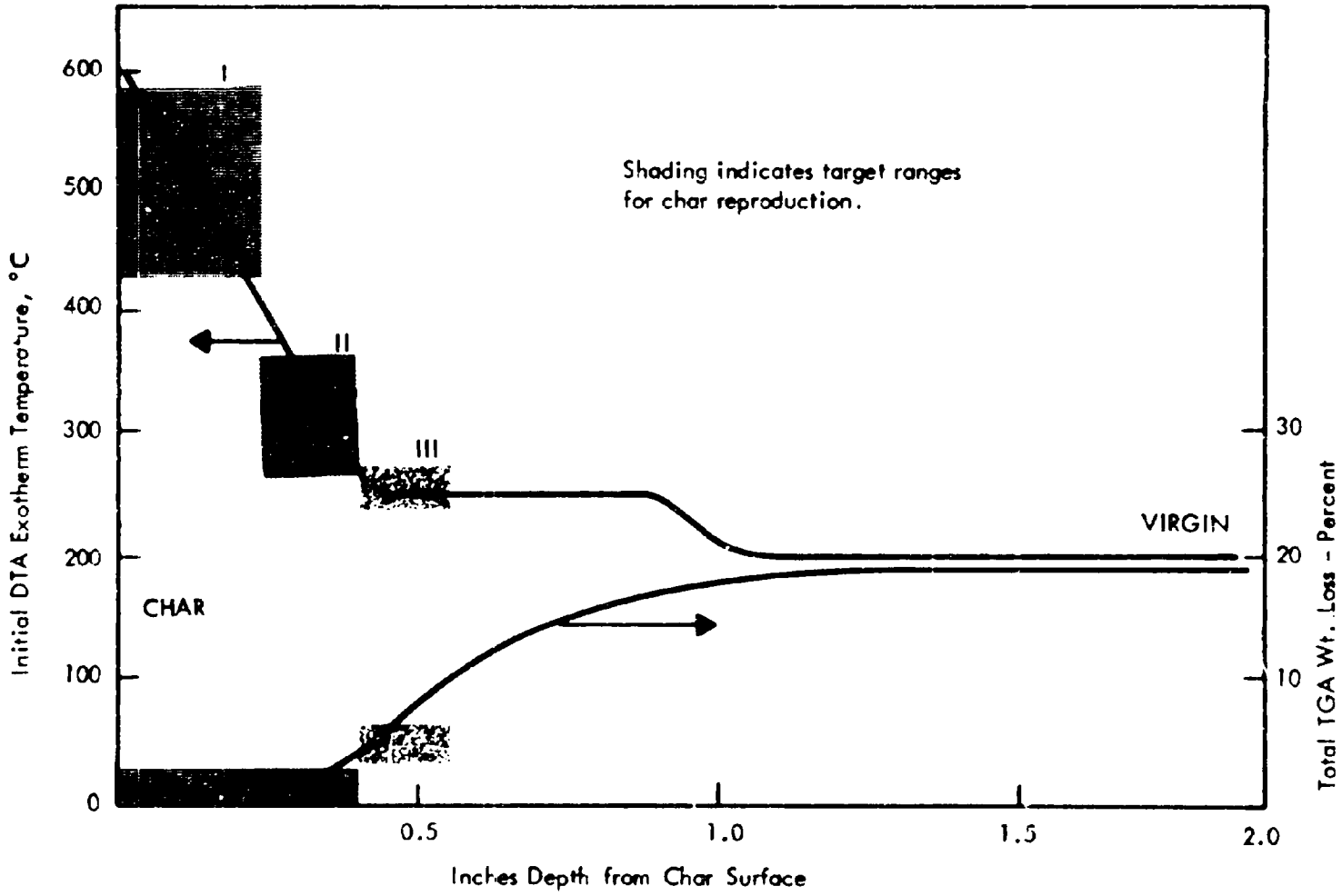

FIGURE 25 MX-4926 CHAR THERMAL ANALYSIS VERSUS DEPTH

Averaged results of duplicate carbon, hydrogen and ash analyses with the remainder attributed to oxygen, are presented in Table VI . The elemental analysis correlated well with TGA, showing hydrocarbon contents proportional to the weight losses measured to 1800°F. This confirms the location of the pyrolysis zone and the presence of redeposited material in the mature char zone. The partition of the elements among the constituents in the char (Table VI) provided more descriptive data for correlation with other characteristics. The constant volume of cloth and filler indicated by photomicrographic analysis provided an initial basis for carbon partition and the assumed stoichiometry for the remaining constituents, resin, pyrolysis residue, and trapped condensation cure reaction water allowed complete partition of the elements.

The constant volume of cloth and filler was first used to calculate char surface elemental analyses assuming no other constituents and the virgin elemental analysis assuming a resin concentration per the prepreg specifications. Excellent agreement with the experimental elemental analysis was obtained, verifying the constant concentrations of cloth and filler. At other depths in the char, stoichiometric balances assumed that all oxygen existed in residual phenolic (specimen H-3), that the ratio of hydrogen atoms to seven carbon atoms in phenolic resin was 5.5 (specimen H-5), or that all carbon not fixed in cloth and filler was in phenolic resin (remaining specimens). Of course, the use of phenolic resin stoichiometry to represent hydrocarbon material deposited in the mature char zone simply represents the presence of unknown hydrocarbon material. The results of the partition of the major element, carbon, are plotted in Figure 26 .

INTERNAL "GRAPHITIZATION" PROFILE

Both top and bottom surfaces of all char slices H-1 through H-6 of column W-2 were used in X-ray diffraction tests to establish a measure of "graphitization" versus depth in the char. The maximum diffraction intensities recorded for the two predominant crystal spacings for graphite are plotted in Figure 27 . The 3.37 Å crystal spacing is the most sensitive, as expected. High background intensities in the virgin and pyrolysis zones indicated some crystallinity, but broad peaks indicated primarily amorphous carbon. This agrees with polarized light photomicrographic examinations showing that fiber ends in this region were partly anisotropic. The peak intensities in the virgin MX-4926 from all fabricators reproduced the nozzle value within ± two counts at 3.37 Å

The decrease in diffraction intensities from the surface to virgin material values at a depth of 0.25 inches was selected as the primary characteristic defining the outer char zone, zone I, for thermophysical measurements. "Graphitization" at

TABLE VI MX-4926 CHAR ELEMENTAL ANALYSIS AND ESTIMATED PARTITION

Nozzle Throat sample 11-C, radial column W-3

CHAR SPECIMENS			ELEMENTAL ANALYSES TOTAL WT. %				OXYGEN PARTITION		HYDROGEN PARTITION			CARBON PARTITION		
Depth Code	Depth	App. Dry Density g/cm^3	Ash	H	O	C	In Phenolic Wt. %	In Water Wt. %	In Water Wt. %	In Phenolic Wt. %	H/7C in Phen. (atoms)	Cloth & Filler Wt. %	In Phenolic Wt. %	Pyrolysis Residue Wt. %
H-1	0.5	1.1	0.6	0.3	0	99.1	0	0	0	--	--	77.2	0	21.9
H-3	0.25	1.12	0.8	0.55	0.75	97.9	0.75	0	0	0.55	(12)	76.8	3.9	17.2
H-5	0.45	1.13	0.65	0.73	2.62	96.0	1.77	0.78	0.09	0.63	5.5	76.1	9.3	10.6
H-7	0.65	1.19	0.6	1.60	6.0	91.8	3.7	2.3	0.29	1.3	5.6	72.3	19.5	0
H-9	0.85	1.37	0.8	2.1	7.6	89.5	5.1	2.5	0.31	1.8	5.7	62.9	26.6	0
H-11	1.05	1.39	0.6	2.1	8.2	89.1	5.2	3.0	0.37	1.7	5.3	61.9	27.2	0
Virgin	1.82	1.44	0.6	2.3	8.7	88.4	6.0	2.7	0.34	2.0	5.9	59.8	28.6	0

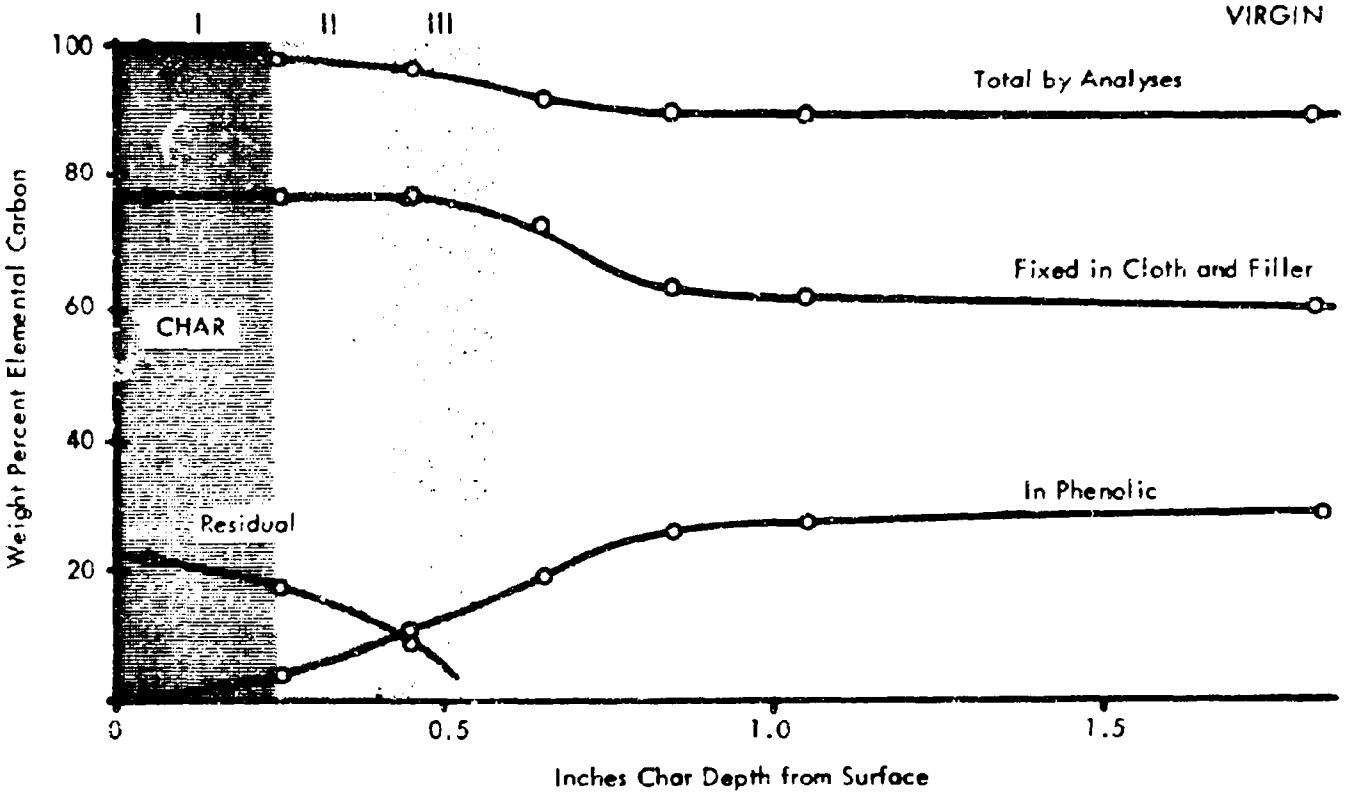

FIGURE 26 MX-4926 CHAR ELEMENTAL CARBON PARTITIONED

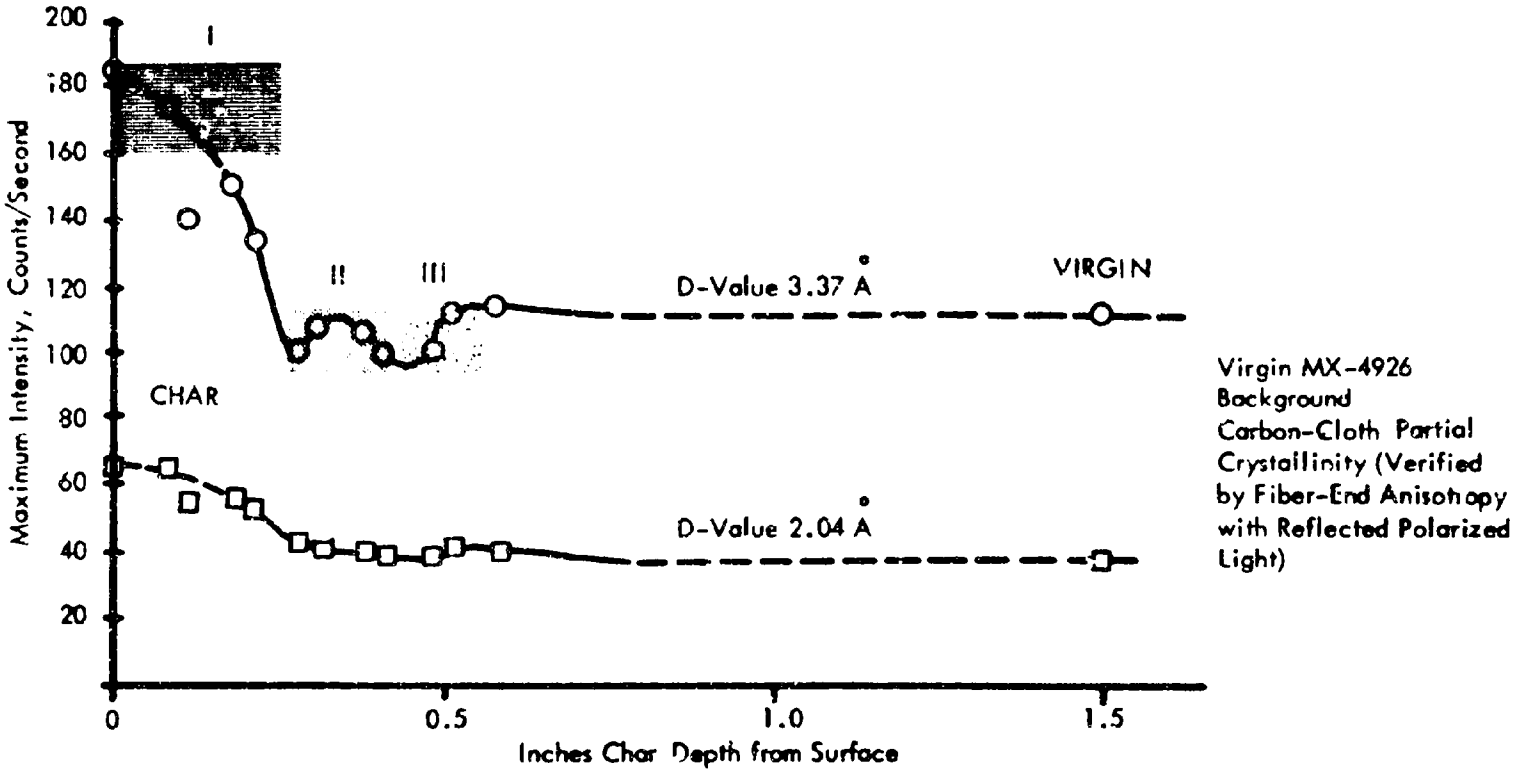

FIGURE 27 MX-4926 CHAR GRAPHITIZATION, X-RAY DIFFRACTION INTENSITY VERSUS CHAR DEPTH

the char surface was almost equal to that for virgin FM-5014 material containing graphite cloth. Photomicrographic analysis alone did not show maximum anisotropy at the surface, which indicates graphitization of carbon cloth fiber or filler material not discernable by photomicrographic analysis. Just below the surface, the diffraction intensities correlate with the visible concentrations of anisotropic material deposited at pore surfaces and between or around fibers.

COMPUTER PREDICTED INTERNAL ABLATION HISTORIES

Computer predictions of density and temperature by Aerotherm were transformed to functions of depth from the final char surface and interpolated to produce the plots in Figure 28 . The temperature histories show that the surface cools so rapidly by radiation after shutdown that the outer char regions are effectively quenched in the active ablation state without surface recession. The continued pyrolysis during the after-soak period that consumes the pyrolysis zone existing at shutdown is also apparent. The close agreement between computed and measured final density profiles shown in Figure 22 justifies using the computer results for establishing both the post-test char density and temperature histories. The temperature limits for char zones I, II, and III were established by computing peak temperatures at the zone boundaries. A water quench at 132 seconds during the cool-down was not included in the analysis, but the curves indicate that the probable effects were negligible on char above 1200°F, the lower limit of zone III.

Since the computer results plotted in Figure 22 show that the pyrolysis zone formed during the firing no longer exists, it is necessary to assume that pyrolysis zone material resulting from the after-soak is representative of that existing during active ablation. This is substantiated by the elemental analysis which assumed that undecomposed material was phenolic and that the residual decomposed material was simply carbon. On this basis, chemical changes in the solid state are always the same for a given extent of pyrolysis, and pyrolysis can be defined in terms of the large density/porosity changes.

The assumption that pyrolysis zone material can be described on the basis of density/porosity characterisitcs forms the basis for extrapolating thermal conductivity data to an active ablation pyrolysis zone as discussed in section IX. The necessity for extrapolation is a consequence of the rate effects encountered in pyrolysis. An illustration of the effects of pyrolysis rates is provided by the isotherms on the density versus time plot in Figure 28 . The apparent density existing at a given temperature decreases rapidly as the internal heating rate decreases

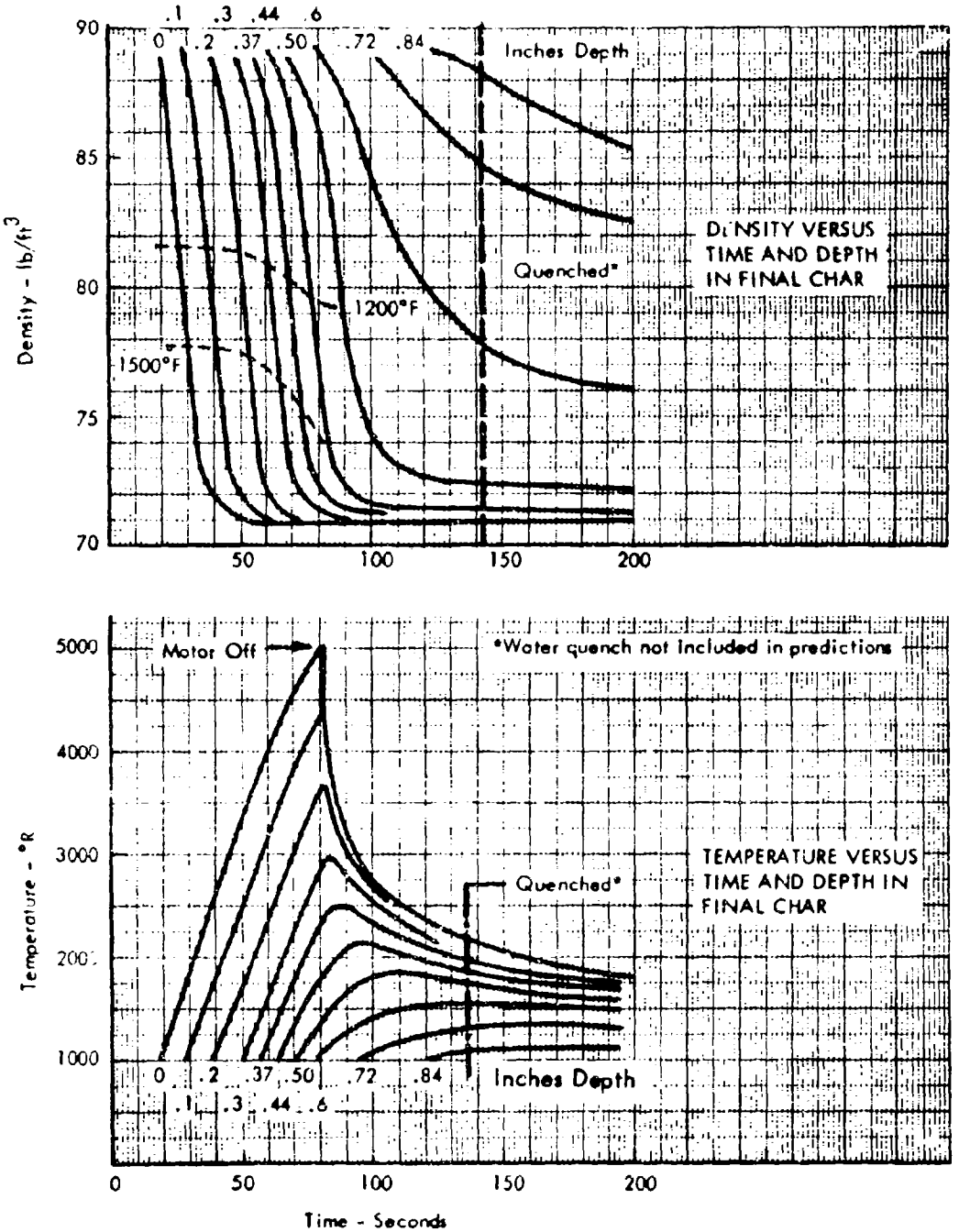

FIGURE 28 MX-4926 PREDICTED INTERNAL HISTORIES

at the beginning of the after-soak period. Both the post-test and furnace chars represent low heating rate states in the pyrolysis zone, and neither can fully represent active ablation pyrolysis at temperatures where rate controlled pyrolysis is occurring. Partially pyrolyzed post-test chars and furnace chars produced at 1200°F may represent the state of the material existing up to 2500°F during active ablation.

SECTION VI

FM-5055A PHENOLIC-CARBON CHAR CHARACTERISTICS

Characterization of FM-5055A phenolic-carbon chars indicated that their properties were sufficiently similar to those of MX-4926 phenolic-carbon, that thermal conductivity and specific heat data for the latter can be used for the former until actual thermophysical properties are measured for the FM-5055A chars.

Since the plasma charred specimens were received late in the program, and only one of the models was considered suitable for characterization, the results on FM-5055A are not as extensive as on the other materials. The results are presented as a function of depth from the char surface and discussed in terms of the major ablation zones with MX-4926. Subzones I, II, and III in the mature char are not designated in the FM-5055A results, since reproduction in the form of thermophysical property specimens was not required and the responses of plasma samples are not necessarily typical of those obtained in full scale applications.

VISIBLE CHARACTERISTICS

The uneven laminate spacings in the FM-5055A phenolic carbon plasma test model are apparent in the photomicrographs in Figure 29 . However, the following characteristics that affect thermophysical properties are similar to those of MX-4926 and FM-5014.

1. Porosity increases gradually through the pyrolysis zone and pore shapes are elongated parallel to the adjacent fibers. This is consistent with the density/porosity measurements.

2. The concentration of deposited or residual anisotropic material visible under polarized light decreases as a function of depth below the char surface. This is confirmed by the X-ray diffraction results.

3. The anisotropic "graphitized" material forms fairly continuous paths along fiber and pore surfaces as in MX-4926.

The major differences apparent between FM-5055A and MX-4926 phenolic carbons are related to the different mechanical loading during ablation. The MX-4926 phenolic carbon nozzle was not free to expand or contract due to the nozzle

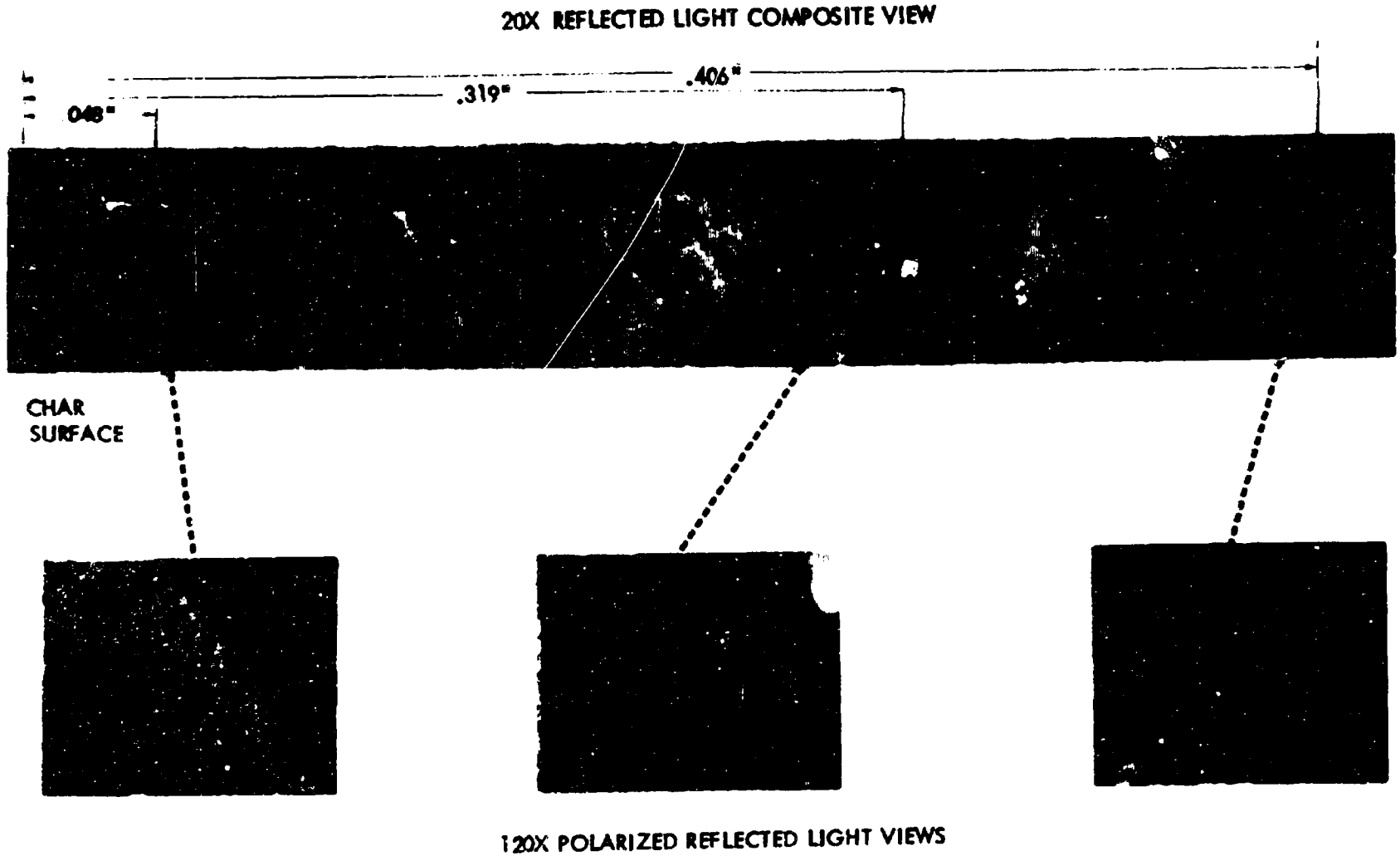

FIGURE 29 FM-5055A CHAR PHOTOMICROGRAPHS ON PLANE PERPENDICULAR TO SURFACE

geometry and structure. The relatively unrestrained FM-5055A did not exhibit significant microcracking in the virgin material below the pyrolysis zone and delaminations in the char did not crack open completely during cool down.

DENSITY AND POROSITY PROFILE

The apparent dry density and connected porosity profiles for FM-5055A are given in Figure 30. The small specimens available for these measurements limit the accuracy of the connected porosity measurement to approximately ±25 percent. Solid density and total porosity measurements on powdered samples in the gas pycnometer could not be accurately made on these samples. The agreement between measured and predicted density profiles is poor in this material, due primarily to poor laminate quality. However, the density and connected porosity profiles correlate with other measurements in the same way as for the other materials.

On the basis of apparent dry density and connected porosity, the mature char zone extends from the surface to approximately 0.3 inches depth, and the pyrolysis zone from 0.3 inches to 0.8 inches depth. The boundary at 0.3 inches is not sharply defined due to some partial delamination extending to a depth of 0.5 inches. This also accounts for the peak in connected porosity occurring at 0.44 inches depth and the tendency for porosity to increase continuously toward the char surface.

The boundary between the mature char zone and pyrolysis zone is defined best in the Radocon data versus depth shown in Figure 31. The largest delaminations are also apparent in the Radocon data. The Radocon data taken on a path parallel to the char surface in Figure 31 illustrates the nonuniformity of the density gradients in the plasma test chars. Only plasma test model number 20 had a flat portion on the side-to-side Radocon density traces made to identify uniform density samples for characterization.

THERMAL STABILITY PROFILE

Total TGA weight loss to 1800°F versus char depth is plotted in Figure 32. The content of thermally unstable material is proportional to the apparent density and to the hydrocarbon content indicated by elemental analyses in the same way as on the other post-test chars. Analysis of nodes in the TGA data was not conducted because this analysis proved to be of little value in the case of the other materials.

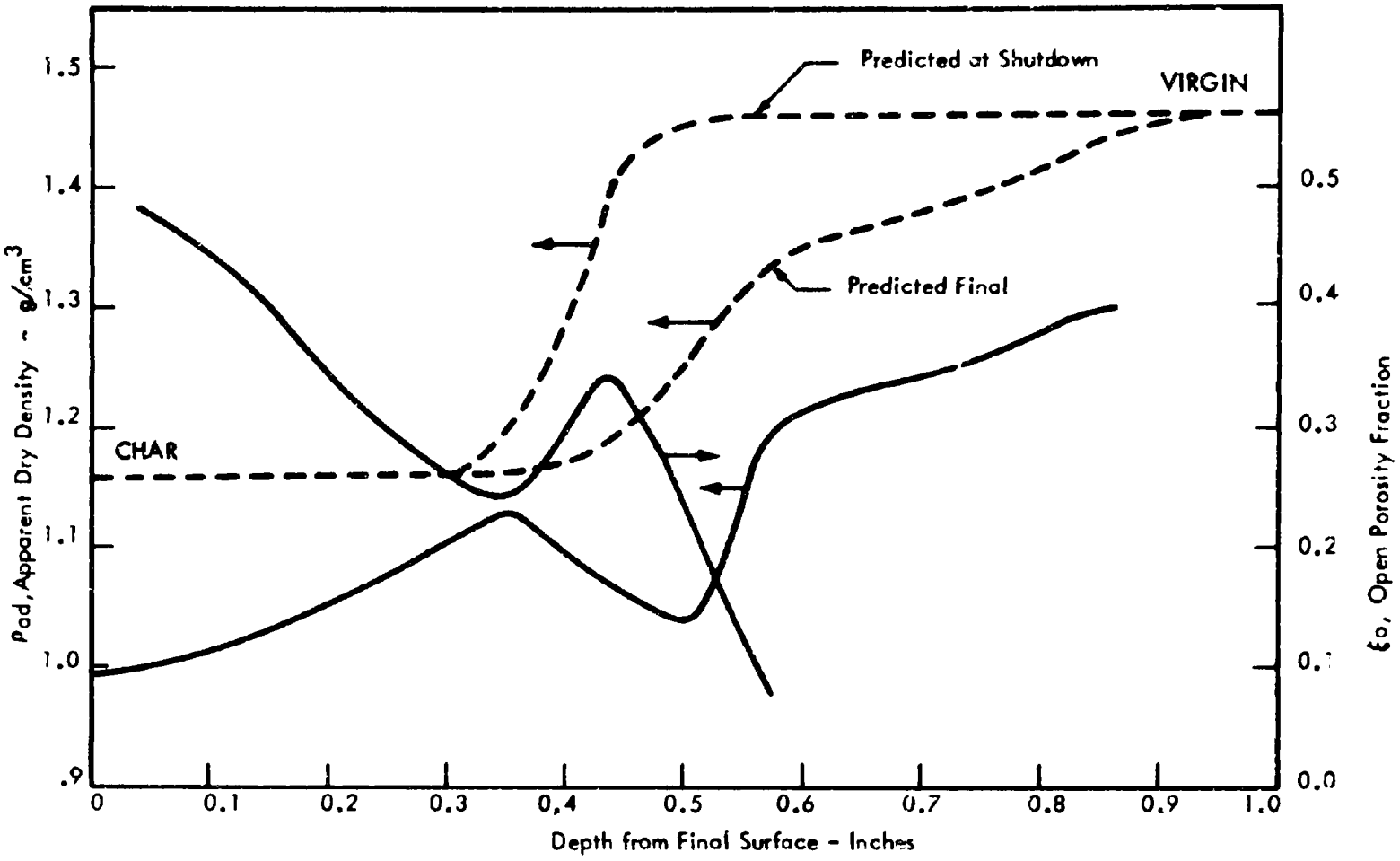

FIGURE 30 FM 5055A PLASMA CHAR DENSITY AND POROSITY

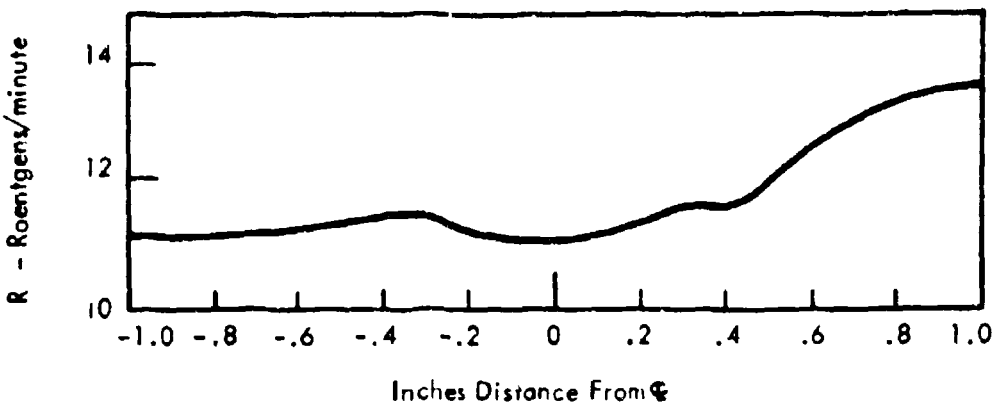

PROFILE PARALLEL TO SURFACE - 1/4" DEPTH

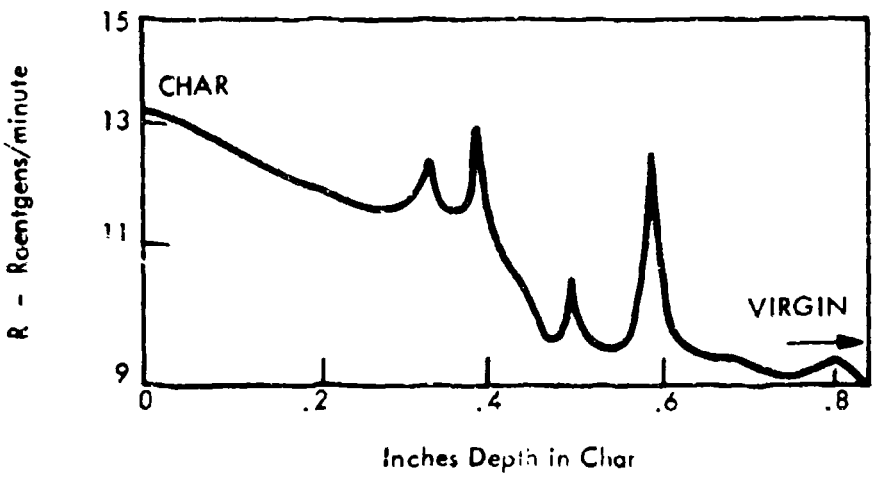

PROFILE VERSUS DEPTH

FIGURE 31 FM-5055A RADOCON X-RAY TRANSMISSION PROFILES

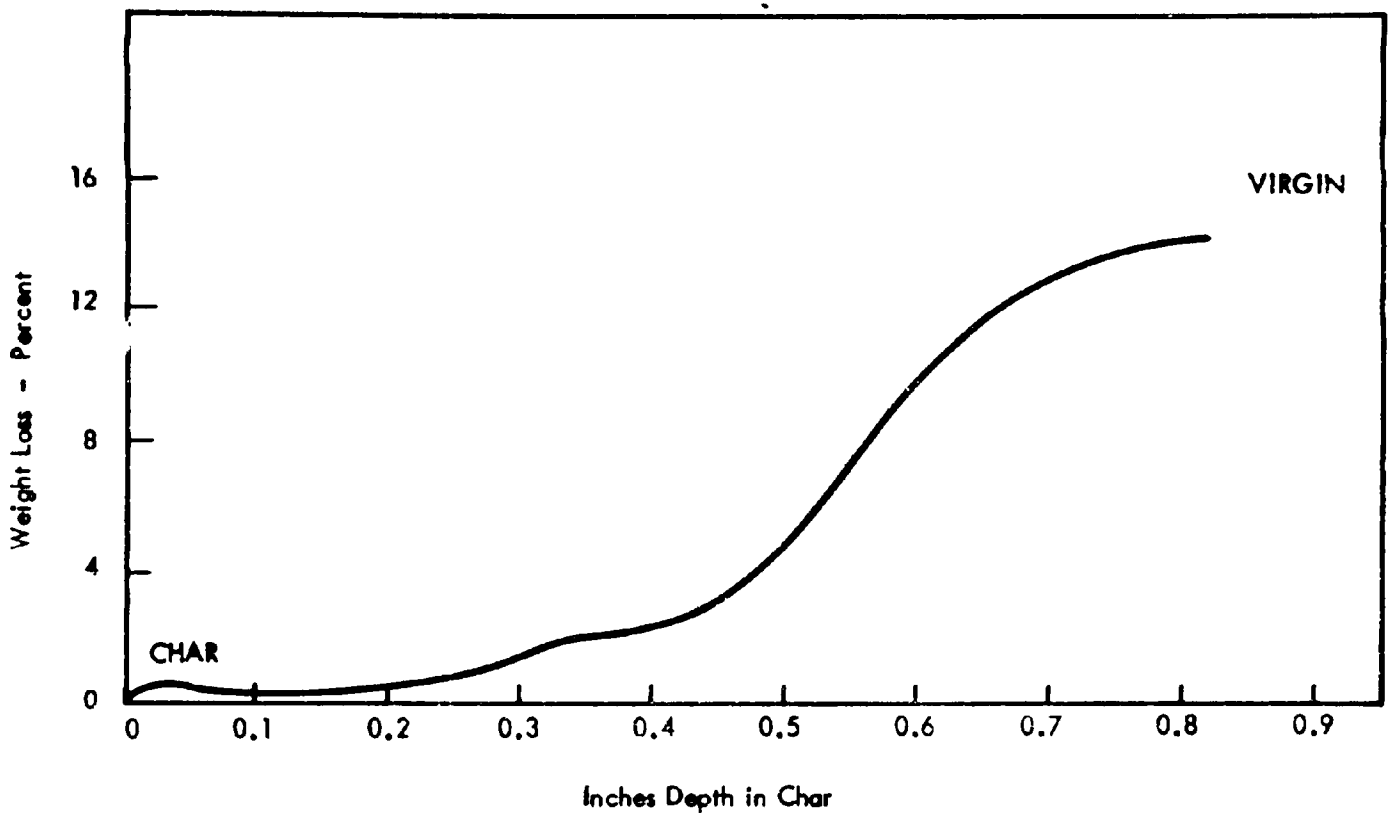

FIGURE 32 FM-5055A TOTAL TGA WEIGHT LOSS VERSUS CHAR DEPTH

Since the significance of the DTA measurements in air on the other materials could not be established, an attempt was made to obtain endotherm data by DTA measurements in helium. The responses were so small relative to data on stable reference samples that no analyses could be made.

COMPOSITION PROFILE

The results of carbon-hydrogen analyses on char depth slices are presented in Figure 33 . Since the reinforcement concentrations varied significantly versus depth in the char, no basis for partition of the elemental analysis of FM-5055A was available. The data follows the same trends through the mature char and the pyrolysis zone as in the other materials. The results parallel the results of TGA analysis where weight loss is associated with the presence of hydrocarbon material and increasing hydrocarbon content corresponds to increasing apparent density versus depth in the pyrolysis zone.

INTERNAL "GRAPHITIZATION" PROFILE

X-ray diffraction intensity at 3.37 Å on the top and bottom surfaces of char depth slices is plotted versus char depth in Figure 34 . The x-ray diffraction results follow the trend in concentration of anisotropic material visible under polarized light. The values at the surface are nearly as high as surface values obtained on FM-5014 phenolic graphite, while virgin values are near those of MX-4926 phenolic carbon. The leveling-off toward virgin material values occurs at the same peak predicted temperature observed in the other materials, 2900°F, at a depth of 0.25-inches which suggests that char zone I would extend that deep in the FM-5055A plasma test char.

There are several factors that may account for the high "graphitization" level at the surface of this material relative to the other phenolic-carbon material, MX-4926. Both FM-5055A phenolic carbon and FM-5014 give high x-ray diffraction intensities at the surface, and since both have the same resin and filler, the results may be controlled by graphitization of pyrolysis decomposition residue and filler. The temperature-time histories in the plasma tests indicate that the period of exposure to temperatures over 2900°F in the FM-5055A char is from two to four times as long as in the nozzle chars, while the maximum temperature is nearly the same. Of course, the internal pressures, pyrolysis gas flow rates, and other variables that would affect cracking of pyrolysis gases and "graphitization" processes are also different in the plasma test models. At present it is not known which of these or other factors are significant, but the influence of "graphitization" in the application of thermal conductivity data from MX-4926 to FM-5055A must be considered, as discussed in Section IX.

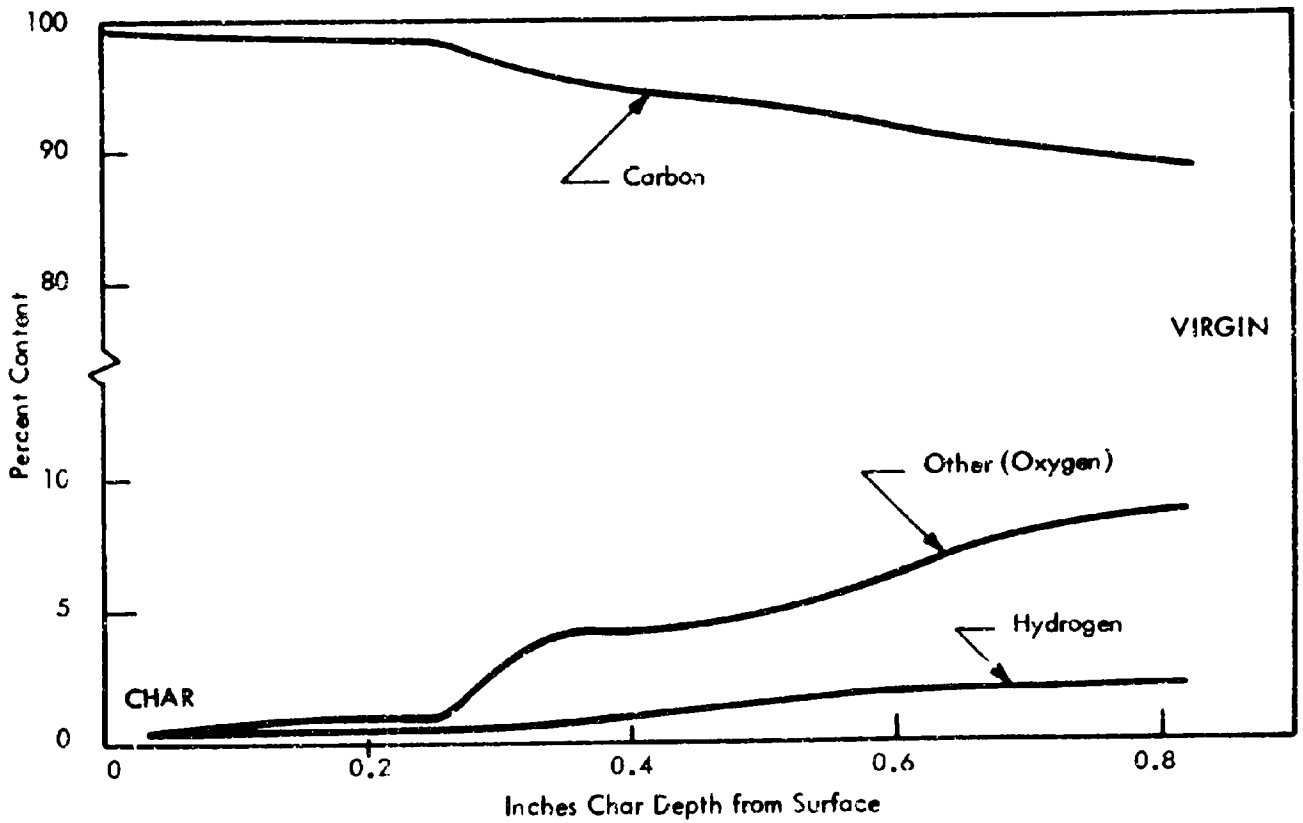

FIGURE 33 FM-5055A COMPOSITION VERSUS DEPTH

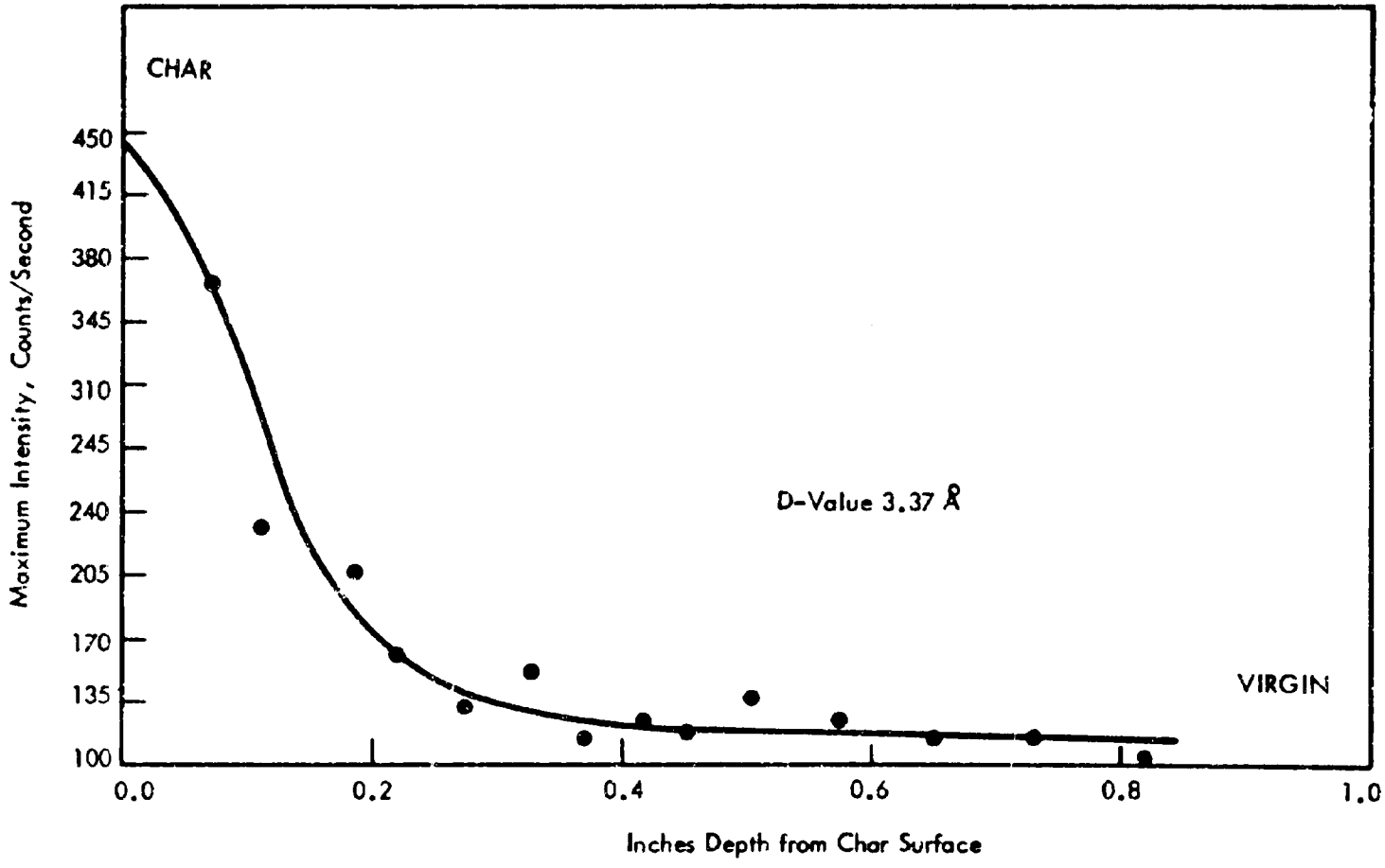

FIGURE 34 FM-5055A CHAR GRAPHITIZATION, X-RAY DIFFRACTION INTENSITY VS. CHAR DEPTH

COMPUTER PREDICTED INTERNAL ABLATION HISTORIES

Predicted density and temperature versus time and depth for the FM-5055A plasma test specimen are given in Figure 35 . The computer results predicted a total surface recession of only 0.005 inches, which was neglected in constructing these plots. The major difference between these plasma test histories and those of the rocket firings is the two to four times longer exposure to very high temperatures in the outer portion of the char. This is a result of the combined effects of a low initial heat flux and the lack of surface recession. The plasma tests were started at a cold wall heat flux of 94.3 Btu/ft^{2}sec. that was held for 5 seconds, increased linearly to 494.5 Btu/ft^{2}sec. over the next 30 seconds, and then held at that value to the end of the run. This cycle was an approximation of a reentry heating cycle.

The predicted and final density profiles for this material shown in Figure 30 were not in as good agreement as on the rocket nozzle chars. This is due to several factors such as the probable deviation from one dimensional heat flow used in the computer and the fact that the models were of relatively low density compared to the normal material specifications used as computer inputs. This last factor accounts for most of the difference between predicted and final densities on this material. The test models were instrumented with an axially inserted thermocouple at 0.75 inches depth to give a check on the temperature predictions. Comparison of the predicted and measured responses at 0.75 inches in Figure 35 shows good agreement, considering that the thermocouple readings would be expected to be lower due to side heat losses and the losses along the wires due to axial insertion. Based on this comparison the computed predictions are considered substantially correct.

The general observations made in reference to the internal histories on MX-4926 also hold for this material.

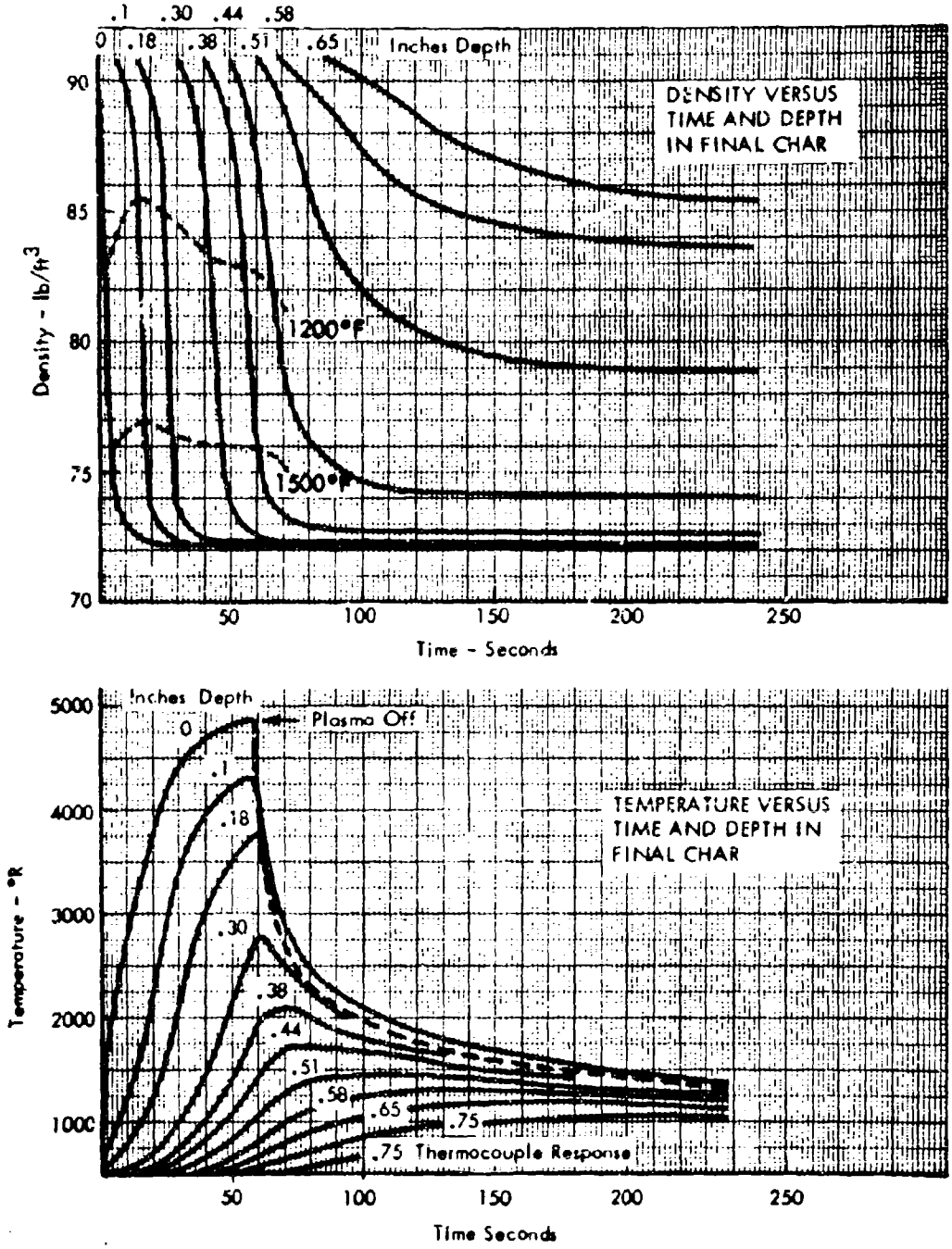

FIGURE 35 FM-5055A PREDICTED INTERNAL HISTORIES

SECTION VII

FM-5014 PHENOLIC GRAPHITE CHAR CHARACTERISTICS

Characterization of the char from the FM-5014 phenolic-graphite nozzle throat from the Titan 3C-10 120-inch solid strap-on motor provides a complete physical and chemical description of the post-test char as a function of depth. The results are presented in the same manner as for MX-4926 phenolic carbon so that the characteristics of the two types of chars may be easily compared.

VISIBLE CHARACTERISTICS

The major visible differences between FM-5014 and MX-4926 were the greater char depth on FM-5014 and absence of delamination in the char, or microcracking extending through the pyrolysis zone, and of anisotropic deposits on pore surfaces. Reflected light examinations were made on the radial plane shown in Figures 36 and 37 . Low magnification observations were made before potting, Figure 36, for maximum visual discrimination of light and dark bands in the char. Potted and polished thin sections, located as in Figure 38 , were used for combined transmitted and reflected light analysis of spatial characteristics and polarized light observations of anisotropic "graphitized" material. Results of thin section A are illustrated in Figures 38 through 40 . The absence of anisotropic material other than graphite cloth fibers is apparent.

The combined results of all photographic analyses and relationships with other analyses are described below.

Char Characteristics

Alternate dark and light bands 0.1-inch thick were visible to a depth of 0.9 inches. The bands from the char surface to a depth of 0.4 inches were parallel to the surface while most bands below this depth made a -4° angle with the char surface in the downstream direction.

Density/porosity measurements of H series char depth specimens established that dark bands were of higher open porosity and higher apparent solid density while light bands were of lower open porosity and greater apparent dry density. The

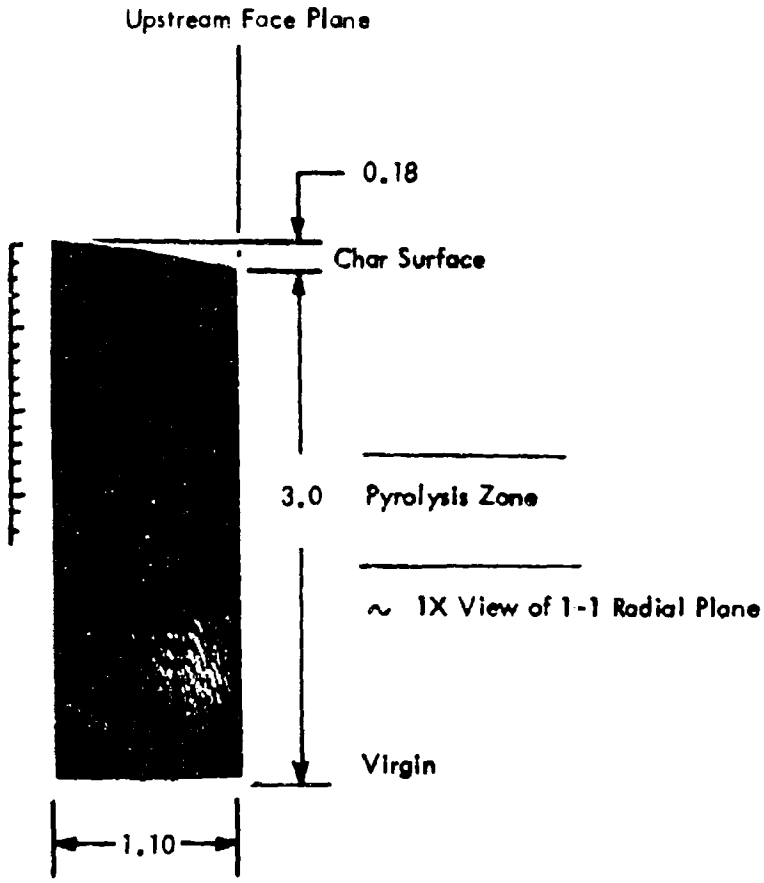

Nozzle Throat Segment B-1, Sample W-1

FIGURE 36 FM-5014 CHAR SURFACE AND VISUAL ZONES

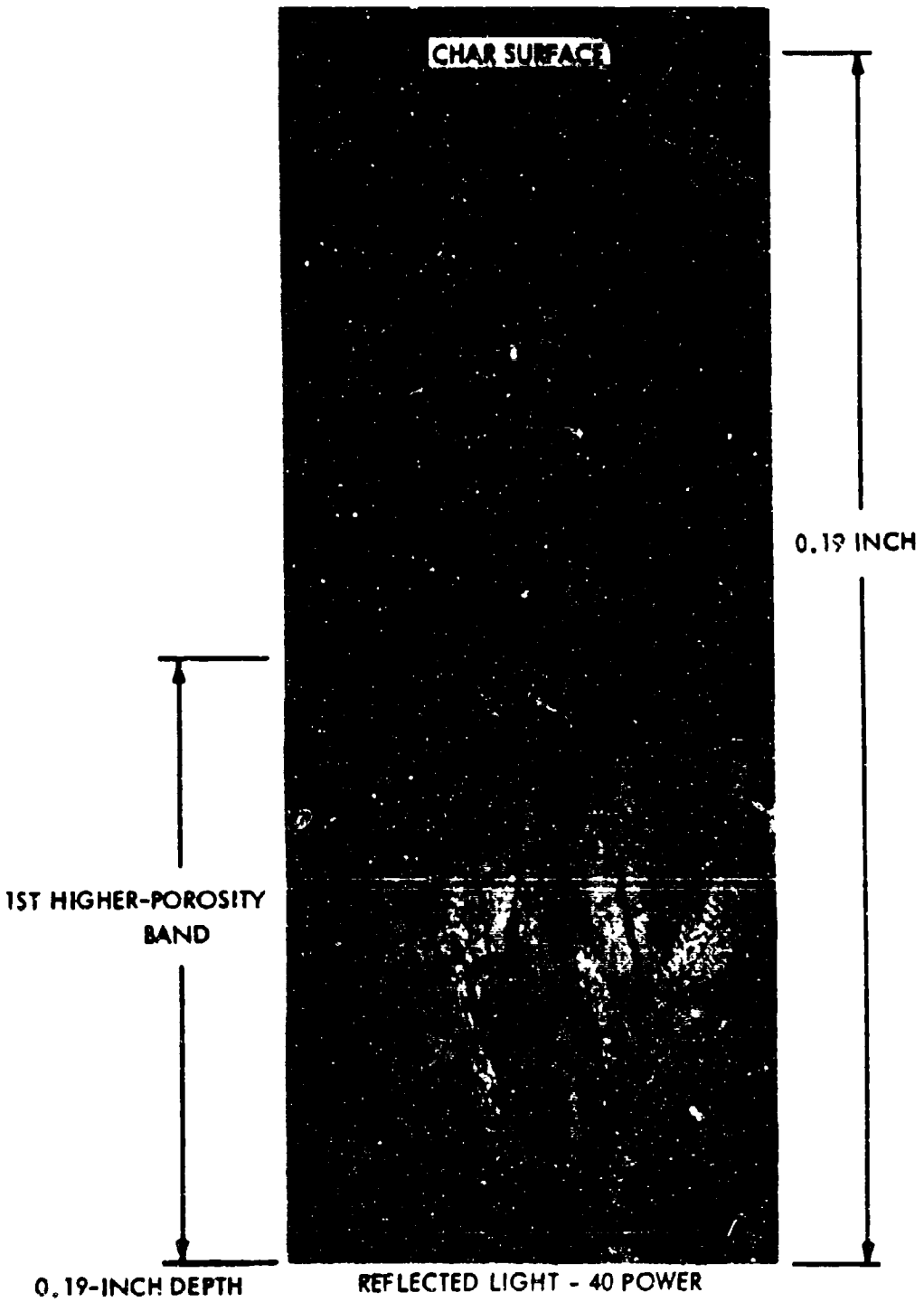

FIGURE 37 FM-5014 CHAR AT THE SURFACE LOCATION USED FOR PHOTOMICROGRAPHIC STRIP ANALYSIS

CHAR SURFACE

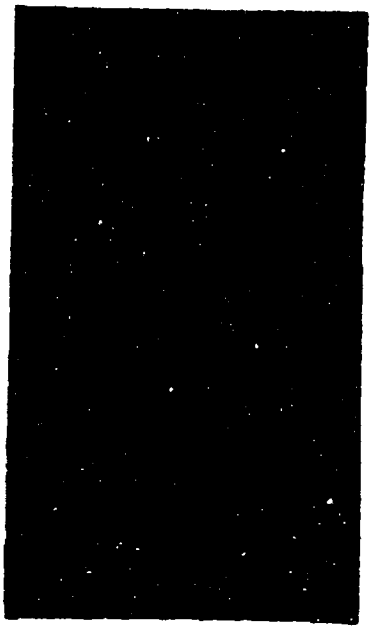

REFLECTED LIGHT 2X VIEW

TRANSMITTED I GHT 2.5X VIEW

PLANE PARALLEL WITH CLOTH LAYERS
UPSTREAM FACE OF B-1

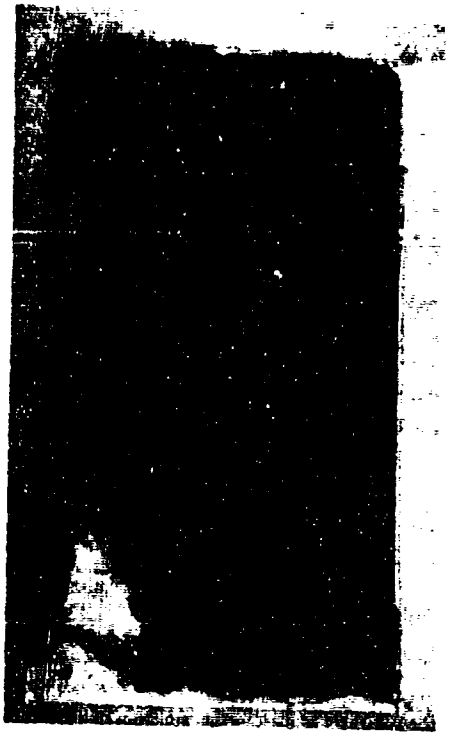

FIGURE 38 FM-5014 CHAR THIN SECTION A VIEWS

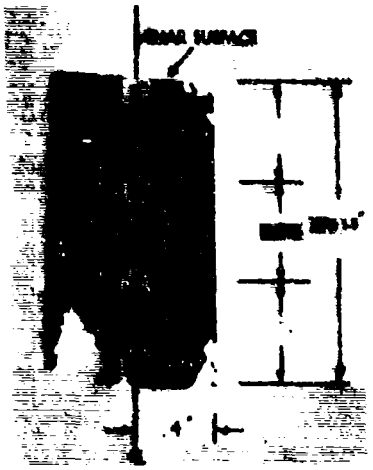

THIN SECTION A
OF
FM-5014

SPECIMEN ROTATION ANGLES

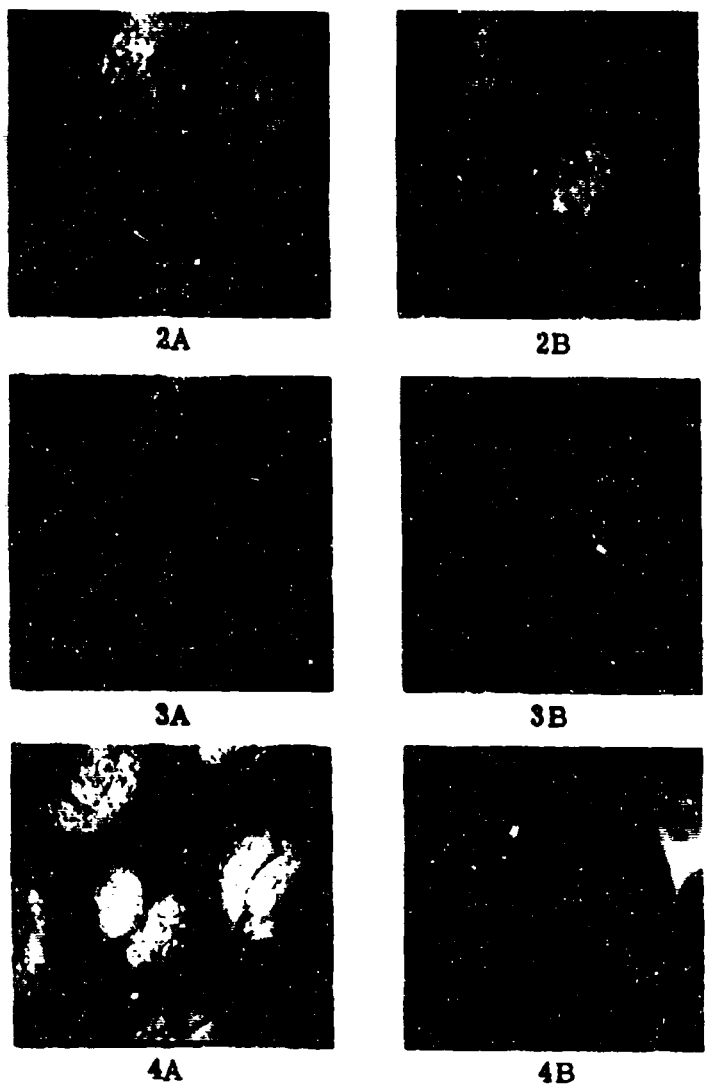

Anisotropic graphite fibers appear alternately light and dark with 90° rotation in polarized light.

FIGURE 39 FM-5014 CHAR ANISOTROPY 25X PHOTOMICROGRAPHIC ANALYSES WITH POLARIZED-REFLECTED LIGHT

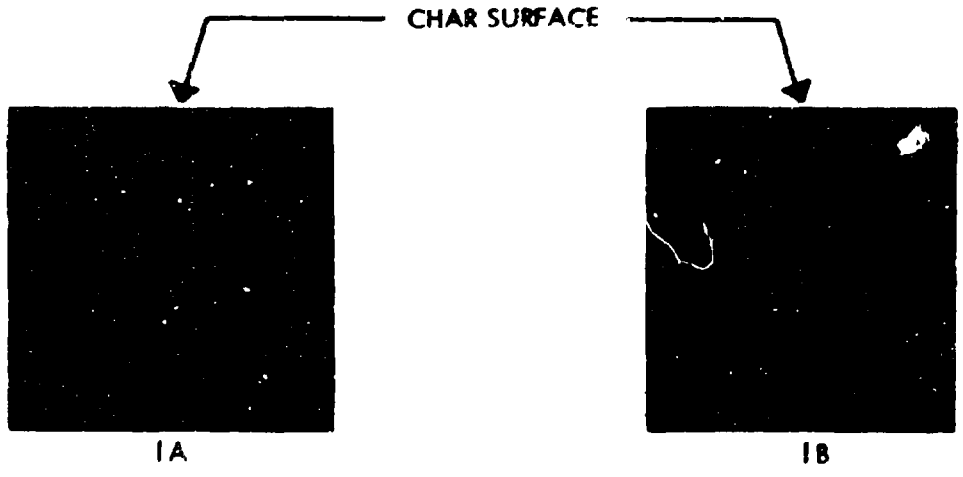

MAGNIFIED VIEWS OF 1A AND 1B

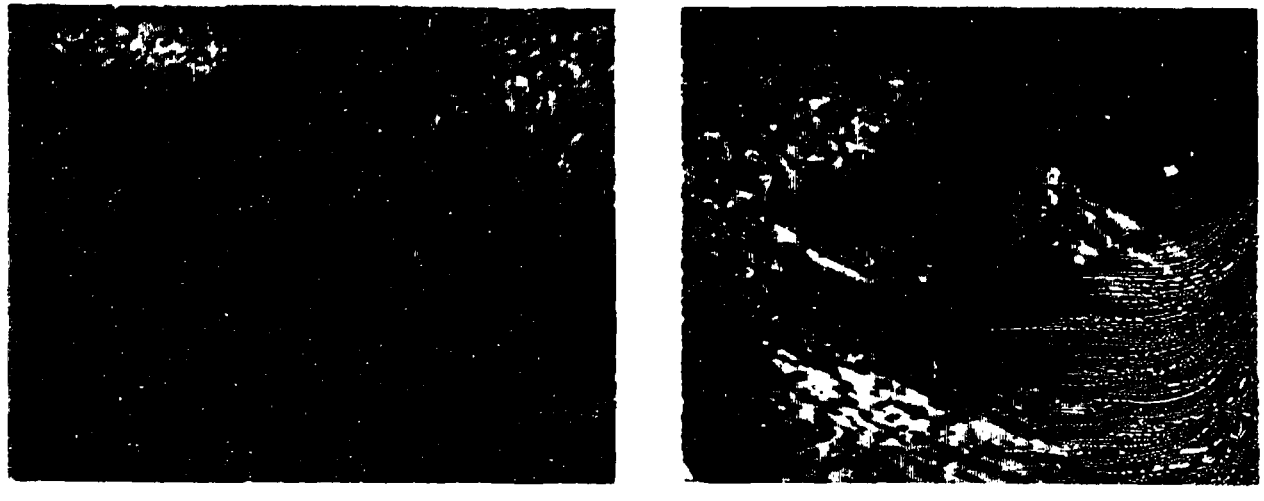

MAGNIFIED VIEWS MADE FROM CENTRAL PORTIONS OF THE 25X PHOTOMICROGRAPHS 1A and 1B AT THE SURFACE OF THIN SECTION A SHOWING NO INTER-FIBER ANISOTROPY.

FIGURE 40 FM-5014 CHAR ANISOTROPY WITH POLARIZED-REFLECTED LIGHT

most prominent band, a light band between 0.4 to 0.5 inches depth, coincided with the region of greatest apparent density and least porosity in the mature char zone. The second most prominent band was a 0.2-inch wide light band below 0.9 inches depth coinciding with the beginning of the pyrolysis zone. A third prominent visible zone was a black band from a depth of 1.1 inches to 1.5 inches coinciding with the pyrolysis zone.

Both inter-yam and inter-fiber porosity were visible to a 1-inch depth. The largest pores or microcracks were the inter-yam type with 80 micron (0.0032 inch) maximum width. These were concentrated mainly in the repetitive dark bands and at the char surface. That microcracking did not extend through the pyrolysis zone , a significant difference from the phenolic carbon materials, is believed related to the lesser pyrolysis shrinkage noted in furnace char preparation and may explain the relative lack of delaminations in the FM-5014 char. Lack of delamination is also believed to be related to the construction of the nozzle in ring segments; the net char shrinkage was resolved in large cracks at the weakly bonded ring joints.

No anisotropic or "graphitized" material other than the graphite cloth fibers was discernible under polarized reflected light. Dark inter-fiber areas in both polarized light rotations in Figures 39 and 40 indicate the lack of anisotropic material on pore surfaces.

Graphite-Cloth Matrix Characteristics

As in the tape wrapped MX-4926, there was no visible volume degradation of reinforcement fibers and the volumetric spacing and concentration of cloth layers and yams appeared constant versus char depth. Cloth layers were oriented at an angle of 83° from the char surface upstream direction. Yam orientations between plies were random. Mean fiber diameter was estimated to be 0.00032 inches. In one plane with fill yams oriented at 60° and warp yams oriented at 30° to the char surface, counts of 27 fill yams per inch and 28 warp yams per inch were obtained. These are higher than prepreg values, indicating compression. A count of 63 cloth layers per inch indicated that approximately 56 percent compression had occurred during fabrication.

DENSITY AND POROSITY PROFILE

Figure 41 illustrates the inverse proportionality between apparent dry density and open porosity obtained on char depth slices and the comparison of measured and computer predicted densities in the post-test char. These results are on H-series

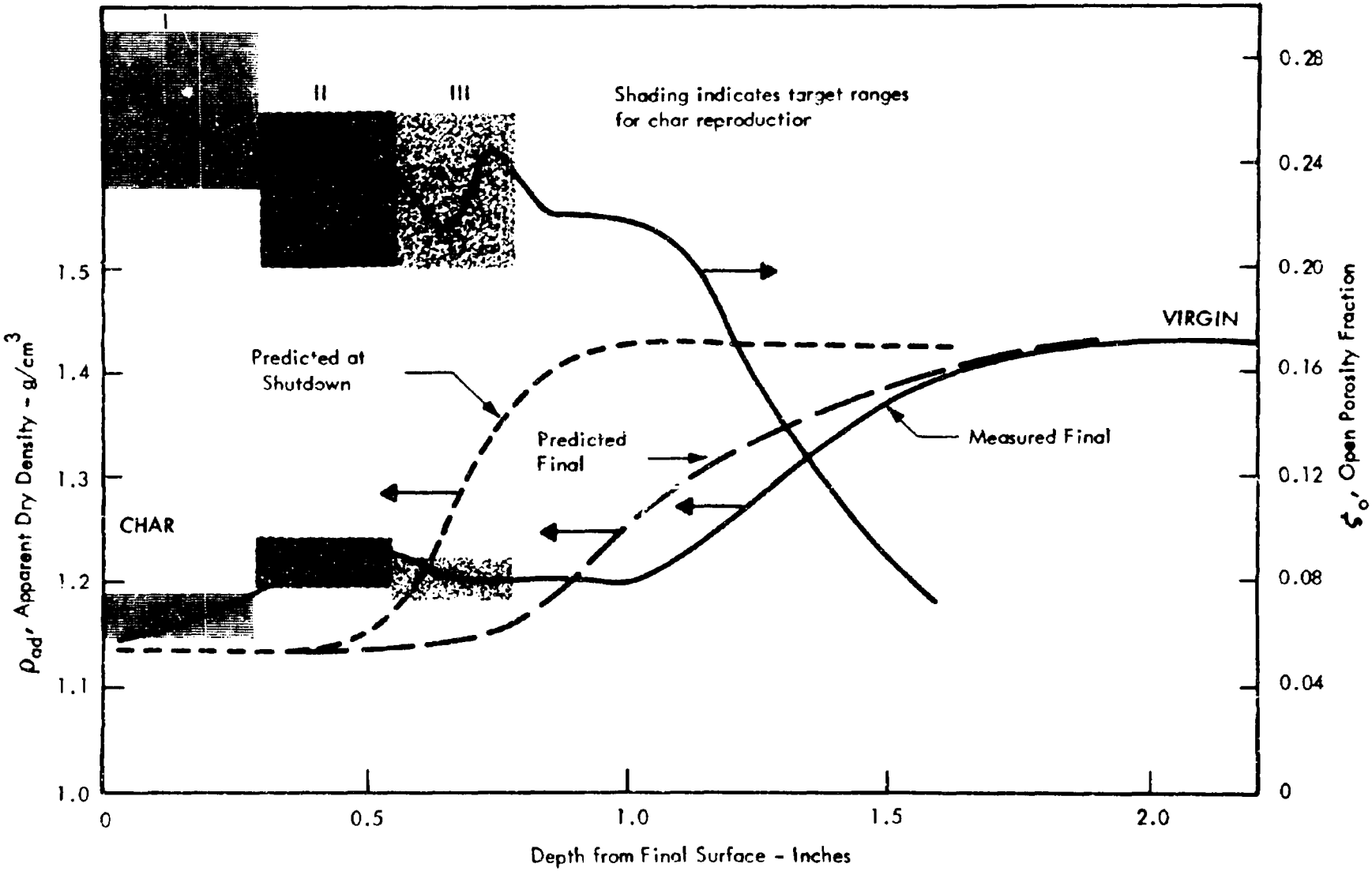

FIGURE 41 FM-5014 NOZZLE CHAR DENSITY AND POROSITY

char depth slices taken parallel to the surface to a depth of 0.4 inches and at -4° to the surface below 0.4 inches. These results yield the same conclusions as for MX-4926 phenolic carbon and validate the use of a porosity correlation of thermal conductivity data. The measured ρ_{ad} is higher than predicted in the mature char zone due to the presence of thermally unstable material deposited during the cooling period. Both thermal and elemental analyses show the presence of material that could not exist at the temperatures encountered in the mature char during the motor firing period.

The apparent density profiles given by Radocon X-ray transmission measurements are shown in Figure 42 . An abrupt decrease in apparent density at the char surface is clearly shown by the greater resolution of the Radocon measurements. This data was verified by supplementary direct density measurements on the surface slice of column W-3. The apparent density at the surface decreases to below 0.8 g/cm^3 and open porosity increase to above 0.6. The solid density at the surface is then over 2.1 g/cm^3.

All other data are presented in terms of porosity in Figures 43 and 44 . Complete data for both char depth slice orientations show similar behavior of porosity versus depth. The total and open porosity curves are an average of three measurements on each of three specimens per zone and all values were within ±5 percent of the average. Both total porosity and closed porosity are lower than for MX-4926, and total porosity and solid density do not increase with depth in the char. As with MX-4926, the behavior of total porosity from zone to zone was reproduced in the furnace chars for thermophysic property measurements, however better agreement between open porosity measurements on zone specimens and char depth slices was obtained on FM-5014 due to the small amount of very large porosity. The open and penetrated porosity values are more similar to MX-4926 for the same reason. Typical mercury porosimeter data on a char depth slice are shown in Figure 43 . Continuously increasing values at the high pressure end of the run were attributed to compression of the specimen, which would tend to make the results low in the fine porosity range.

The porosity data indicates that the mature char zone ends at approximately a 0.8-inch depth, in agreement with all other analyses. Below 0.7 inches the increasing proportion of fine voids is characteristic of this material. At this depth the difference between penetrated and open porosity is believed to be fine voids not resolved by the mercury porosimeter or closed due to specimen compression. Closer to the surface the difference is probably large voids as in the case of MX-4926. Apparent densities increase and porosities decrease steadily in the pyrolysis zone and converge on virgin material values beyond a depth of 1.8 inches.

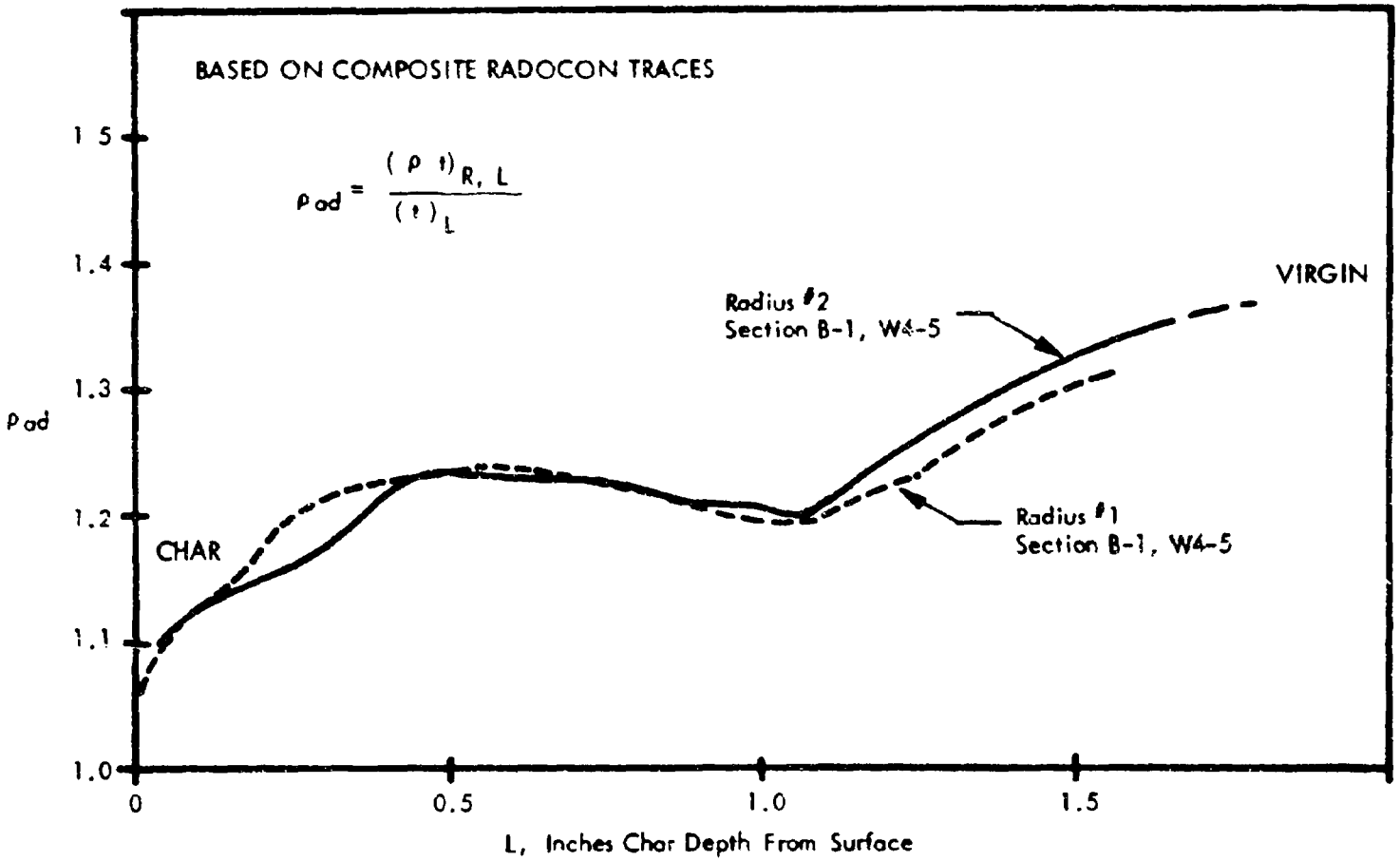

FIGURE 42 FM-5014 CHAR DENSITIES CALCULATED FROM X-RAY TRANSMITTANCE CORRELATIONS WITH DENSITY-THICKNESS PRODUCT

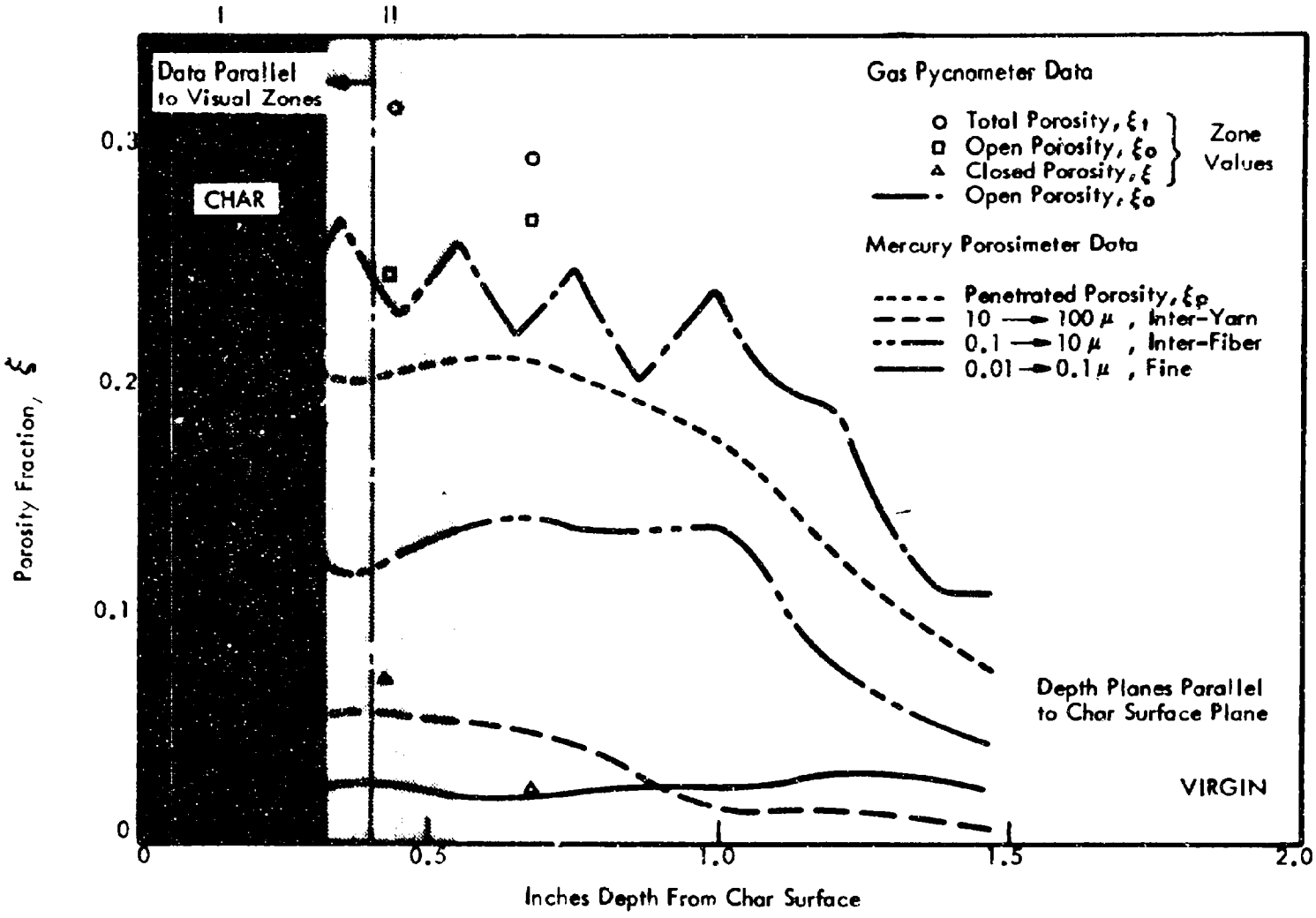

FIGURE 43 FM-5014 CHAR POROSITY FRACTIONS VS. DEPTH

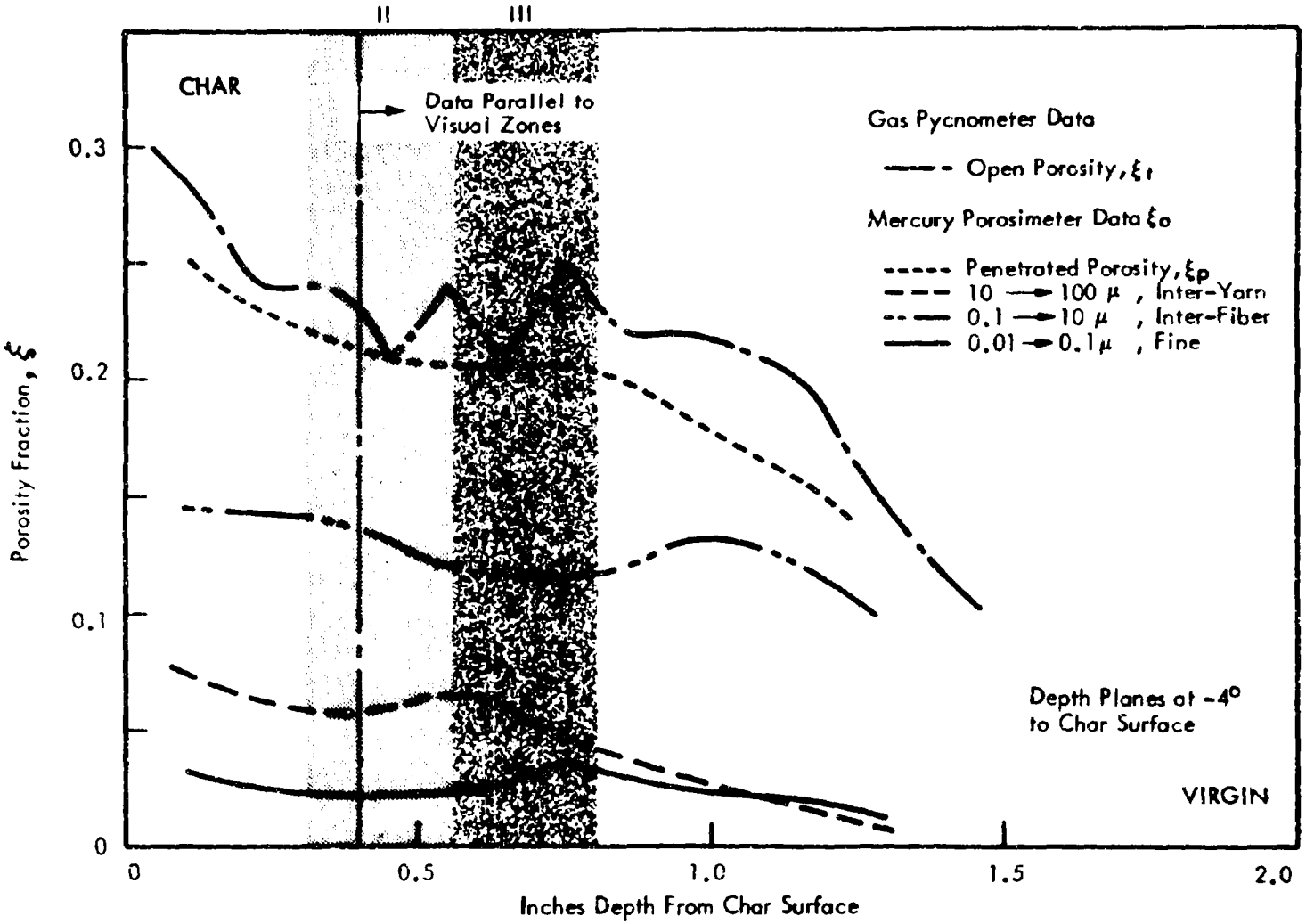

FIGURE 44 FM-5014 CHAR POROSITY FRACTIONS VS. DEPTH

THERMAL STABILITY PROFILE

Tables VII and VIII present the results of TGA and DTA analyses on depth slices from the FM-5014 post-test char. As was the case for MX-4926, values of two parameters were dependent upon depth in the char, the TGA total weight-loss and the initial temperature, T_a, of the first exotherm in the air DTA. These data are plotted versus char depth in Figure 45 . The total weight-loss data is easily interpreted as a measure of thermal stability of all material at any depth in the char. However, the DTA data appeared to be a function of both pyrolysis and "graphitization", whereas in MX-4926 it seemed to be related only to "graphitization."

The weight-loss data indicates that the mature char zone extends to a depth of approximately 0.85 inch. While apparent density and porosity data suggest that the mature char zone might extend to as deep as 1.0 inch, both the TGA weight-loss data and the elemental analysis data indicate that the density/porosity profile is affected by a high content of pyrolysis residue. The temperature of the first node in both the TGA and DTA results increases over pyrolysis zone values at a depth of 1.05 inches, but this is believed to be related to chemical changes from partly pyrolyzed phenolic rather than a transition from the pyrolysis zone to the mature char zone.

A weight-loss peak in the mature char zone at 0.45-inch depth indicates a large amount of hydrocarbon pyrolysis products, in agreement with elemental analysis. This deposition occurred during cool-down at a region of maximum apparent density and minimum open porosity in the mature char. These products showed very stable node characteristics, believed indicative of a high temperature cracking fraction.

COMPOSITION PROFILE

Composition versus depth in the post-test char was obtained by microcombustion analysis. Electron beam microprobe analysis of a char slice at 0.75-inch depth showed the presence of 1 to 2 percent chlorine and less than 1 percent potassium. Spark analysis of ash from the carbon-hydrogen analysis indicated small amounts of Al, Fe, and Si and traces of Ca, Cu and Mg.

Microcombustion analysis on duplicate char depth slices for total carbon, hydrogen and ash with the remainder attributed to oxygen are summarized in Table IX . The results of the partition of the elemental analysis are also shown. These results confirm that thermally unstable hydrocarbon material was deposited below 0.2 inch

TABLE VII FM-5014 CHAR THERMOGRAVIMETRIC ANALYSIS RESULTS, HELIUM ATMOSPHERE

Specimens	Char Depth (inches)	ρs Solid Density (g/cm^3)	*Incremental Weight Loss % Between Temperature Nodes, Dry Basis												Cumulative Weight Loss % Dry Basis	
			0		1		2		3		4		Maximum		1800°F	Max T(°F)
			T(°F)	%	T(°F)	%	T(°F)	%	T(°F)	%	T(°F)	%	T(°F)	%	%	%
H-1 (W-2)	0.046	1.59	R.T.	0	500	0.3	1300	0.1	1800	0.3			1810	0	0.5	0.5
H-2 (W-3)	0.154	1.63	R.T.	0	320	0.31	550	0.21	1800	0			1810	0	0.52	0.52
H-3 (W-3)	0.252	1.55	R.T.	0	1100	0.9	1800	0.4					1840	0.2	1.3	1.5
H-4 (W-1)	0.351	2.00	R.T.	0	1800	0							-	-	0	-
H-5 (W-3)	0.450	1.56	R.T.	0	1200	1.5	1800	0.9					1860	1.9	2.4	4.3
H-6 (W-3)	0.55	1.62	R.T.	0	430	1.81	880	0.42	1780	0.14	1800	0.14	1830	0.14	2.51	2.65
H-7 (W-3)	0.65	1.53	R.T.	0	700	0.9	1070	0.1	1550	0.5	1800	0.1	--	--	1.6	--
H-8 (W-3)	0.75	1.61	R.T.	0												
H-9 (W-3)	0.85	1.54	R.T.	0	800	0.8	1150	0.4	1550	1.2	1800	0.4	--	--	2.8	—
H-10 (W-3)	0.95	1.54	R.T.	0												
H-11 (W-3)	1.05	1.53	R.T.	0	1000	0.4	1800	3.9					1830	0	4.3	4.3
H-13 (W-3)	1.25	1.52	R.T.	0	550	0.4	1600	8.1	1800	0.2			—	--	8.7	—
H-15 (W-3)	1.451	1.50	R.T.	0	800	0.6	1800	11.5					1860	0.3	12.1	12.4
Near Virgin	3.0	1.45	R.T.	0	800	3.3	1100	8.8	1400	2.7	1800	0.2			15.0	15.0

*Constant rate of temperature increase with time, 9.5 to 10°F/min. from R.T. to near 1800°F in helium atmosphere with nodes denoting apparent changes in rate of percent weight loss.

TABLE VIII FM-5014 CHAR DTA-IN-AIR CHARACTERIZATION RESULTS

Black Segment B-1, With H-Specimens Cut From Radial Columns Parallel To Zones For W-1 And W-3, And Parallel To Surface For W-2

CHAR SPECIMENS				NET EXOTHERMIC EVENTS Line 1: Heat $\Delta H_r/\omega$ or $1/\omega \int \mu V dt = \sum \Delta H_r \omega$, (microvolts °C/mg) Line 2: Temperatures at peak microvolts, T_p (°C) Line 3: Temperatures at start - T_o and end - T_c (°C) Line 4: Peak microvolts, μV_p							Total Heats $\Delta H_r/\omega$ and Temp. Limits: Initial T_o Final T_c
Designation Codes		Depth from Surface (inches)	Weight ω (m-gm)	Items	R-1	R-2	R-3	R-4	R-5	R-6	
Depth	Radial Col.										
H-1	(W-2)	0.046	11.44	$\Delta H_r/\omega$ T_p T_o/T_c μV_p		1322 800°C (563) (863) 145			1052 863°C (790) (905) 200	96 890°C (863) (926) 25	2470 T_o = 563°C T_c = 926°C
H-2	(W-1)	0.154	11.24	$\Delta H_r/$ T_p T_o/T_c μV_p		1285 753°C (500) (815) 135		1140 824°C (727) (874) 216			2425 T_o = 500°C T_c = 874°C
H-3	(W-1)	0.252	13.74	$\Delta H_r/\omega$ T_p T_o/T_c μV_p		775 694°C (500) (745) 120	681 745°C (679) (811) 160	1254 811°C (713) (867) 250			2710 T_o = 500°C T_c = 867°C
H-3	(W-3)	0.252	12.84	$\Delta H_r/\omega$ T_p T_o/T_c μV_p		1800 779°C (513) (849) 180			960 849°C (780) (910) 212		2760 T_o = 513°C T_c = 910°C
H-4	(W-1)	0.351	13.72	$\Delta H_r/\omega$ T_p T_o/T_c μV_p		1564 729°C (519) (800) 170		641 794°C (713) (854) 150			2205 T_o = 519°C T_c = 854°C
H-5	(W-3)	0.45	10.34	$\Delta H_r/\omega$ T_p T_o/T_c μV_p		569 671°C (510) (716) 73	505 716°C (636) (771) 95	966 783°C (682) (854) 120			2040 T_o = 510°C T_c = 854°C

TABLE VIII CONT'D

CHAR SPECIMENS				NET EXOTHERMIC EVENTS Line 1: Heat $\Delta H_r/\omega$ or I/ω $\int \mu V_{dt} = \sum \Delta H/\omega$ (microvolts °C/mg) Line 2: Temperatures at peak microvolts, T_p (°C) Line 3: Temperatures at start - T_o and end - T_c, (°C) Line 4: Peak microvolts, μV_p							Total Heats $\Delta H_r/\omega$ and Temp. Limits: Initial T_o Final T_c
Designation Codes		Depth from Surface (inches)	Weight ω (m-gm)	Items	R-1	R-2	R-3	R-4	R-5	R-6	
Depth	Radial Col.										
H-6	(W-3) & (W-1) Same	0.55	13.0	$\Delta H_r/\omega$ T_p T_o/T_c μV_p		685 648°C (470) (700) 110	923 705°C (628) (779) 180	847 770°C (700) (844) 160			2455 T_o = 470°C T_c = 844°C
H-7	(W-3)	0.65	12.68	$\Delta H_r/\omega$ T_p T_o/T_c μV_p		634 614°C (450) (668) 95	1104 700°C (600) (778) 172	1022 778°C (700) (884) 172			2760 T_o = 450°C T_c = 884°C
H-9	(W-3)	0.85	13.78	$\Delta H_r/\omega$ T_p T_o/T_c μV_p	623 544°C (365) (635) 73		868 711°C (520) (803) 118	1014 803°C (680) (863) 167			2505 T_o = 365°C T_c = 863°C
H-11	(W-3)	1.05	10.98	$\Delta H_r/\omega$ T_p T_o/T_c μV_p	178 400°C (300) (473) 17	462 520°C (414) (600) 57	326 661°C (563) (710) 50	1334 780°C (629) (843) 135			2300 T_o = 300°C T_c = 843°C
H-13	(W-3)	1.25	14.73	$\Delta H_r/\omega$ T_p T_o/T_c μV_p	782 529°C (223) (608) 76		428 670°C (563) (734) 95	418 734°C (670) (790) 92	782 806°C (704) (863) 145		2410 T_o = 223°C T_c = 863°C
H-15	(W-3)	1.45	16.82	$\Delta H_r/\omega$ T_p T_o/T_c μV_p	338 430°C (210) (510) 40	545 536°C (400) (600) 97	243 625°C (540) (676) 53	131 676°C (613) (708) 45	1168 803°C (613) (856) 162		2425 T_o = 210°C T_c = 856°C
Virgin	(W-3)	2.26	14.42	$\Delta H_r/\omega$ T_p T_o / T_c μV_p	686 536°C (200) (612) 61		303 650°C (536) (727) 37		1081 811°C (612) (813) 113		2070 T_o = 200°C T_c = 873°C

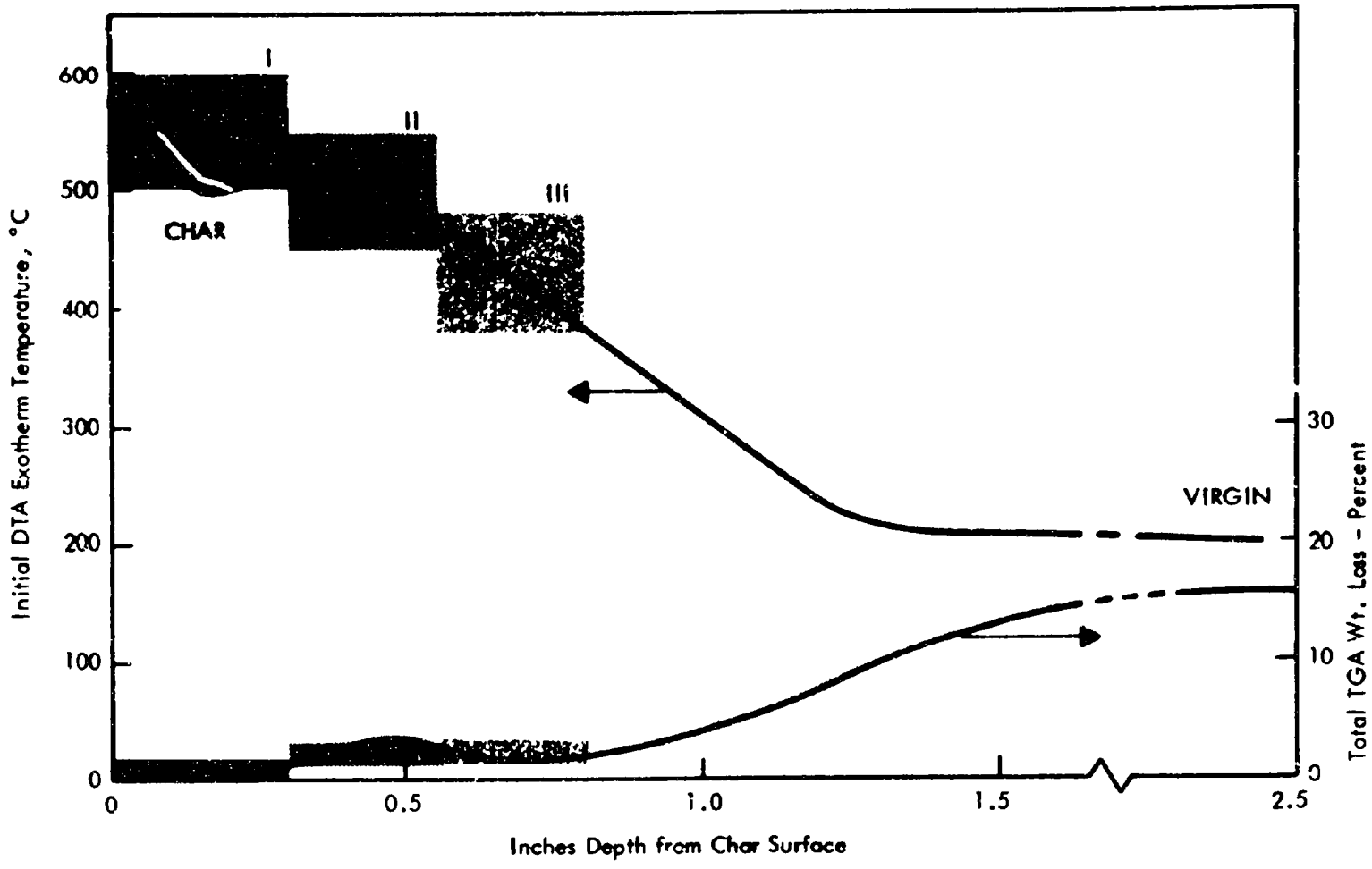

FIGURE 45 FM-5014 CHAR THERMAL ANALYSIS

TABLE IX FM-5014 CHAR ELEMENTAL ANALYSIS AND ESTIMATED PARTITION

Block Segment B-1, radial column, W-3 parallel to zones, except specimen H-1

CHAR SPECIMENS			ELEMENTAL ANALYSES TOTAL WT. %				OXYGEN PARTITION		HYDROGEN PARTITION			CARBON PARTITION		
Depth Code	Depth	App. Dry Density g/cm^3	Ash	H	O	C	In Phenolic Wt, %	In Water Wt. %	In Water Wt. %	In Phen. Wt. %	H/C in Phen. (atoms)	Cloth & Filler Wt. %	In Phenolic Wt. %	Pyrolysis Residue Wt. %
H-1	.046	1.151	0.3	0.2	0	99.5	0	0	0	0.2	--	72.1	0	27.4
H-3	0.25	1.183	0.1	0.2	0.7	99.0	0.51	0.18	0.02	0.18	5.5	70.1	2.70	26.2
H-5	0.45	1.232	0	0.36	1.74	97.9	0.65	1.09	0.14	0.22	5.5	67.4	3.42	27.1
H-6	0.55	1.225	0	0.4	2.6	97.0	0.34	2.26	0.28	0.12	5.5	67.8	1.80	27.4
H-7	0.65	1.207	0	0.5	2.8	96.7	0.68	2.11	0.26	0.23	5.5	68.9	3.60	24.2
H-9	0.85	1.205	0	0.9	3.20	95.9	2.29	0.91	0.11	0.78	5.5	69.0	12.0	14.9
H-11	1.05	1.207	0	1.1	3.3	95.6	3.14	0.16	0.02	1.08	5.5	68.9	16.5	10.2
H-13	1.25	1.279	0.05	1.56	4.49	93.9	4.49	0	0	1.56	5.5	65.0	23.6	5.3
H-15	1.45	1.357	0.33	1.74	5.03	92.9	5.03	0	0	1.74	5.5	61.2	26.4	5.3
Virgin	2.26	1.432	0.15	2.08	7.57	90.2	6.14	1.43	0.18	1.90	5.0	58.0	32.2	0

In the mature char. Deposited material was also indicated by the TGA weight-loss results and by high apparent density relative to computer predictions in the mature char zones. Pyrolysis product redeposition is not included in the computer predictions.

The elemental analysis partition was developed on the basis of the constant volume concentration of carbon in cloth and filler shown in photomicrographic analysis. This is the same basis used for MX-4926 and it was verified in the same way by calculating the elemental analyses of virgin and char surface material. At other depths in the char, stoichiometric balances were made assuming that the ratio of hydrogen atoms to seven carbon atoms in phenolic resin was 5.5 (specimens H-3 through H-11) and that the total oxygen content existed in residual phenolic (specimens H-13 and H-15). The results of carbon partition are plotted in Figure 46 .

INTERNAL "GRAPHITIZATION" PROFILE

X-ray diffraction on the top surfaces of char depth slices established the profile of char "graphitization" shown in Figure 47 . The diffraction intensities at the char surface are about twice the levels for the virgin material. Since no inter-fiber anisotropy was discernible by photomicrographic analyses with polarized light, the additional graphitization in the mature char must be attributed to small crystallites of graphite in residual or filler material or further graphitization of fibers. The decrease in diffraction intensities from the surface to virgin material levels at a depth of 0.3 inches was the primary characteristic defining char zone I in this material.

COMPUTER PREDICTED INTERNAL ABLATION HISTORIES

Predicted densities and temperature versus time and depth for the FM-5014 nozzle throat are given in Figure 48 . The results are similar to those on MX-4926 except that deeper charring and milder temperature gradients result from the longer exposure time and higher thermal conductivity for this material. Ablation after shutdown is more extensive since more heat is stored in the deeper char. The general observations made in reference to the internal histories on MX-4926 also hold for this material.

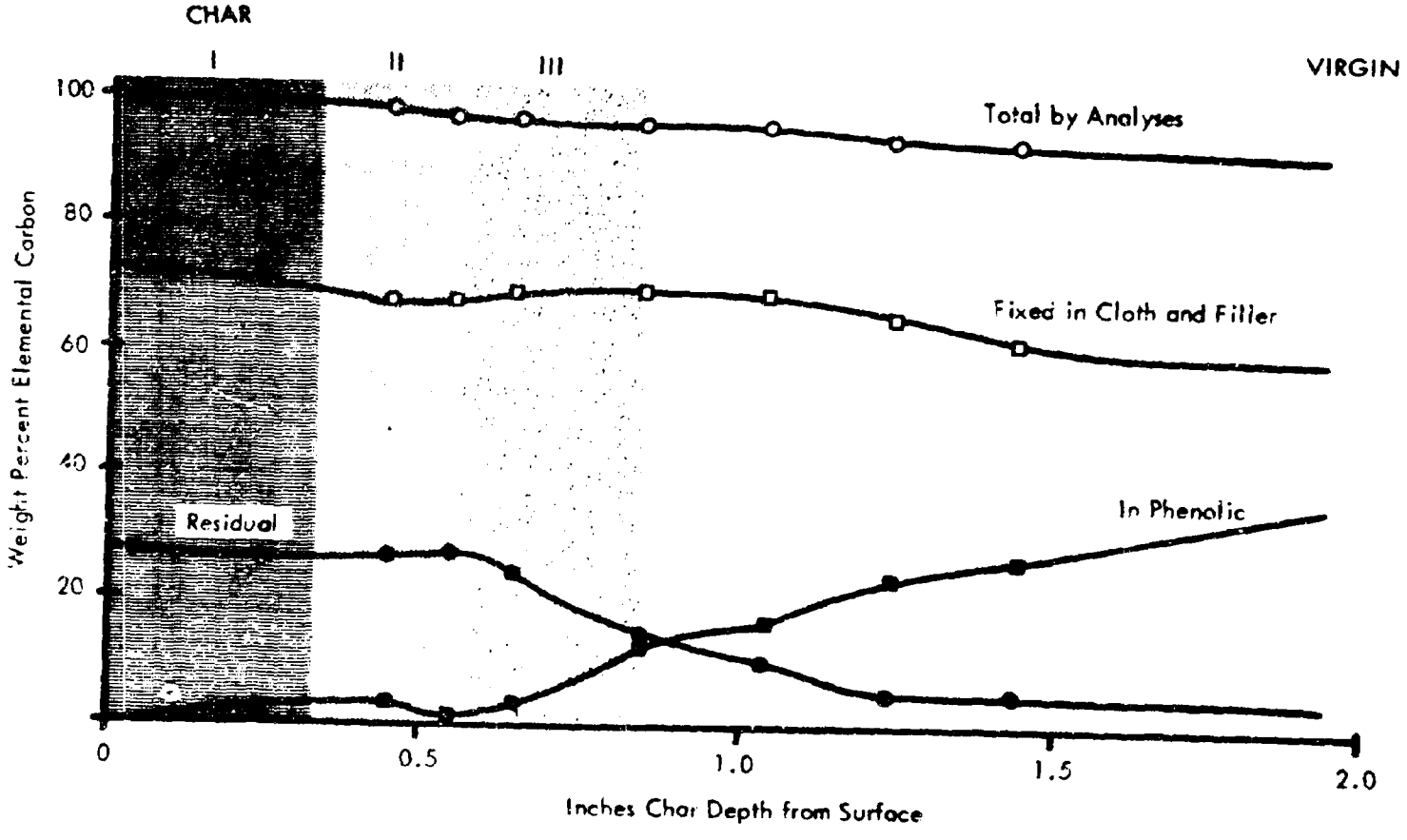

FIGURE 46 FM-5014 CHAR ELEMENTAL CARBON PARTITION

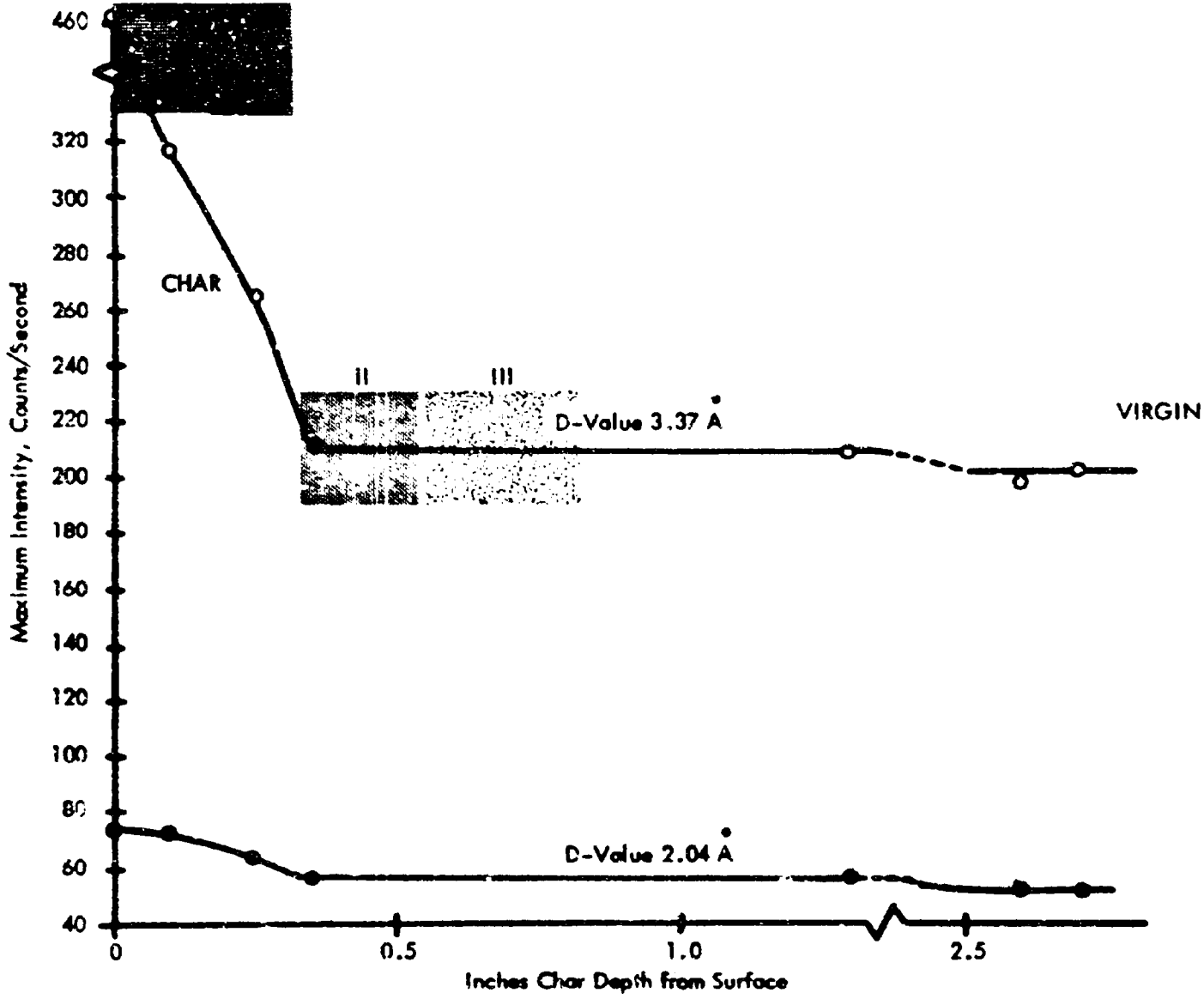

FIGURE 47 FM-5014 CHAR GRAPHITIZATION, X-RAY DIFFRACTION INTENSITY VERSUS CHAR DEPTH

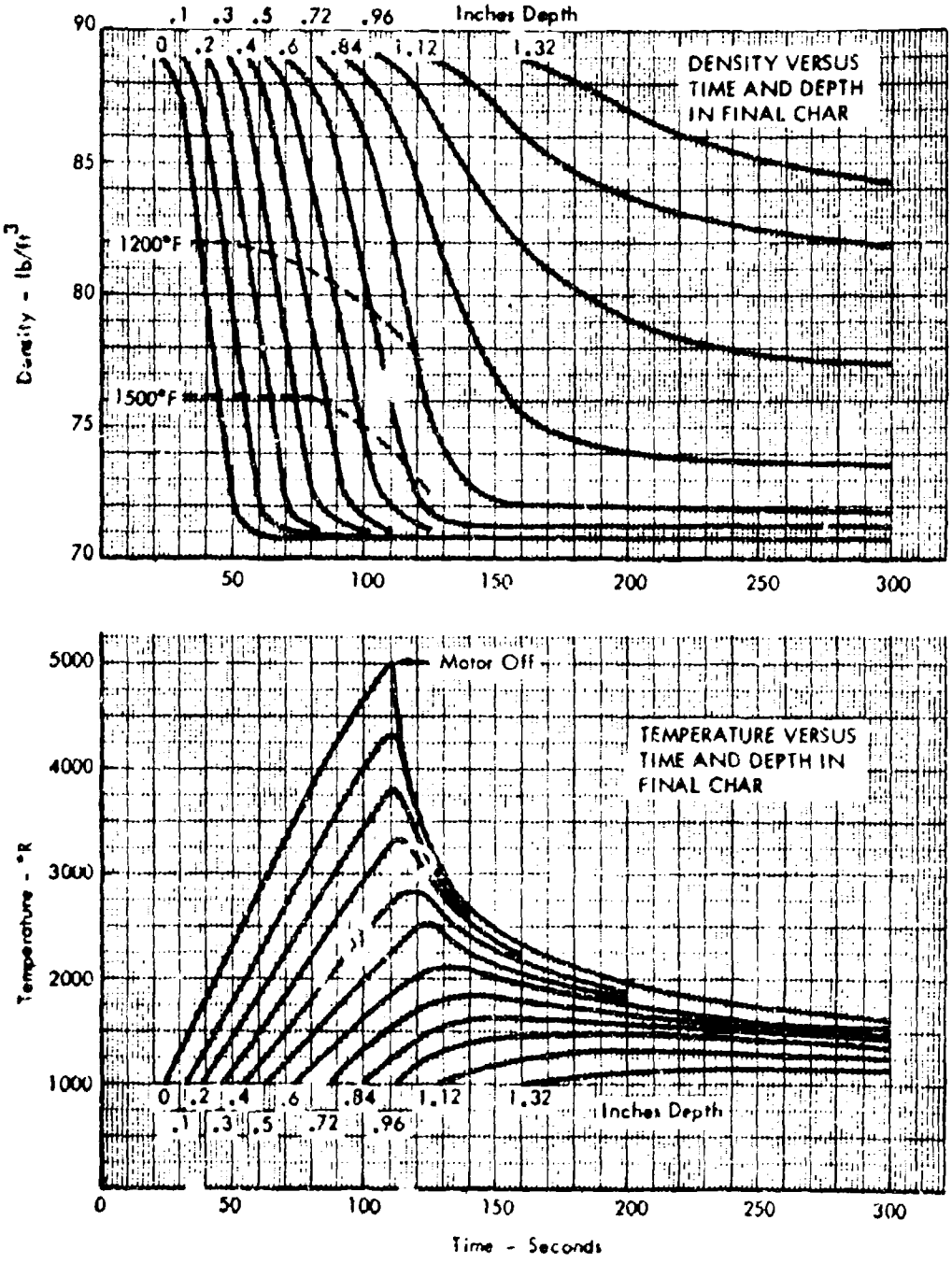

FIGURE 48 FM-5014 PREDICTED INTERNAL HISTORIES

SECTION VIII

CHAR SAMPLES FOR THERMOPHYSICAL PROPERTIES

This section defines the subzones in the mature chars of the nozzle throat materials, MX-4926 phenolic-carbon and FM-5014 phenolic-graphite. Furnace charring methods used to reproduce these subzones, designated as zones I, II, and III, in the form of large samples for thermophysical property measurements are described. A summary of the results of complete characterization on the thermophysical property samples, required for analysis of the property data, is given.

CHAR ZONE DEFINITION

The quantitative description of the post-test nozzle chars provided by characterization enabled the selection of three distinct subzones in the mature char layer for thermophysical property measurements. Measurements on each of these zones plus the virgin material enables defining changes in thermophysical properties accompanying ablation in these materials. The mature char subzones and the virgin material of both MX-4926 and FM-5055A are described as follows:

Char Zone I - This stable surface zone is characterized by a significant amount of graphitization, high porosity, high residual carbon content, and absence of phenolic resin. This zone has experienced temperatures from 2900°F on the inner boundary to 4600°F on the outer hot face.

Char Zone II - This stable middle char zone is similar to zone I except that there is no graphitization and pyrolysis is complete for both the nozzle chars and the chars produced at low heating rates in the laboratory. This zone has experienced temperatures from 1900°F to 2900°F.

Char Zone III - This zone includes the outer portion of the pyrolysis zone and is similar to zone II except that it contains some unpyrolyzed phenolic and contains less residual carbon. The inner boundary of this zone is arbitrarily placed at a level which has experienced a 1200°F maximum temperature.

Virgin Zone - The [illegible] material unaffected by heating except for volatilization losses not exceeding [illegible] percent by weight. The density and composition are those of the original ablator with a total porosity less than 3 percent. The upper temperature limit of this zone is 500°F for MX-4926 and 700°F for FM-5014.

The characteristics of each of these zones in the MX-4926 and FM-5014 mature chars are summarized in Tables X and XI and were used as targets for establishing furnace charring methods. No attempt was made to duplicate the thermally unstable material deposited during cool down in the zone I and II chars because these deposits are not characteristic of an ablating char. All zone characteristics were duplicated except that unavoidable shrinkage accompanying the pyrolysis of the unrestrained furnace chars resulted in higher apparent density and lower porosity than measured on the post-test nozzle chars.

THERMOPHYSICAL PROPERTY SAMPLE PRODUCTION

Virgin material from the nozzle segment was used to prepare FM-5014 char samples, but the MX-4926 nozzle segment virgin material was insufficient to provide all the samples required. Therefore, a virgin block purchased from TRW was used for the MX-4926 char samples. It was produced from prepreg remaining from nozzle production and its density was close to that of the nozzle. Oversize slabs with the required laminae orientations for the thermal conductivity specimens were rough-cut using a 16-inch reinforced, aluminum oxide, abrasive wheel. Virgin specimens were machined directly from the rough cut slabs and char specimens were machined after the charring cycles using conventional lathes and grinders. Thermal expansion and specific heat specimens were machined from the slab material adjacent to the portion used for thermal conductivity specimens.

Table XII lists all thermal property specimens produced from the slabs described above and gives the code identifications used in this report. In addition, expansion and specific heat specimens were also machined directly from the virgin and char of the MX-4926 nozzle-throat to enable direct comparison of real and analogue char materials for one ablator. Data from these specimens are designated as "nozzle" data in the discussion of thermal expansion and specific heat results.

The furnace char analogues of zones I, II, and III were produced by charring virgin slabs in an argon atmosphere in an induction-heated graphite retort, shown in Figure 49. Each slab was supported by posts inserted into the base plate. Up to four slabs were charred at the same time to insure uniformity. After the loaded retort was placed into a ceramic-potted, water-cooled induction coil, fine graphite powder was added as thermal insulation between the coil and susceptor and over the cover. Heating cycles were controlled with two interchangeable cam program controllers - one for Type R thermocouple control to 2500°F and the second for radiometer control between 2500°F and 5000°F - which activated a 100 KW, 9600 cycle induction power supply.

TABLE X
CHARACTERISTICS OF PRIMARY ZONES IN MX-4926 NOZZLE

Characteristic	CHAR ZONE VALUES			Virgin Zone Values
	I	II	III	
Depth Range, inches	Surface to 0.25	0.25 to 0.4	0.4 to 0.55	>1.5
Temperature Range - °F	4500 - 2900	2900 - 1900	1900 - 1200	500 - 70
Density - g/cm^3	1.12 ± 0.02	1.13 ± 0.02	1.13 ± 0.02	1.44 ± 0.02
Porosity fraction, ϵ_c	0.28 ± 0.04	0.28 ± 0.04	0.28 ± 0.04	< 0.01
X-Ray Diffraction Intensity (D-value 3.37Å) Counts/Second	Up to 185 (160 Nominal)	105 ± 10	105 ± 10	(N.A.)
Anisotropy Location under polarized light	Pore and inter-fiber Surfaces	None	None	(N.A.)
Helium TGA total Weight Loss - %	1 ± 1	1 ± 1	3 ± 1	< 4% at 500°F
Air DTA Initial exotherm temperature - °C	500 ± 75	300 ± 50	250 ± 20	200 ± 20

TABLE XI
CHARACTERISTICS OF PRIMARY ZONES IN FM-5014 NOZZLE

Characteristic	CHAR ZONE VALUES			Virgin Zone Values
	I	II	III	
Depth Range, inches	Surface to 0.3	0.3 to 0.55	0.55 to 0.8	> 2.0
Temperature Range, °F	4500 - 2900	2900 - 1900	1900 - 1200	500 - 70
Density, g/cm^3	1.17 ± 0.02	1.22 ± 0.02	1.20 ± 0.02	1.43 ± 0.02
Porosity Fraction, ε_c	0.27 ± 0.03	0.23 ± 0.03	0.23 ± 0.03	< 0.03
X-Ray Diffraction Intensity (D-Value 3.37Å) Counts/Second	Up to 500 (350 Nominal)	210 ± 20	210 ± 20	(N.A.)
Anisotropy Location under Polarized Reflected Light	Graphite Fiber Only	Graphite Fiber Only	Graphite Fiber Only	(N.A.)
Helium TGA Total Weight Loss %	1 ± 1	2.5 ± 1	2 ± 1	< 4 at 700°F
Air DTA Initial Exotherm Temperature, °C	550 ± 50	500 ± 50	430 ± 50	200 ± 20

TABLE XII SLAB AND SPECIMEN IDENTIFICATION - VIRGIN PLASTIC AND FURNACE CHAR

MATERIAL	ZONE	SPECIMEN CODE	SLAB FABRIC LAMINATION ANGLE, degrees to surface	PROPERTY SAMPLES - NUMBER AND LAMINATION ANGLE [1]			MAX. TEST TEMPERATURE °R
				Conductivity (to heat flow direction)	Thermal Expansion (to dilation direction)	Specific Heat (angle not applicable)	
MX-4926 PHENOLIC-CARBON	Virgin	PC-V-0	0	1, normal	1, parallel	2	960
		PC-V-20	20	1, 70°	——	—	960
		PC-V-45	45	1, 45°	——	—	960
		PC-V-90	90	1, parallel	1, normal	—	960
	III	PC-III-0	0	1, normal	1, parallel	—	1560
		PC-III-20	20	1, 70°	——	—	1560
		PC-III-45	45	1, 45°	3, 45°	—	1560
		PC-III-90	90	1, parallel	1, normal	—	1560
	II	PC-II-0	0	1, normal [2]	——	—	2960
		PC-II-20	20	1, 70°	——	—	2960
		PC-II-45	45	1, 45°	——	—	2960
		PC-II-90	90	1, parallel	——	—	2960
	I	PC-I-0	0	1, normal [2]	1, parallel	—	4460
		PC-I-20	20	1, 70°	——	—	4460
		PC-I-45	45	1, 45°	——	—	4460
		PC-I-90	90	1, parallel	1, normal	1	4460
FM-5014 PHENOLIC-GRAPHITE	Virgin	PG-V-0	0	1, normal	1, parallel	2	1160
		PG-V-90	90	1, parallel	1, normal	—	1160
	III	PG-III-0	0	1, normal	1, parallel	—	1560
		PG-III-90	90	1, parallel	1, normal	—	1560
	II	PG-II-0	0	1, normal	——	—	2960
		PG-II-90	90	1, parallel	——	—	2960
	I	PG-I-0	0	1, normal	1, parallel	1	4460
		PG-I-90	90	1, parallel	1, normal	—	4460

[1] Angle established along cloth bias in MX-4926; random cloth orientation in FM-5014

[2] Conductivity data in error - not reported

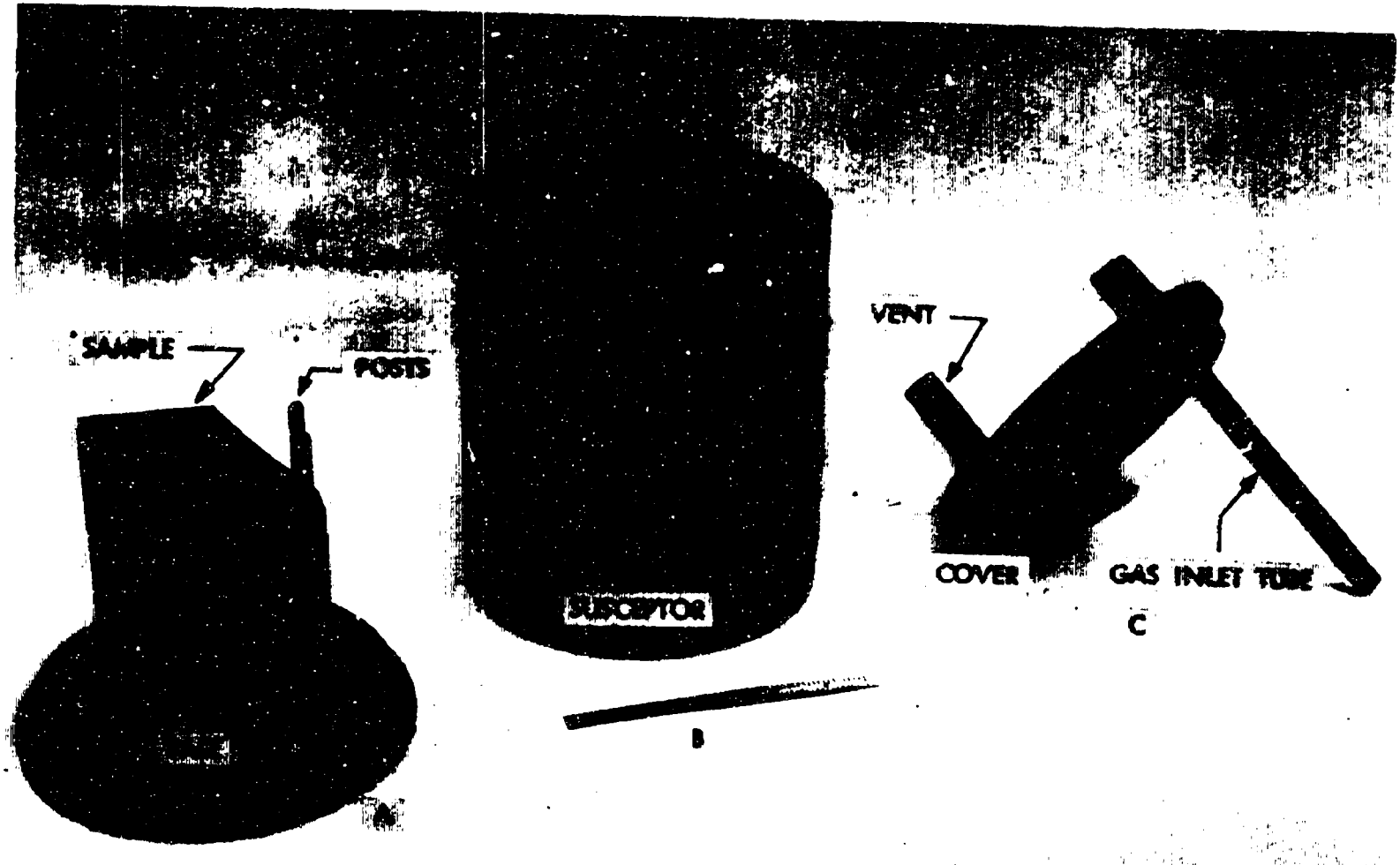

FIGURE 49 COMPONENT PARTS OF GRAPHITE RETORT

A large number of heating cycles were tried to establish the fastest cycle that would not cause delamination. The MX-4926 material was much more sensitive in this respect, so that the common heating cycle used for both materials was established by the behavior of MX-4926. Selection of the maximum furnace temperature for producing zone III chars, 1200°F, was based on weight lost on heating to 1800°F in TGA tests of test pieces. The maximum furnace temperature for zone II and I chars, 2500°F and 4000°F respectively, was based on X-ray diffraction analysis for "graphitization" on trail furnace slabs. The zone I samples were processed so that they were sufficiently graphitized that they were like near-to-the-surface chars, thereby yielding stable samples for measurements at the highest temperatures.

The furnace charring cycles for zones II and III are shown in Figure 50. The stepwise holding at several temperatures was found necessary for minimizing delaminations and precluded varying heating rates to modify sample characteristics. The sample characteristics were established primarily by the maximum temperature reached. All zone I furnace chars were first subjected to the zone II cycle to complete all pyrolysis and then rerun on the cycle given in Figure 51 to graphitize to zone I condition.

The thermal stability of each virgin and furnace char material for thermophysical property measurements was verified in advance by a five-hour temperature soak at the highest hot face temperature expected in the thermal conductivity tests. TGA tests on portions of the rough-cut virgin slabs shown in Figure 52 gave a 4 percent weight loss on FM-5014 at 700°F and indicated that virgin MX-4926 could not be heated above 500°F if greater weight loss was to be avoided. Temperature limits of 700° F and 500°F were then established for virgin thermal properties. The TGA data shown in Figure 53 indicated that 1000°F should be the temperature limit for zone III chars. Stability was verified for a vacuum test environment in a Cahn Vacuum Microbalance by a weight loss of only 0.13 percent in 2.5 hours at 1000°F and 10^{-2} Torr. The thermal stability limits for zone II and I char samples were the same as the maximum charring temperatures, 2500°F and 4000°F respectively, since negligible changes in weight or X-ray diffraction intensity resulted from continued heating at these temperatures.

The fact that the "graphitization" during all furnace charring trials was found to be a function of temperature, but not time, was the basis for assuming that "graphitization" during ablation could be considered independent of any rate effects, i.e., extent of "graphitization" at any temperature is independent of the heating rate in reaching that temperature. This assumption simplified the extrapolation of thermal conductivity data in the "graphitized", fully pyrolyzed char as described in section IX. Although the difference between active ablation heating rates and heating rates obtainable in a furnace does not permit direct evaluation of this assumption, the fact that "graphitization" in the zone II and I post-test chars was reproduced at temperatures on 400°F to

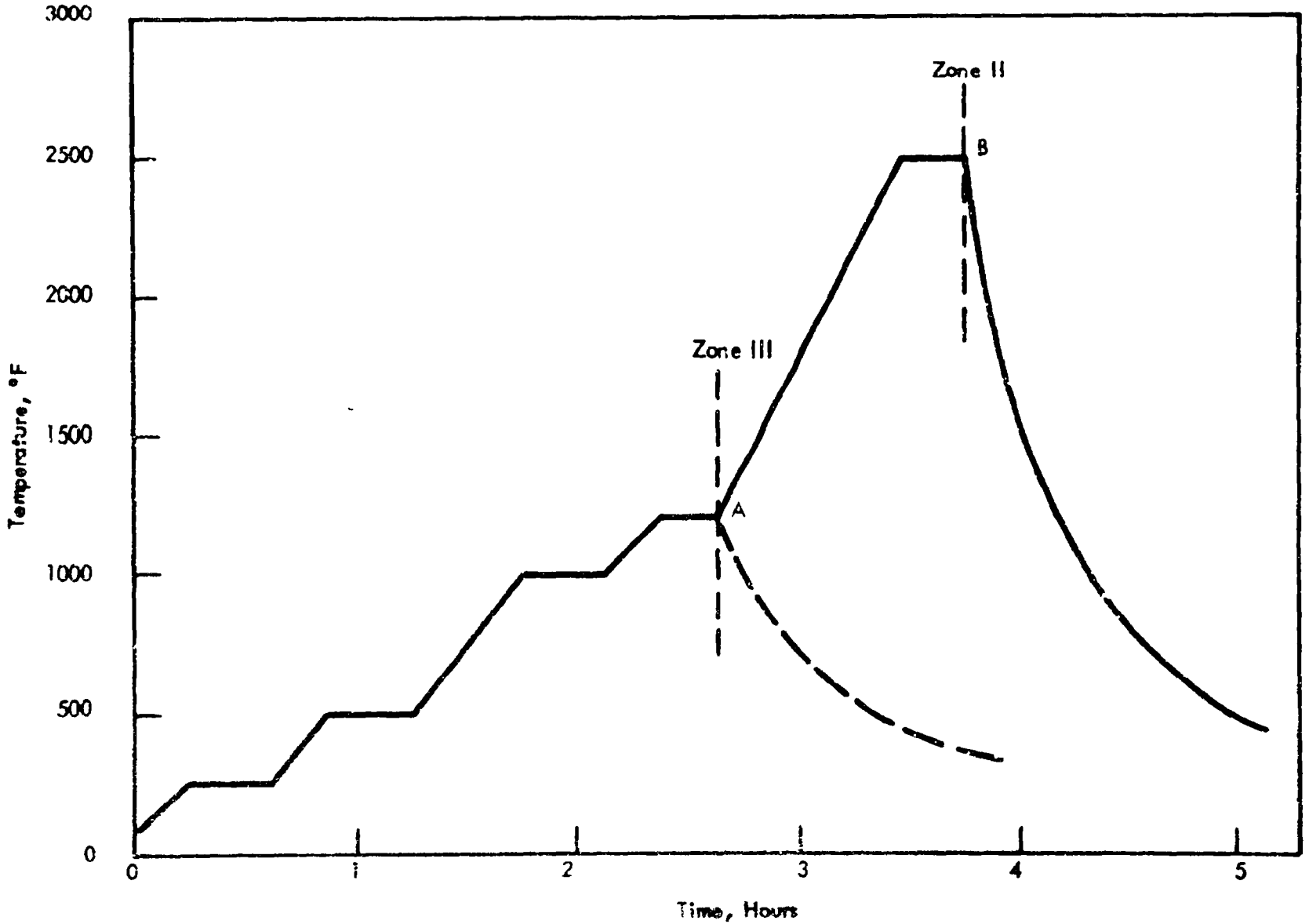

FIGURE 50 FURNACE HEATING SCHEDULE FOR PRODUCTION OF ZONE II AND III CHAR SPECIMENS

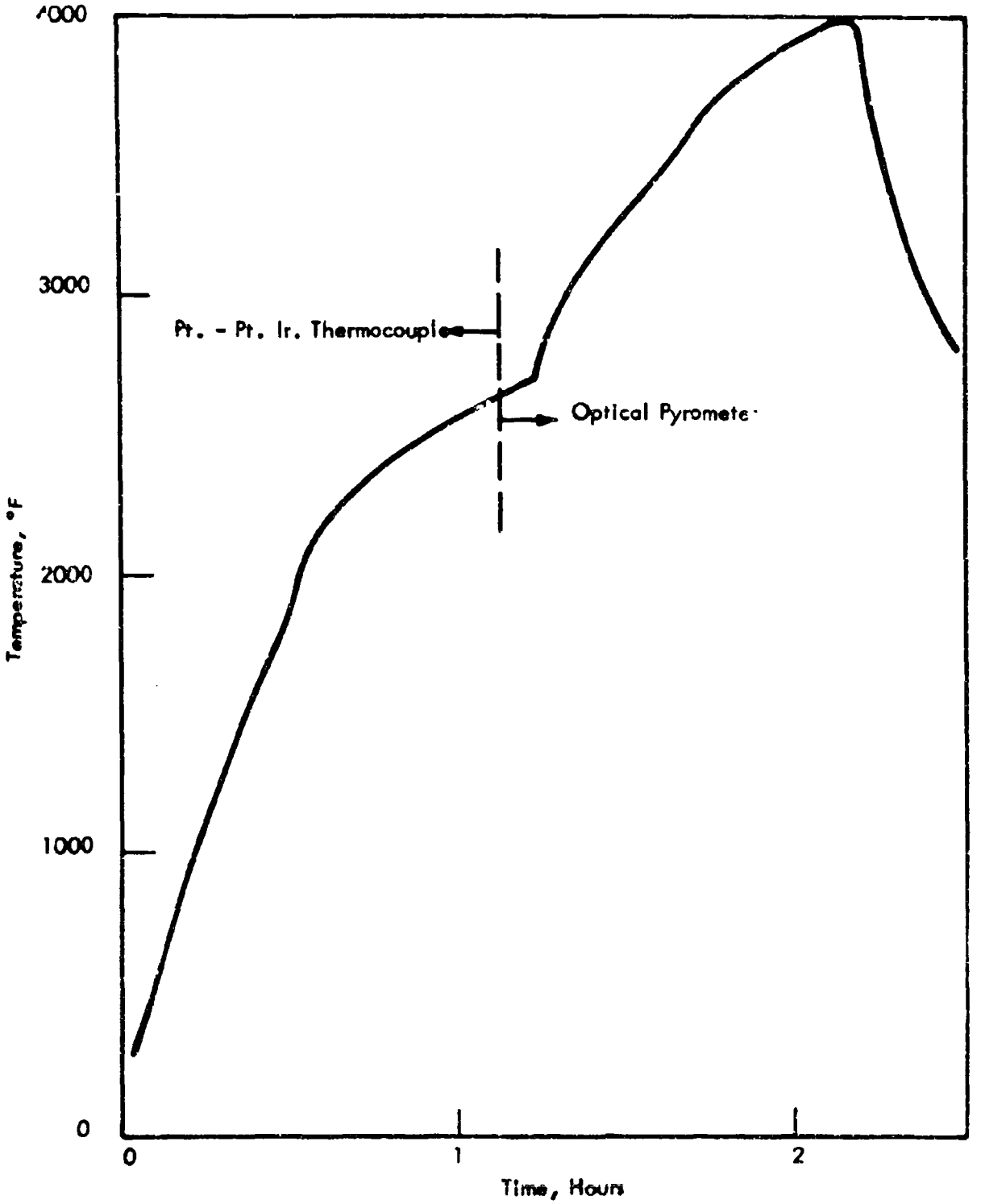

FIGURE 51 RECORD OF MEASURED TEMPERATURE VS. TIME FOR FINAL HEATING OF ZONE I SPECIMENS

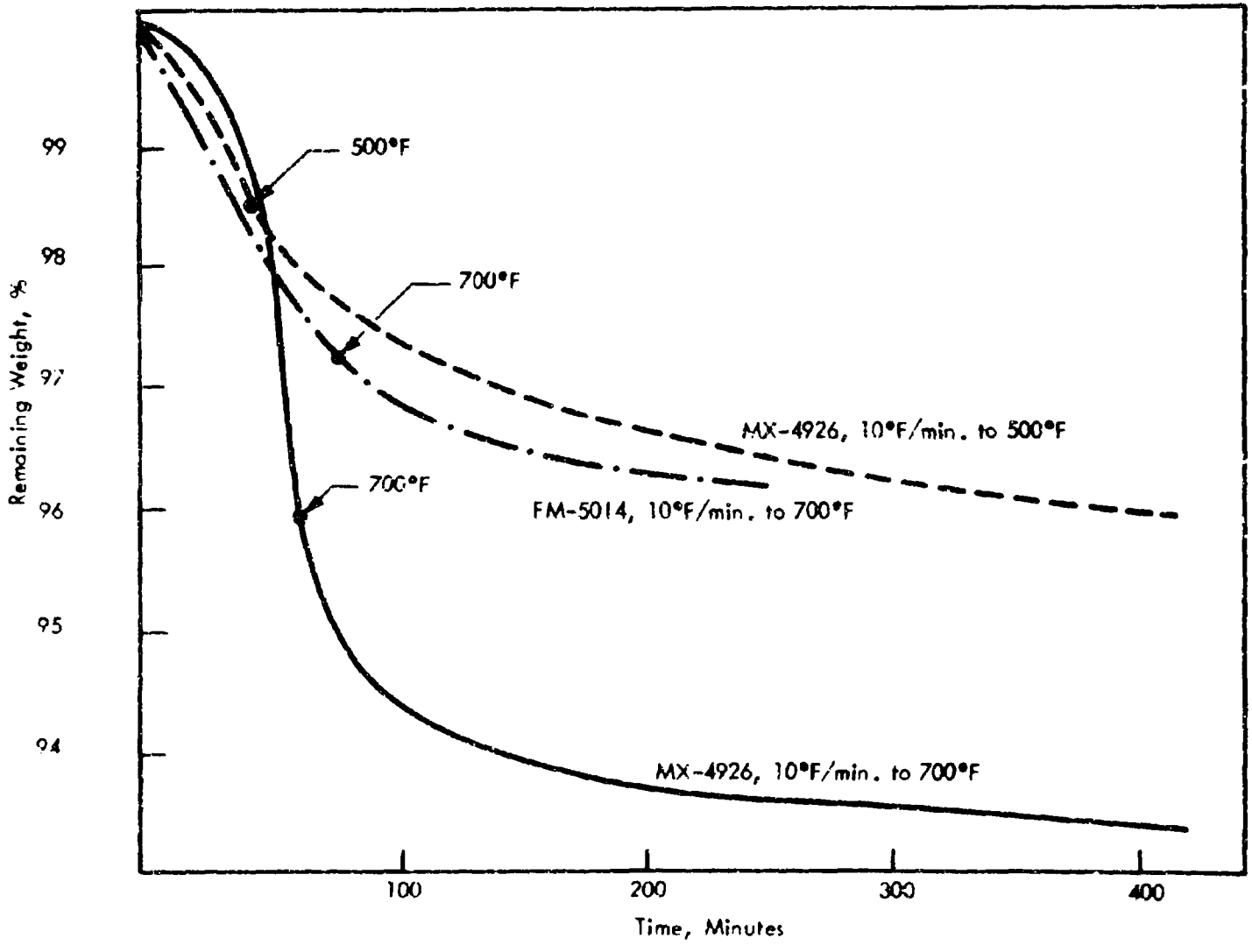

FIGURE 52 VIRGIN SAMPLE TGA REMAINING WEIGHT VS. TIME

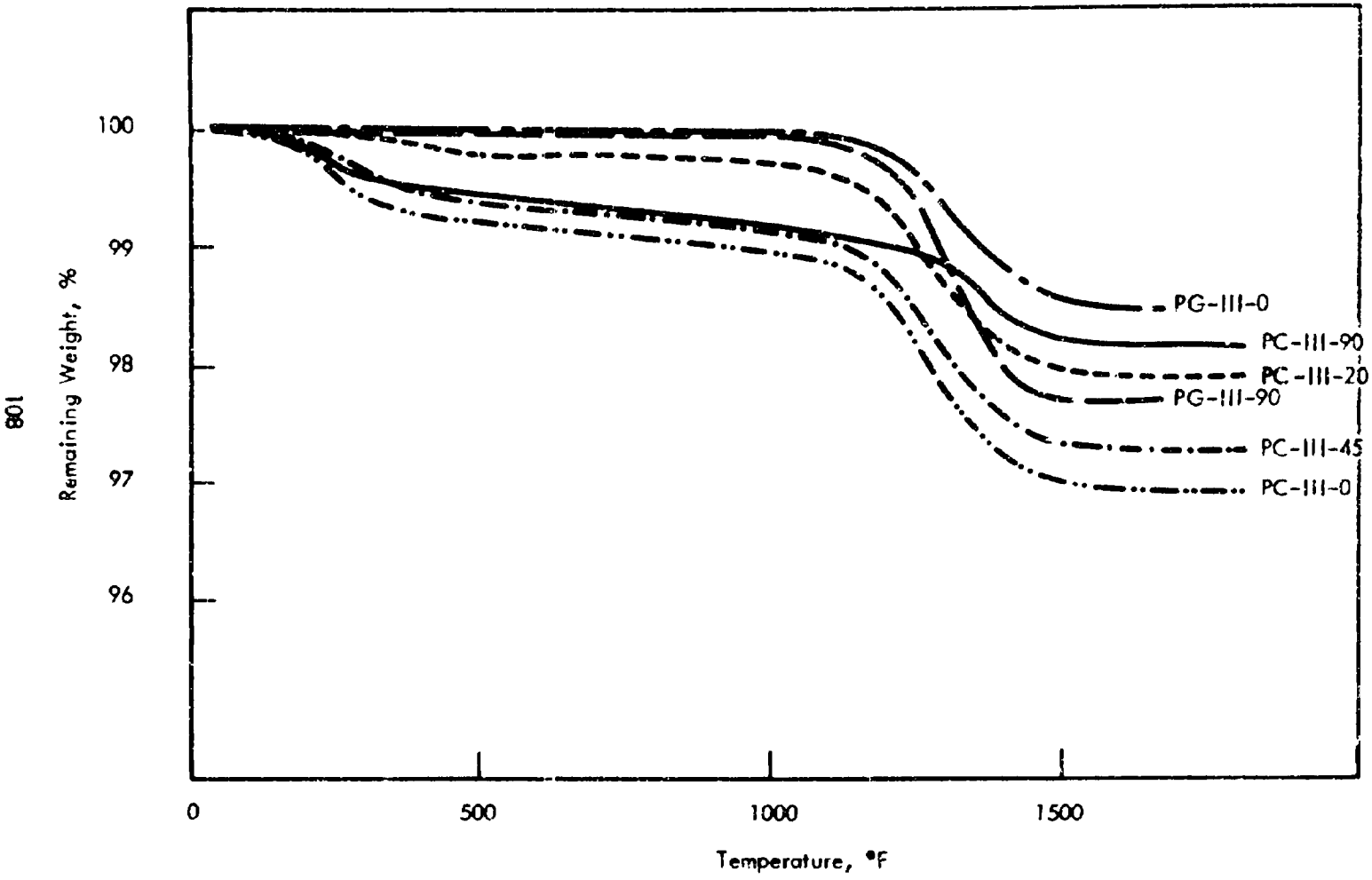

FIGURE 53 TGA OF ZONE III FURNACE CHARS

500°F lower in furnace chars is taken as evidence that "graphitization" rate effects are small compared to pyrolysis rate effects. In pyrolysis rate controlled zone III, equivalent furnace chars were obtained at 900°F lower temperatures than active ablation chars. That pyrolysis rate effects cannot be ignored in applying thermal conductivity data was previously discussed in section V.

THERMOPHYSICAL PROPERTY SAMPLE CHARACTERISTICS

Furnace chars were characterized in the same manner as post-test chars. DTA measurements were omitted, since, as previously discussed, they were uninterpretable. Microcombustion elemental analyses were run only on zone III chars, since virgin analyses were already available and zones II and I were completely pyrolyzed. All characterization prior to thermophysical property measurements utilized portions of the furnace slabs adjacent to the thermal conductivity specimens. This program has emphasized density/porosity measurements because of the assumption that conductivity is markedly porosity dependent and because of furnace char slabs with controlled and uniform density were desired. The Radocon X-ray transmission measurement of density turned out to be very suitable for chars. The only deviations from the required char uniformity (± 0.02 2 gm/cm^3) were in the 0-degree and some of the 20-degree orientation samples which tended to have lower apparent density near the edges due to delamination at the edges. Since the expected strong effect of porosity on thermal conductivity was verified during the conductivity measurements, density/porosity measurements were made on the center portion of the thermal conductivity specimens after they were tested, whenever time permitted. These test values include any effects of the exposure to the property measurement environment.

Furnace slab and conductivity sample characterization results for char zones I, II, and III are summarized in Table XIII. The two types of values agree well except for specimens PC-II-90 and PC-III-0, which apparently had a tendency to contract in the 90-degree orientation and expand or delaminate in the 0-degree orientation during the thermal conductivity measurements. Generally good agreement of before and after test values from different portions of the furnace char slab verified that the samples were uniform and stable during the measurements.

It was anticipated that future more detailed correlation of porosity with thermal conductivity would require a knowledge of the pore size distribution. Therefore, the limited number of furnace char slab portions available for density/porosity characterization were assigned to one or the other of the two destructive tests: determination of true solid density and total porosity or determination of the size distribution of open pores. This accounts for the alternate appearance of ρ_s, and ξ_t or ξ_p and size distributions in Table XIII. The nondestructive determination of ξ_o was conducted on all of these specimens. Two sets of ξ_p and size distribution results are missing due to equipment failure during the runs. In general, the furnace chars have a lower fraction

TABLE XIII FURNACE CHAR SPECIMEN CHARACTERISTICS

Code	Furnace Wt. Loss %	TGA Wt. Loss %	X-Ray Diffraction Intensity, Ar 3.37 A	P_{ext} Slab Value	P_{ext} After K Test	P_t Slab Value	P_t After K Test	P_{as}	ϵ Total Slab Value	ϵ Total After K Test	ϵ_o	$\epsilon_{\geq .75\mu}$	$\epsilon_{\leq .012\mu}$	ϵ_p	$\epsilon_{.012-0.1\mu}$	$\epsilon_{0.1-1\mu}$	$\epsilon_{1-10\mu}$	$\epsilon_{10-75\mu}$
PC-III-90	14.1	1.8	----	1.29	1.46	1.97	1.97	1.73	.345	.259	.254	----	----	----	----	----	----	----
PC-III-0	15.1	3.7	----	1.26	.11	----	2.06	1.79	----	.461	.296	.049	.164	.083	.017	.012	.042	.003
PC-III-20	15.3	2.1	----	1.28	.24	1.83	1.97	1.76	.301	.371	.281	----	----	----	----	----	----	----
PC-III-45	14.8	2.7	----	1.24	.23 .24	----	2.21 2.09	1.77	----	.444 .407	.300	.043	.097	.097	.014	.018	.059	.009
PC-III-90	17.4	0.0	116	1.45	----	1.92	----	1.76	.354	----	.303	----	----	----	----	----	----	----
PC-II-0	17.6	0.0	104	1.23	.18 1.28	----	2.26 2.21	1.93	----	.478 .421	.363	.035	.204	.124	.009	.014	.080	.004
PC-II-20	17.7	0.0	104	1.22	1.21	1.82	2.03	1.68	.330	.404	.274	----	----	----	----	----	----	----
PC-II-45	17.6	0.0	112	1.24	----	----	----	1.86	----	----	.335	.027	.177	.131	.011	.014	.092	.005
PC-I-90	17.6	----	176	1.22	----	1.48	----	1.43	.176	----	.147	----	----	----	----	----	----	----
PC-I-0	19.3	----	200	1.16	1.14	----	1.46	1.46	----	.230	.206	----	----	----	----	----	----	----
PC-I-20	17.6	----	188	1.27	1.30	1.51	1.48	1.43	.192	.122	.147	----	----	----	----	----	----	----
PC-I-45	17.8	----	212	1.19	----	----	----	1.46	----	----	.196	.042	0.0	.154	.004	.012	.074	.004
PC-III-0	14.0	1.5	----	1.28	1.37	----	1.66	1.56	----	.175	.180	----	----	----	----	----	----	----
PC-III-90	13.5	2.3	----	1.25	1.26	1.57	1.63	1.54	.252	.227	.188	----	----	----	----	----	----	----
PC-II-0	16.5	0.0	224	1.23	1.23	----	1.88	1.71	----	.346	.281	.034	.055	.191	.009	.060	.094	.006
PC-II-90	15.3	0.0	256	1.26	1.26	1.77	1.94	1.74	.288	.351	.276	----	----	----	----	----	----	----
PC-I-0	16.3	----	388	1.25	1.30	----	1.60	1.60	----	.188	.219	.037	0.0	.204	.010	.055	.010	.079
PC-I-90	16.6	----	380	1.26	1.28	1.62	1.61	1.55	.222	.205	.187	----	----	----	----	----	----	----

of the large interfiber and interlaminar "pores" and a corresponding lower ξ_t than do the equivalent nozzle chars, probably a result of the shrinkage of unrestrained specimens in the furnace during pyrolysis and the related delamination in nozzle chars restrained by attachment to virgin material.

Partition of the results of elemental analyses on zone III furnace slabs showed that both furnace char materials had a higher H_2O content but the same range of phenolic hydrocarbon content as the post-test nozzle chars. The amount of pure carbon pyrolysis residue was the same in both nozzle and furnace chars of FM-5014 material, but the results indicated that MX-4926 zone III furnace chars had slightly less carbon pyrolysis residue than the zone III nozzle char. The MX-4926 PC-III-90 specimen had the lowest phenolic content, consistent with the fact that it had the lowest TGA weight loss of the MX-4926 zone III furnace char.

The internal appearance of zone I furnace char specimens is shown in Figures 54 and 55. Under polarized light, the MX-4926 material shows a high concentration of "graphitized" residual material between fibers, just as in the nozzle chars. Although FM-5014 nozzle chars contained no "graphitization", the amount of "graphitization" in FM-5014 furnace chars was very low compared to MX-4926 furnace chars, thereby maintaining the relative effect of graphitization in the two materials. Even though furnace charring conditions are very different from active ablation, the "graphitization" phenomena of each nozzle char was reproduced in the furnace chars.

Characterization of virgin materials for thermophysical property measurements consisted simply of verifying their uniformity and establishing that all target values for the virgin zone in Tables X and XI were met. Radioscan density surveys showed the virgin specimens to be uniform within ± 0.008 g/cm^3 of the target values. The only other requirement for virgin sample characterization was assurance that the laminates met the material specification requirements for tensile strength. For FM-5014, strength had been measured by the nozzle fabricator. For MX-4926, samples from the TRW blocks were selected because they were made from nozzle prepreg, reproduced the nozzle density, and were of generally excellent quality. There was insufficient material available to conduct mechanical property tests in addition to all the other tests.

Reflected Light

Polarized Reflected Light

PC-1-0

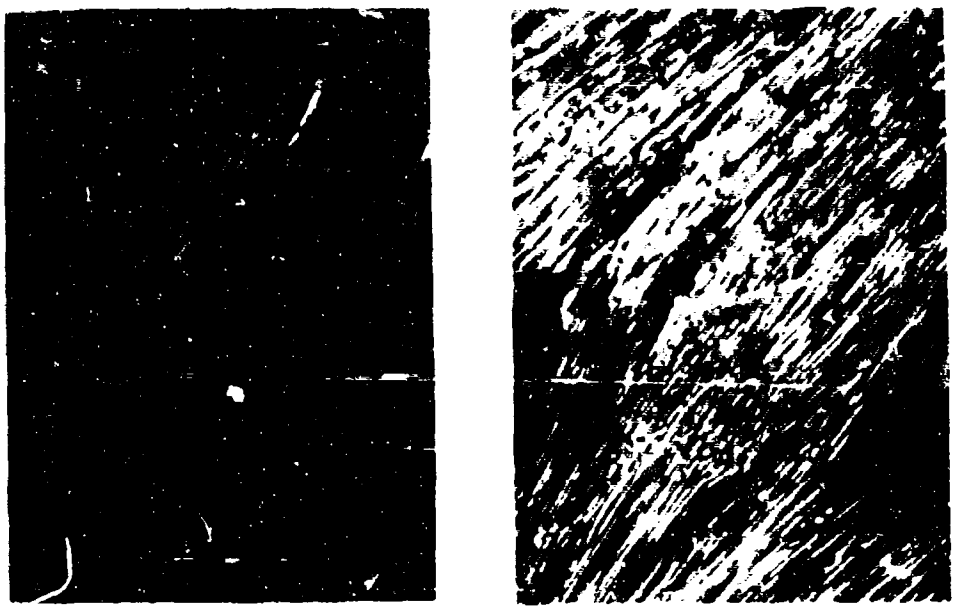

PC-1-90

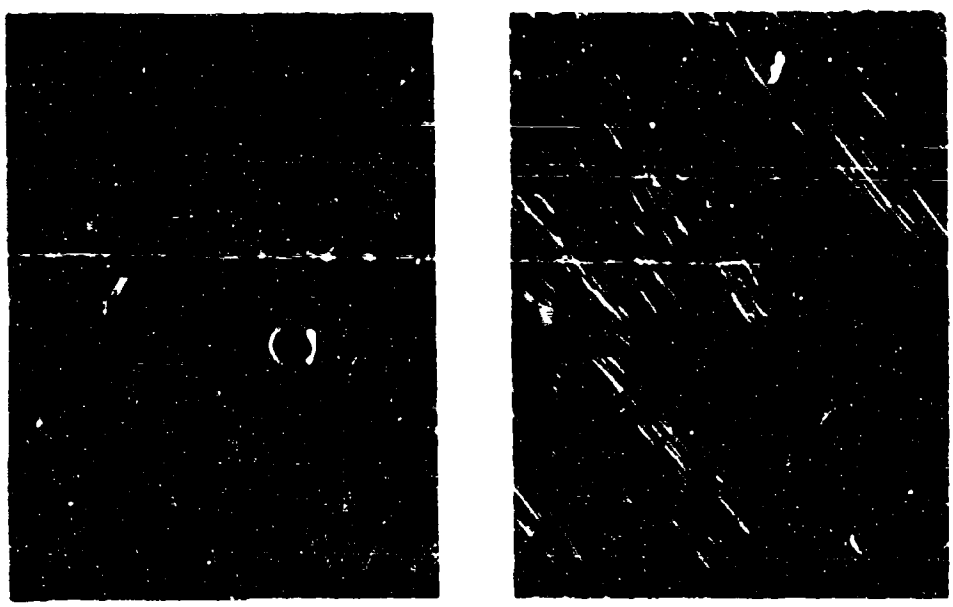

FIGURE 54 MX-4926 ZONE I FURNACE CHAR PHOTOMICROGRAPHS, 100X

Reflected Light

Polarized Reflected Light

PG-1-0

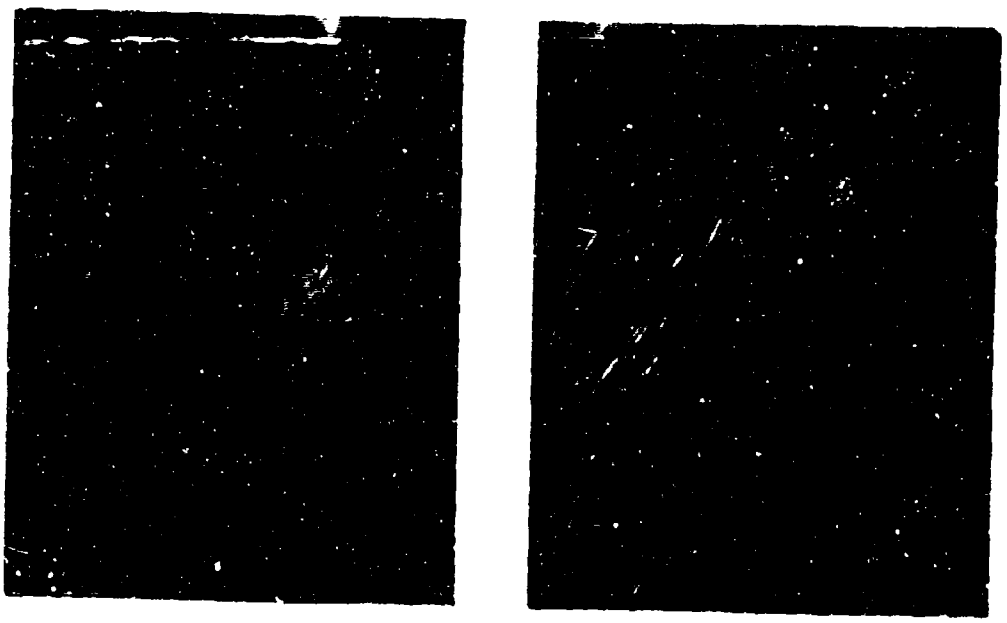

PG-1-90

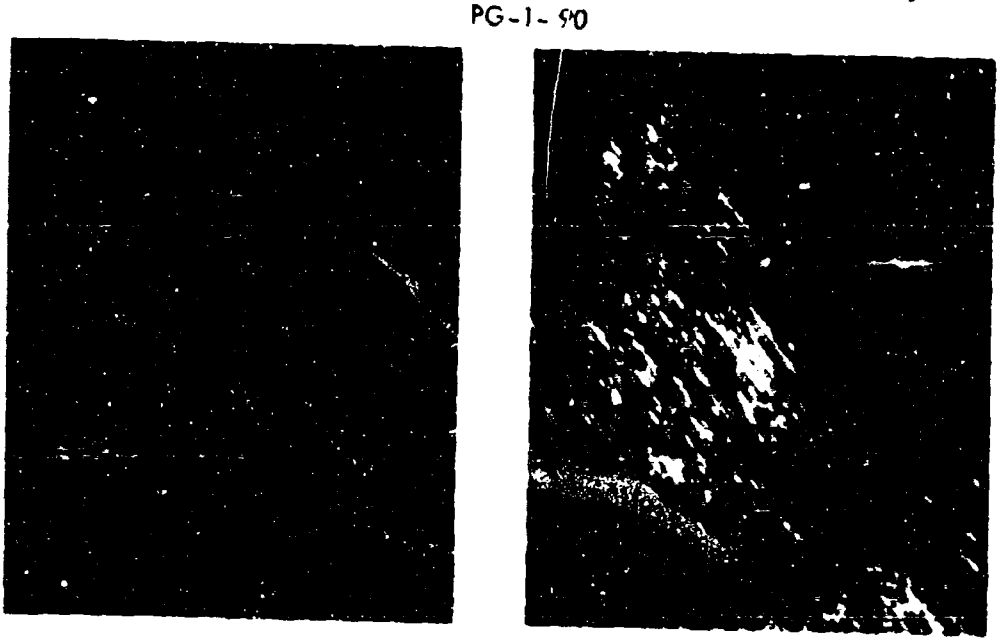

FIGURE 55 FM-5014 ZONE I FURNACE CHAR PHOTOMICROGRAPHS, 100X

SECTION IX

THERMAL CONDUCTIVITY MEASUREMENTS

TEST METHODS

Thermal conductivity was measured by a steady-state, one-dimensional heat flow, comparative method using disk-shaped specimens. This method uses a heat meter of known conductivity in series with the specimen to measure the heat flux common to both. Thermocouples are placed along the axis of the specimen at known locations to measure the temperatures. The conductivity of the specimen is then calculated from the usual one-dimensional formula, $K = \frac{Q}{\Delta T A/d}$. Q is the measured heat flux through the test volume of the specimen, A/d is the test area to thermocouple spacing ratio in the specimen, and ΔT is the temperature difference between the axial specimen thermocouples.

A one-dimensional steady-state heat flow measurement method is desirable and highly practical for several reasons. Steady-state methods yield the highest accuracy attainable in thermal conductivity measurements because the conductivity is the only variable involved in a steady flow of heat through a material. By forcing the steady heat flow to be one-dimensional, the amount of required information is reduced and the interpretation of the data is simplified. The attainment of truly one-dimensional heat flow of the proper magnitude through a specimen is complicated by many factors, especially in highly anisotropic specimens. The two main considerations are radial heat fluxes within the specimen and control of axial temperature gradients through the specimen and heat meter.

Test Apparatus

The self-guarding disk comparative technique permits control of these factors. Generally, the experimental arrangement consists of a heater, the disk specimen, and the heat-flow meter with attached heat sink all in series, with each element thermally bonded to the next. Figure 56 will help in the visualization of the physical arrangement of the components in the discussion to follow.

Control of axial temperature gradients is important because the gradient in the heat meter is used to compute the steady state heat flux in the specimen, and the gradient in the specimen is required for the calculation of its thermal conductivity. If the gradient in either the specimen or the heat meter is too small, individual temperature errors will constitute a large percentage of the measured temperature gradient, and cause a large error in the computed conductivity. If the gradient is too large, the resulting mean conductivity will not apply at the corresponding arithmetic mean temperature if the conductivity is a non-linear function of temperature.

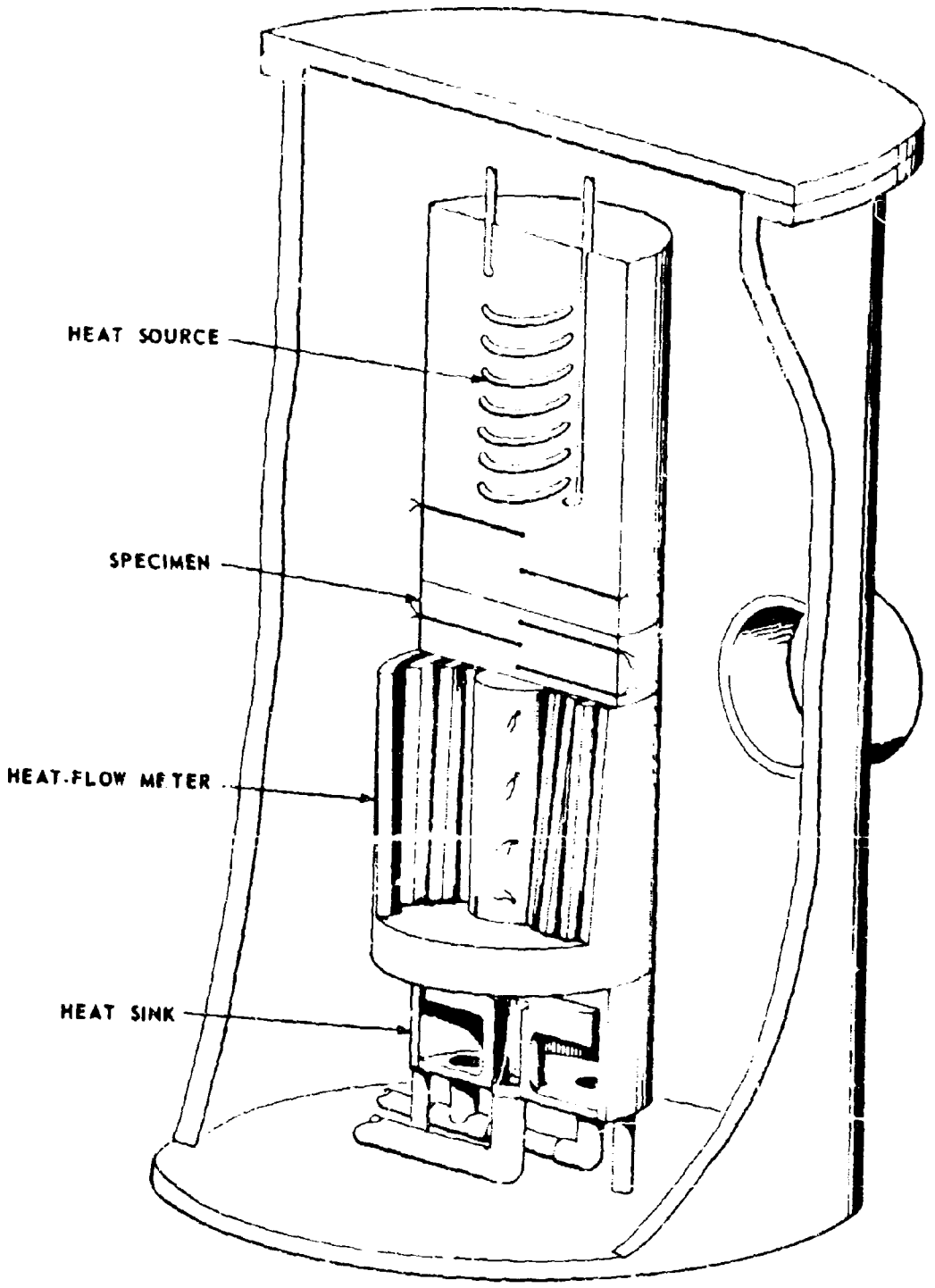

FIGURE 56 DISK THERMAL CONDUCTIVITY APPARATUS - VIRGIN SPECIMENS

The test apparatus was designed to provide optimum control of the axial temperature gradients. First, the gradients in the specimen and in the heat meter were made nearly equal by matching the conductivity of the meter to that of the specimen. Since pyroceram 9606 approximates the conductivity of the virgin materials, it was used for the low-temperature measurements on the virgin specimens. Similarly, type 347 stainless steel was used for the high temperature measurements because its conductivity approximates those of the char specimens. Second, the gradient was controlled within the desired range by varying the thermal resistance between the specimen and the heat meter, thereby controlling the level of heat flux in the system. For the low temperature virgin and zone III specimens, either one or three pads of woven graphite cloth were placed between the specimen and the heat meter. For zone II and I specimens, the number of pads used (maximum of ten) depended on the specimen lamination angle and the highest test temperature expected.

Radial heat fluxes must be minimized, because the conductivity is calculated from the axial flux leaving the specimen and entering the heat meter. Depending on its direction, a radial flux will either add to or subtract from the axial flux measured by the heat meter, thus introducing error in the conductivity determination.

Radial heat fluxes are extremely difficult to eliminate in the one-dimensional, axial flow technique, and usually can only be minimized by a prudent choice of specimen diameter-to-thickness ratio and the use of appropriate heat shielding around the curved surface of the specimen and heat meter. Only the central 1-inch-diameter specimen is utilized as the test volume. The remainder of the specimen acts as a guard against radial loss of heat from the test core. An optimum practical choice of specimen diameter-to-thickness ratio exists for each specimen, depending on the level of conductivity and the degree of specimen anisotropy expected. In general, the high values of diameter-to-thickness ratio are better.

Radial heat flow in the heat-flow meters is minimized by a series of guard cylinders. Only the innermost 1-inch-diameter cylinder is used as the meter for measuring heat flow from the 1-inch-diameter specimens test core. The construction of the heat-flow meters is illustrated in Figures 56 and 57 .

The heat shielding around the specimen and heat meter was designed to fit the temperature range that was to be experienced. The virgin and zone III specimens were tested in one atmosphere pressure of argon, so care was taken to prevent heat transfer by convection. For the zone II and zone I specimens, which were run

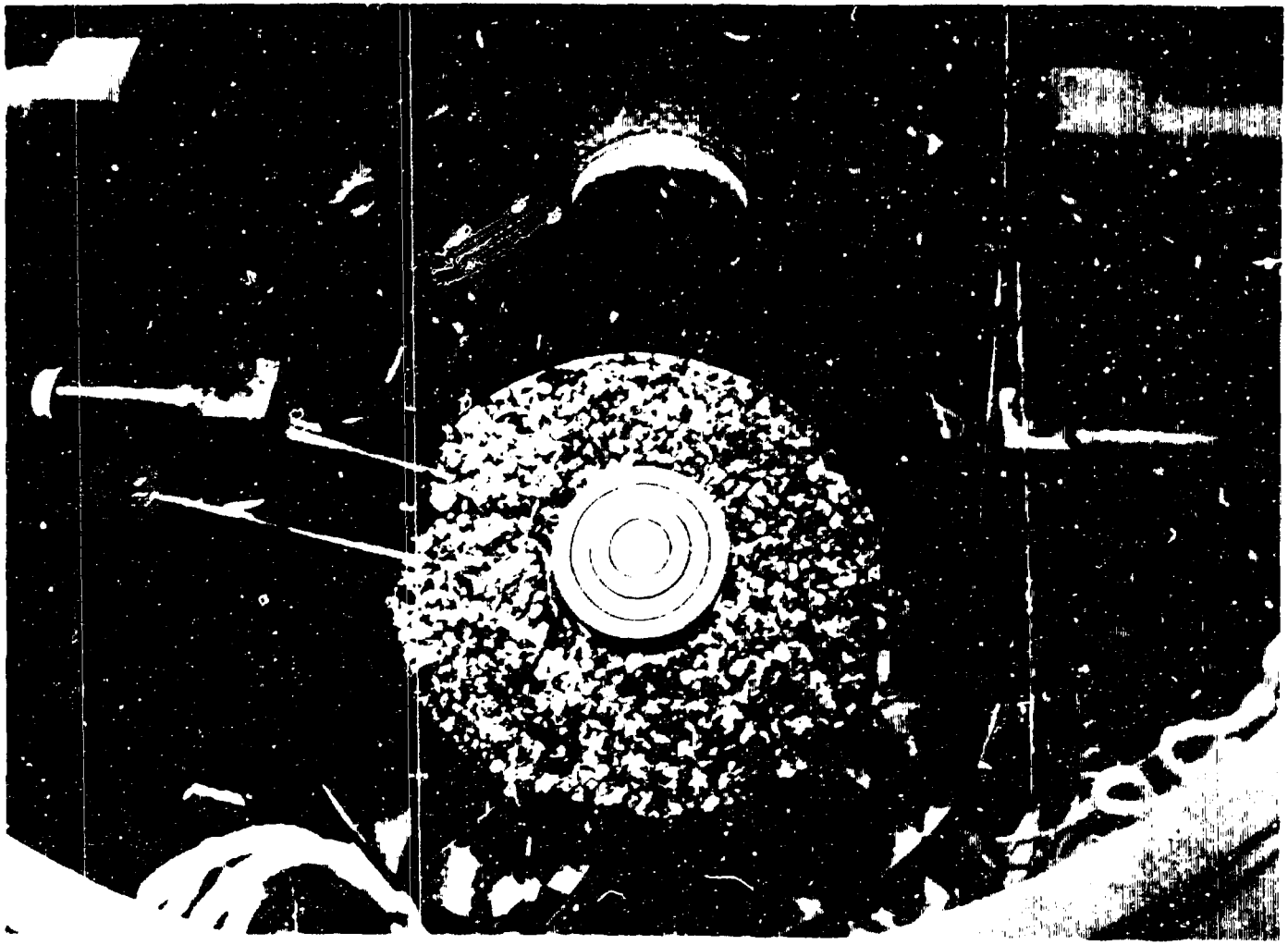

FIGURE 57 INTERIOR OF HIGH-TEMPERATURE THERMAL CONDUCTIVITY APPARATUS SHOWING THE TOP OF THE HEAT-FLOW METER WITH GUARD ANNULI FOR DISK SPECIMEN

in vacuum, shielding against radiation losses was of prime importance. The actual shielding arrangements used in zone III, II, and I measurements were variations of those shown schematically in Figure 58 .

Conduction-type heaters were used in the low-temperature virgin and zone III material measurements. These heaters, shown in Figures 56 and 58 , consisted of massive metal blocks internally heated electrically. The metal block which had high conductivity relative to the specimens distributed the heat generated by the resistance heater. The weight of the metal block kept the specimen flat against the heat-flow meter below and discouraged delamination of the specimen. In the virgin and zone III measurements, one layer of woven graphite cloth was placed between the heater block and the specimen to make uniform the heat distribution over the surface of the specimen by filling the small gaps between the heater and specimen surfaces caused by macroscopic variations in the surfaces of the specimen.

Zone II and I measurements dictated the use of radiation heaters in order to provide the temperature and flux density required. For the zone III specimens, a tantalum radiation heater was used. A molybdenum cylindrical block of the same diameter as the specimen was placed on the specimen to keep it flat against the meter below and to reduce the possibility of delamination. Again, one layer of graphite cloth provided a conduction bond between the weight and the specimen. For the zone I measurements, a graphite paddle heater was used, and a tungsten cylindrical block weighted the specimen. No graphite cloth was used between the tungsten block and specimen in this case because radiation heat transfer reduces the effect of surface irregularities on the thermal bond between the block and specimen. Figure 58 shows the positioning of the heaters, specimen weights, and specimens.

Chromel-alumel thermocouples were used in the virgin and zone III char materials, platinum-rhodium and tungsten-rhenium in the zone II chars, and tungsten-rhenium in the zone I chars. The thermocouple bead was bonded to the specimen with a high temperature, graphite-base cement. A good thermal bond between thermocouple and specimen is essential to insure precision and accuracy in the differential temperature measurements required for the calculation of the thermal conductivty.

Test Procedure

The measurement procedure, after appropriate setup involving instrumentation, insulation, and environment control, entailed the recording of temperatures in the specimen and heat-flow meter at each of several thermal equilibria. These data permitted calculation at each equilibrium of three values of thermal conductivity -

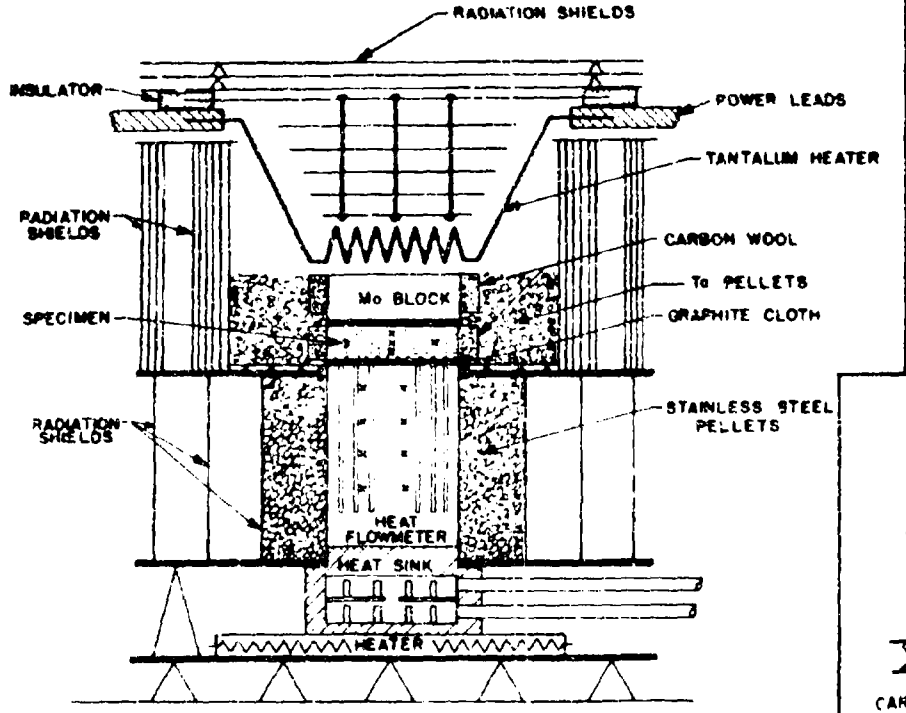

HEATER, SPECIMEN AND HEAT FLOWMETER ASSEMBLY WITH ASSOCIATED SHIELDING FOR ZONE 2 CHAR MEASUREMENTS

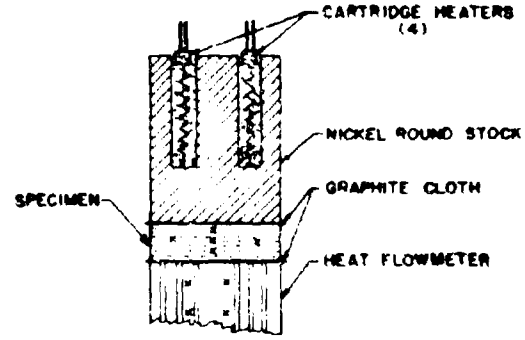

HEATER, SPECIMEN AND HEAT FLOWMETER ASSEMBLY FOR ZONE 3 CHAR MEASUREMENTS. SHIELDING ARRANGEMENT IS SIMILAR TO THAT SHOWN FOR ZONE 2 ASSEMBLY

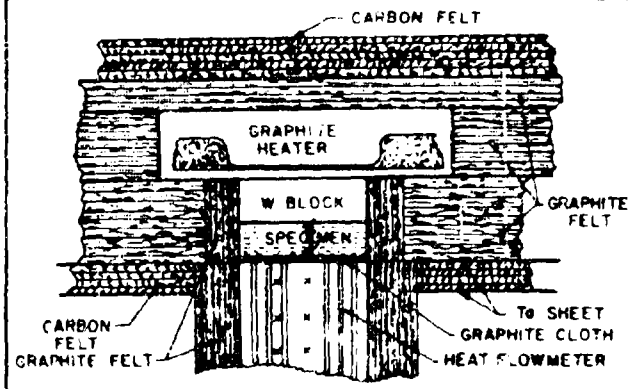

HEATER, SPECIMEN AND HEAT FLOWMETER ASSEMBLY WITH ASSOCIATED SHIELDING FOR ZONE 1 CHAR MEASUREMENTS

FIGURE 58 SCHEMATIC OF THERMAL CONDUCTIVITY APPARATUS SHOWING VARIATIONS IN HEATERS AND SHIELDING REQUIRED FOR EACH TEMPERATURE ZONE

one for the average temperature between each pair of specimen thermocouples. See Figures 56 and 58. Data were recorded at four or more equilibria for each specimen. Most measurements were made at equilibria at successively increasing temperatures, followed by at least one set of measurements at a lower temperature equilibria to determine the effect on the stability of the specimens of the long soak periods required for the measurements at high temperature.

The specimens were machined to appropriate dimensions. In some cases, especially those with 0-degree laminations, it was necessary to lap the flat surfaces of the 3-inch-diameter by 1/2 to 3/4-inch thick disks to achieve plane surfaces. Thermocouple wells were then drilled and thermocouples fitted.

RESULTS OF THERMAL CONDUCTIVITY MEASUREMENTS

Figures 59 through 80 show the measured conductivity values. Data are included for all specimens identified in Table XII, section VIII except PC-II-45 and PC-I-45. Results of measurements on these specimens showed too much scatter to permit good definition of conductivity and there was insufficient time in the program to remeasure them. However, certain correlations appear reasonable, as pointed out in subsequent sections, and these permit the conductivity values for these two specimens to be estimated.

The locations of the curves fitted to the data were weighted on the basis of several factors, discussed in later sections, and represent best estimates of the actual property values. The scales chosen for each curve reflect the accuracy attained in the measurements.

Figures 81 and 82 are composites of the thermal conductivity curves for all zones of the two materials. The following summary points are noted:

(1) Apparent thermal conductivity, or conductance, of these materials is not especially sensitive to temperature in moderate temperature ranges. Effects of photon transfer become obvious above about 2400 R.

(2) The radiation transfer effect appears to be much more pronounced in the FM-5014 material than in the MX-4926.

(3) In general, conductance decreases as pyrolysis increases; this is attributed to a corresponding increase in porosity. However, values for zone I chars were usually higher than those for zone II chars. The higher level in zone I over zone II and in the case of the MX-4926 material, zone II over zone III, is considered to be due to "graphitization."

(4) Comparison of results for all materials shows the dominant effect of the cloth direction on conductivity.

(5) Conductivity of the MX-4926 material appears to be dramatically affected by "graphitization."

(6) The laboratory-charred specimens were extremely stable. No change in the measured thermal conductivity upon return to low temperature from the maximum prescribed temperature limit was discovered, and the appearance of the specimens was unchanged.

ANALYSIS OF THERMAL CONDUCTIVITY RESULTS

In addition to items mentioned in the general statements in the "Results" section above, several other pertinent factors influenced the measured thermal conductivity of the MX-4926 and FM-5014 virgin and char materials. These included porosity, "graphitization," effects of layup angle, effects of anisotropy, and radiation transfer. Also an analysis of errors associated with the test method is considered. These topics are discussed next.

Error Analysis

The apparent symmetry and seemingly simple boundary conditions of the self-guarding disk method suggest that an analytical model could be developed which would describe well the influence of the various experimental parameters on the temperature distribution and heat-flux pattern obtained in a given specimen. However, the boundary conditions are actually quite complex, and simplifications lead to analytical models which are insufficiently definitive and therefore give over-simplified results. Several analytical models which were developed during this study proved inadequate to explain the temperature profiles observed in the instrumental specimens and heat-flow meter. Appropriate complex models could have been developed, but would have required numerical solutions, and therefore, would not have allowed the relative influence of experimental variables to be discerned without extensive parametric studies, particularly in view of the highly anisotropic specimens measured in this program.

For this reason, specimens were instrumented and measured under appropriate conditions in order to demonstrate experimentally the accuracy and reproducibility that could be expected in the measurements conducted. This approach to error analysis was accepted as the most realistic after the difficulty and inadequacy of analytical analysis was proven by the failure of several models to account for the observed temperature profiles.

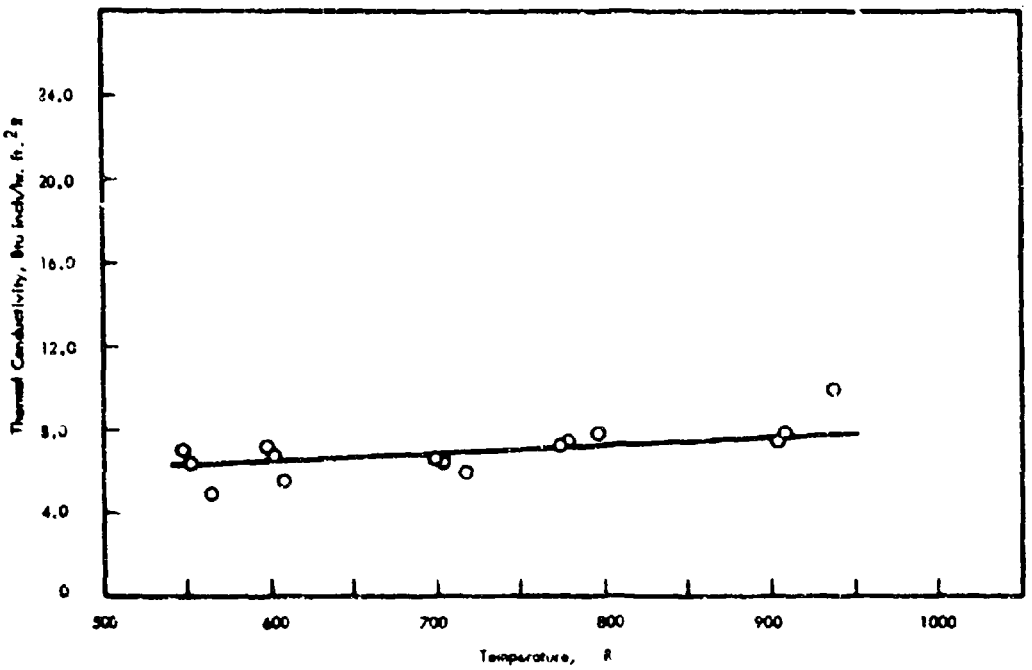

FIGURE 59 THERMAL CONDUCTIVITY OF SPECIMEN PC-V-O (MX-4926)

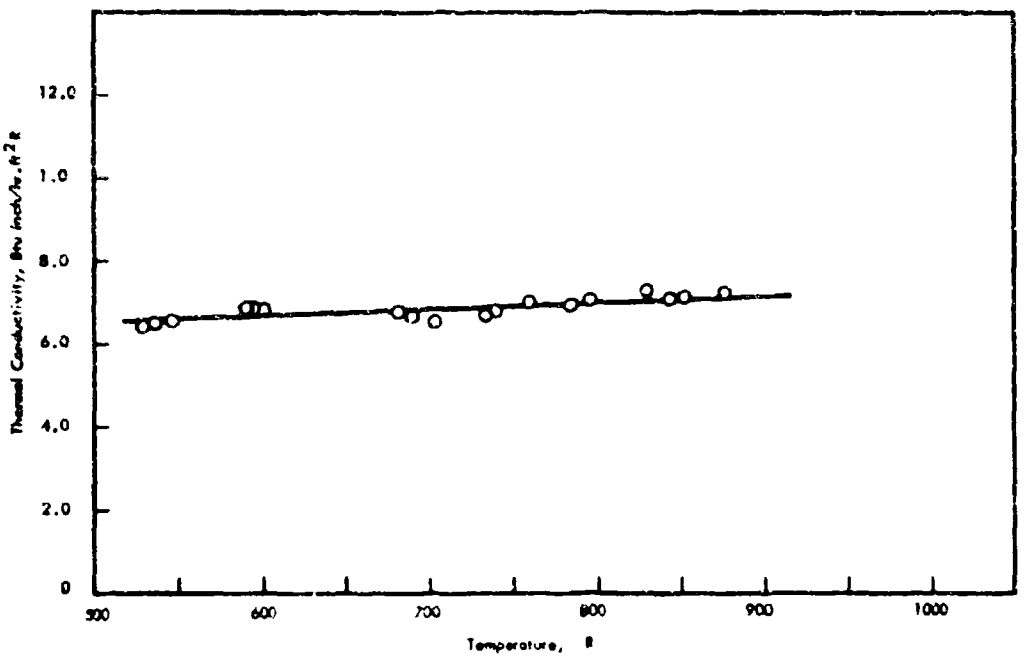

FIGURE 60 THERMAL CONDUCTIVITY OF SPECIMEN PC-V-20 (MX-4926)

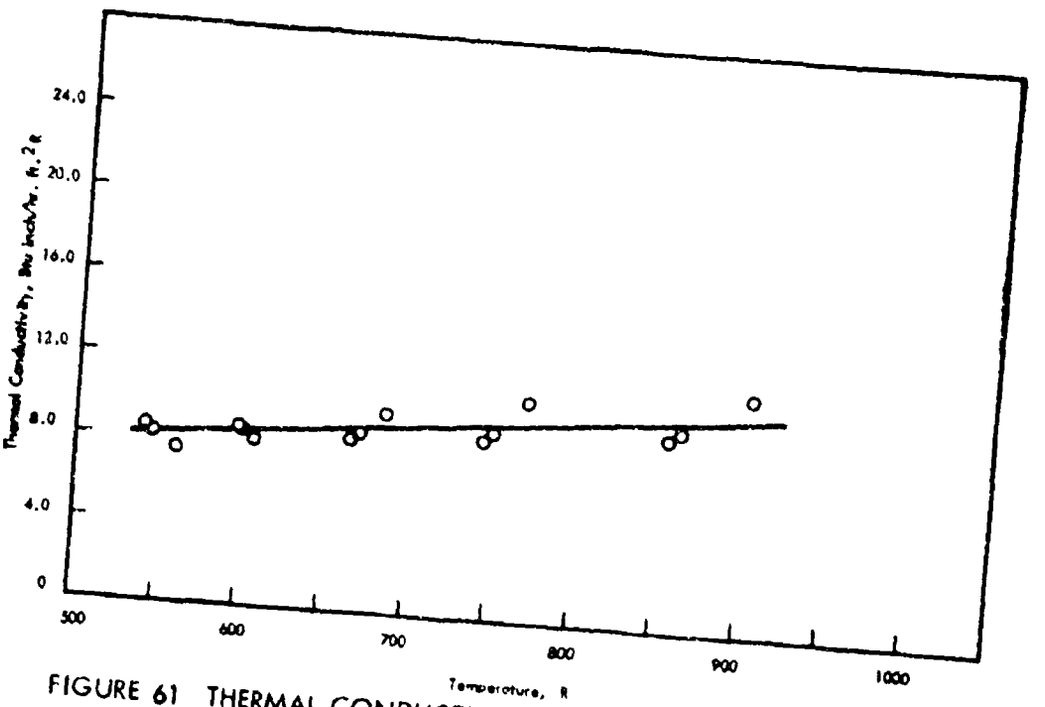

FIGURE 61 THERMAL CONDUCTIVITY OF SPECIMEN PC-V-45 (MX-4926)

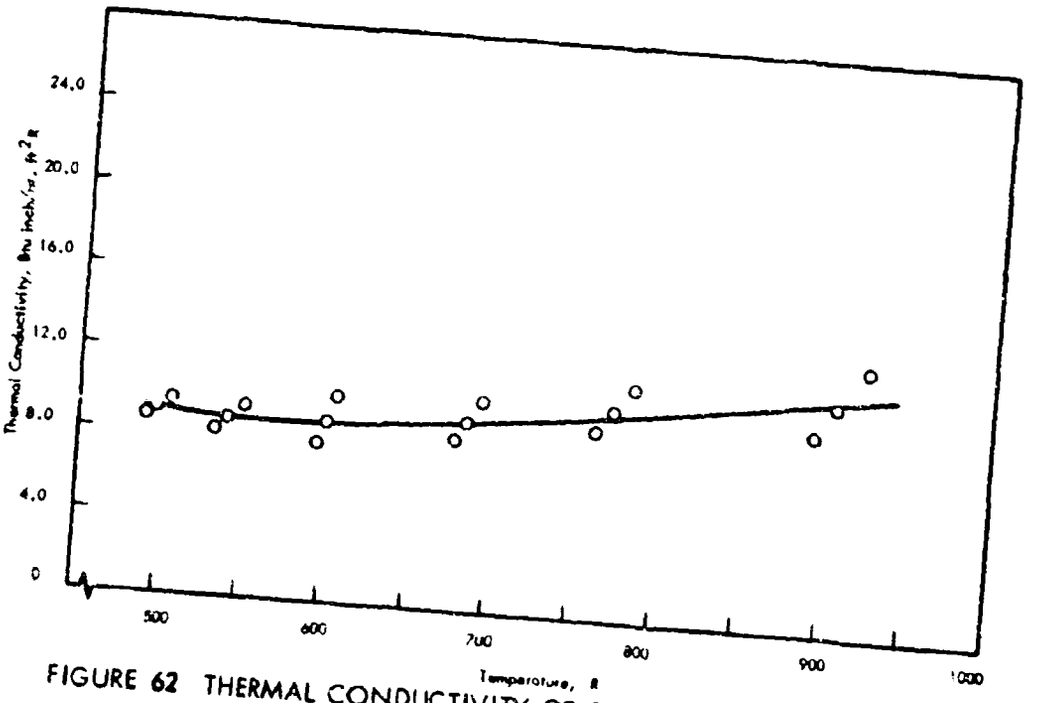

FIGURE 62 THERMAL CONDUCTIVITY OF SPECIMEN PC-V-90 (MX-4926)

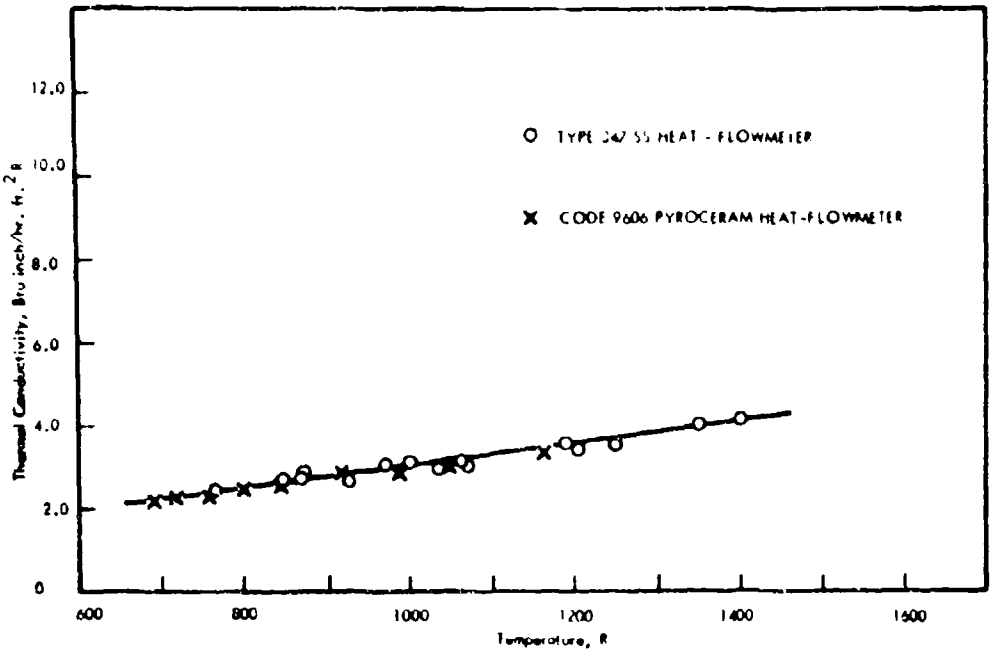

FIGURE 63 THERMAL CONDUCTIVITY OF SPECIMEN PC-III-O (MX-4926)

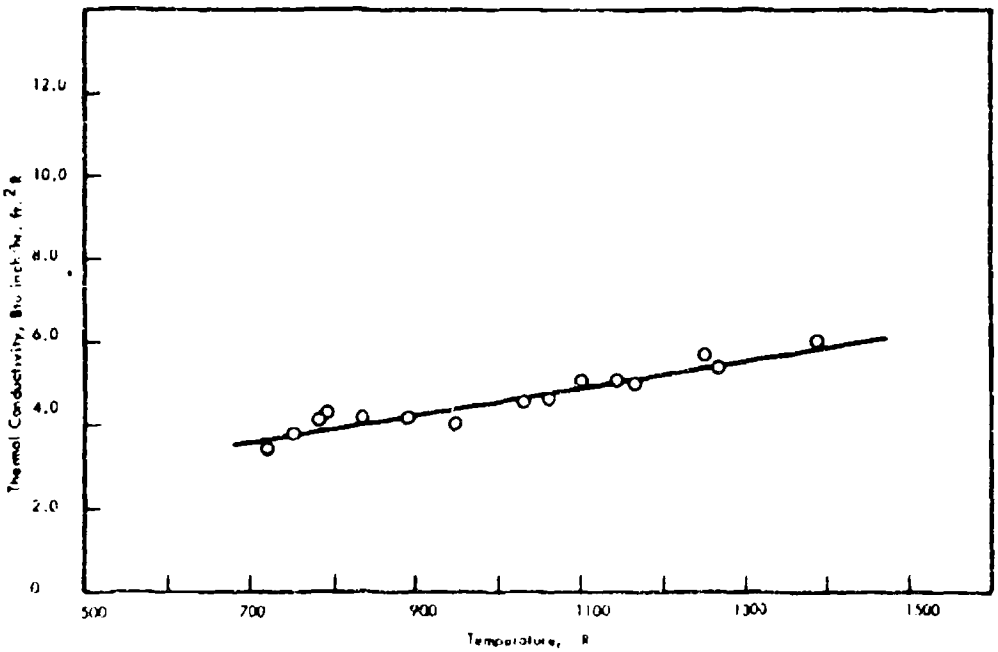

FIGURE 64 THERMAL CONDUCTIVITY OF SPECIMEN PC-III-20 (MX-4926)

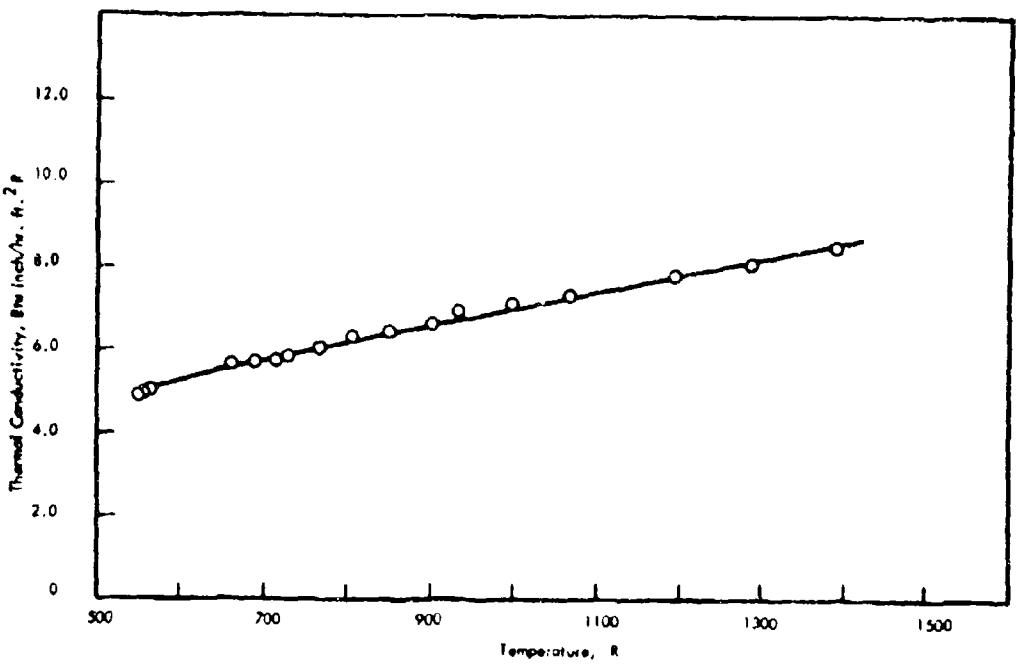

FIGURE 65 THERMAL CONDUCTIVITY OF SPECIMEN PC-III-45 (MX-4926)

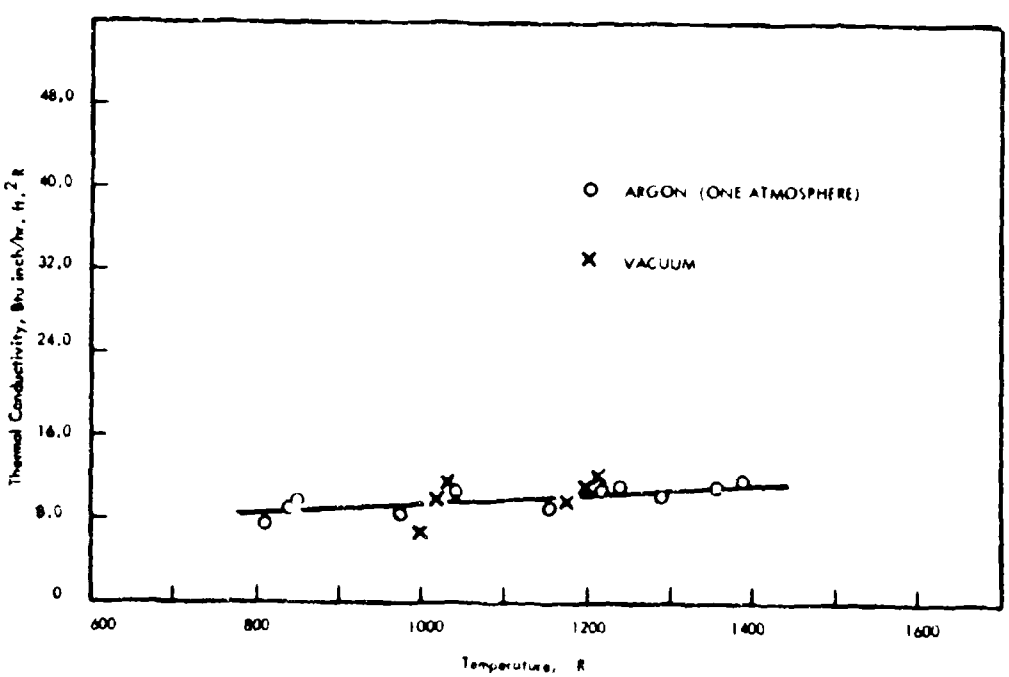

FIGURE 66 THERMAL CONDUCTIVITY OF SPECIMEN PC-III-90 (MX-4926)

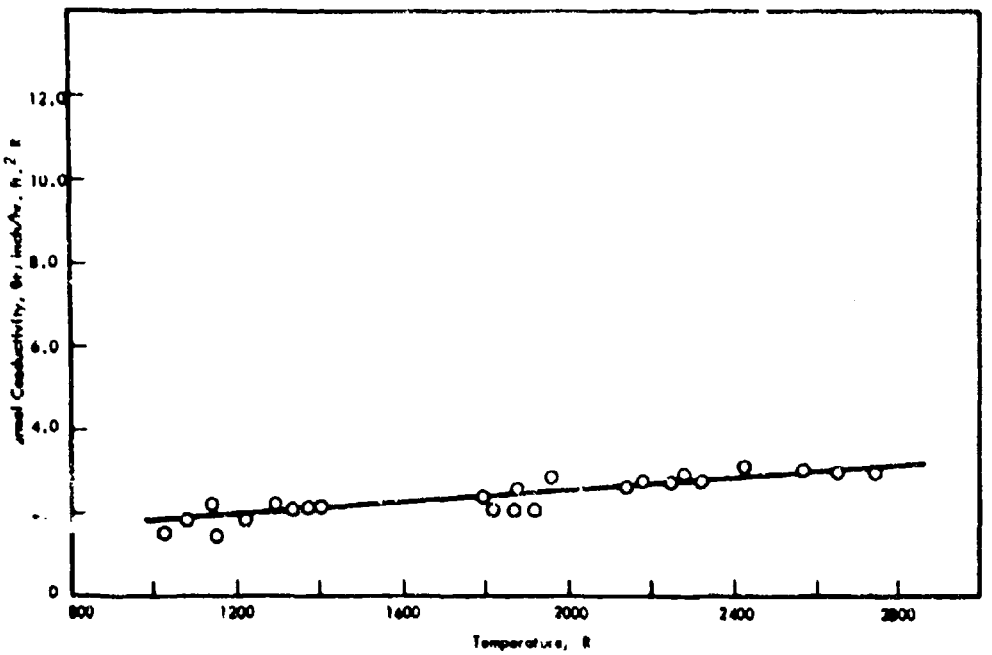

FIGURE 67 THERMAL CONDUCTIVITY OF SPECIMEN PC-II-O (MX-4926)

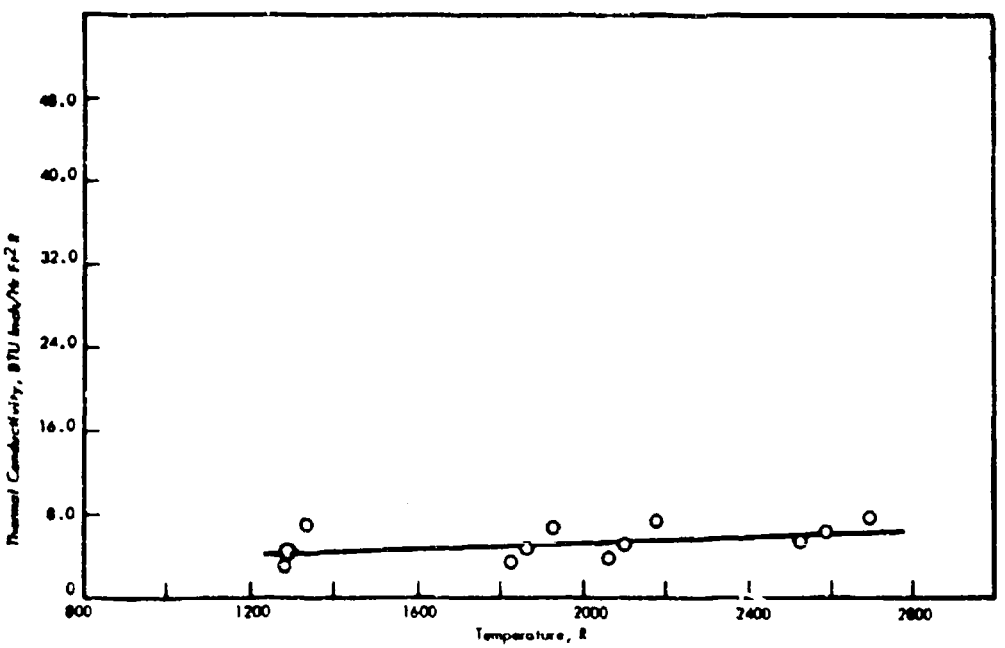

FIGURE 68 THERMAL CONDUCTIVITY OF SPECIMEN PC-II-20 (MX-4926)

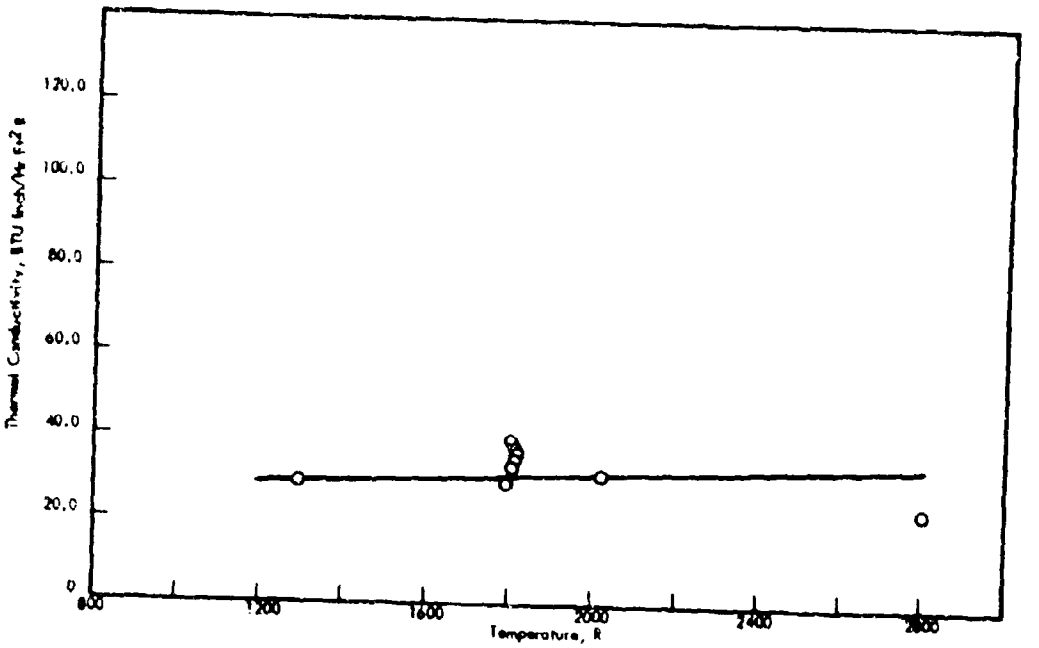

FIGURE 69 THERMAL CONDUCTIVITY OF SPECIMEN PC-II-90 (MX-4926)

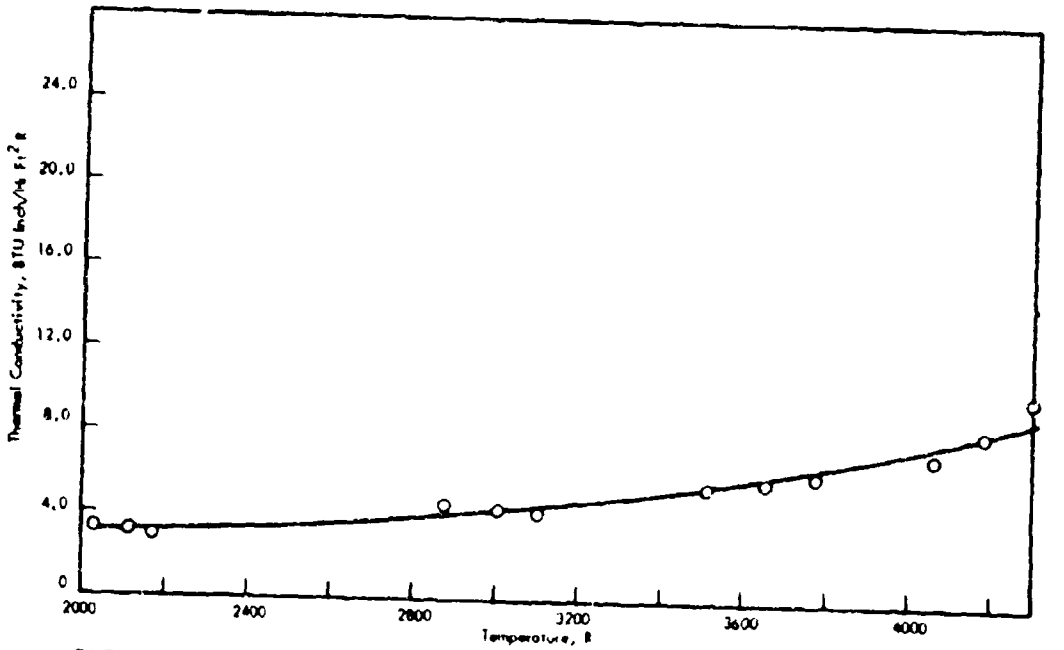

FIGURE 70 THERMAL CONDUCTIVITY OF SPECIMEN PC-I-O (MX-4926)

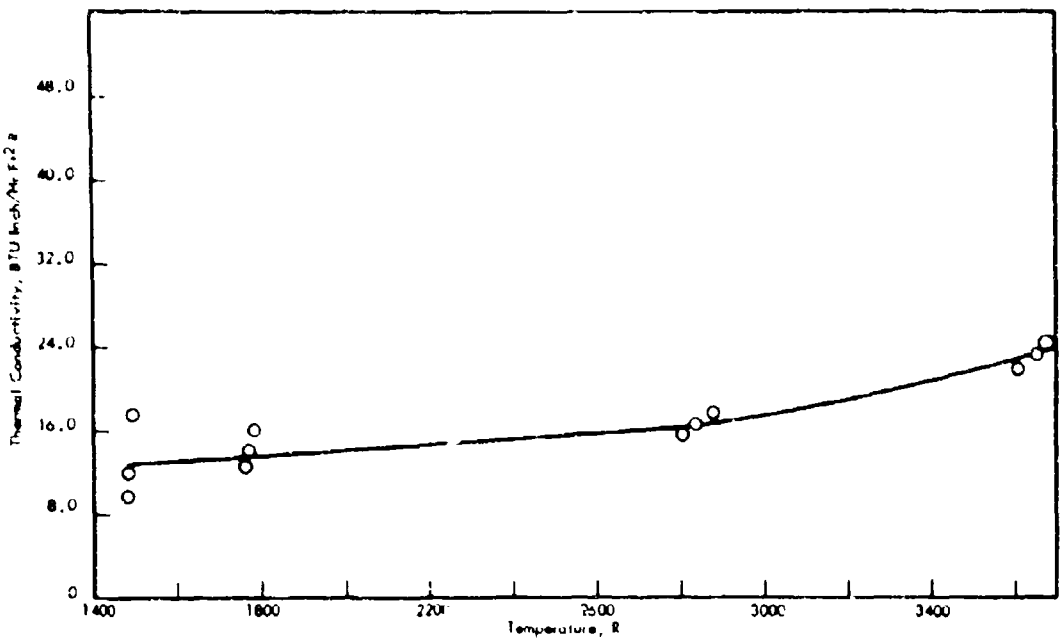

FIGURE 71 THERMAL CONDUCTIVITY OF SPECIMEN PC-I-20 (MX-4926)

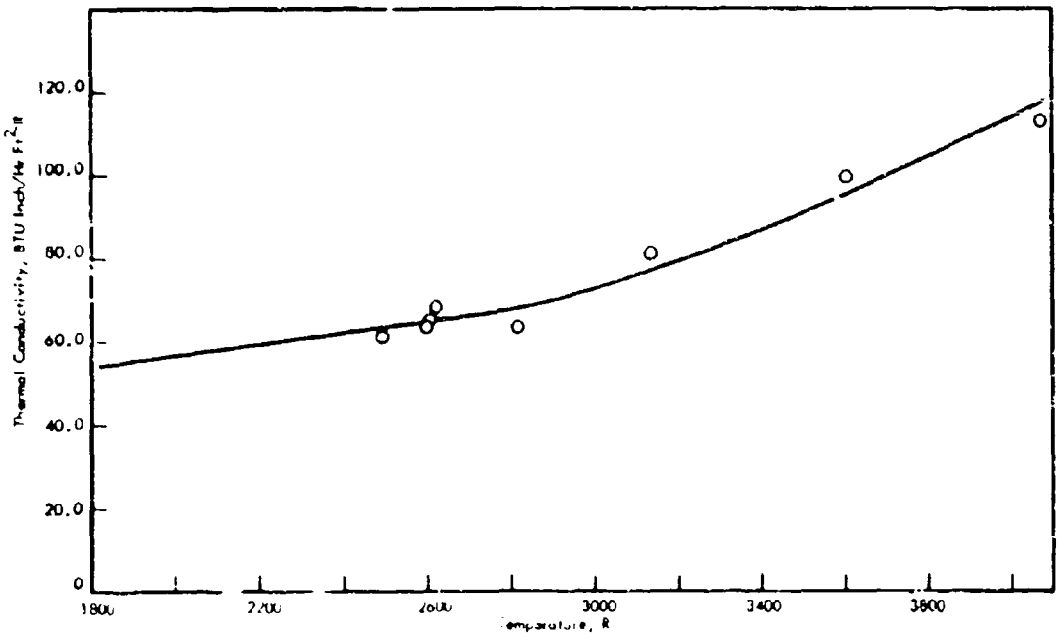

FIGURE 7 THERMAL CONDUCTIVITY OF SPECIMEN PC-I-90 (MX-4926)

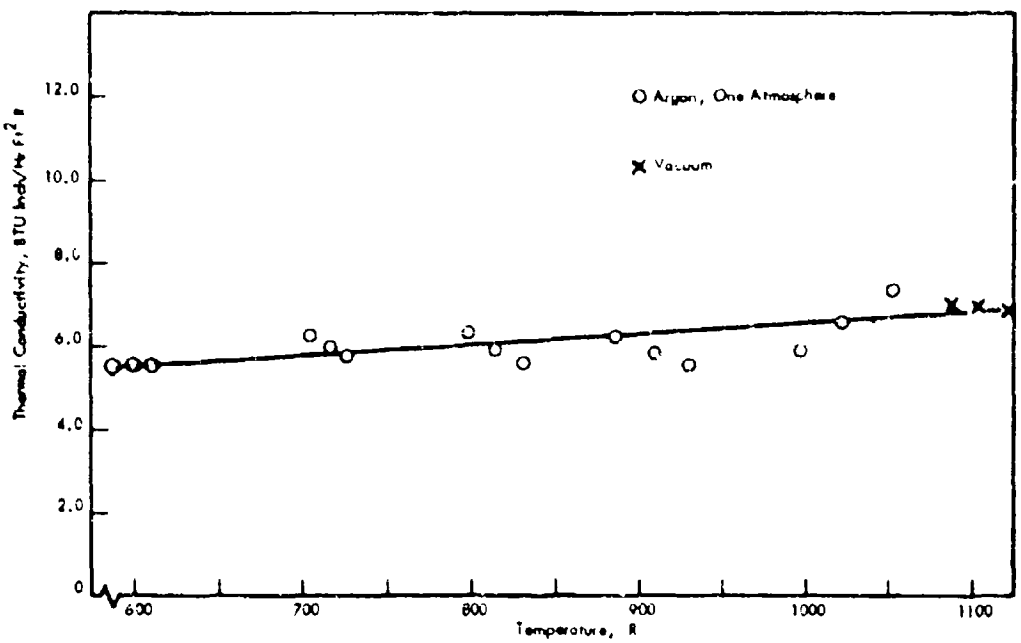

FIGURE 73 THERMAL CONDUCTIVITY OF SPECIMEN PG-V-O (FM-5014)

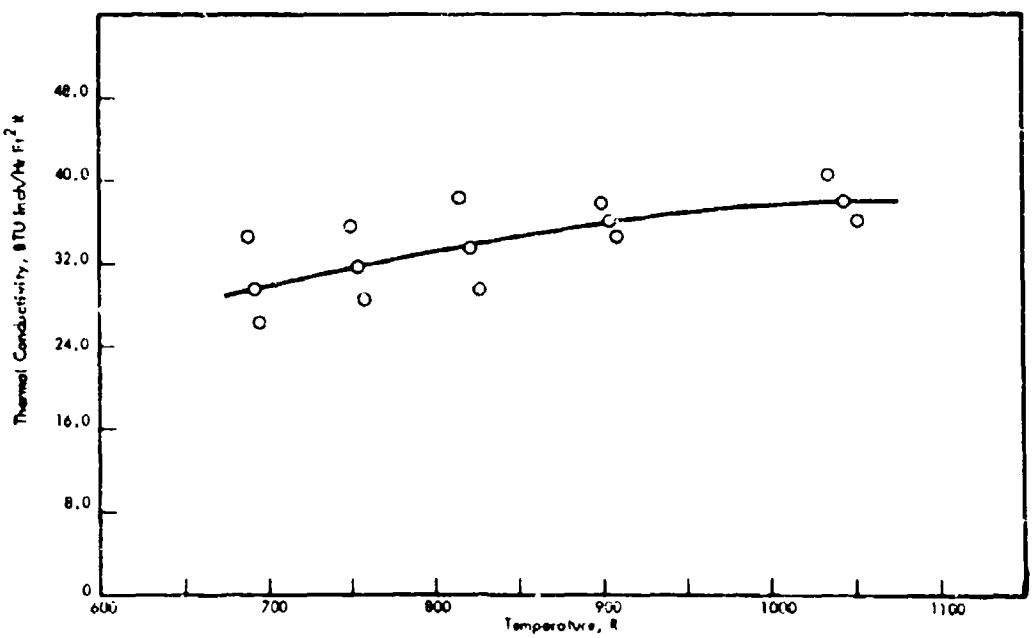

FIGURE 74 THERMAL CONDUCTIVITY OF SPECIMEN PG-V-90 (FM-5014)

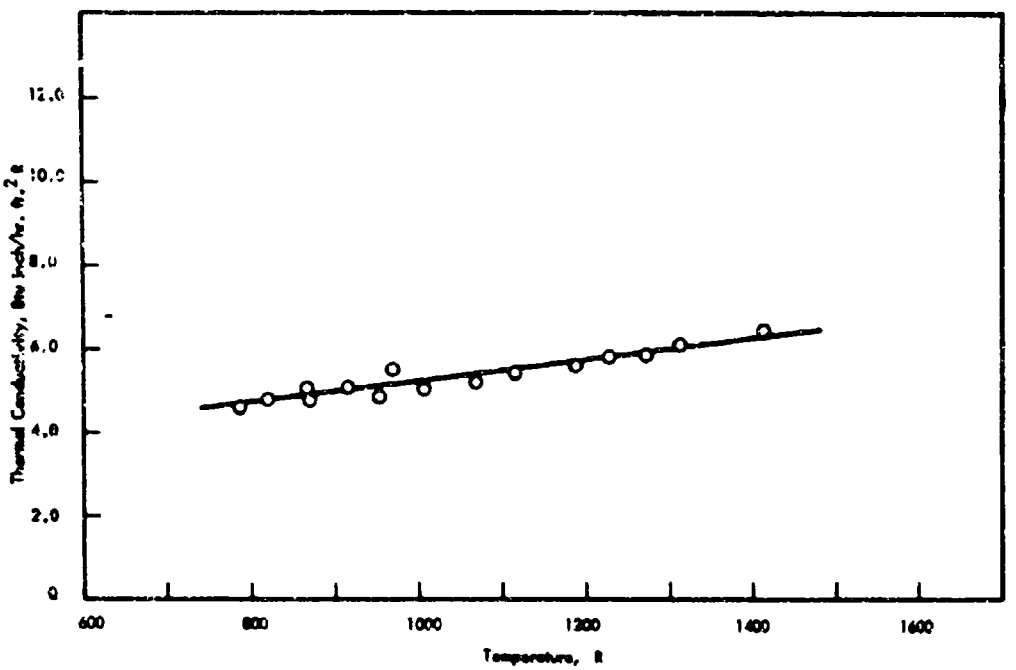

FIGURE 75 THERMAL CONDUCTIVITY OF SPECIMEN PG-III-O (FM-5014)

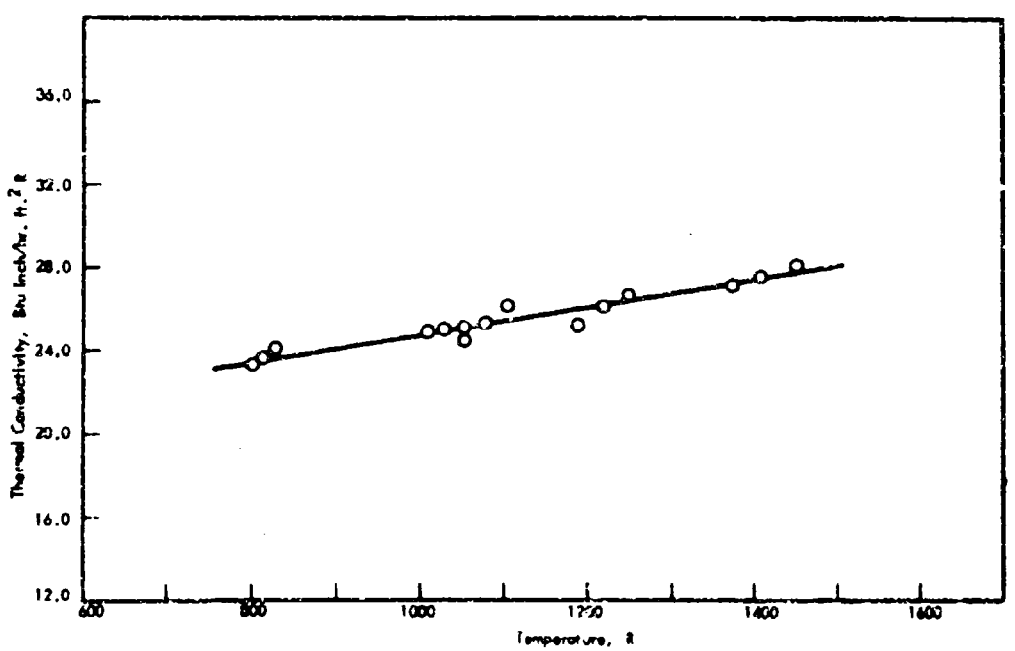

FIGURE 76 THERMAL CONDUCTIVITY OF SPECIMEN PG-III-90 (FM-5014)

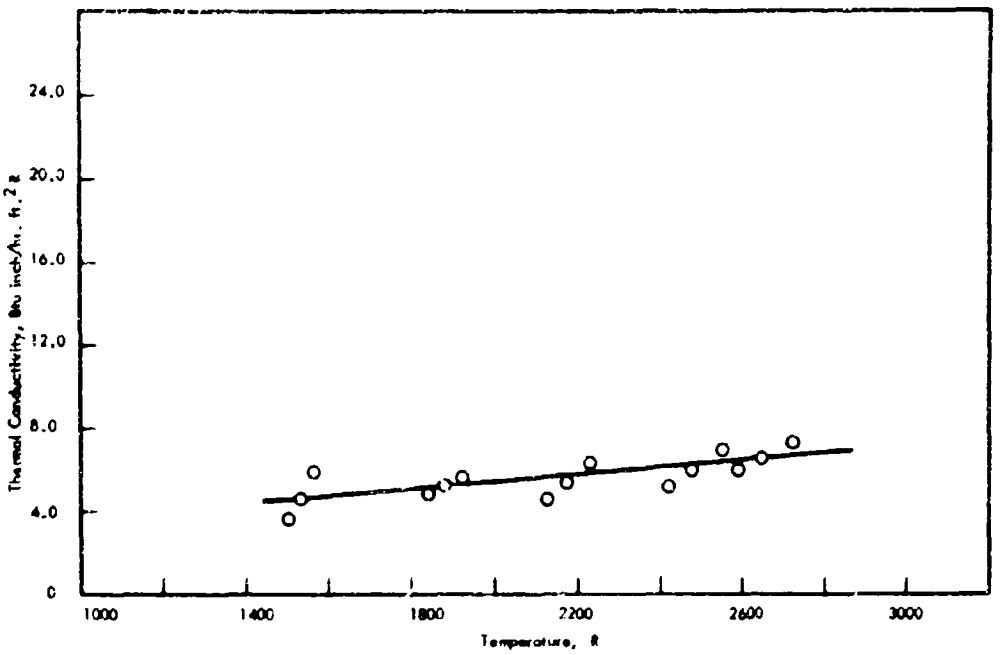

FIGURE 77 THERMAL CONDUCTIVITY OF SPECIMEN PG-11-O (FM-5014)

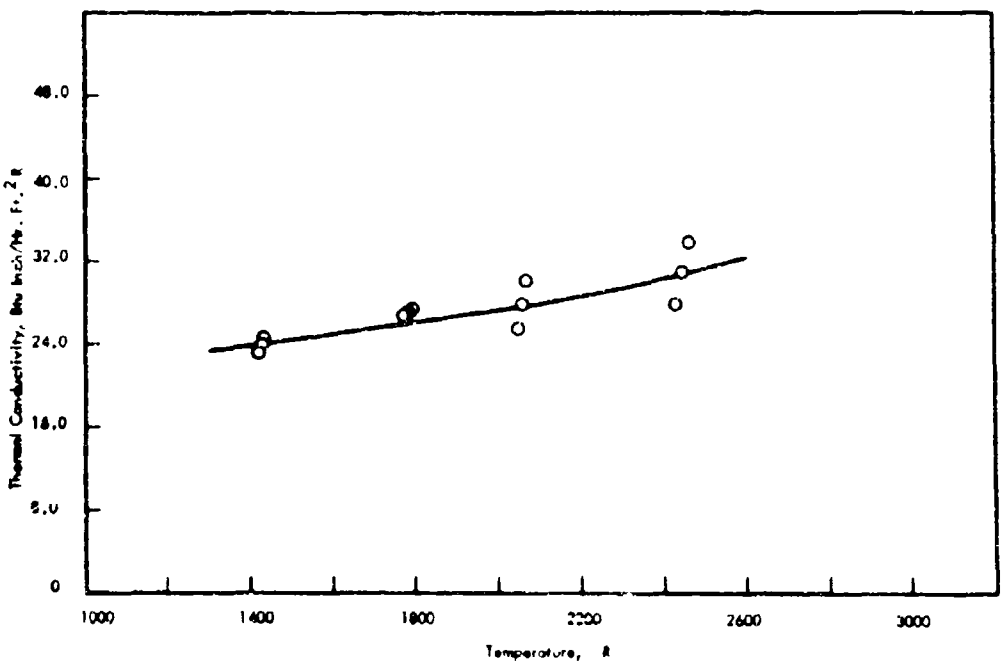

FIGURE 78 THERMAL CONDUCTIVITY OF SPECIMEN PG-11-90 (FM-5014)

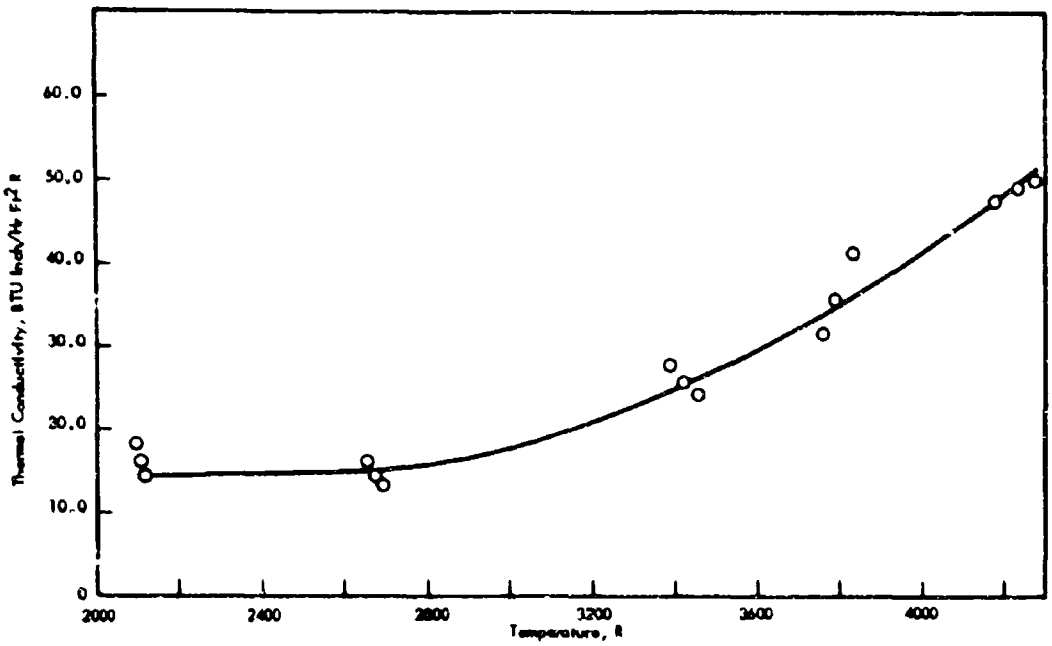

FIGURE 79 THERMAL CONDUCTIVITY OF SPECIMEN PG-I-O (FM-5014)

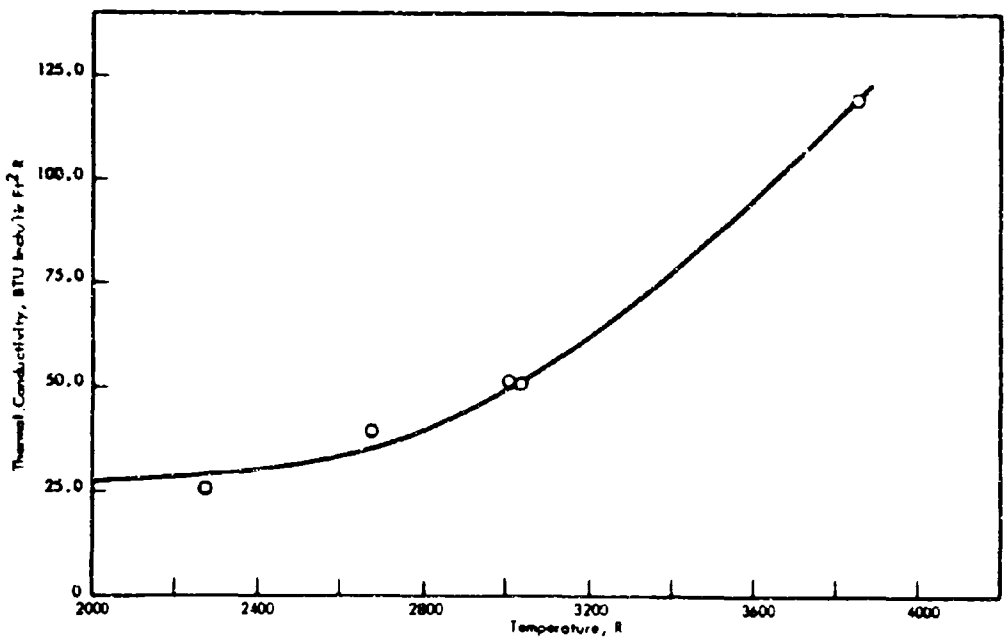

FIGURE 80 THERMAL CONDUCTIVITY OF SPECIMEN PG-I-90 (FM-5014)

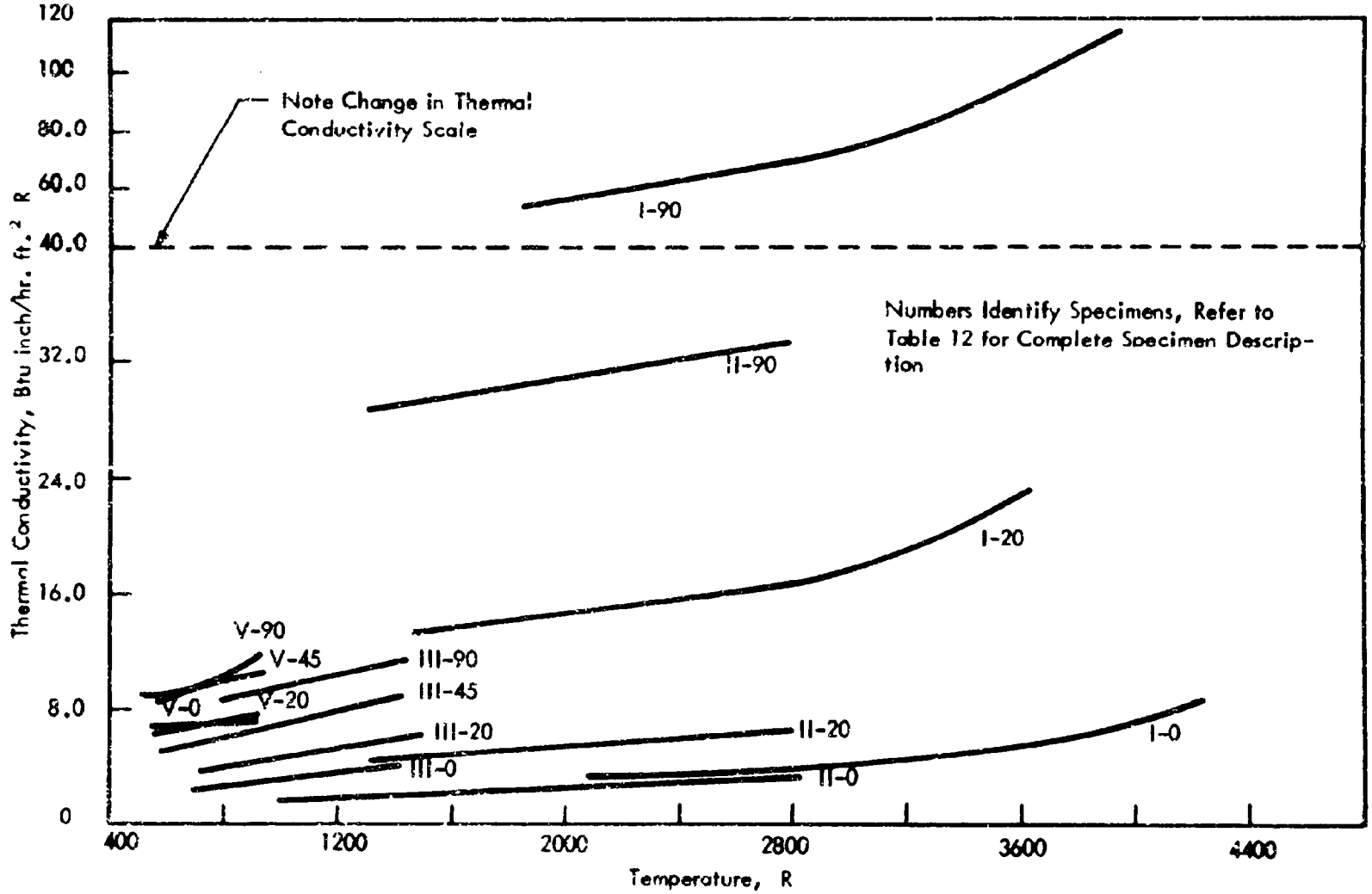

FIGURE 81 COMPOSITE OF THERMAL CONDUCTIVITY DATA FOR MX-4926 (PHENOLIC-CARBON)

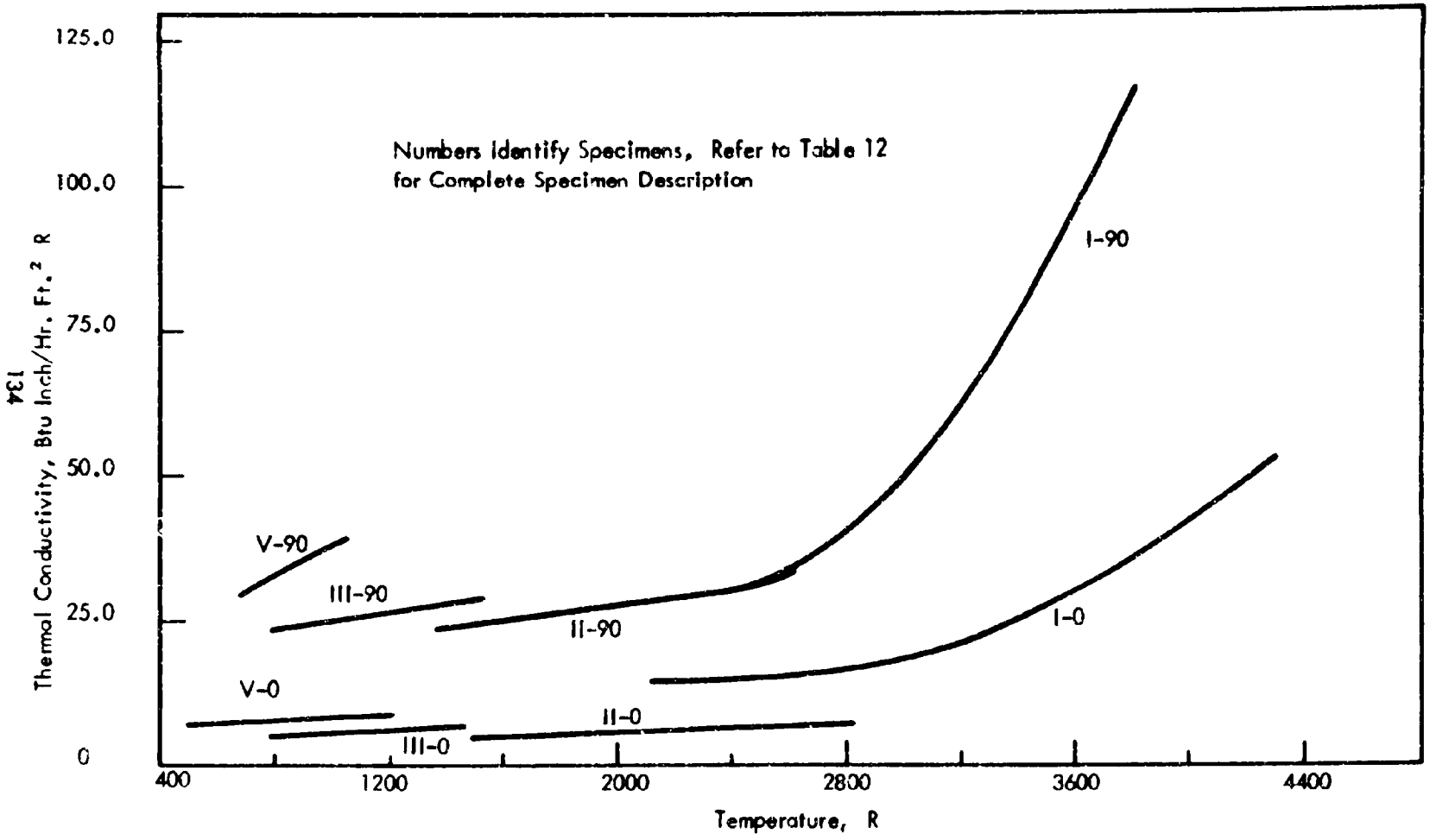

FIGURE 82 COMPOSITE OF THERMAL CONDUCTIVITY DATA FOR FM-5014 (PHENOLIC-GRAPHITE)

The accuracy of the reported measurements is defined as the confidence associated with the values assigned to the specimen conductivities by the curves fitted to the data. The accuracy of the data was limited by the uncertainties associated with thermocouple calibration and thermocouple bead location, heat meter calibration, and measurement technique. The latter refers largely to the effects of heat fluxes developed in the specimen, the graphite cloth thermal resistance elements, and in the heat-flow meter in directions other than that desired for the longitudinal conductivity measurement.

The precision of the measurement refers to the reproducibility of the values obtained, i.e., the limits within which the measurements can be reproduced.

Two of the specimens (PC-II-0 and PC-II-90) were instrumented for use in the error experiments. Both were measured under various boundary conditions which produced variations in measured thermal conductivity due to an accumulation of experimental errors. The observed variations in measured thermal conductivity were then used to estimate probable experimental error. The range of boundary conditions which produced variations in measured conductivity were extreme enough that any other 0- and 90-degree specimens would have a high probability of being measured under conditions included in the range produced in the error experiments. The error for specimens with lamination angles between 0- and 90-degrees was inferred from the two extreme cases. Zone II specimens were chosen for the error experiments because the zone II measurements included more sources of error for the high temperature zone I measurements. Zone I specimens were not considered for the error experiments because of difficulty in reliably instrumenting a high-temperature specimen for extensive measurements.

Details of the procedure and results of this experimental error analysis are presented and discussed in Appendix A.

Because of the procedures followed, the precision and the accuracy are intimately connected. For example, in the error experiment on specimen PC-II-0, the boundary conditions were varied to bracket the conditions under which any 0-degree specimen may have been measured. Then the observed variation of the measured thermal conductivity from the mean was taken as the accuracy limit for the reported thermal conductivity curve. Similarly, any 0-degree specimen may have experienced a set of boundary conditions within the range established with specimen PC-II-0, since the exact boundary conditions experienced by a given specimen had some degree of randomness attached. Thus, its precision in this case was, at worst, the same as the accuracy assigned to the measurement. For this reason the precision and accuracy have the same percentage values.

Utilizing the procedure outlined above, limits for the accuracy and precision for the reported data for all specimens measured in this program were obtained. The details of the procedure appear in Appendix A; results are listed in Table XIV. These error limits include all sources of error outlined here and in the following sections. As such, they should be considered maximum limits. For most of the specimens, the maximum deviation of the measured data points from the curve was less than 1/2 that listed in Table XIV

TABLE XIV SUMMARY OF THE ASSIGNED ACCURACY AND PRECISION LIMITS FOR THERMAL CONDUCTIVITY MEASUREMENTS, IN PERCENT REPORTED VALUE

All 0-degree lamination specimens in zones III and Virgin:	±8
All 0-degree lamination specimens in zones II and I:	±16
All 20-degree lamination specimens in zones III and Virgin:	±10
All 20-degree lamination specimens in zones II and I:	±18
All 45-degree lamination specimens in zones III and virgin:	±12
All 90-degree lamination specimens in zones III and virgin:	±15
90-degree lamination specimens in zone II and zone I, FM-5014 only:	±20
90-degree lamination specimens in zone II and zone I, MX-4926 only:	±25

Correlation of Conductivity and Porosity

As curves were fitted to the conductivity data, it was noticed that the changes in conductivity from one zone to another followed the pattern predicted by the known changes in porosity between zones. Therefore, a semi-quantitative correlation of the thermal conductivity data across zones was developed. In some cases, good correlation of the change in conductivity fron one zone to another, in terms of the changes in porosity of the specimens between these zones, was obvious. The porosity correlation is one of the relationships needed to extrapolate the conductivity data to nonequilibrium states of active chars. It is the primary correlation needed to predict conductivity in the pyrolysis zone. Details relative to the establishment of this correlation are presented in Appendix B. A brief summary of this evaluation as it pertains to the two materials follows.

For the FM-5014, 0-degree lamination material the change in thermal conductivity with continued pyrolysis of the resin from the dense virgin state up to the region where significant "graphitization" of the filler material and resin residue occurred could largely be accounted for simply by a change in porosity of the material. In other words, up to the temperature region where the process of "graphitization" begins to significantly affect the microstructure of the material, the degradation of the resin appears to affect the thermal conductivity only through an associated increase in the porosity of the material, the chemical changes accompanying the pyrolysis process having little influence on the thermal conductivity.

In the FM-5014, 90-degree lamination material the effect on conductivity of the initial pyrolysis of the virgin material could not be accounted for simply by an associated increase in porosity, as in the 0-degree lamination case. This indicates that the pyrolysis reactions do influence the thermal conductivity parallel to the reinforcing fabric to a significant degree. However, for this case the change in thermal conductivity from zones III to II could be attributed to a corresponding increase in porosity from zones III to II, indicating that the influence of the chemical reactions on the thermal conductivity became negligible after pyrolysis had reached the state of development represented by the zone III material.

The breakdown of the porosity correlation from zones II to I in both the 0- and 90-degree lamination angle specimens was interpreted as a measure of the effect of "graphitization" on the thermal conductivity. "Graphitization" occurring in the zone I region resulted in an increase in the apparent conductivity in the 0-degree lamination case by a factor of about 1.8 over the increase which could be expected as a result of the decrease in porosity from zone II to zone I. In other words, "graphitization" resulted in an increase in the solid matrix conductivity for this case.

For the MX-4926 material, the results of the porosity correlation applied to both 0- and 90-degree lamination virgin and zone III specimens gave rise to the same interpretation as that put forth for the FM-5014 0-degree lamination material. That is, for both the 0- and 90-degree lamination case the solid matrix material conductivities for the virgin and zone III materials were nearly the same.

For the MX-4926 material, the greatest effect of "graphitization" seemed to occur in the zone II region. No porosity-thermal conductivity correlation was possible from zone III to zone II for either the 0- or 90-degree lamination cases. However, for the 0-degree lamination case, an approximate correlation existed from zone II to I, although the effect of further "graphitization" seemed to be one of lowering the value of zone I, 0-degree lamination conductivity somewhat below the porosity-predicted value. A surprising result considering the apparent occurrance of "graphitization" in zone II was the low apparent conductivity in the 0-degree specimen. The value was lower than that

predicted by the porosity formulation by a factor of 1.8, so that "graphitization" appeared to have the effect of lowering the solid matrix material conductivity in this case. In the 90-degree lamination case, continuing "graphitization" steadily raised the solid matrix conductivity. This suggests the development of highly oriented crystalline material during the general process of "graphitization" in this material and may be related to the tendency for "graphitized" pyrolysis deposition products to form continuous paths along fibers.

For both materials, good agreement in predicted conductivity ratios across zones was obtained using both total and open porosities, even though the individual values differed significantly in some cases.

"Graphitization" Effects

The effect of "graphitization" on the chars is strikingly evident in the thermal conductivity data for the MX-4926 material in the upward transition in level from zone III to zone II to zone I chars. On the other hand, only relatively small effects were observed for the FM-5014 material. That "graphitization" effects should be more evident on the MX material than on the FM material was expected since the reinforcing fabrics for the two materials were carbon and graphite, respectively. The "graphitization" of the carbon reinforcing cloth was expected to make the MX material perform somewhat like the FM material in zone I. However, the increase in the value of the thermal conductivity for the "graphitized" MX material over the FM material, a factor of two in the low-temperature region of the zone I measurements, was surprising.

This difference probably is related to the mechanics of the "graphitization" process occurring in the MX material, and could depend strongly on the permeability parameters of the material and the efficiency of the carbon reinforcing cloth in cracking the pyrolysis gases that evolve as the specimens are heated. Carbon deposition occurring at the pore sites as some of the fibers themselves became "graphitized" could generate crystal growth and orientation to account for the observed increases in thermal conductivity. Since the MX data show that the solid matrix conductivity in the direction normal to the reinforcing cloth was decreased by the "graphitization" process, the crystalline material would have to be highly oriented with the "a" axis directed along the cloth fibers. The very high conductivities in the direction of the laminates may also be related to the "graphitized" deposits formed in continuous paths along fibers that were noted in photomicrographic analyses. The decrease in material porosity in the high temperature chars could well reflect the deposition and crystal growth processes occurring during "graphitization". There are so many factors that affect the final properties of a graphitic material, such as stresses that may be present during "graphitization", deposition temperature, time-temperature history, etc., that full explanation requires further intensive investigation.

Further references to particular effects of "graphitization" on the thermal conductivity appear in other parts of this section.

Effect of Lamination Angle

Consideration of the thermal conductivity data for the specimens of both materials clearly shows that the reinforcing cloth dominates the thermal conductivity process. Except for the virgin material, the thermal conductivi.. in the direction along the cloth layers is several times that normal to the cloth layers. This suggests that the directions along and normal to the cloth layers may represent the directions of a set of principal conductivity axes. This hypothesis was investigated in some detail as reported in Appendix C.

A comparison between measured conductivities for specimens with a given lamination an[illegible]th values calculated from conductivities obtained at two different angles indicates that the conductivity of the MX-4926 material for any lamination angle can be predicted if knowledge of the conductivity at two angles is available. It is interesting that a $\sin \theta$ relation better applies in the partially pyrolyzed zone III, whereas a $\sin^2 \theta$ relation better applies in zones II and I where "graphitization" has apparently occurred. [illegible] disappearance of the resin as an entity and subsequent "graphitization" of the fille[illegible]d carbon reinforcing cloth have the effect of establishing better defined principal conductivity axes in directions parallel and normal to the reinforcing cloth.

Although the FM-5014 materials were measured at 0 and 90 degrees only, the angular correlation established for the MX-4926 material should also apply with the same degree of accuracy to the FM-5014 material in the temperature region below about 2400 R where radiation transport apparently contributes negligibly to the effective conductivity. Due to the obvious difference in radiation transport characteristics between the FM-5014 and MX-4926 materials, the applicability of the angular correlation at high temperatures, above 2400 R, is doubtful without further experimental investigation for lamination angle effects between 0 and 90 degrees.

Effects of Specimen Inhomogeneity and Anisotropy

The inhomogeneous and anisotropic structures of the materials in this program have a significant effect on their thermal conductivities along the various axes. In the experimental procedures of these measurements, this effect required that considerable care be exercised in determining temperature profiles through the specimens. The difficulty in precisely determining local specimen temperatures resulted in data scatter, particularly in specimens with laminate angles other than 0 degrees.

One principal cause of data scatter was related to the difficulty in obtaining precise thermocouple placement in the specimens. The layered structure of the materials made placement in desired locations [illegible]ry difficult in non-zero-degree specimens. However, post-test measurements of the actual locations permitted the elimination of this source of data scatter.

A more unmanageable data scatter is believed to have been caused by the closeness in thickness of the reinforcing cloth layer and the thermocouple junction. Appendix D discusses this cause of scatter and describes a technique that allowed an estimation of the temperature perturbation required to cause the data scatter observed in the case of specimen PC-III-90, Figure 66 , when it was assumed that the scatter was due to this source. In general, the adjustments afforded by this technique are minor and, on the basis of application to the data for specimen PC-III-90, quite reasonable.

The anisotropy of the specimens limited the precision of thermal conductivity measurements in a third way. In specimens with lamina normal to the direction of heat flow (0-degree lamination), the isotherms within the specimen probably were almost circular. However, due to the anisotropic conductivity of the materials, this was not the case for specimens with lamination angles other than 0 degrees. Since the three specimen thermocouples entered the specimen at different angles to the lamination direction, each could have been influenced to a different degree, depending on the magnitude of radial heat flux within the specimen. Minor radial fluxes in those measurements would not cause significant error in the average level of conductivity, as determined by an appropriately weighted average of the three conductivities measured at each equilibrium. However, they could cause scatter.

To investigate directly this material anisotropy effect on data scatter, an experiment was run in which radial temperature profiles were determined within and around a 90-degree (worst case) specimen. The results are discussed in Appendix D. They indicate that under typical experimental conditions, this characteristic of the material is capable of causing ±5 percent scatter in the data for the non-zero-degree lamination specimens.

Radiation Effects

The total effective or apparent conductivity (sometimes referred to as conductance) of the specimens was the quantity measured in this program. In these measurements, the appearance of a (T^3) function in the effective conductivity at high temperatures is usually attributed to a contribution by internal radiation to the lattice conductivity; Belle[10], Viskanta[11], Bates[12], Kingery[13], and Kellett[15]. Radiation transport through a solid material is determined by the optical parameters and structure of the material. The carbonaceous materials of this program should be quite opaque, suggesting that the radiation effects which appear around 2500 R are due mainly to structure, i.e., specimen porosity. Energy is transported by photon conduction across the pores with increasing efficiency as the temperature of the specimen is increased. (See Loeb[16], Larkin[17], and Francl[18]).

Studies of the radiant energy transport across pores have suggested ways of including the radiation effects in an effective conductivity. One method consists of obtaining an expression for the effective radiant conductivity for the pore in terms of appropriate pore dimensions and material properties, and then combining this conductivity with the conductivity of the solid matrix surrounding the pores.

The work by Loeb[16] and Belle[10] demonstrates this technique. Although the work in these references may combine the pore and solid material contributions in the proper way, the applicability of the results to the present work is limited by the lack of knowledge about the pore conduction term. The data obtained in this program show that the temperature dependence of thermal conductivity at high temperatures is different for the MX-4926 and FM-5014 materials. The porosity shape and size distribution studies did not indicate significant differences between these materials in these respects.

The effects of pores on radiant energy transport through the material can be obtained by investigating the effects of the pore shape and optical parameters on the orientation of the principal conductivity axes of the material in the higher temperature region. Principal axes can be defined only for a sample of the material which is large in comparison to the average pore dimensions and inter-pore spacings. For such a sample, the axes will have a given spatial orientation at low temperature and in a vacuum where the pore conductivity is essentially zero. As the temperature increases into the region where photon conduction across the pores becomes significant, the contribution of the pores will depend on their orientation relative to the principal axes and on their microscopic optical properties.

Consider the case where the heat flux is along a principal axis so that the local isotherm is normal to this axis. If the pores are elliptical with their long axis at some angles other than 0 and 90 to this principal axis, the net heat flux transported across the pores generally will not be normal to the local isotherm. This will tend to distort the isotherm to a degree that depends upon the local absolute temperature and in effect destroys the orientation of the principal axes which was established at low temperature with negligible pore contribution. The optical parameters of the material enter in the same way. Regardless of the pore orientation, the heat flux transported across the pore will depend upon the bi-directional reflectance associated with the pore shape and material. The net result is a local principal axis orientation which depends in part on the local absolute temperature.

This mechanism could enter into an explanation of the observed differences between the high temperature conductivities of the FM-5014 and MX-4926 materials. Another result would be the break down of the angular correlation discussed in the section "Effect of Lamination Layup Angle" at high temperatures. A complete explanation requires more thorough investigation than measurement of the apparent conductivity.

EXTRAPOLATION OF VALUES TO NONEQUILIBRIUM STATES OF ABLATING CHARS

The thermal conductivity versus temperature results obtained on this program have been shown to be strongly affected by pyrolysis generated porosity and by "graphitization" in the char. If pyrolysis and "graphitization" were both simple functions of temperature, a single conductivity versus temperature relationship for a given layup angle could be obtained by interpolation between values measured in the virgin and char zones. The char characterization results indicated that this could be done for "graphitization" effects but not for pyrolysis generated porosity effects because the pyrolysis process is significantly affected by rates as well as temperature during the ablation process. Pyrolysis proceeds at slow rates relative to the rate of temperature increase at any depth in the ablator. The faster the temperature increases, the greater the extent of pyrolysis lags the equilibrium value and pyrolysis is then said to be rate controlled. This means that "graphitization" effects on conductivity can be combined in the measured temperature dependence of thermal conductivity during ablation, but that pyrolysis generated porosity effects must be separately super-imposed versus temperature to obtain the complete conductivity versus temperature curve applicable to any specific ablation application or heating rate.

The post-ablation char characterization results showed that porosity is produced in proportion to the amount of pyolysis, and the thermal conductivity results showed that an increase in porosity reduces thermal conductivity. The extent of pyrolysis can be expressed for broad ablation material categories in terms of X_p, the fraction of the original resin content that is pyrolyzed. In virgin material the pyrolyzed resin fraction, X_p, is zero and the total porosity, ξ_t, is zero while in the mature char the pyrolyzed resin fraction is one and porosity is fully developed to the constant total value, ξ_{tc}, typical of mature char. In depth ablation computer programs normally express pyrolysis as a reduction in apparent density, ρ_a, from a fixed value for virgin material, ρ_v, to a fixed value for mature char, ρ_c. The pyrolyzed resin fraction may be obtained from computer results by the following relationship:

$$X_p = \left(1 - \frac{\rho_a - \rho_c}{\rho_v - \rho_c}\right) \tag{5}$$

Using equation (5) and available computer predictions of density versus temperature, the pyrolyzed resin fraction versus temperature for the entire range of potential applications of phenolic-carbon and phenolic-graphite were obtained as shown in Figure 83. Pyrolysis generated porosity develops in proportion to the pyrolyzed resin fraction so the appropriate value of porosity, ξ_t, for use in correcting the conductivity data at any temperature is given by:

$$\xi_t = X_p \, \xi_{tc} \tag{6}$$

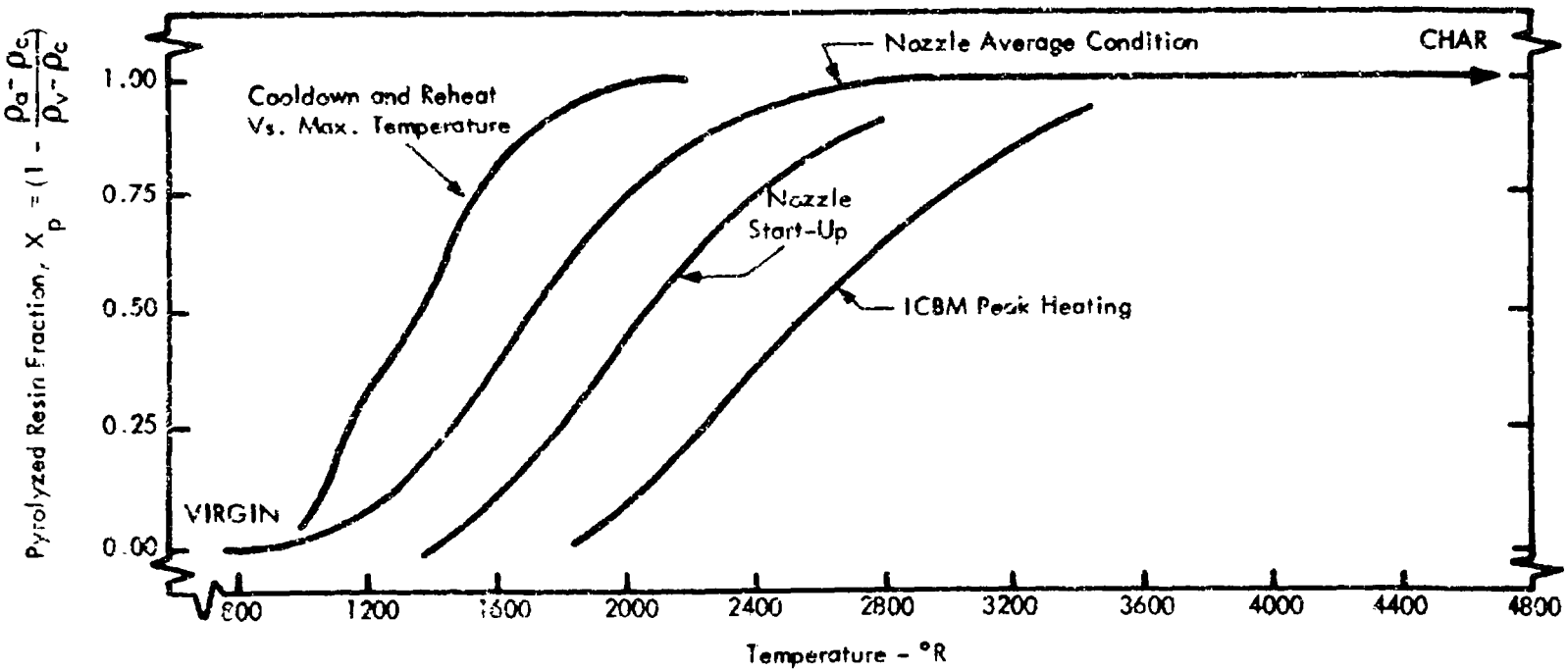

FIGURE 83 - TYPICAL PREDICTED PYROLYSIS VERSUS TEMPERATURE FOR CARBON AND GRAPHITE REINFORCED PHENOLICS

Since porosity develops in proportion to the pyrolyzed resin fraction and lowers thermal conductivity, the wide range in possible resin fraction results shown in Figure 83 indicates the wide range in the possible effects of pyrolysis on a thermal conductivity versus temperature relationship. The curves for nozzle conditions and cooldown or reheat periods were obtained from the Aerotherm computer predictions used in nozzle char characterization. The ICBM peak heating curves are from Boeing computer runs and are believed to represent the most severe conditions possible since the char surface is near the maximum temperature limit in the sublimation regime.

The remainder of this section describes the development of the thermal conductivity data correlation and presents the method of extrapolation to all states of ablation up to 4500°F. The final result is a conductivity versus temperature curve, since the data in this form is easily visualized and utilized in computer ablation analyses. Final results for a single layup angle appear as illustrated in Figure 84, where the range of effects of the rate controlled pyrolysis given in Figure 83 are illustrated.

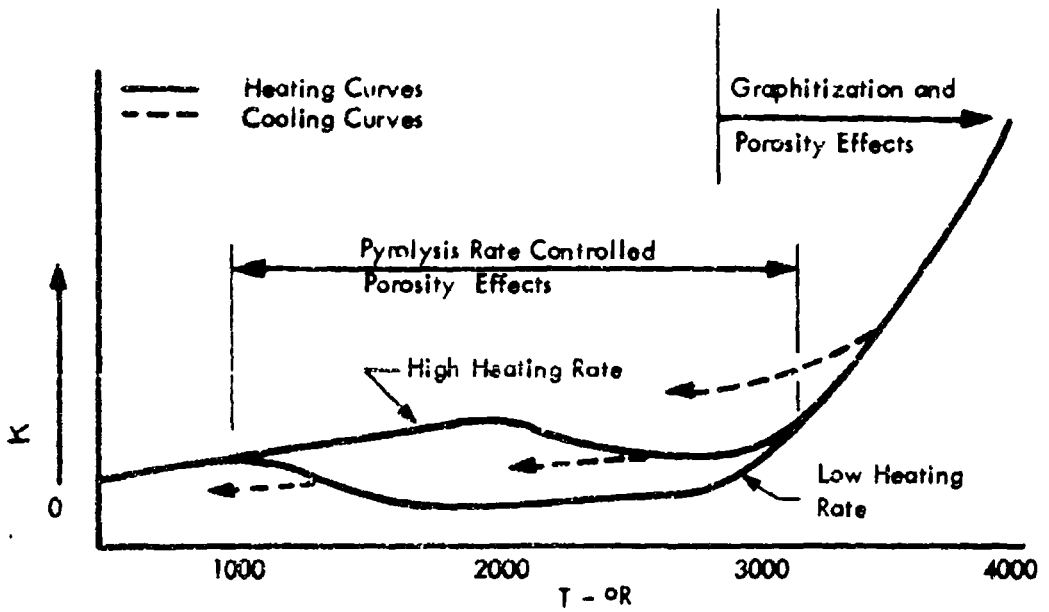

FIGURE 84 BEHAVIOR OF K VERSUS T

It can be seen that where rate controlled pyrolysis effects occur, no single K versus T curve can represent all applications, or even pyrolysis rate changes during a single application. Figure 84 also illustrates the fact that irreversible material changes result in an altered K vs. T relationship applicable during cooldown or reheat cycles.

It was beyond the scope of this program to develop a complete analytical correlation of thermal conductivity data for direct use in all computer predictions. Conductivity data is presented in a generalized format as a first step so that the specific K versus T relationship for specific applications can be extrapolated. This generalized data was derived from the measured conductivities for both the 0- and 90-degree layup angles by removing the effect of the pyrolysis generated porosity in the specimen, resulting in predicted conductivities for zero porosity material. All that is necessary to obtain the conductivity required for any active ablation condition is to apply the porosity correlation described earlier to the zero porosity data. Data for intermediate layup angles is obtained by applying the layup angle correlation to porosity corrected data for 0- and 90-degree layup angles. It is hoped that users will formulate the results so that this is done as part of the computer prediction of ablation performance. This should be possible by developing thermal conductivity equations as a function of both temperature and apparent density along with any associated programming changes required.

Development of Data for Extrapolation

The development of data from which the conductivity needed for any specific problem may be obtained is described for the FM-5014 material. The equations developed in Appendix B, "Correlation of Thermal Conductivity and Porosity", were used to relate the solid component of thermal conductivity of each specimen to a theoretically dense sample of the same material on the basis of pore shapes and pore volume fraction. These equations were applied to the data curves for the porous specimens below 2400°R where a radiation component became apparent to calculate the solid component of conductivity, K_s, of theoretically-dense material. The K_s data curves were then extrapolated versus temperature to cover all cases of active ablation. By using only the data from the low temperature regions of zone I where no radiation transport effects were yet apparent the approximation of zero pore conductivity assumed in the porosity correlation was satisfied. The resulting curves for 0- and 90-degree layup angles appear in Figure 85. The temperature regions of actual measurements of conductivity on porous specimens are indicated. The virgin specimens represent theoretically dense material so that the virgin data required no conversion.

The agreement between virgin and porosity adjusted zone III curves is very good considering the chemical changes taking place between the virgin and zone III states. The change in conductivity from virgin to zone III material in the 90-degree case cannot be accounted for only by a porosity increase. An assumed transition from virgin material to zone III is indicated by a dashed line. Greater detail in the porosity correlation such as an inclusion of the effects of size distributions may improve the results.

The effects of "graphitization" show up in Figure 85 as discontinuities in the solid component curves between zones II and I. Furnace charring studies indicated that

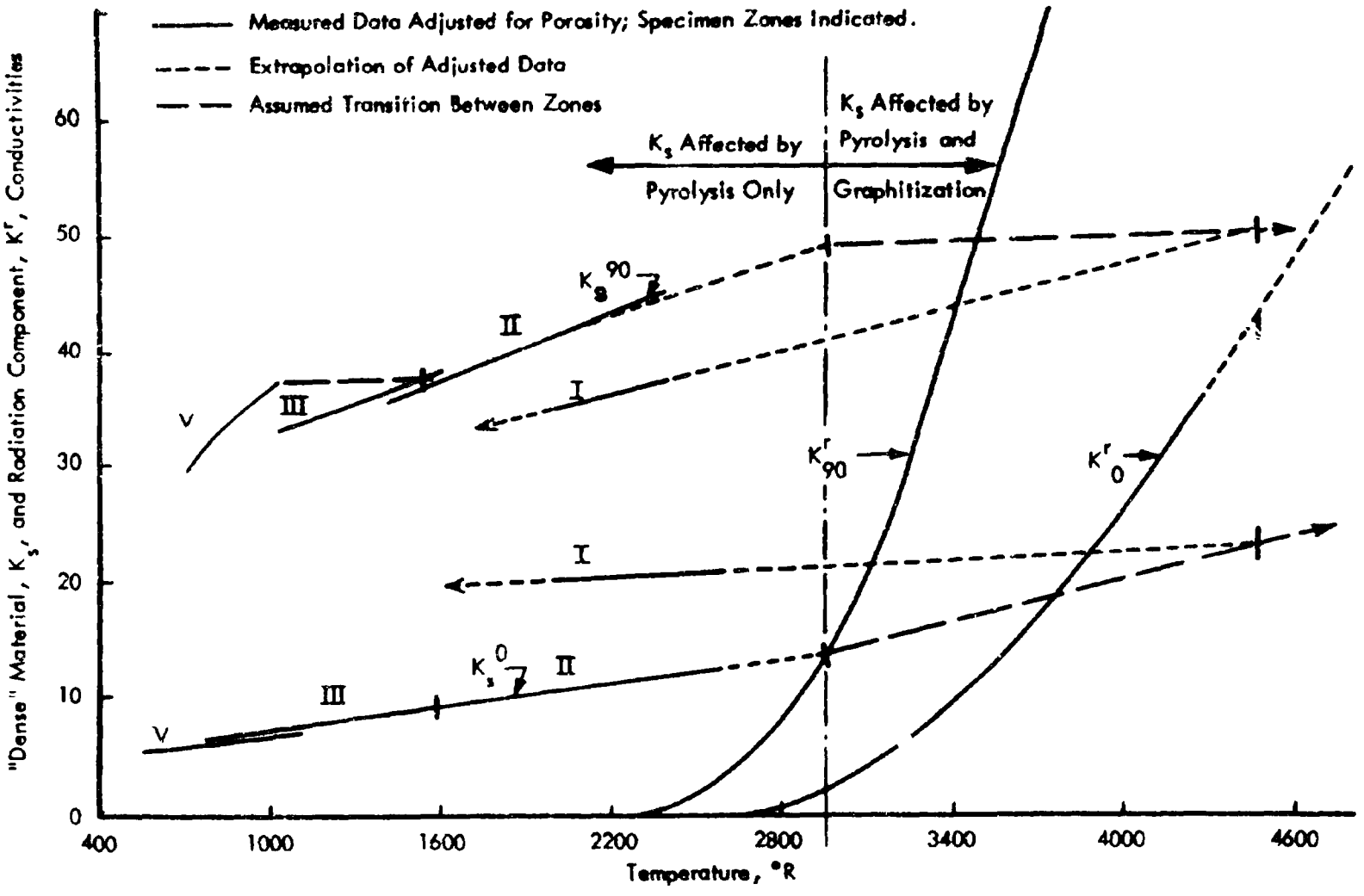

FIGURE 85 - CORRELATION OF THERMAL CONDUCTIVITY RESULTS, FM-5014 PHENOLIC GRAPHITE

"graphitization", although a strong function of the maximum specimen temperature reached, was independent of the heating rate or soak time at the maximum temperature. A linear increase in "graphitization" effect versus temperature was assumed beginning at the temperature at which the zone II specimens were charred, 2960°R, and passing through the temperature at which the zone I specimens were charred, 4460°R. This appears in Figure 85 as the dashed lines between the zone II and zone I data. As better knowledge of "graphitization" threshold temperature and rate become available, the dashed transfer path can be adjusted.

In order to generalize at temperatures higher than 2400°R, the radiation component of the thermal conductivity had to be separated from the measured conductivity. This was done by assuming that the straight-line, low-temperature portion of the zone I measurements represented the solid conductivity, and then extrapolating this portion of the data curve up through the higher temperature range. The difference between the measured and extrapolated solid conductivities above 2400°R was then assumed to be the radiation transport contribution, K^r, to the total effective conductivity. These differences are plotted as K_{90}^r and K_0^r in Figure 85, representing the radiation conductivity components for the 90- and 0-degree specimens. As a result, the effective conductivity for the theoretically dense materials represented by the curves in Figure 85 is given by the sum of the dense material solid conductivity, K_s, and the radiation component conductivity, K^r. Phenomenologically, the radiation is now by means of absorption and re-radiation through a dense material rather than primarily across pores. If enough were known about the properties of the material, an explicit relation could be sought for the radiation conductivity component associated with specimen porosity in terms of temperature, optical parameters, pore fraction, and pore dimension, Belle [10], Kingery [13], and Larkin [17]. Without the necessary additional information, the radiation components obtained for the 0- and 90-degree specimens were assumed to apply to material of different porosity from that of the specimens measured. For material of higher porosity fraction or larger pore dimensions, the radiation components of Figure 85 will be low, and for material with lower porosity fraction or smaller pore dimensions than those of the specimens measured, they will be high.

The smoothed results of the data extrapolation shown in Figure 85 are given in Figure 86. Solid lines show the "dense" material solid component of conductivity, K_s, applicable to active ablation and the radiation component, K^r, applicable to all periods. Dotted lines show typical K_s results applicable to cooling or reheat periods, e.g. the case of a rocket nozzle after shutdown, where the temperature at the intersection with the solid K_s curve was reached during ablation. The specific case where cooling began after full "graphitization" (Zone I) had been reached in the region of the ablator under consideration is indicated for both 0- and 90-degree lamination material. These cooling cycle curves are simply the zone I K_s data and

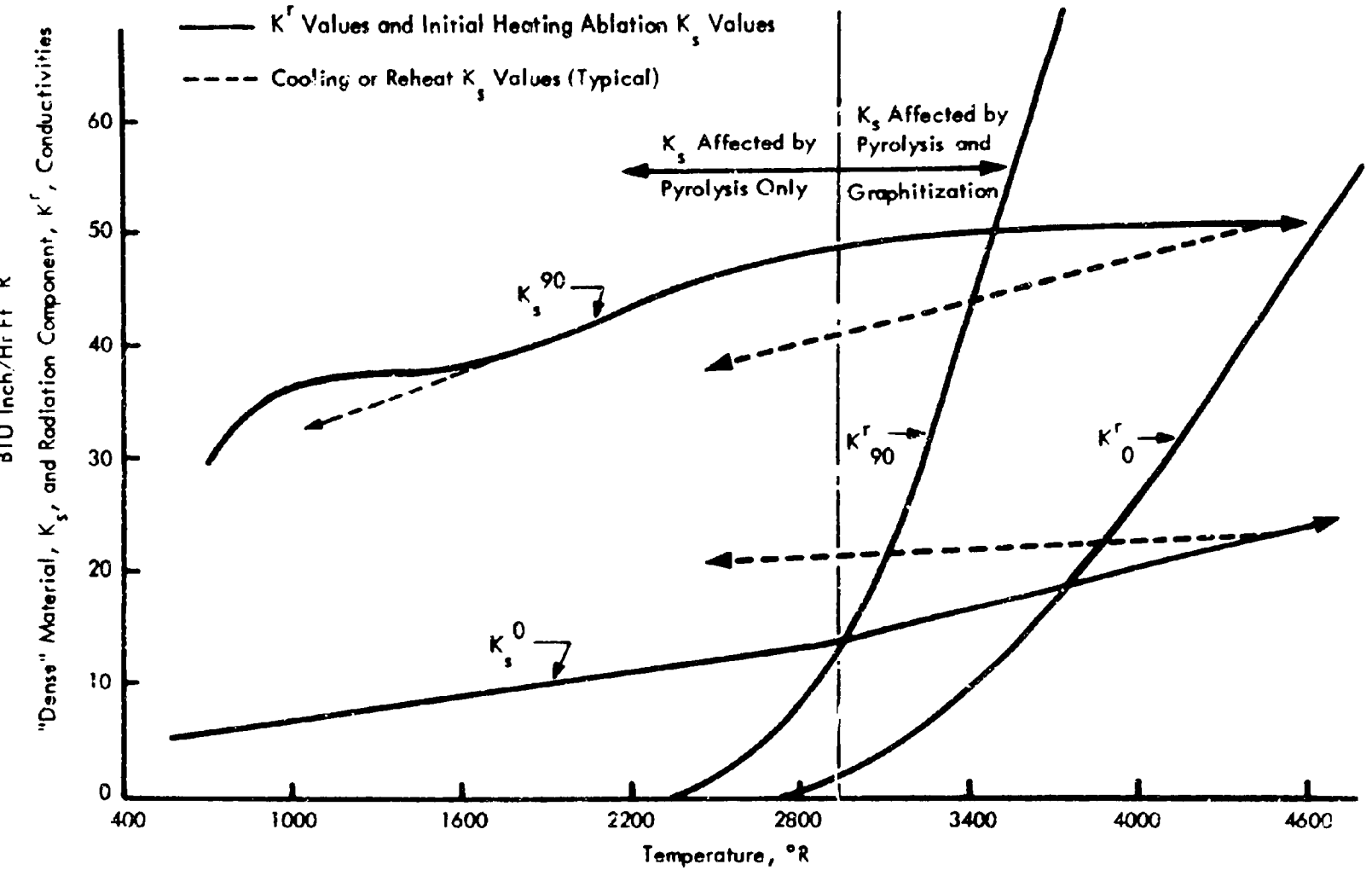

FIGURE 86 - THERMAL CONDUCTIVITY FOR USE IN EXTRAPOLATION PROCEDURE, FM-5014 PHENOLIC GRAPHITE

they may be extrapolated as far into the low temperature region as required. Straight line "dense" material cooling curves from either lower or higher temperatures in the region affected by "graphitization" must be estimated using the available data as a guide to the appropriate slope. "Dense" material cooling curves are the same as the solid line heating curves in the region indicated to be affected by pyrolysis only, except for K_s^{90} between 1000 and 1600°R. "Dense" material data applicable to cooling or reheat periods must be corrected for the equilibrium value of porosity associated with the maximum temperature reached as indicated by the appropriate pyrolyzed resin fraction in Figure 83. Full use of the available data indicates that each depth increment in the char has a different K versus T curve applicable to cooling or reheating depending on the level of irreversible material change due to pyrolysis or "graphitization" that is achieved. This was previously illustrated in Figure 84.

From the above discussion, the Thermal conductivity data from FM-5014 0- and 90-degree lay-up angle, θ, material applicable to any oblation problem are extrapolated from the data of Figure 86 by correcting the "dense" material solid conductivity, K_s^{θ}, for pyrolysis, generated porosity and adding the radiation component, K_{θ}^{r}. "Dense" material K_s^{θ} is corrected for porosity using the porosity developed in Appendix B and substituting Equation (6) to obtain porosity values corresponding to the appropriate pyrolysis rate with the aid of Figure 83 or available in-depth computer predictions. This extrapolation procedure is summarized in Equation (7) used to obtain the conductivity for lay-up angles of 0 or 90 degrees at each temperature.

$$K_{\theta} = \left[\frac{1 - X_p \xi_{tc}}{1 + X_p \beta \xi_{tc}}\right] K_s^{\theta} + K_{\theta}^{r} \qquad (7)$$

where:

K_s^{θ} = "Dense" material solid component of conductivity

K_{θ}^{r} = Radiation component of conductivity

θ = Layup Angle, 0 or 90 degrees

β = Pore shape factor;
4/5 for θ = 0° layup angle
1/8 for θ = 90° layup angle

ξ_{tc} = Final chars total porosity obtained from ablative char characterization;
0.31 for FM-5014
0.45 for MX-4926

X_p = Pyrolyzed resin fraction from Figure 83 or from equation (5) and available computer predictions of apparent density versus temperature.

Equation (7) will reproduce the measured Thermal conductivities to within two percent at the highest temperatures.

The extrapolation procedure for MX-4926 is identical to that for FM-5014. Figure 87 shows the development of the "dense" material solid component curves and the radiation component curves for MX-4926. "Graphitization effects are more evident than in the FM-5014 material, and therefore knowledge of the threshold temperature for significant "graphitization", and its rate of progress with temperature are more crucial for the application of this extrapolation procedure. The dashed transition lines between the maximum temperatures for zones III and II as shown in Figure 87 are based on the assumption that the strong effects of "graphitization" on Thermal conductivity in MX-4926 begin just beyond maximum temperature of zone III. In MX-4926, two stages of "graphitization" were represented by zones II and I, whereas only one stage, zone I, was found for the FM-5014 material. The smoothed results of the MX-4926 data extrapolation for use in Equation (7) are given in Figure 88. These curves cre interpreted in the same way as for FM-5014.

To obtain the Thermal conductivity for layup angles, θ, other than 0 and 90 degrees, the porosity corrected results for both 0 and 90° layup angles from Equation (7) are combined in the layup angle correlation developed in Appendix C. The results are assumed to apply for all cloth orientations within the laminate plane. The most widely applicable form of the layup angle correlation is given by Equation (8).

$$K_\theta = K_0\left[1+\left(\frac{K_{90}}{K_0}-1\right)\sin^2\theta\right] \qquad (8)$$

Equation (8) applies for all cases except for layup angles above 45 degrees in the virgin or pyrolysis zones, where substitution of $\sin\theta$ for $\sin^2\theta$ will give better fit to the experimental data.

Summary of Extrapolation Procedure

The extrapolation procedure developed above is considered to make maximum use of the information gained in this measurement program. The procedure is summarized as follows:

Initial Heating Active Ablation Cycle –

The conductivity of 0 - and 90 - degree layup angle material at each temperature point of interest is obtained from the data of Figures 86 or 88 by correcting the "dense" material solid conductivity, Ks, for the effects of pyrolysis generated porosity and

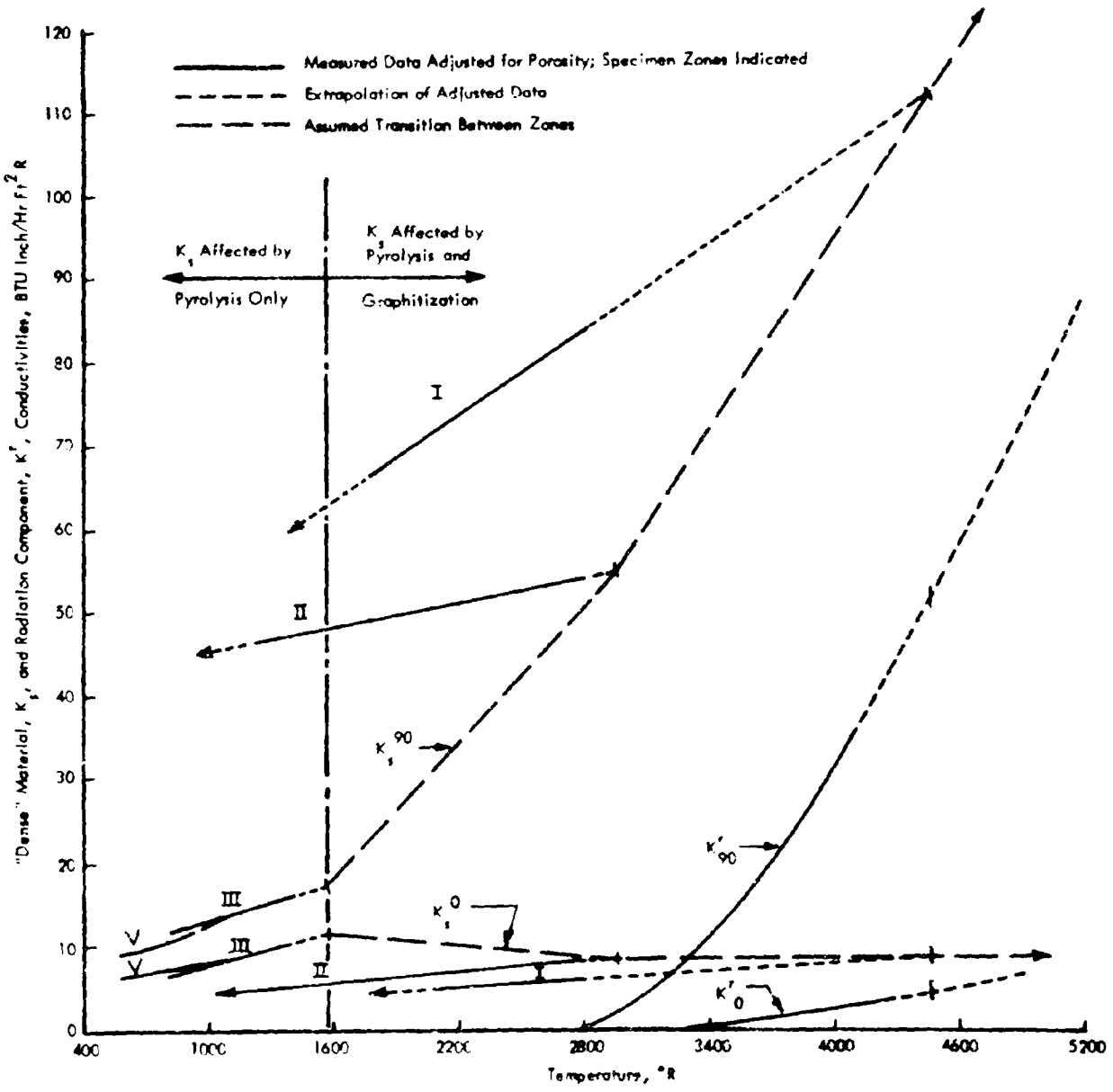

FIGURE 87 CORRELATION OF THERMAL CONDUCTIVITY RESULTS, MX-4926 PHENOLIC CARBON

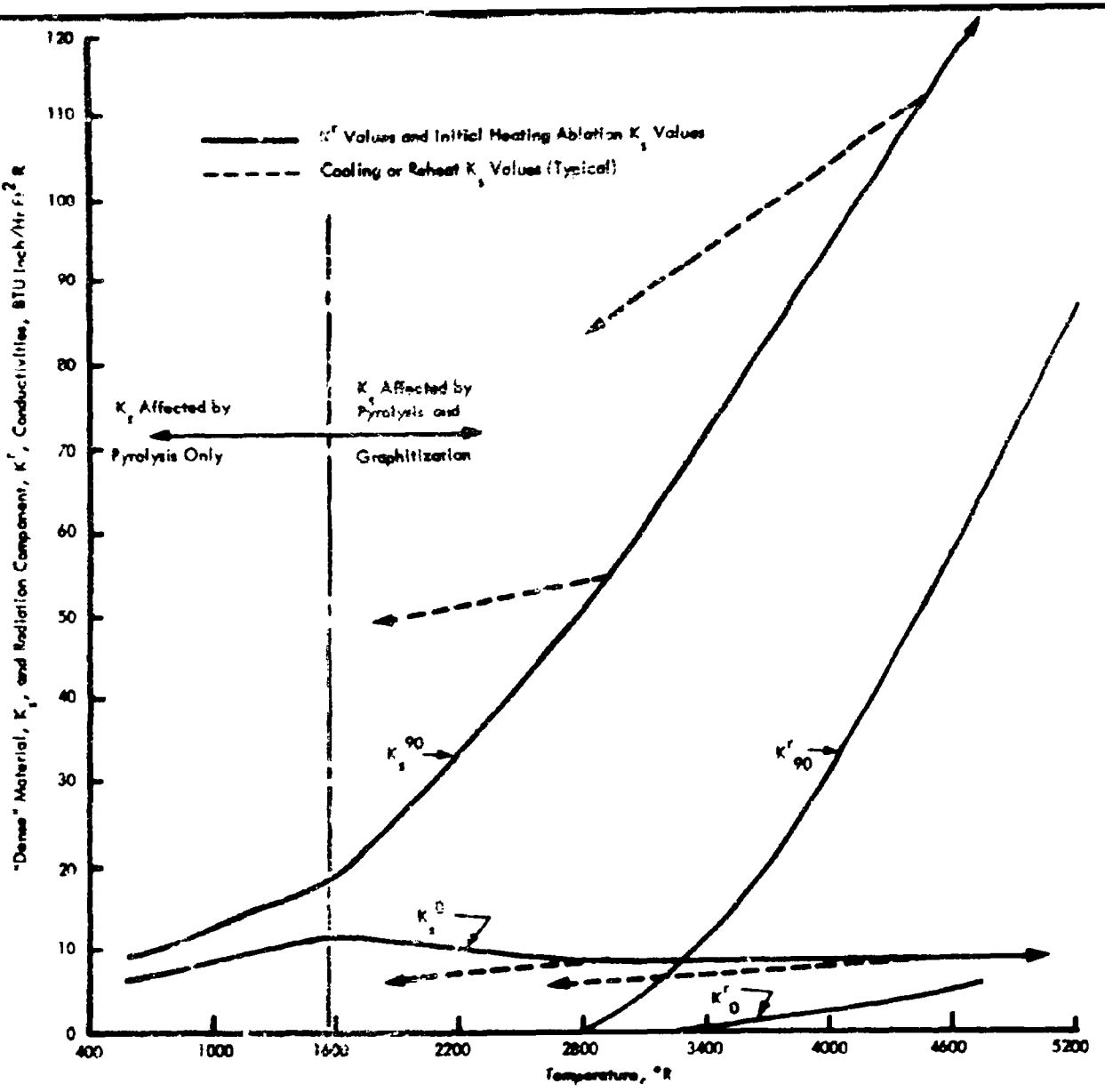

FIGURE 88 THERMAL CONDUCTIVITY FOR USE IN EXTRAPOLATION PROCEDURE, MX-4926 PHENOLIC CARBON

adding the radiation component, K^r; using Equation (7). Use of Equation (7) also requires pyrolyzed resin fraction versus temperature data, which may be estimated for each temperature point from Figure 83 or may be obtained for specific cases from Equation (5) and available computer predictions of apparent density versus temperature.

Full use of this procedure would show the conductivity versus temperature in the pyrolysis zone to be continuously varying during ablation applicationdue to the range of rate controlled pyrolysis shown in Figure 83.

Conductivity data for layup angles between 0 and 90 degrees are obtained by substituting the results obtained above for both 0 and 90 degrees into the layup angle correlation, Equation(8).

Cooling or Reheat Cycle -

The procedure is the same as given above for the initial heating ablation cycle, except the dotted lines in figures 86 and 88 must be used as a guide to estimating the K_s data applicable in the regions where K_s has been affected by graphitization. A separate dotted line should be interpolated between those given to represent the K_s data for material that has attained any temperature during initial heating in the region affected by graphitization, e.g. each element of thickness in a cooling or reheating char has a separate conductivity curve. In addition, the pyrolyzed resin fraction used in Equation (7) to correct K_s for porosity effects now is fixed at a single value for each maximum initial heating temperature on the cooldown and reheat curve in Figure 83. Therefore, each element of thickness in a cooling or reheating pyrolysis zone also has a separate conductivity curve versus temperature, each curve being lower than the initial heating K_s curve in proportion to the extent of porosity developed. Such cooling cycle data was illustrated in Figure 84.

If any reheating cycle extends beyond the maximum temperature that was experienced during the initial heating, the conductivity data above this previous maximum temperature is obtained in the same manner as for initial heating.

Remarks on Extrapolation

The extrapolation procedure was presented to allow generalization of conductivity values to arbitrary porosity and to demonstrate pyrolysis and "graphitization" effects on the thermal conducrivity. It was assumed that "graphitization" was a function of the temperature attained by the material. The material porosity was a determinable function of rate controlled pyrolysis so that the active ablator differs from the pre-charred specimens only through its porosity-temperature history. The forms of Equations (5), (6) and (7) were chosen to allow easy calculation of the apparent conductivity for an ablator with known mature char porosity, under the assumption that

the pyrolysis and "graphitization" effects present in the ablator were approximated by those in the test specimens, and that the radiation contribution in the ablator will be similar to that found in the test specimens. Equation (7) was of a form to give back the measured conductivity data when used as prescribed in conjunction with Figures 86 and 88, but is not theoretically correct if the radiation contribution is allowed to increase indefinitely with temperature. Ever if the pore conductivity were allowed to approach infinity, the heat flux, and thus the total effective conductivity for the material, would be limited by the finite conductivity of the solid matrix.

In fact, the thermal transport processes active in the char at high temperatures are not understood. The work of Rasor and McClelland [7] in determining the thermal conductivities of several graphites up to their sublimation temperatures indicated that the apparent conductivity dropped exponentially towards zero above 5500 R. Those authors attributed the decrease in thermal conductivity to thermally activated lattice vacancy formation, based on the conception that thermal transfer is predominately by means of elastic lattice waves. On the other hand, recent work on graphite by Kaspar [14] has indicated that the predominant transport process may be electronic in nature at temperatures above 3600 R. Until the thermal transport process is understood, it will be difficult to separate the radiative component from the effective thermal conductivity and extrapolate data to higher temperatures with any degree of confidence. In addition to these considerations, the additional possibility of a direct influence on the effective thermal conductivity due to the substantial thermal gradients (up to 50,000 R/inch) met in active ablators is raised by Engelmann and Schmidt [19].

APPLICATION OF MX-4926 RESULTS TO FM-5055A

The characterization of the FM-5055A post test chars showed that, up to the point where "graphitization" begins, the behavior of FM-5055A during ablation is similar to that of MX-4926. At least through the pyrolysis zone then, the conductivity of MX-4926 should be applicable with resonable accuracy to FM-5055A, since in this range the data is primarily a function of the type of reinforcement, the layup angle and the development of porosity during pyrolysis. Although "graphitization" along pores and around fibers will have a strong effect on conductivity parallel to the fabric in both materials, the "graphitization" in FM-5055A proceeds further during ablation. Therefore, between the initiation of "graphitization" and where the conductivity is controlled primarily by the radiation component, direct measurements of FM-5055A chars are required for accuracy. The application of MX-4926 data to FM-5055A in the "graphitization" range should be limited to where the heat flux is nearly normal to the fabric, in which case the effect of graphitization on conductivity is comparatively small.

SECTION X

SPECIFIC HEAT MEASUREMENTS

SPECIFIC HEAT TEST METHOD

Specific heat was computed from heat content (enthalpy) data generated in an ice calorimeter.

Apparatus

Enthalpy measurements were made in a Bunsen ice calorimeter of the type described by Ginnings and Corruccini[1]. In this instrument, heat from a specimen melts ice in equilibrium with water in a closed system. The resulting volume change of the ice-water system is determined by weighing displaced mercury (in contact with the water) as the system expands or contracts. The ratio of heat input to the mass of mercury displaced is a constant for the apparatus. There is no temperature change in the calorimeter during specimen cooling because all heat transfer occurs at the ice point.

Figure 89 is a schematic of the calorimeter used for this program as described by Deem and Lucks[2]. As the previously heated, encapsulated specimen is dropped into the central chamber of a double-wall vessel, it releases heat to the ice-covered finned section which is enclosed in water in equilibrium. The portion of heat given up by the specimen only is determined by subtracting the contribution made by the capsule from the total, this former amount being evaluated by a separate drop of an empty capsule. As the ice melts, mercury from an external accounting system enters the inner vessel through a tube to make up the volume difference of ice melting. The total volume of mercury displaced while the specimen cools from its drop temperature to the ice point is accurately measured. The heat quantity transferred is related to the weight of mercury by a constant measure by Ginnings, et al [3,4,5] and by Battelle to be 270.48 joules per gram of mercury.

Test Procedure

Each specimen was sealed in a capsule to provide a protective atmosphere for the high temperature measurements. Either type 347 stainless steel or tantalum capsules were used depending on the specific temperature range.

Initial measurements on the virgin material used sealed type 347 stainless steel capsules at one atmosphere of helium. Under this condition, a discontinuity was observed in the enthalpy-temperature relation which was believed to be due to

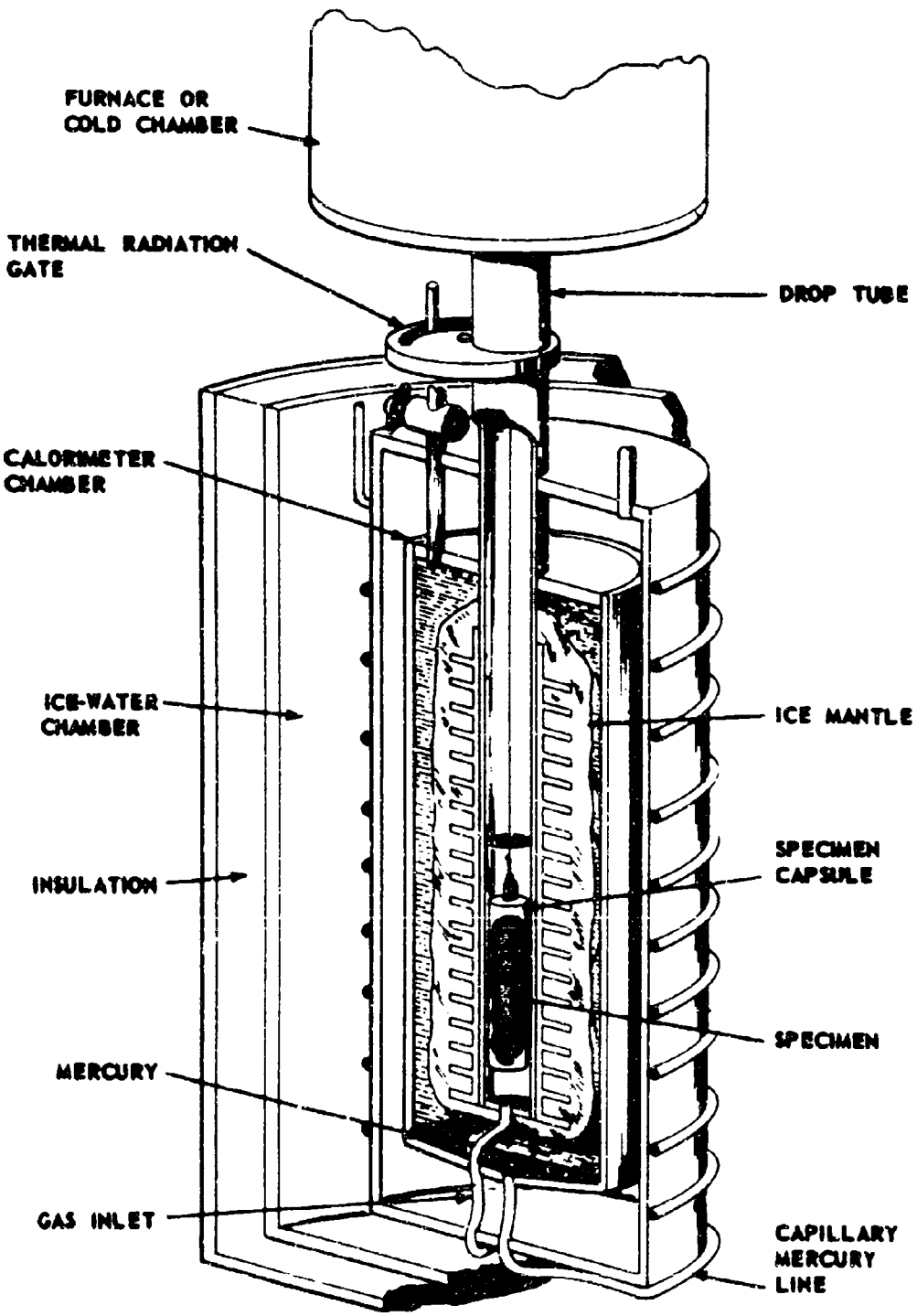

FIGURE 89 BUNSEN ICE CALORIMETER

the heat of vaporization of a component of the specimen, or of some material absorbed by the specimen. Therefore, additional measurements were made with the capsules vented, thus allowing the vapors present to escape and produce a more continuous enthalpy-temperature relation. These latter measurements are believed to be appropriate for the material. Data from both measurements are given in Appendix E.

SPECIFIC HEAT RESULTS

Enthalpy measurements were made on virgin and zone I chars only of MX-4926 and FM-5014. Zone II and III chars were not measured because the specific heat was assumed to be relatively insensitive to the intermediate char states, whereas the virgin and zone I chars were considered to represent the extremes of the specific heat variation. The virgin measurements were made at low temperatures to avoid further pyrolysis, while the zone I chars were measured up to 4460 R. In each case data were taken at enough points to establish a clear definition of the property versus temperature.

Power series equations were fitted to the data by a least squares method. The first derivatives of these equations give the expression for specific heat.

MX-4926 Phenolic-Carbon

For this material, measurements were made on two specimens each of the virgin and zone I char materials, one specimen being prepared by laboratory procedures, while the other was cut from the nozzle of an ablative component.

The enthalpy-temperature relations for the two virgin materials and the two zone I char materials are given in Appendix E. Equations for the observed enthalpy values are as follows:

MX-4926 Virgin Material:

$$H_T = -2.943 \times 10^2 + 0.4094\,T + 4.562 \times 10^4\,T^{-1} \quad (492\text{-}960\ R) \qquad (9)$$

MX-4926 Virgin Material - Nozzle A:

$$H_T = -2.894 \times 10^2 + 0.3958\,T + 4.720 \times 10^4\,T^{-1} \quad (492\text{-}960\ R) \qquad (10)$$

MX-4926 Zone I Char Material:

$$H_T = -3.538 \times 10^2 + 0.3779\,T + 1.732 \times 10^{-5}\,T^2 + 8.312 \times 10^4\,T^{-1} \quad (492\text{-}4460\ R) \qquad (11)$$

MX-4926 Zone I Char - Nozzle Material:

$$H_T = -3.628 \times 10^2 + 0.3896\,T + 1.480 \times 10^{-5}\,T^2 + 8.421 \times 10^4\,T^{-1} \quad (492\text{-}4460\ R) \qquad (12)$$

where:

H_T = enthalpy, Btu lb^{-1}

T = temperature, R

The first derivatives of Equations (9) through (12) give the specific heat equations as follows:

MX-4926 Virgin Material:

$$C_p = 0.4094 - 4.562 \times 10^4\,T^{-2} \quad (492\text{-}960\ R) \qquad (13)$$

MX-4926 Virgin Material - Nozzle A:

$$C_p = 0.3958 - 4.730 \times 10^4\,T^{-2} \quad (492\text{-}960\ R) \qquad (14)$$

MX-4926 Zone I Char Material:

$$C_p = 0.3779 + 3.464 \times 10^{-5}\,T - 8.312 \times 10^4\,T^{-2} \quad (492\text{-}4460\ R) \qquad (15)$$

MX-4926 Zone I Char - Nozzle Material:

$$C_p = 0.3896 + 2.960 \times 10^{-5}\,T - 8.421 \times 10^4\,T^{-2} \quad (492\text{-}4460\ R) \qquad (16)$$

where:

C_p = specific heat, Btu $lb^{-1}\,R^{-1}$

T = temperature, R

Figures 90 and 91 show the specific heat-temperature relation for MX-4926 material calculated from the preceding equations.

FM-5014 Phenolic-Graphite

Measurements were made on one specimen each of the virgin and zone I char materials. The specimens were prepared in the laboratory; no nozzle specimens were employed.

The enthalpy-temperature relations for the virgin material and the zone I char material are given in Appendix E.

Equations for the observed enthalpy values are as follows:

FM-5014 Virgin Material:

$$H_T = -3.577 \times 10^2 + 0.4223\,T + 7.581 \times 10^4\,T^{-1} \quad (492\text{-}1160\ R) \qquad (17)$$

FM-5014 Zone I Char Material

$$H_T = -3.766 \times 10^2 + 0.3976 + 1.297 \times 10^{-5}\,T^2 + 9.004 \times 10^4 + T^{-1} \quad (492\text{-}4460\ R) \qquad (18)$$

where:

H_T = enthalpy, Btu lb^{-1}

T = temperature, R

The first derivatives of Equations (17) and (18) give the specific heat equations as follows:

FM-5014 Virgin Material:

$$C_p = 0.4223 - 7.581 \times 10^4\,T^{-2} \quad (492\text{-}1160\ R) \qquad (19)$$

FM-5014 Zone I Char Materials

$$C_p = 0.3976 + 2.594 \times 10^{-5}\,T - 9.004 \times 10^4\,T^{-2} \quad (492\text{-}4460\ R) \qquad (20)$$

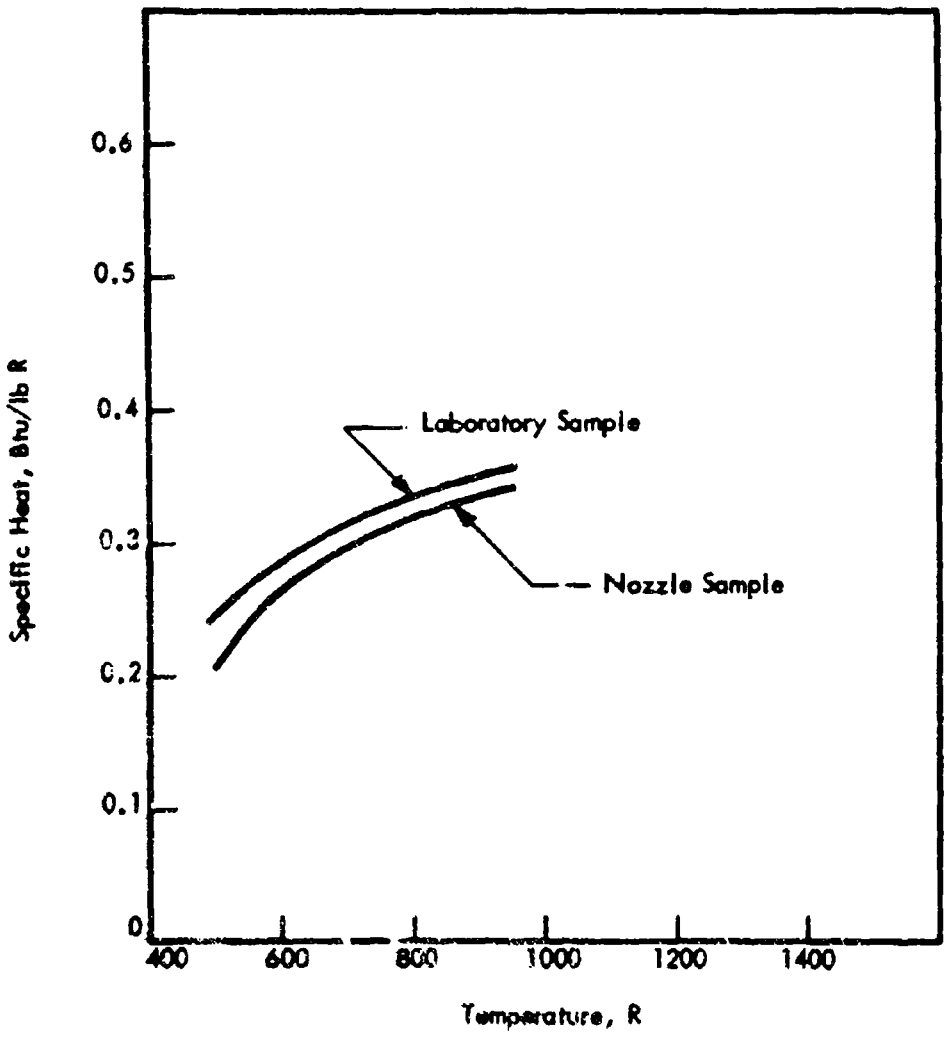

FIGURE 90 SPECIFIC HEAT-TEMPERATURE RELATION FOR MX-4926 (VIRGIN) MATERIALS

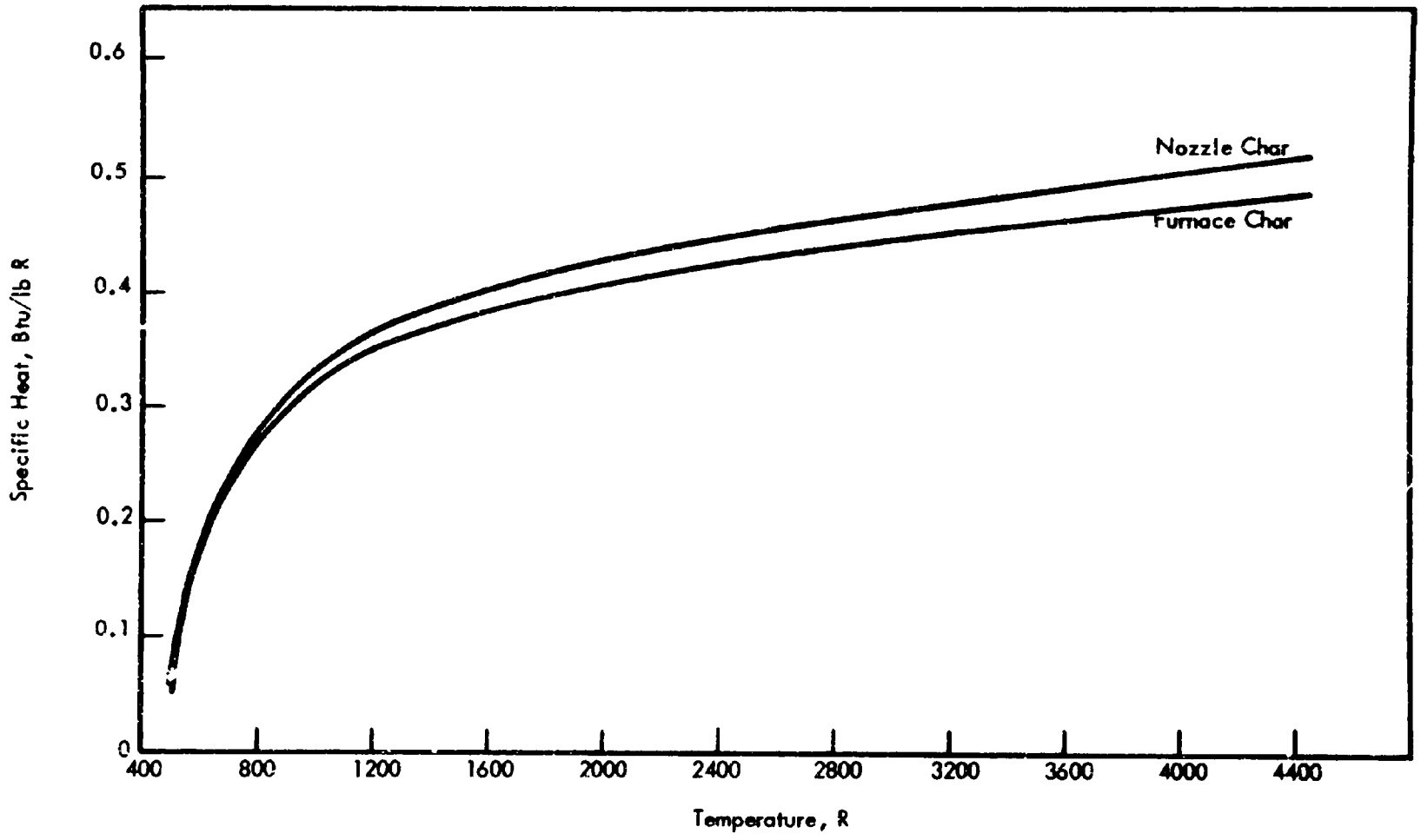

FIGURE 91 SPECIFIC HEAT-TEMPERATURE RELATION FOR MX-4926 (ZONE I) CHAR MATERIALS

where:

C_p = specific heat, Btu lb^{-1} R^{-1}

T = temperature, R

Figures 92 and 93 show the specific heat-temperature relation for the FM-5014 material calculated from Equations (19) and (20).

ANALYSIS OF SPECIFIC HEAT MEASUREMENTS

Error Analysis

Errors associated with heat content measurements by the ice calorimeter may be classed as systemic errors or as those associated with temperature and mercury weight measurement. The systemic errors can be minimized through calibration of the instrument either absolutely or by measuring reference standard materials. Errors in temperature or mercury weight measurements usually result in lack of precision in the data.

System performance was frequently checked by heat content measurements of NBS standard Al_2O_3. During the most recent 150 such measurements, performed before and during this program, all observed values were within ±0.8 percent of absolute in the temperature range 490 - 1900 R, and within ± 1.5 percent of absolute in the range of 1900 - 4500 R. In addition, calibration was checked periodically by introducing a known heat content (electrically) and comparing it with the amount measured through mercury volume displacement. The most recent such measurement indicated an error of -0.06 percent. This is smaller than errors in measurement of a standard material, so no correction was applied.

The precision of data for a given specimen is a measure of the accuracy with which temperature and mercury displacement measurements are made. In this program, several repeat measurements were made at nearly identical temperatures. The agreement of heat content values at a given temperature was generally within ±3 percent. This is reasonable in view of a nominal ± 2 percent error in temperature measurements, and considerably less than ± 1 percent error in mercury weight measurements.

The overall accuracy for the measurements may be assumed conservatively to be within ± 5 percent.

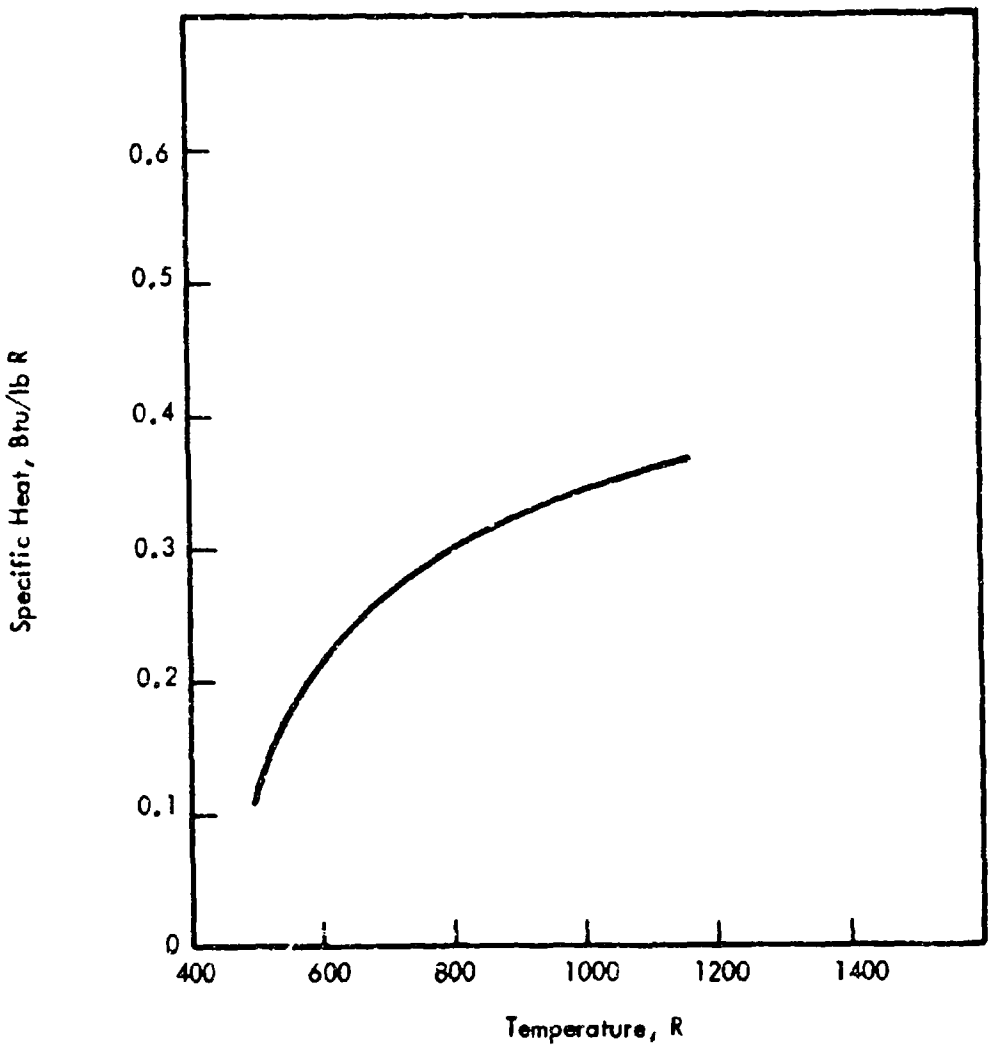

FIGURE 92 SPECIFIC HEAT-TEMPERATURE RELATION FOR FM-5014 (VIRGIN) MATERIAL

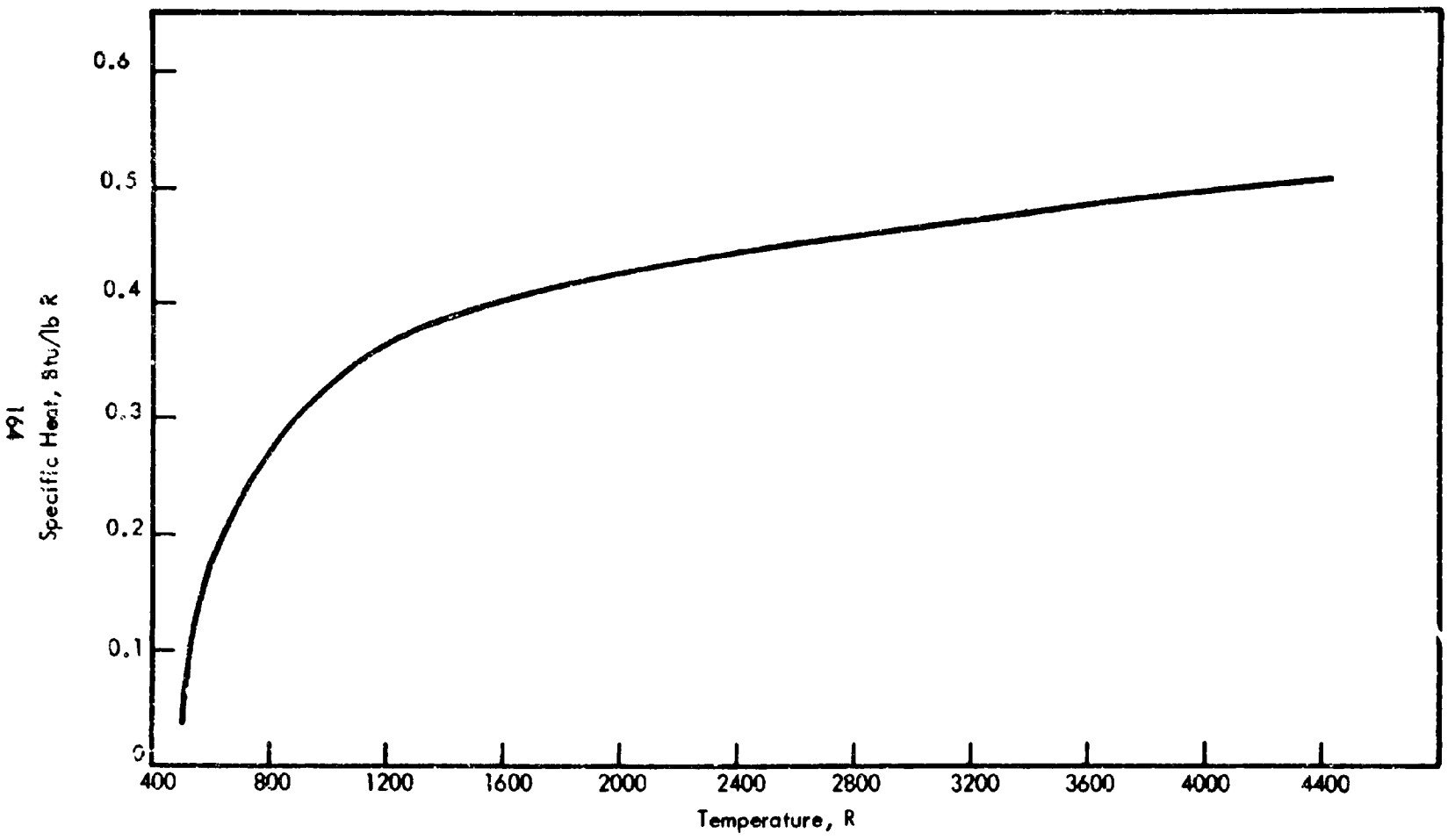

FIGURE 93 SPECIFIC HEAT-TEMPERATURE RELATION FOR FM-5014 (ZONE I CHAR) MATERIAL

Comparison with Published Data

Only one reference was found on specific heat measurements on the materials of this program. The values of Pears, et al, [6] for the specific heat of virgin MX-4926 material agreed well with those measured in this program.

EXTRAPOLATION OF VALUES TO NONEQUILIBRIUM STATES OF ABLATING CHARS

While specific heat measurements in this program were performed on only the virgin and zone I char states of the materials, it is desirable to have some information on the property of the material during the various stages of pyrolysis during ablation. Since the values of virgin and zone I char are similar at the beginning of temperature range in which pyrolysis occurs, it is reasonable to extrapolate the virgin data to cover the case during pyrolysis.

Information available on these materials indicates that under conditions of rapid ablation the virgin state can exist to temperatures as high as 1800 R. If the curves for virgin materials in Figures 90 and 92 are extrapolated to this temperature region, and the curves for zone I chars in Figures 91 and 93 are added, the specific heat for intermediate char zones can be estimated. Figures 94 and 95 show these curves. The shaded area between curves represents the zone of partial pyrolysis. Specific heat moves from virgin material values to char values in proportion to the appropriate pyrolized resin fraction discussed in Section IX and illustrated in Figure 83.

The specific heat for the zone I chars of these materials at very high temperatures can be estimated by extrapolation of curves through the present data, and by assuming that the materials behave like graphite at the higher temperatures. The initial extrapolation can be made using Equations (15), (16) or (20). Since the third term $\left(\frac{C}{T^2}\right)$ approaches 0 at the higher temperatures, the equations will assume the form $T(A + BT)$, a straight line. The high temperature char specific heats are nearly the same for both materials. Equation (16) for MX-4926 nozzle char gives results within ± 1% of those for FM-5014 laboratory chars given by Equation (20). Equation (15) for MX-4926 Laboratory chars gives results within -5% of those from Equation (20).

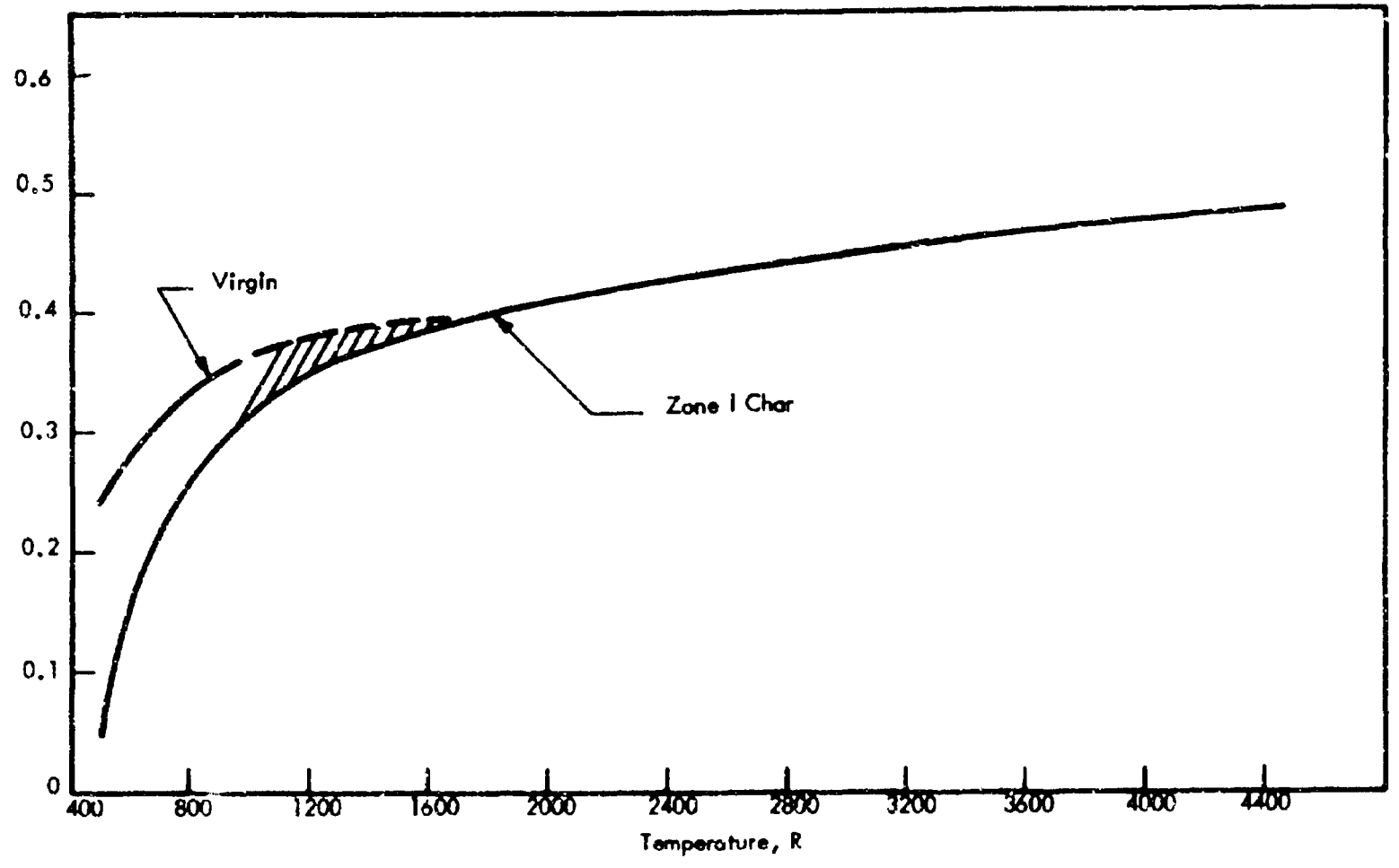

991
Specific Heat, Btu/lb R

FIGURE 94 COMPOSITE SPECIFIC HEAT CURVES FOR MX-4926 MATERIAL (LABORATORY SPECIMENS)

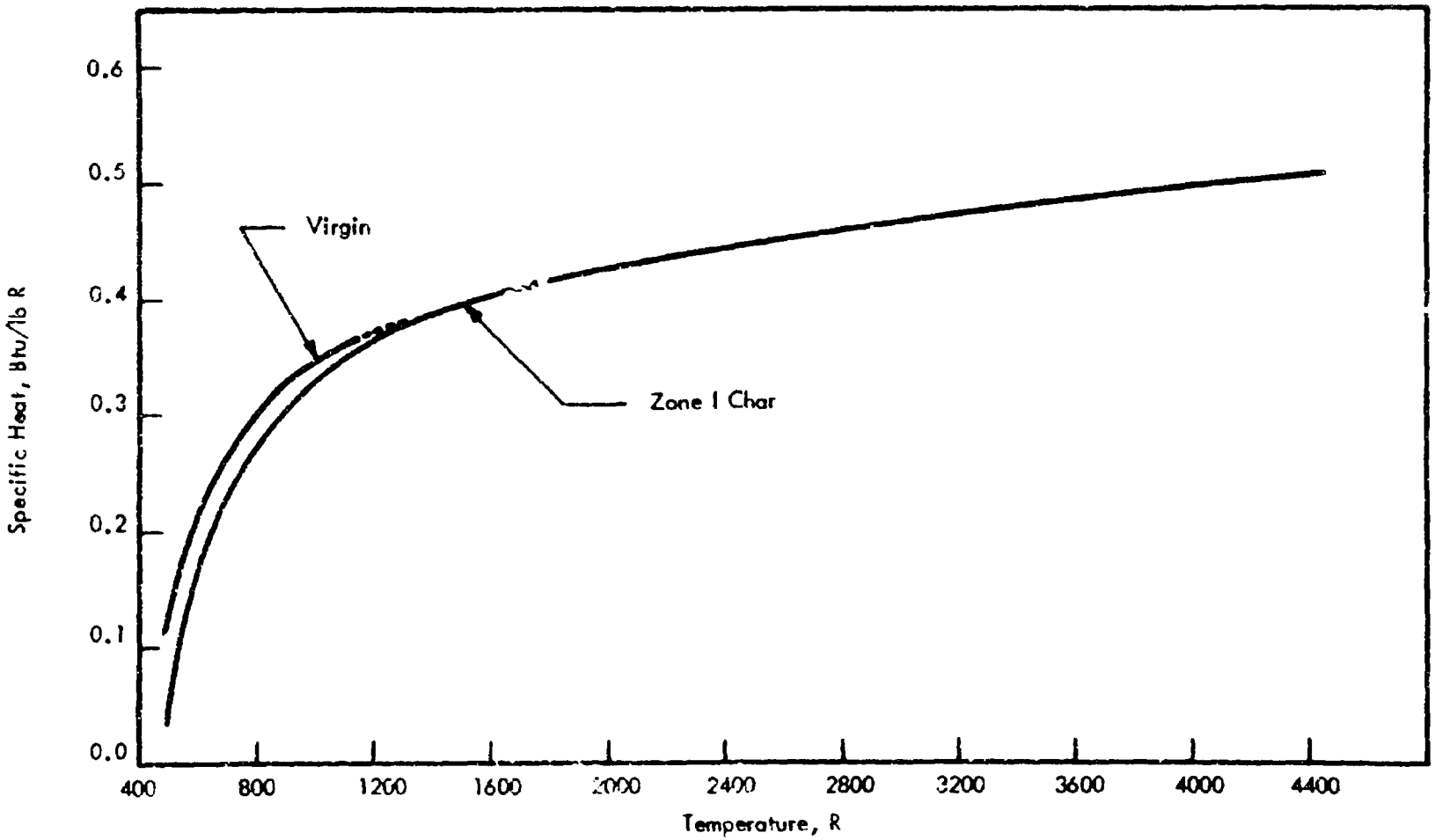

FIGURE 95 COMPOSITE SPECIFIC HEAT CURVES FOR FM-5014 MATERIAL

SECTION XI

THERMAL EXPANSION MEASUREMENTS

THERMAL EXPANSION TEST METHOD

Linear thermal expansion measurements of the MX-4926 and FM-5014 materials in the virgin, zone III char and zone I char states were made by a comparative technique using dilatometers. Zone II chars were not measured. It was assumed that the zone III and zone I chars would represent the extremes in the expansion variations. Two types of dilatometers were used, a low-temperature manual dilatometer for the virgin and zone III materials, and a high-temperature automatic recording dilatometer for the zone I materials.

Low-Temperature Apparatus

Figure 96 shows schematically the vertical, quartz-tube dilatometer used for virgin and zone III specimens. In this dilatometer the total expansion of a specimen being heated is measured by a dial indicator which is graduated in 0.0001-inch divisions and can be read approximately to ±0.00003 inches. A chromel-alumel thermocouple, embedded in the specimen, is used to measure its temperature.

High-Temperature Apparatus

The linear thermal expansion measurements of zone I chars were made in a recording dilatometer, illustrated in Figure 97. The specimen is supported on a graphite structure in the tantalum tube furnace. The relative displacement of the upper and lower platforms due to differential expansion between the specimen and adjacent structure is transmitted through the structure to the linear-variable-differential transformer (LVDT) in the cool zone. A signal from the LVDT proportional to the specimen expansion is displayed on one axis of an X-Y plotter as the specimen is heated, while a signal from a tungsten-rhenium thermocouple, positioned in close proximity to the specimen, is displayed on the other axis of the plotter. The electrical power input to the tube furnace is regulated by a programmed proportional temperature controller to produce a temperature increase and decrease of the specimen at a rate of 6 R per minute. At the higher temperature, the temperature is periodically measured by optical pyrometry through a quartz window in the dilatometer-vessel wall.

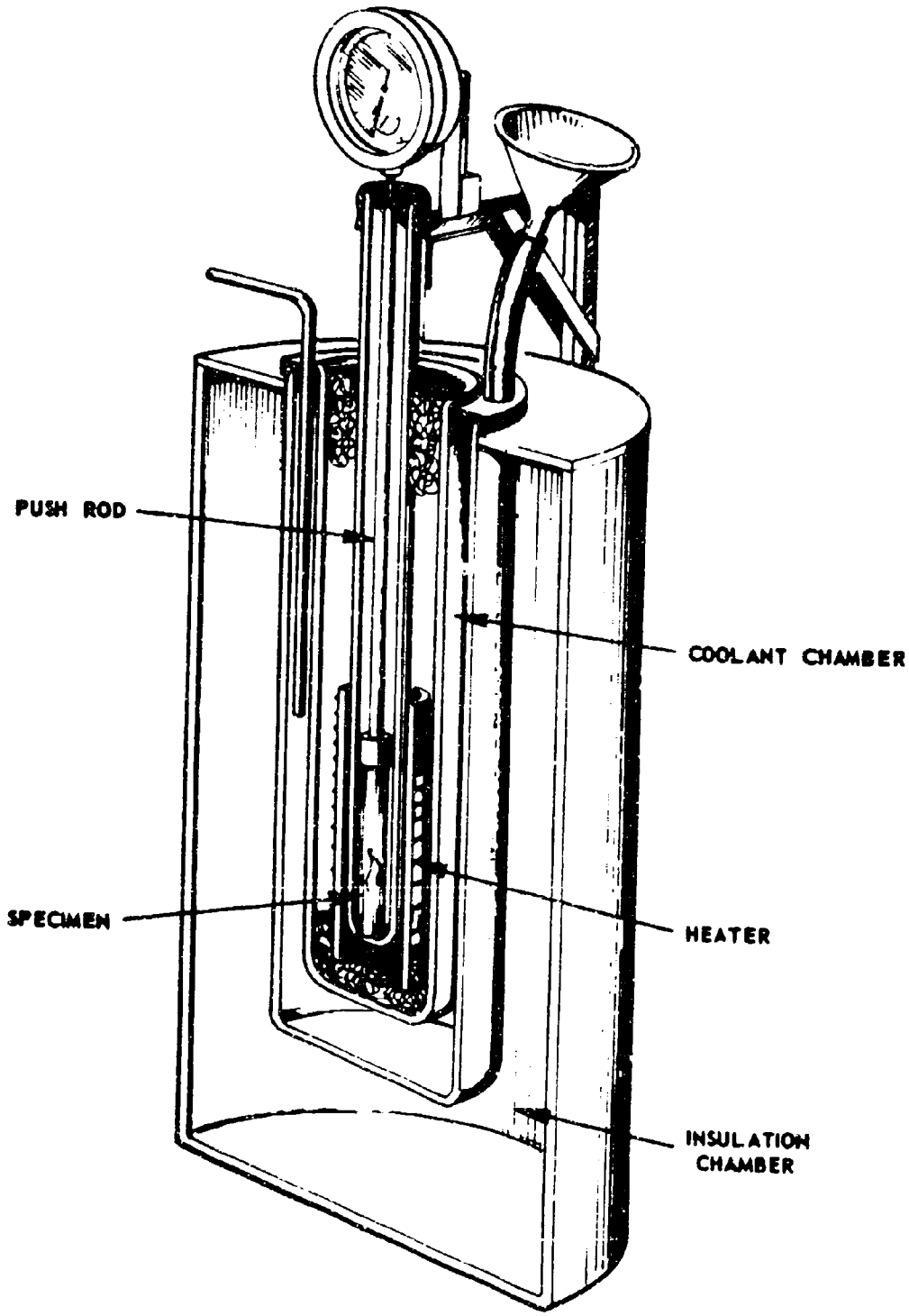

FIGURE 96 LOW-TEMPERATURE DILATOMETER

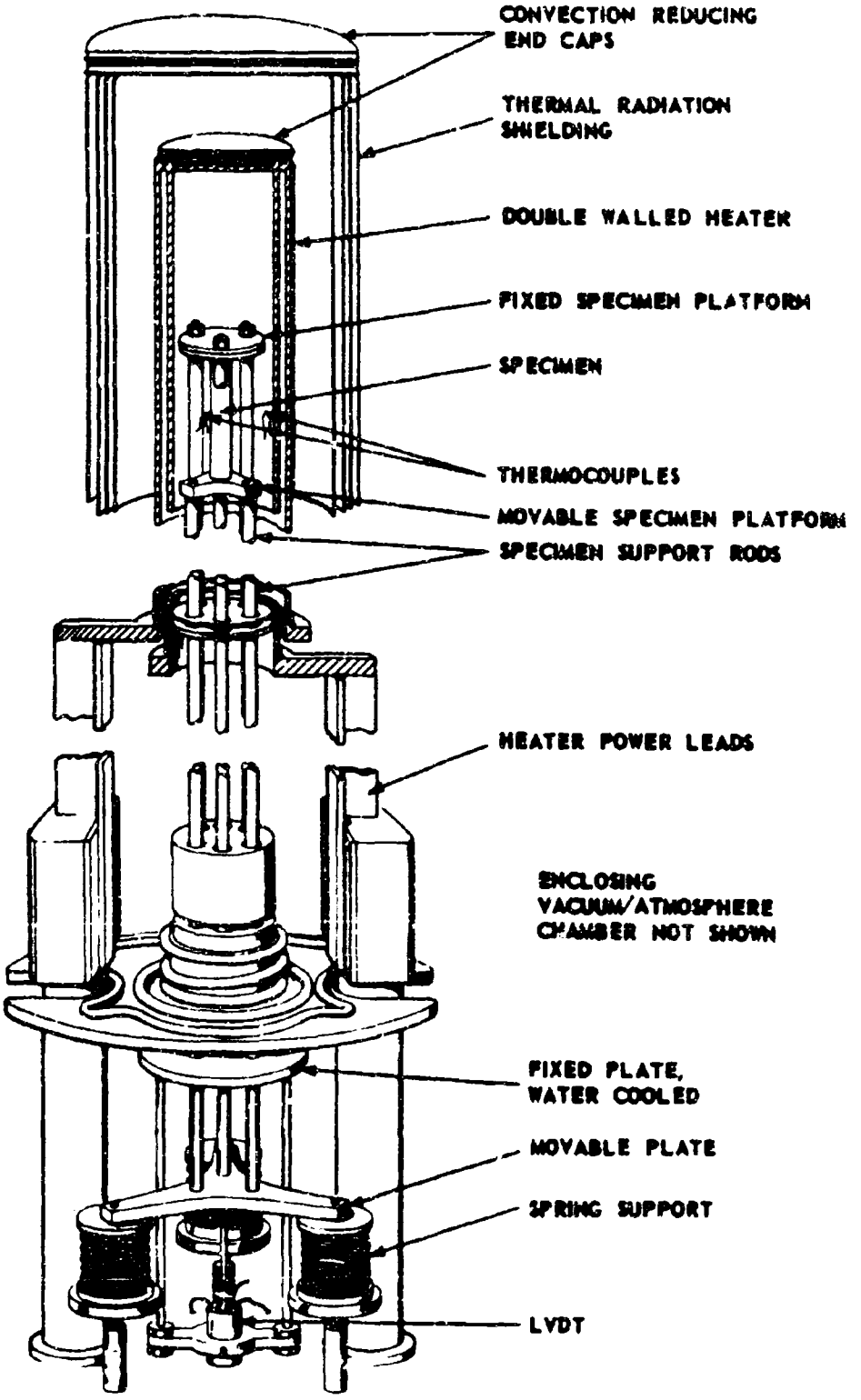

FIGURE 97 HIGH-TEMPERATURE DILATOMETER ASSEMBLY

Test Procedure

The room-temperature density of each specimen was calculated from length, diameter and weight measurements before and after each expansion measurement. The virgin and zone III materials were measured in the low temperature dilatometer in a flowing argon atmosphere. Temperature and dial indicator readings were taken simultaneously during heating and cooling. The specimen heater was regulated manually. The linear expansion-temperature data were corrected for the effect of the quartz structure. Heating and cooling rates were maintained manually at 6 degrees R per minute.

Zone I material was measured in the high-temperature dilatometer under flowing argon after evacuation. The total expansion-temperature data as recorded on the X-Y plotter were corrected for the effect contributed by the graphite structure. This correction is determined through measurements on materials of known thermal expansion. The heating and cooling rates were maintained at 6 degrees per minute throughout the measurements.

THERMAL EXPANSION RESULTS

Measurements were made on laboratory-prepared specimens of virgin, zone III char, and zone I char of both the MX-4926 and FM-5014 materials. In addition, specimens in these zones cut from MX-4926 ablative nozzle component material were measured.

All measurements were made from room temperature to the thermal stability limits for each zone given in section VIII.

For each material specimens having laminations normal and parallel to the long axis (expansion direction) were tested. In addition, a specimen of MX-4926 zone III char having a 45 degree lamination angle was measured. As in the thermal conductivity specimens, the lamination angle in MX-4926 was defined along the bias direction in the uniformly oriented carbon cloth reinforcement and the lamination angle in FM-5014 was established in randomly oriented graphite cloth reinforcement.

Because the resin portion of the specimens has a much greater coefficient of expansion than the reinforcing fabric, the specimens with fabric laminations normal to the long axis had the greater expansion. This was more evident in the virgin and zone III chars than in the zone I chars. Permanent dimensional changes occurred in almost every specimen as a result of the thermal expansion measurements.

MX-4926 Phenolic Carbon

Figures 98 through 106 show the expansion-temperature relations for the MX-4926 specimens.

It is interesting to note the similarity between the virgin and zone III chars. In the nozzle specimens with laminations normal to the axis of the specimen, the shape of the curves are similar. In the zone I chars, both the laboratory char and nozzle char exhibited similar characteristics, Both specimens with parallel laminations exhibited an inflection between 3500 to 3900 R and had a permanent length increase at room temperature. Both specimens with normal laminations had a permanent shrinkage at room temperature.

Difficulty was encountered in obtaining the thermal expansion of MX-4926 char nozzle material (zone III) with the laminations normal to the longitudinal axis, Figure 101 The specimen had to be cut to less than 1/2-inch in length to obtain a sound specimen. The large amount of expansion in the heating portion may have been caused by delamination of the specimen.

An attempt was made to determine the temperature at which MX-4926 zone III char material starts to deform permanently. A step-type heating schedule was used wherein the specimen was heated to 850 R, cooled to 760 R, then heated to 940 R, and back to 850 R, etc., to 1570 R, and then cooled to room temperature. It was anticipated that the point at which the expansion did not double back on itself would be the "elastic limit" of the material. Figure 104 illustrates this heating schedule. The specimen did not double back on itself at any point. By contrast, a stainless steel specimen, of known expansion, was subjected to this same program and did double back on itself over the whole program. Therefore, the effect illustrated in Figure 104 is a characteristic of the material rather than of the apparatus. No mechanism to explain this effect has been found.

Figure 105 shows a specimen of the same material taken adjacent to the first specimen and measured at a normal heating cycle. Figure 106 shows a third specimen measured at a much slower heating rate with 1/2-hour holds at the bottom of the step heating. This change in heating rate did not eliminate the effect observed in Figure 104 .

FM-5014 Phenolic Graphite

Figures 107 through 109 show the expansion-temperature relation for the FM-5014 specimens.

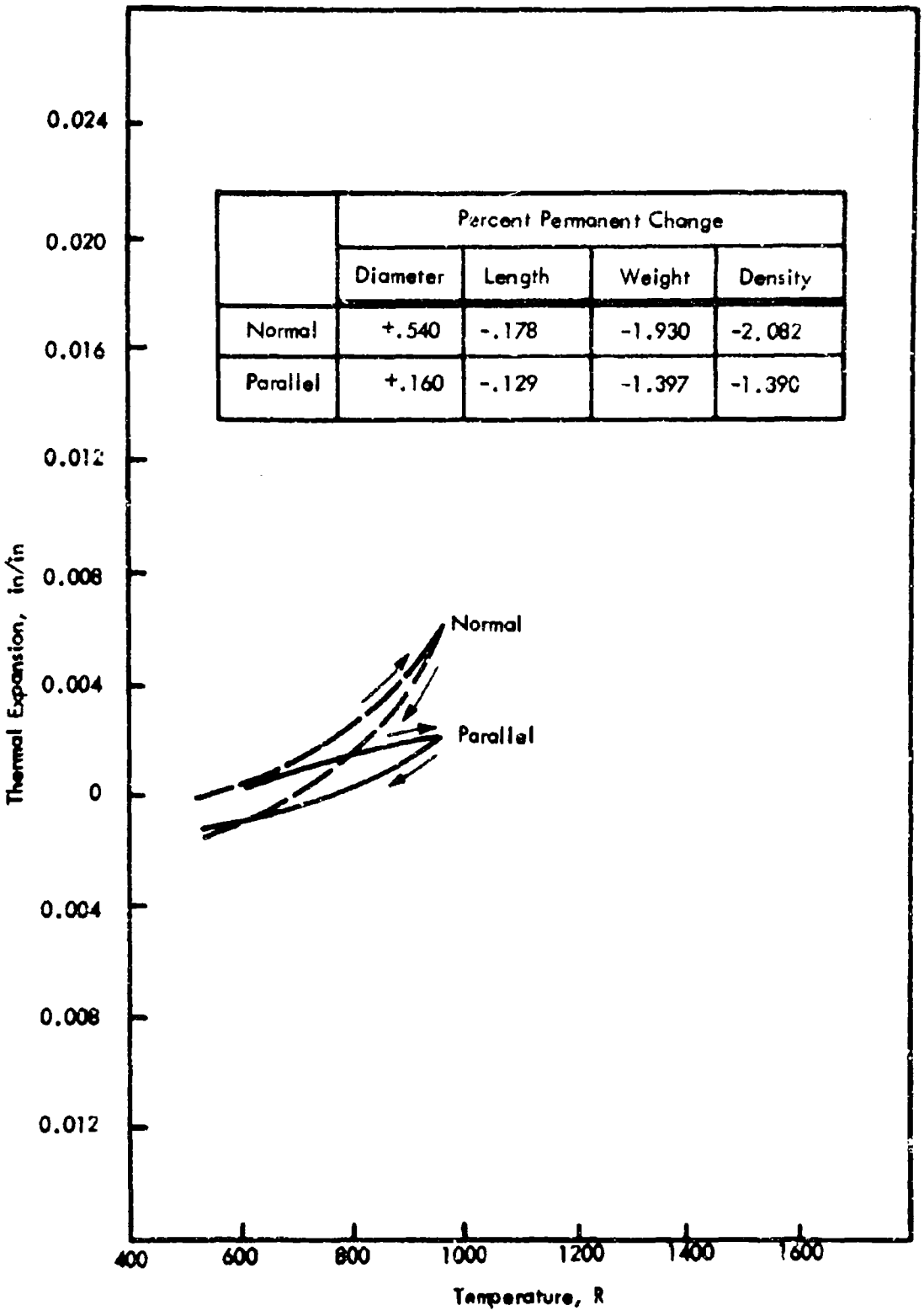

	Percent Permanent Change			
	Diameter	Length	Weight	Density
Normal	+.540	-.178	-1.930	-2.082
Parallel	+.160	-.129	-1.397	-1.390

FIGURE 98. THERMAL EXPANSION OF MX-4926 VIRGIN MATERIAL, NORMAL AND PARALLEL TO LONGITUDINAL AXIS

	Percent Permanent Change			
	Diameter	Length	Weight	Density
Normal	-.110W 0 T	+.077	-1.756	-2.11[illegible]
Parallel	-.077	-.048	-1.690	-2.083

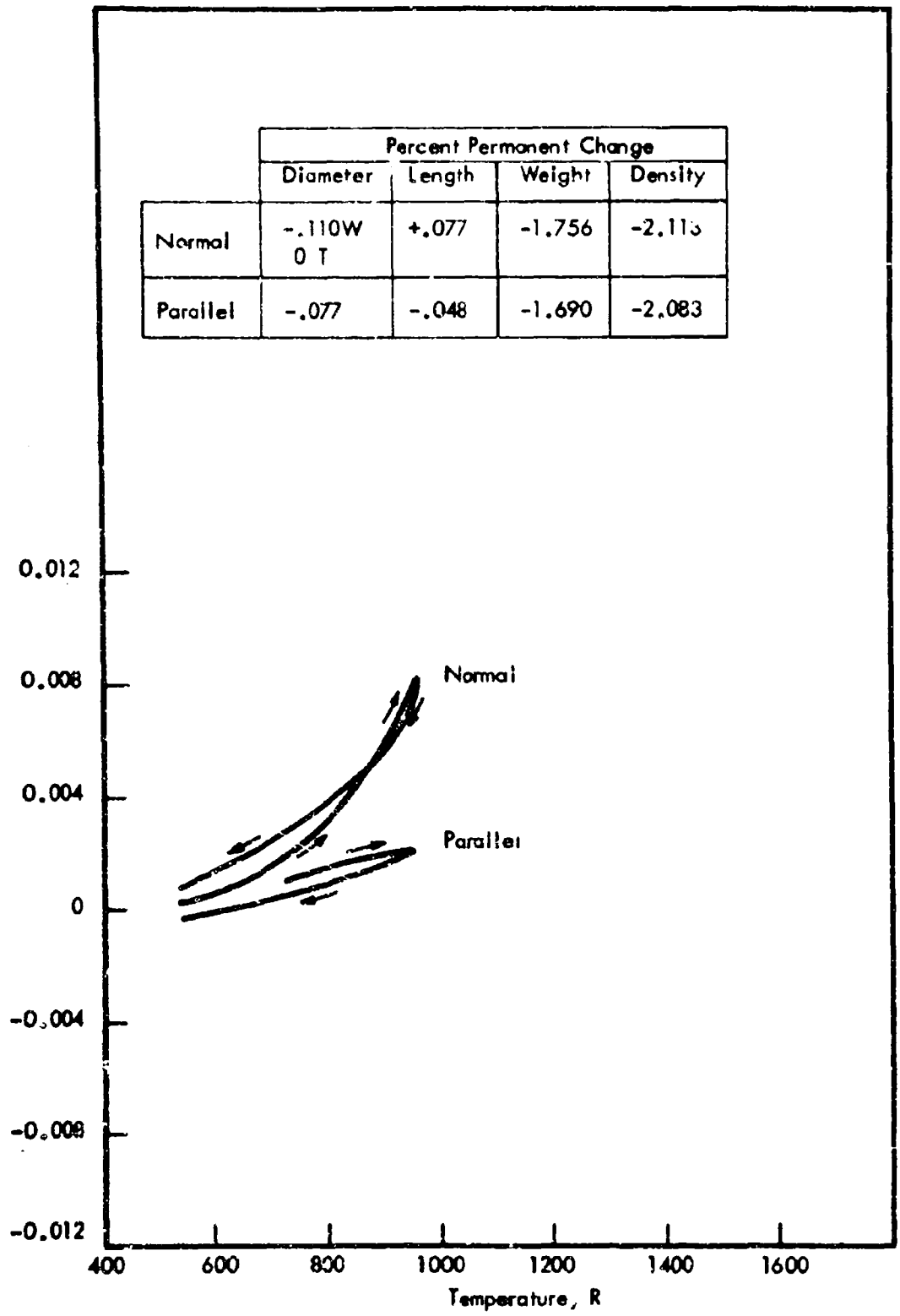

FIGURE 99 THERMAL EXPANSION OF MX-4926 VIRGIN MATERIAL, PARALLEL (NOZZLE "C") AND NORMAL (NOZZLE "D") TO LONGITUDINAL AXIS

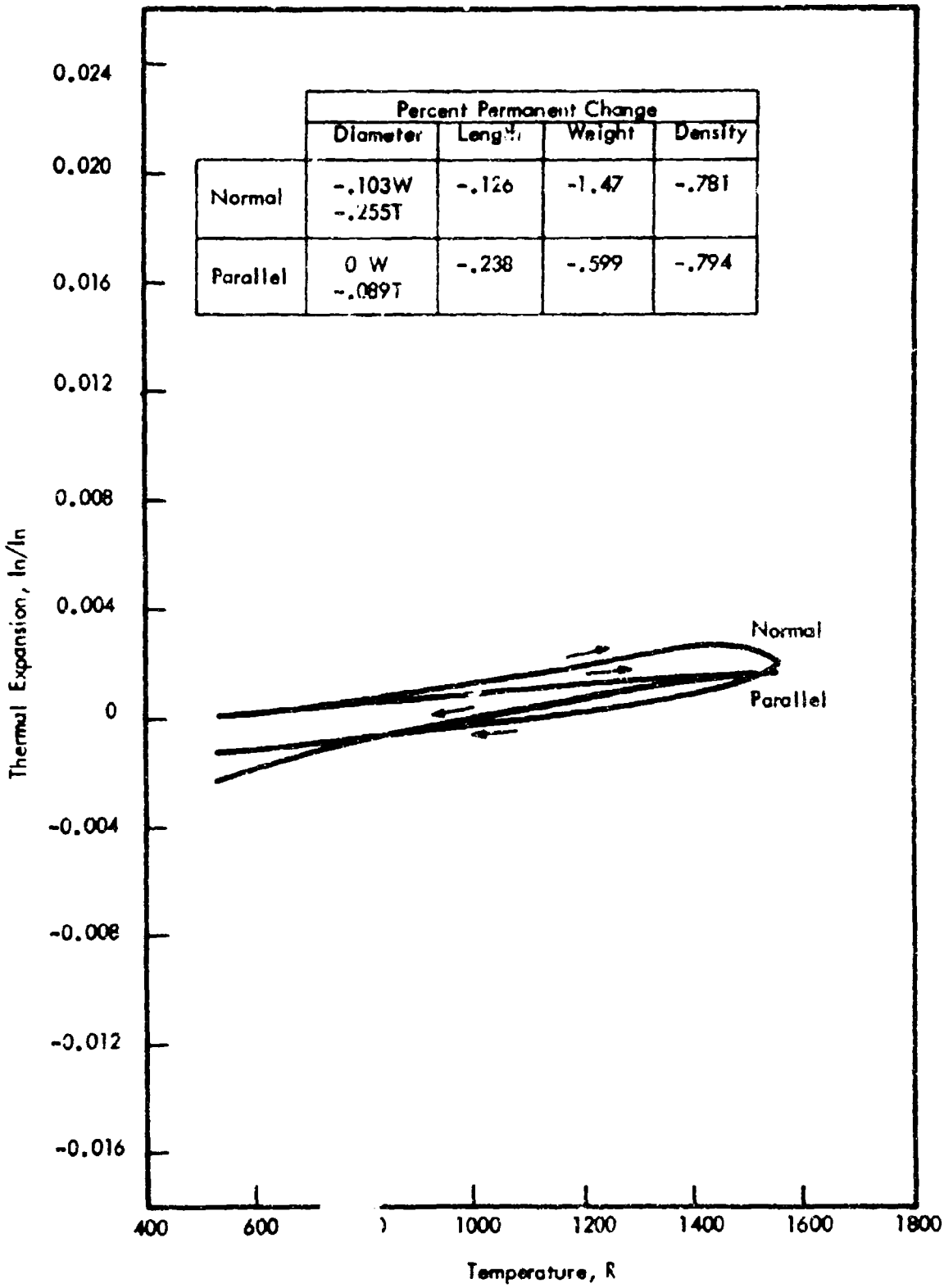

FIGURE 100 THERMAL EXPANSION OF MX-4926 LABORATORY CHAR MATERIAL, (ZONE III), NORMAL AND PARALLEL TO LONGITUDINAL AXIS

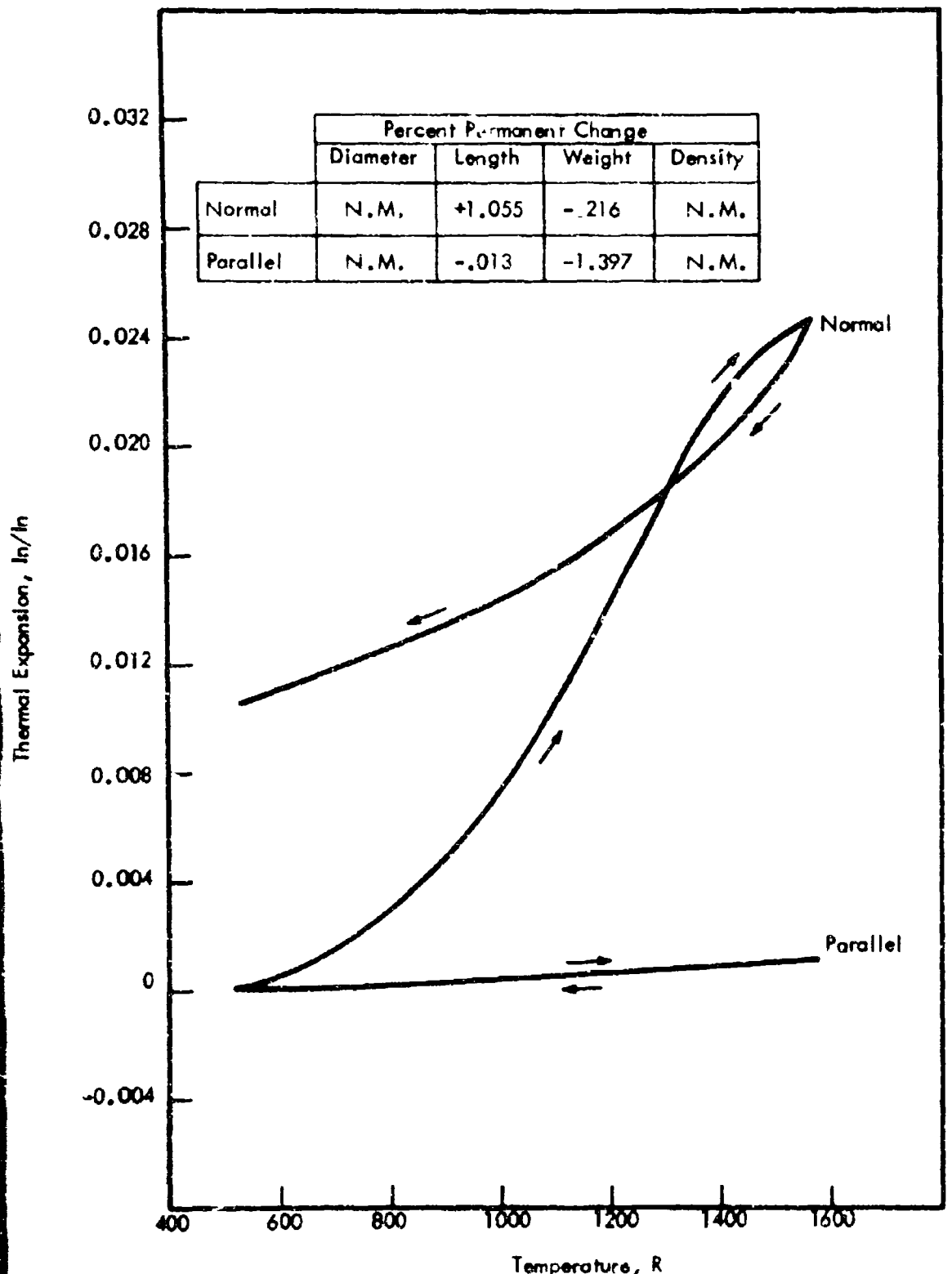

FIGURE 101 THERMAL EXPANSION OF MX-4926 CHAR NOZZLE MATERIAL (ZONE III), NORMAL AND PARALLEL TO LONGITUDINAL AXIS

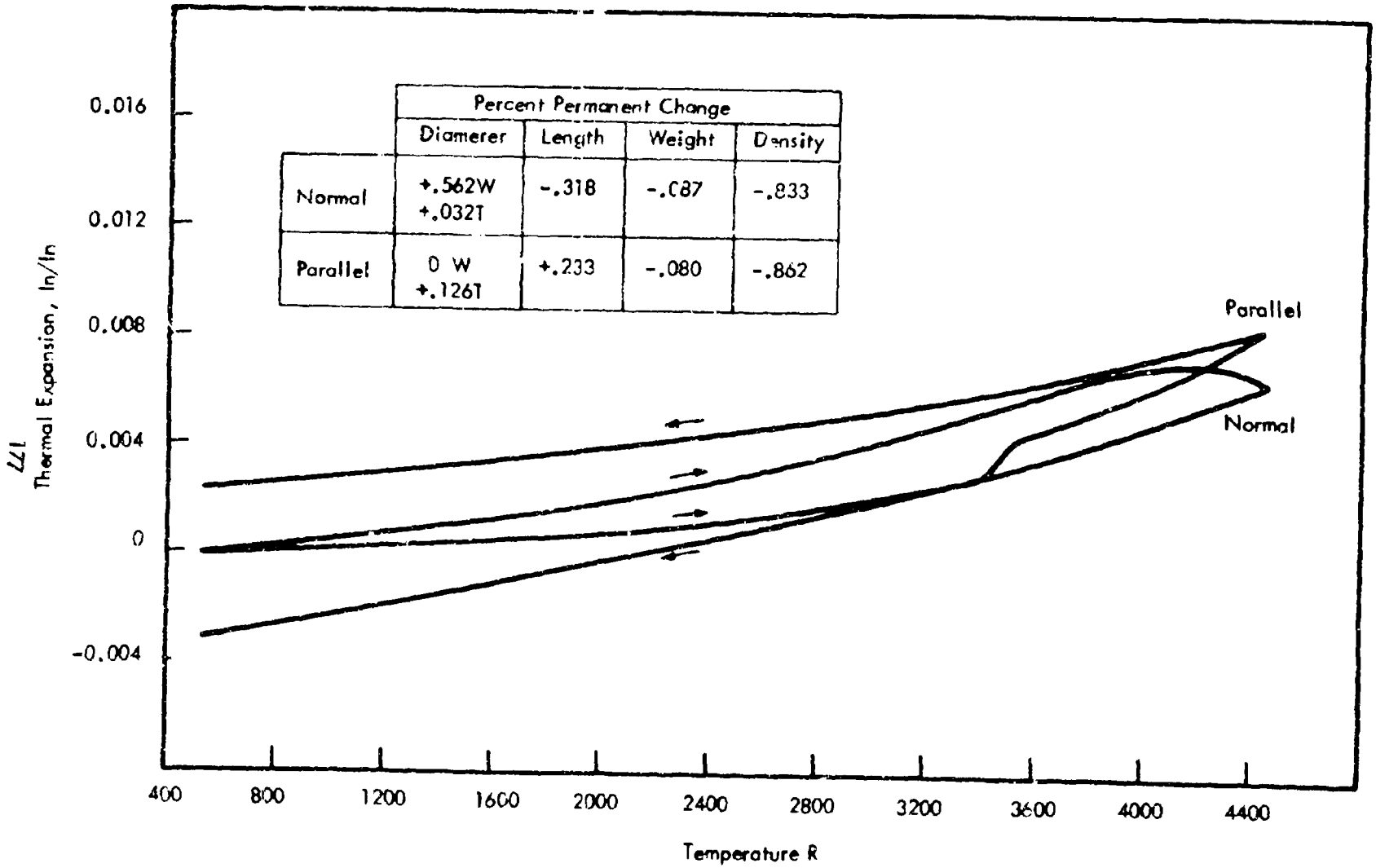

FIGURE 102 THERMAL EXPANSION OF MX-4926 LABORATORY CHAR MATERIAL (ZONE I), NORMAL AND PARALLEL TO LONGITUDINAL AXIS

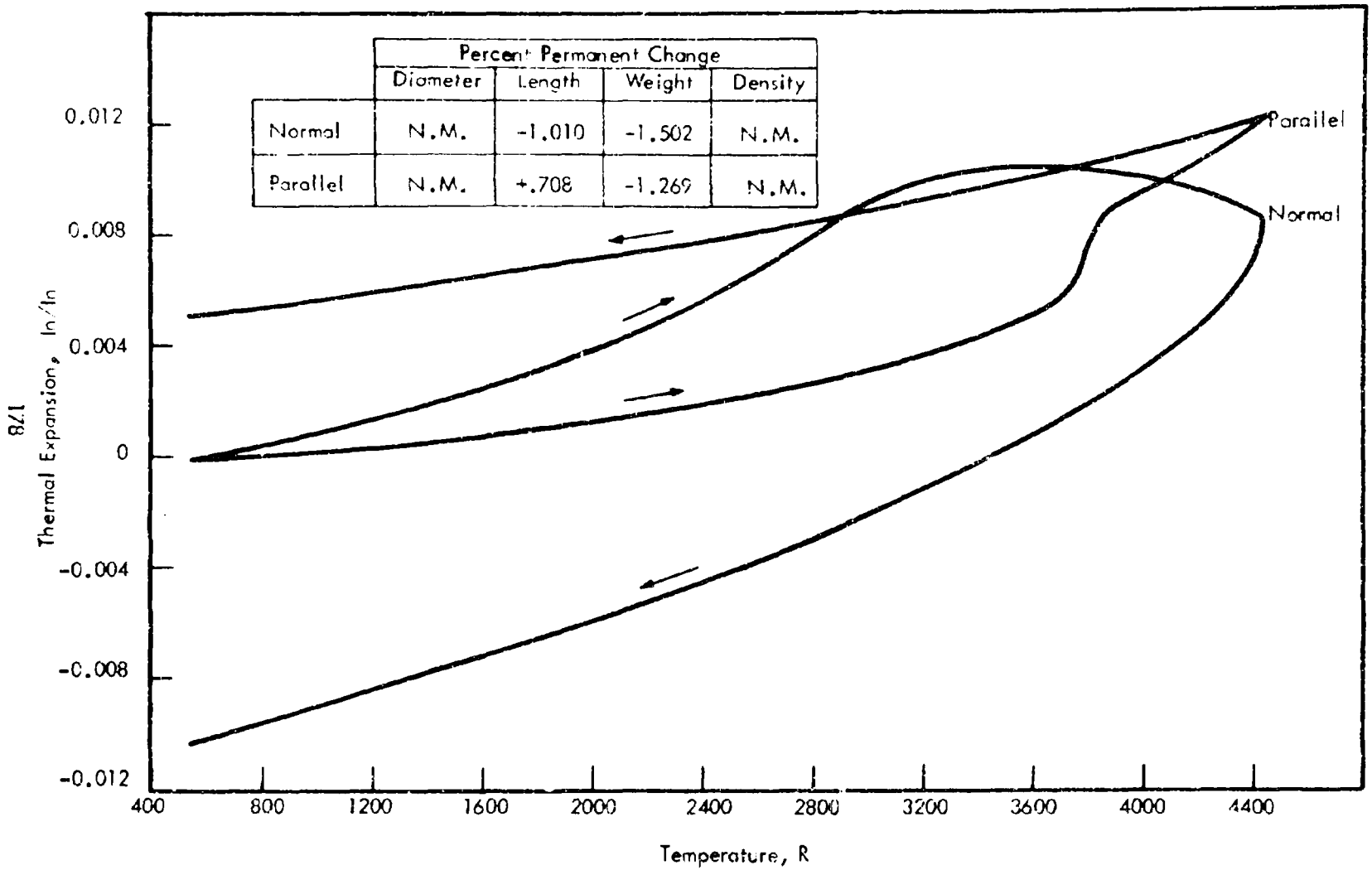

FIGURE 103 THERMAL EXPANSION OF MX-4926 CHAR NOZZLE MATERIAL (ZONE I), NORMAL AND PARALLEL TO LONGITUDINAL AXIS

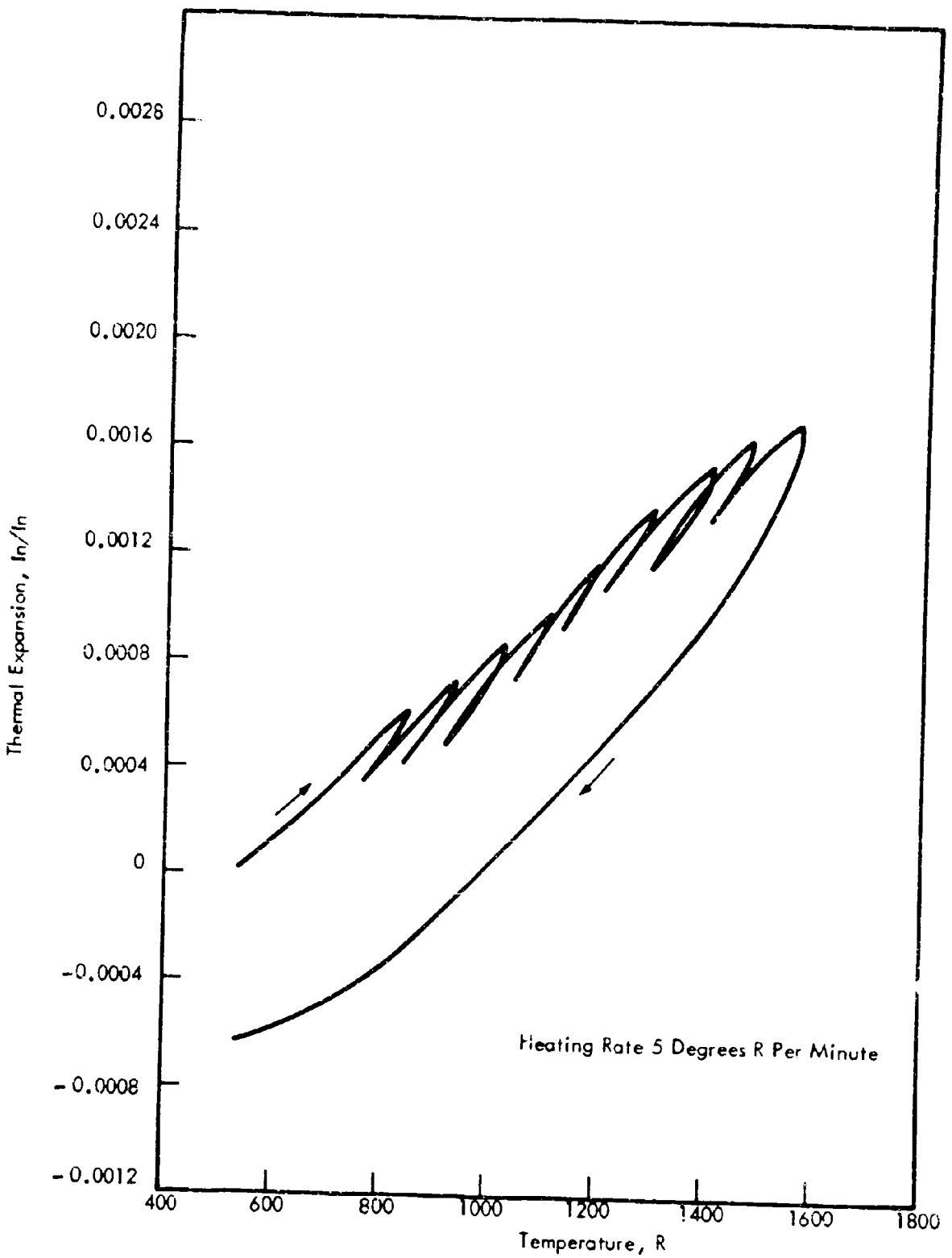

FIGURE 104 THERMAL EXPANSION OF MX-4926 (ZONE III) LABORATORY CHAR, LAMINATIONS 45 DEGREES TO LONG AXIS

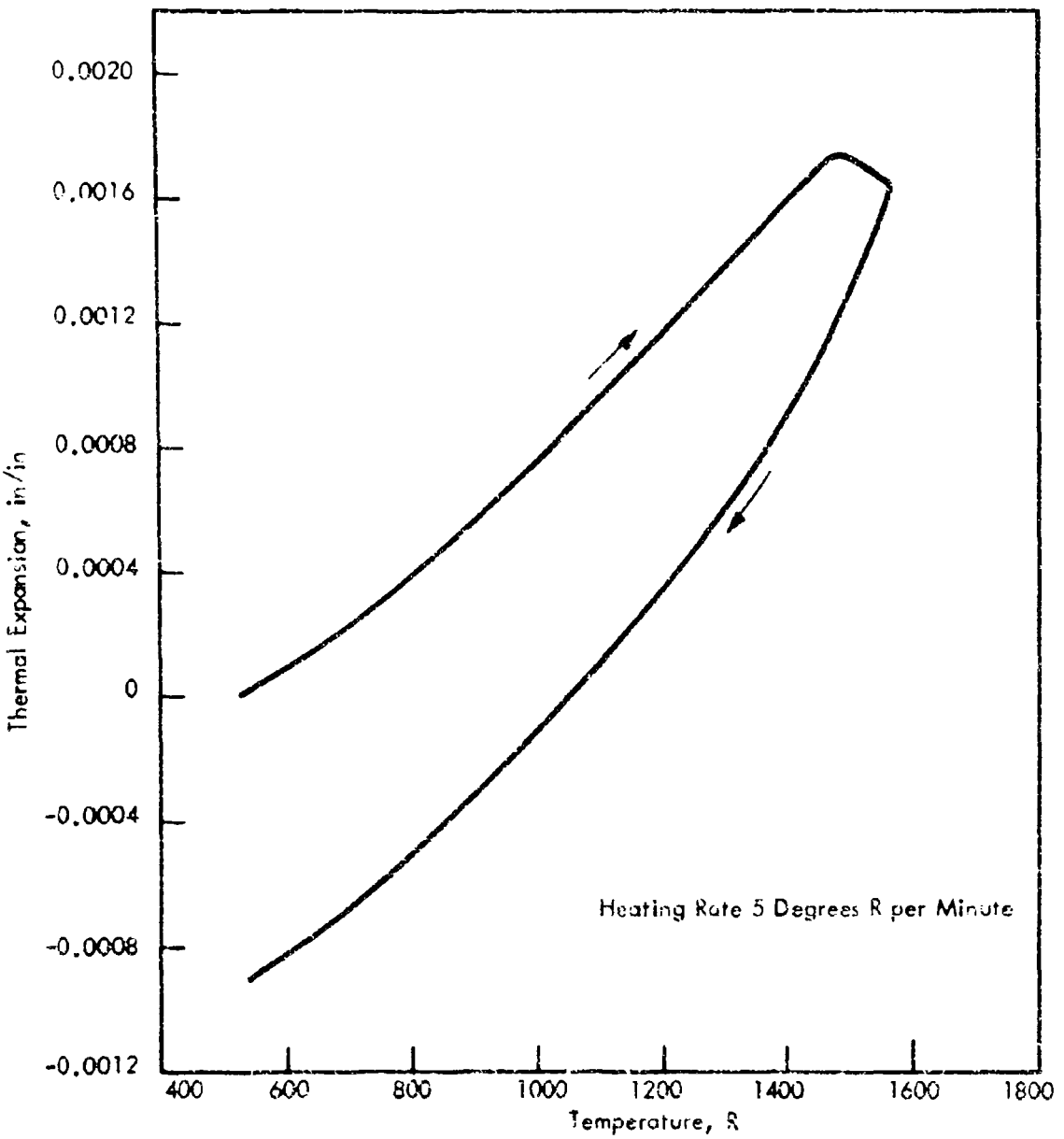

FIGURE 105 THERMAL EXPANSION OF MX-4926 (ZONE III) CHAR, LAMINATIONS 45 DEGREES TO LONG AXIS

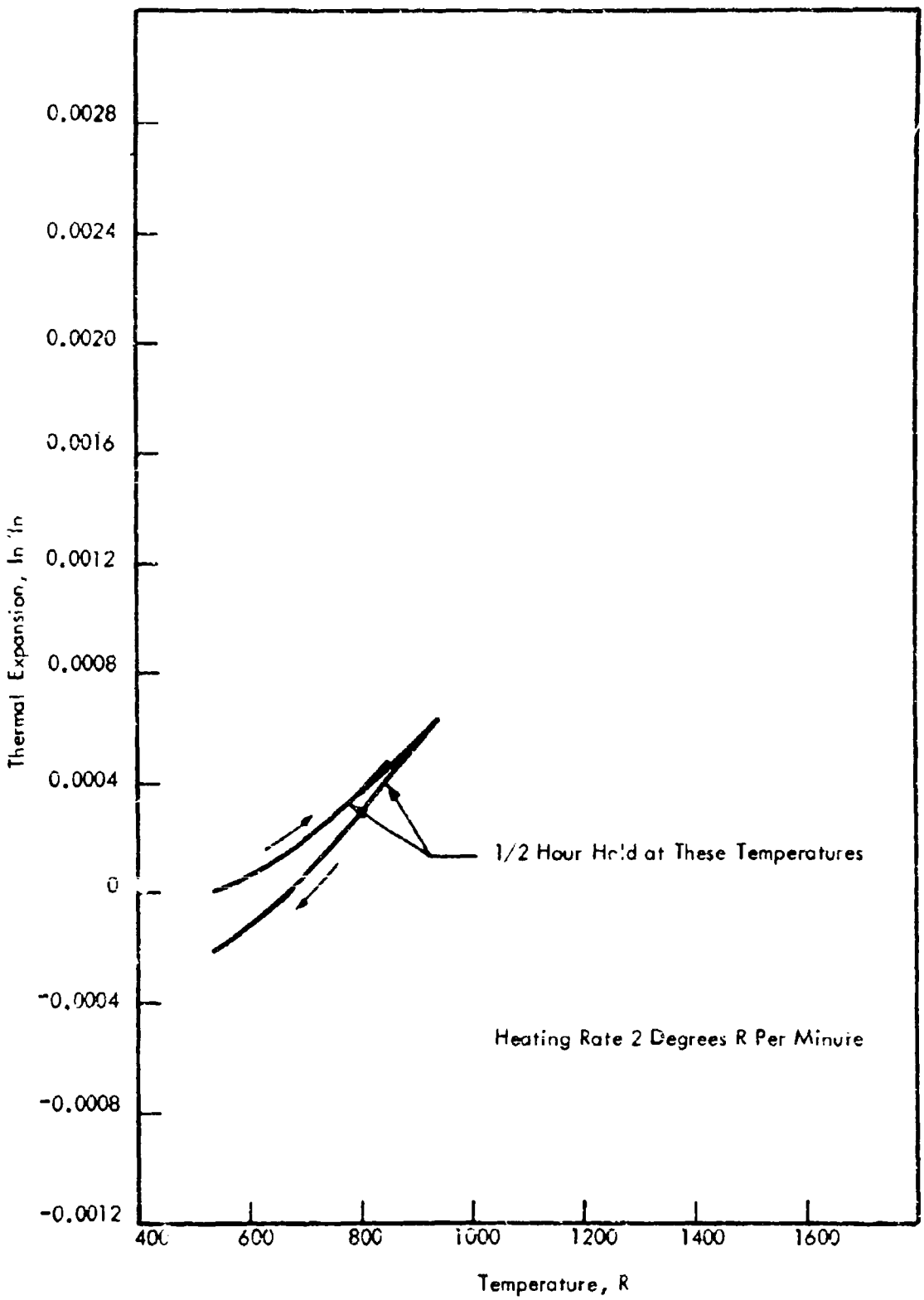

FIGURE 106 THERMAL EXPANSION OF MX-4926 (ZONE III) LABORATORY CHAR MATERIAL, LAMINATIONS 45 DEGREES TO THE LONGITUDINAL AXIS

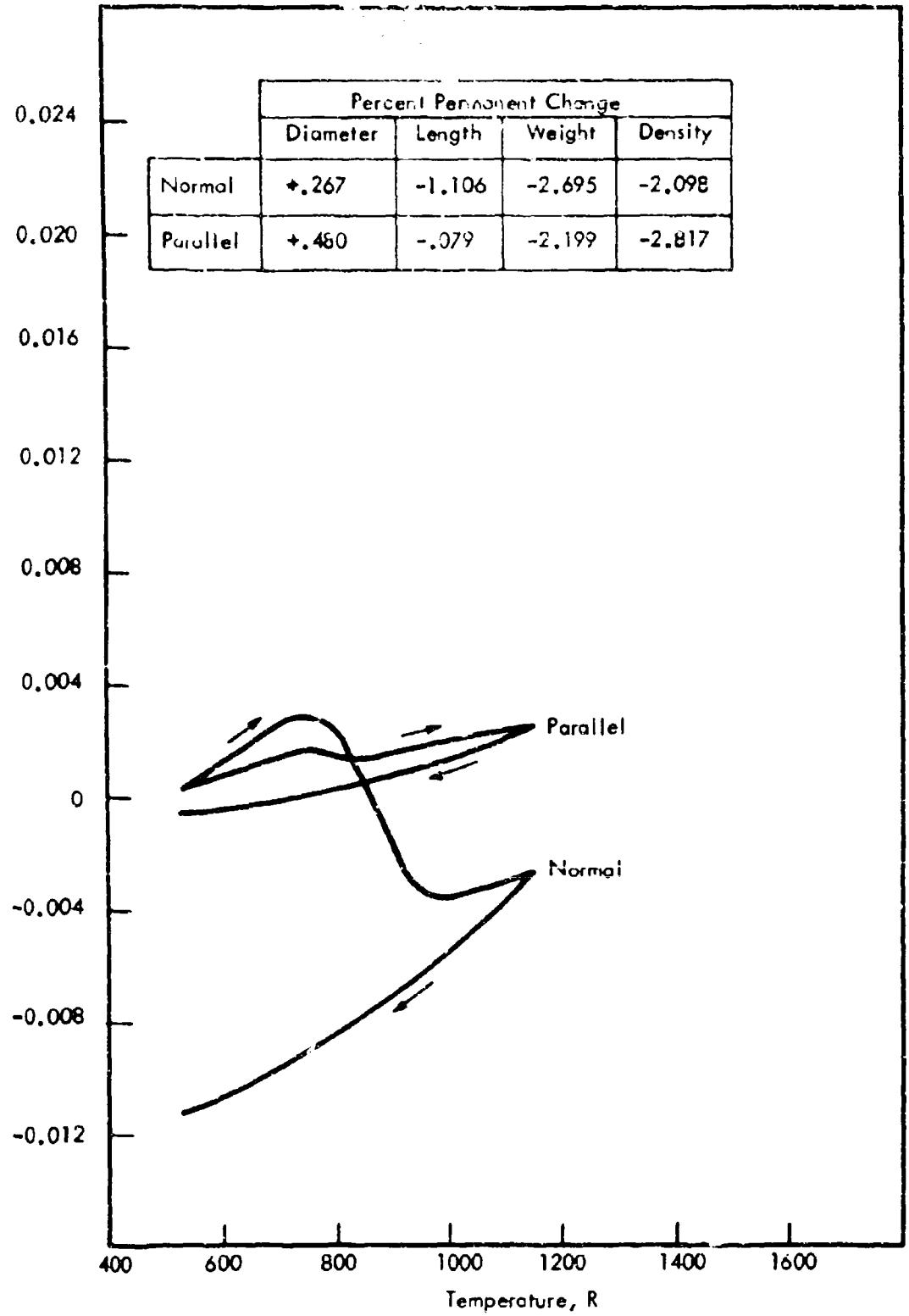

FIGURE 107 THERMAL EXPANSION OF FM-5014 VIRGIN MATERIAL. NORMAL AND PARALLEL TO LONGITUDINAL AXIS

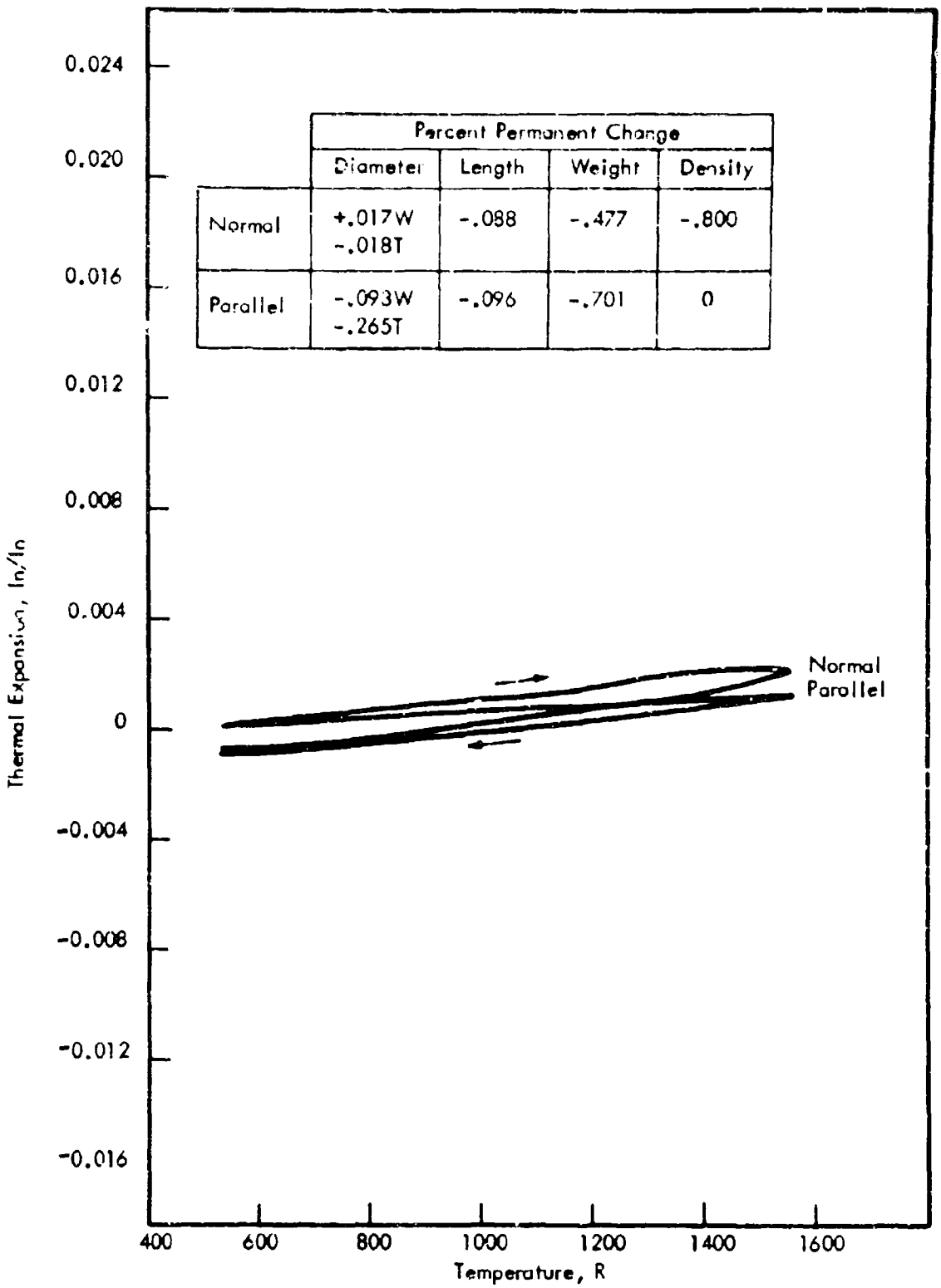

FIGURE 108 THERMAL EXPANSION OF FM-5014 CHAR MATERIAL (ZONE III) NORMAL AND PARALLEL TO LONGITUDINAL AXIS.

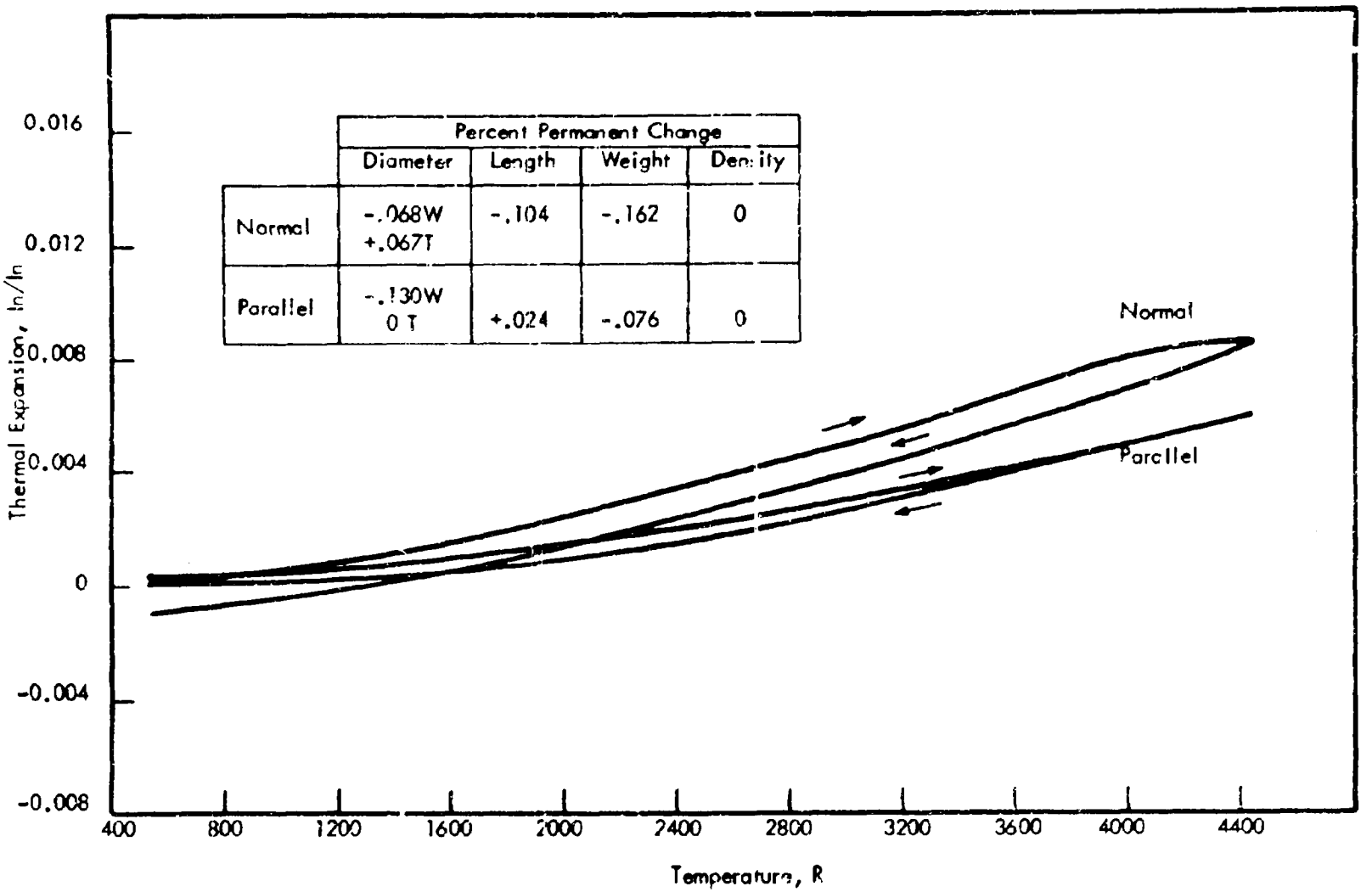

FIGURE 109 THERMAL EXPANSION OF FM-5014 CHAR MATERIAL (ZONE I), NORMAL AND PARALLEL TO LONGITUDINAL AXIS

The virgin specimen having normal laminations had an extremely large shrinkage between 750 and 1000 R. This amount of shrinkage was not exhibited by any of the other virgin materials.

ANALYSIS OF THERMAL EXPANSION RESULTS

Error Analysis

With each series of linear-expansion measurements it is routine practice to make calibration measurements using standard specimens. Type 316 stainless steel and molybdenum specimens are used as standards for the different temperature ranges. Any deviation from the literature values (8) and (9) of these materials is applied to the unknown sample as a correction. The high-temperature dilatometer is calibrated periodically by inserting a precision micrometer barrel in place of the structure and checking this known movement as displayed on the X-Y plotter. The main sources of error are considered to be the temperature measurements and the accuracy of the expansion values for standard materials.

The overall error for the measurement is considered to be less than ± 3 percent.

Data Significance - Combined Thermal Expansion and Pyrolysis Shrinkage

Expansion data is required for computer analysis of stresses during ablation. However, the stresses induced by shrinkage during pyrolysis also must be considered. The magnitude of these shrinkage effects, which tend to offset expansion measurements, is illustrated in the following table.

FURNACE CHARS - AVERAGE PERCENT TOTAL SHRINKAGE

	MX-4926		FM-5055A	
	Perp Lam.	Para. Lam.	Perp. Lam.	Para. Lam.
Zone III	2.9	0.30	2.3	0.22
Zone II	5.5	0.57	3.2	0.33

Since the total pyrolysis shrinkage is more than the total thermal expansion, it is useless to rely on thermal expansion measurements alone in the analyses. Furthermore, the anisotropy of the materials, which is responsible for the difference in expansion between the perpendicular and parallel to the laminate directions, must also be considered in any analysis. Before a meaningful thermal stress analysis can be performed, however, methods of measuring and analytically combining the separate effects of expansion, shrinkage and anisotropy must be developed.

SECTION XII

CONCLUSIONS

A thorough characterization has been accomplished on two post-test chars from 120-inch solid rocket nozzle throats, tape-wrapped MX-4926 phenolic carbon and rosette-molded FM-5014 phenolic graphite, and on one plasma test char representing reentry applications, molded FM-5055A phenolic carbon.

Characterization provided a microstructural and chemical definition of three distinct zones representing major changes occurring in the mature char. These were a "graphitized" zone near the char surface, an "ungraphitized" but fully porous and pyrolyzed intermediate zone, and a third zone containing some residual unpyrolized phenolic, which represented the transition into the pyrolysis zone. These zones and the virgin material precursor were reproduced in the form of large slabs to provide stable specimens for thermophysical property measurements. Thermal conductivity, specific heat and thermal expansion measurements by Battelle Memorial Institute established the variations in these properties to 5000°R expected during active ablation. Char characterization provided a basis for extrapolating from properties measured on stable char analogues to nonequilibrium states existing during active ablation.

Thermal conductivity measurements on both MX-4926 and FM-5014 showed that the values are dependent on porosity generated during pyrolysis, on the amount of "graphitization" of the char, and on the lamination angle relative to the heat flow path. The development of porosity was dependent upon the rate of pyrolysis which is in turn heating rate dependent. "Graphitization" was essentially independent of heating rate and depended upon the maximum temperature attained.

Low layup angles relative to the char surface resulted in lower thermal conductivity in all stages of ablation. As layup angle is decreased, virgin material conductivity decreases, pyrolysis generated porosity lowers conductivity more effectively, and char "graphitization" increases conductivity less.

Equations correlating conductivity with significant material changes during ablation were established and used to develop generalized conductivity data and a method of extrapolation of conductivity to various temperatures for other ablation applications. Because pyrolysis rates affect development of porosity quite markedly, the conductivity versus temperature relationship varies for each heating rate experienced by the pyrolysis zone. Pyrolysis generated porosity irreversibly decreases conductivity, so conductivity versus temperature in the pyrolysis zone during cooling or reheating periods is lower than for initial heating. Due to irreversible "graphitization" effects, conductivity versus temperature relationships applicable to cooling or reheating periods in the mature char are also different than for initial heating. Each level of pyrolysis or "graphitization" gives an indivual conductivity curve applicable to these periods.

Specific heats of samples taken from the nozzle chars and of samples of furnace reproduced chars were in good agreement and values for the virgin material were higher than "graphitized" mature char at low temperatures. Char specific heats were similar to those of graphite. Third order equations for enthalpy and specific heat as a function of temperature for both virgin and charred material were established for use in computer predictions of ablation performance. Averaging the small differences between virgin and char values through the pyrolysis zone will account for all pyrolysis rate effects.

All thermal expansion results of either nozzle or furnace chars showed large, permanent dimensional changes regardless of the maximum test temperature. No general correlation of expansion data applicable to active ablation was possible. The tendency for phenolic laminates to shrink in a direction normal to the laminates during pyrolysis causes greater dimensional change on unrestrained material than does thermal expansion.

SECTION XIII

RECOMMENDATIONS

1. Thermophysical properties of refractory fiber reinforced ablative chars above 5000°R should be determined by extension of the techniques developed on this program to ascertain the significance of additional transport mechanisms and the effect of the large temperature gradients occurring in ablation.

2. Characterization and thermophysical property measurements on char analogues should be conducted for an actual phenolic-carbon reentry char to evaluate the effect of additional "graphitization" noted on FM-5055A plasmo test chars simulating reentry

3. The techniques developed on this program should be applied on material representing variations in a given type such as phenolic-carbon to establish data for performance trade studies between types and provide guidance for improvement of ablator insulating effectiveness.

4. Thermal conductivity should be measured for more levels of porosity and "graphitization" to reduce the extrapolation required to account for the effects of these changes during ablation.

5. Methods should be developed to measure both pyrolysis shrinkage and thermal expansion in reinforced phenolic ablators to enable analysis of thermally induced strains during ablation.

6. Characterization and thermophysical property measurements should be conducted on other ablators, particularly the widely-used phenolic silica type where porosity effects may be greater due to low reinforcement conductivity.

APPENDIX A

DETAILS OF ERROR ANALYSIS FOR THERMAL CONDUCTIVITY MEASUREMENTS

The estimates of accuracy and precision of the thermal conductivity data were obtained from the results of two separate experiments designed to indicate the accumulated effects of all sources of experimental error on the measured thermal conductivity values. The accuracy and precision of the data were determined by the uncertainties associated with thermocouple calibration, thermocouple bead location, heat-meter calibration, and measurement technique. The latter includes many factors, such as the effects of radial heat fluxes in the anisotropic specimens, thermal resistance elements, and the heat-flow meter on the measured conductivity value; the effects associated with variations in thermocouple-specimen thermal bonds due to inhomogeneity of specimen material, heater-power fluctuations, and possible thermocouple deterioration due to environmental factors. Many of these sources of error interact and so are correlated in the error experiments. For this reason, the experimental approach to error estimation is considered realistic.

The error experiments were performed on one 0-degree and one 90-degree lamination specimens. When the errors for these extreme cases were determined, errors for the specimens with lamination angles between these two extremes could be inferred.

For studies relating to 0-degree lamination specimens, an experiment was performed on specimen PC-11-0. This specimen was measured under a range of conditions which produced variations in measured thermal conductivity due to the accumulated sources of error mentioned above. The range of boundary conditions was extreme enough that measurements on any other 0-degree lamination specimen would have a high probability of falling within this range.

To investigate the possibility of radial heat flow, specimen PC-11-0 was instrumented with two radial thermocouples in addition to the three used in the calculation of the thermal conductivity of the specimen. These were placed at distances of approximately 3/4 inch and 1 inch from the center of the specimen, and at approximately its midplane. Also, a thermocouple was cemented with graphite-base cement to the 1/4-inch thick layer of carbon felt insulation which was placed around the curved surface of the specimen. This was also at about the midplane of the specimen, and gave a measure of temperature of the carbon felt insulation relative to the specimen temperature during the measurements.

Several measurements of conductivity were made on this specimen at approximately the same average specimen temperature, but with varying temperature differences across the flat faces of the specimen. The flat-face temperature differences were varied by changing the thermal resistance between specimen and heat meter, done by varying the number of woven graphite cloth pads placed there. The reduced data for

all data points appear in Figure A-1 and in Table A-1. The table is ordered in positively increasing temperature differences between the one-inch radial thermocouple, T_1, and the insulation thermocouple, T_I, because the radial heat flux is proportional to this quantity. In the 0-degree specimens, radial heat flow should have been nearly symmetric about the centerline of the specimen.

The temperature differences between the one-inch radial thermocouple, T_1, and the insulation temperature, T_I, correlated well with the difference between the average specimen temperature, T_A, and the insulation temperature, as seen in Table A-1; both the temperature differences, $(T_A - T_I)$ and $(T_1 - T_I)$, indicated the same direction for the radial heat flux in all cases. The column labeled $q_{(S-I)}$' refers to the direction of radial heat flow as indicated by these two temperature differences; minus indicates heat flow from the insulation to the specimen, plus indicates heat flow from the specimen to the insulation. (It should be noted that the curve for the data of Figure 67 was weighted toward those points where $q_{(S-I)}$ was indicated to be near zero.)

Also listed in Table A-1 for each equilibrium are the number of graphite pads used as thermal resistance units in the experiment, an increasing number of pads giving increasing thermal resistance between the specimen and heat-flow meter, and thus a smaller temperature difference across the specimen. The temperature difference, ΔT, across the specimen is listed in the last column. Arrows are drawn between those values of ΔT which were obtained at approximately the same average specimen temperature. Comparison of the two sets of data so indicated shows that $q_{(S-I)}$ changed from minus to plus as ΔT was changed at the fixed value of T_A. The data at $T_A \approx$ 1875 R were the most complete since $q_{(S-I)}$ changed from minus, to near zero, to plus in this case. The two cases indicated by the two sets of arrows probably represent the extreme in heat flow patterns experienced by the 0-degree lamination specimens. In the cases where $q_{(S-I)}$ is minus, the temperature difference across the specimen was also large in relation to the cases where $q_{(S-I)}$ was positive for the same average specimen temperature. This, together with the fact that $q_{(3/4-1)}$ was always positive, indicates that in the cases of large ΔT's at the lower values of T_A, the high temperature portion of the specimen was hotter, or as hot, as the insulation and lost heat to it, whereas the lower temperature portion of the specimen was heated by heat flowing from the insulation. In the cases of larger thermal resistance between specimen and meter, ΔT across the specimen was smaller, the specimen tended to be at a higher temperature than the insulation, and heat flowed from the specimen to the insulation along its entire thickness.

Figure A-1 shows the data obtained for specimen PC-11-0 along with the temperature differences across the specimen experienced at each equilibrium. The accuracy in the thermal conductivity values for the 0-degree specimens is based on the variation of conductivity shown in this figure at 1875 R. It is considered that this variation in conductivity with boundary conditions represents the worst case experienced in zones II and I by the 0-degree specimens. Also, the variations in conductivity in this case

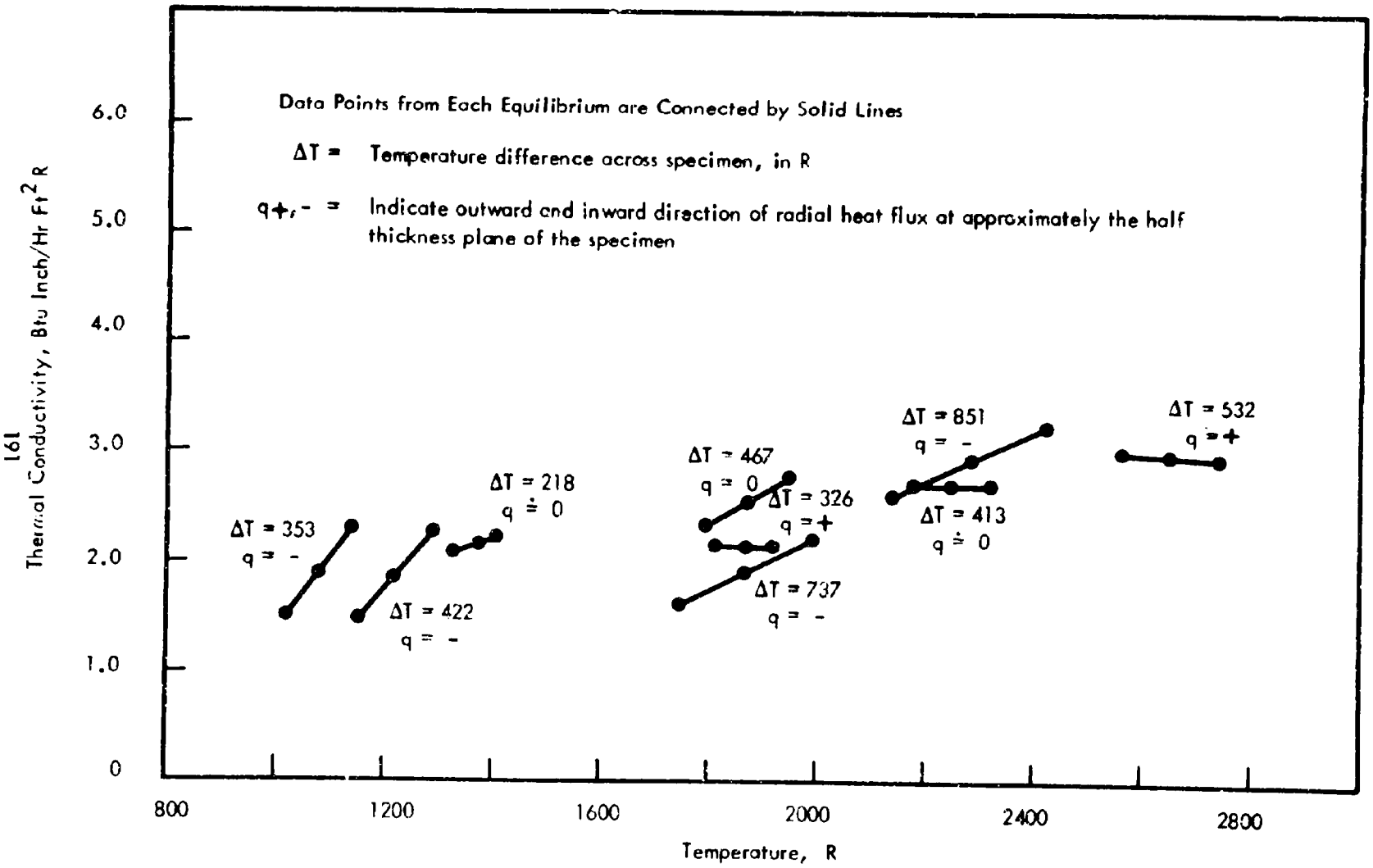

FIGURE A-1 EFFECT OF RADIAL HEAT FLUXES ON THE THERMAL CONDUCTIVITY OF SPECIMEN PC-11-0 (MX-4926)

TABLE A-1 PERTINENT INFORMATION ON THE ERROR DETERMINATION EXPERIMENT PERFORMED ON SPECIMEN PC-11-0

N	T_1-T_1	T_A-T_1	T_A	$T_{3/4}-T_1$	$T_{3/4}-T_1$	$q_{3/4-1}$	q_{S-1}	ΔT
1	-82.4	-87.6	1390	+48.2	-34.2	+	-	737
1	-62.6	-51.2	1809	+37.5	-25.2	+	-	851
1	-47.9	-69.4	604	+30.1	-17.8	+	-	353
1	-45.5	-72.3	740	+26.5	-19.0	+	-	422
10	-9.9	+24.7	913	~	~	~	0	218
5	-6.8	+14.2	1415	+27.9	+21.0	+	0	467
10	+1.1	+37.6	1800	+27.2	+26.1	+	0	413
10	+2.3	+33.1	1410	~	~	~	+	326
10	+7.6	+61.1	2210	+17.1	+24.6	+	+	532

N — The number of graphite pads placed between the specimen and heat meter. This determined the thermal resistance and therefore, the temperature difference obtained across the specimen.

T_1 & $T_{3/4}$ — The temperature at one-inch and 3/4-inch distances from the center of the specimen at approximately the midplane of the specimen. All temperatures in degrees R.

T_1 — The temperature at approximately the midplane of the specimen of the carbon felt insulation surrounding the curved surface of the specimen.

T_A — The average temperature of the specimen as calculated from the hot and cold flat surface temperatures which were obtained by extrapolation from the three central specimen thermocouples.

$q_{3/4-1}$ — Indicates the direction of radial heat flow at approximately the midplane of the specimen as given by $(T_{3/4}-T_1)$. Plus indicates heat flow outward from the central test volume of the specimen.

q_{S-1} — Indicates the direction of radial heat flow at approximately the midplane of the specimen as given by (T_1-T_1). Plus indicates heat flow from the specimen to the surrounding insulation, zero indicates near zero radial heat flow, minus indicates heat flow from the insulation into the specimen.

ΔT — The temperature difference between the hot and cold flat surface of the specimen at the particular equilibrium.

include the accumulated uncertainties in specimen thermocouple calibration, thermocouple bead location, radial heat flux effects, heater-power fluctuations, possible thermocouple changes and the uncertainty related to the heat-meter function of determining the value of the heat flux through the test volume of the specimen.

To calculate the mean deviation of the thermal conductivities at the temperature of 1875 R, Figure A-1 was used to obtain the necessary conductivity values. Using K = 2.55 for the $\Delta T = 467$ equilibrium, K = 2.15 for $\Delta T = 326$, and K = 1.90 for $\Delta T = 737$, the mean value for K at 1875 R is 2.20. The largest deviations within the three conductivity values from this mean value are plus 13.6 and minus 15.9 percent. The uncertainty in the thermal conductivity for the 0-degree lamination specimens of both materials for zone II and I are thus taken to be ±16 percent.

For the virgin and zone III, 0-degree lamination specimens, time in the program did not permit experiments of the type described above. However, because a conduction heater was used for measurement of these zones rather than the radiation type heater as used in zones II and I, and the lower temperatures required in virgin and zone III measurements, several of the problems encountered in the high-temperature measurements simply did not arise in the lower-temperature zones. Less conduction of heat along thermocouple assemblies, more predictable insulation temperatures relative to the specimen temperatures, more reliable, easily handled chromel-alumel thermocouples, and other similar factors all contribute to increasing the accuracy of the virgin and zone III thermal conductivity measurements over that attained for the zone II and I measurements. For these reasons, an overall uncertainty of ±8 percent is assigned to the thermal conductivity data for the 0-degree lamination specimens of both materials for zones III and virgin.

An experiment similar to that performed on specimen PC-11-0 was planned for specimen PC-11-90. For reasons described in Appendix D, "Thermal Conductivity Data Scatter and Adjustments", the anisotropy of the 90-degree lamination specimens gave rise to more uncertainty in the values of measured thermal conductivity than was the case for the more symmetric, 0-degree lamination specimens.

A specimen, PC-11-90, was instrumented to indicate the asymmetrical heat flow pattern developed during measurement*. The planned variations in thermal resistance between the specimen and heat meter to note the effect on the measured value of thermal conductivity were not totally successful due to data scatter introduced by specimen anisotropy. For the error estimation of the thermal conductivity for the 90-degree lamination specimens, the results of Table D-1 are relied upon to indicate some of the cause for uncertainty, but the error estimate itself must be made on the basis of experience with, and degree of confidence in, the measurement technique. Accordingly, it is considered that the data presented for the 90-degree lamination

- - - - - - - - - -

*Table D-1 gives the results of the measurements which are discussed in Appendix D in some detail.

specimens in zones II and I for the FM-5014 material, PG-II-90 and PG-I-90, have an uncertainty of ±20 percent. In the case of the 90-degree, zone II and I, MX-4926 specimens, an additional uncertainty was added to compensate for difficulties in obtaining consistent heat-flow meter readings late in the program. For these two materials, PC-II-90 and PC-I-90, an uncertainty of ±25 percent is considered appropriate.

For the same reasons as given above for the 0-degree lamination specimens, the uncertainty in reported thermal conductivity curves for both materials in the virgin and zone III specimens is less than in the zone II and I specimens. For the 90-degree lamination specimens of both materials for zones III and virgin, an overall uncertainty of ±15 percent is assigned.

The accuracy and precision of the thermal conductivity measurements for the specimens with lamination angles between 0 and 90 degrees will be between the limits established for the 0- and 90-degree specimens. Since severe anisotropic effects begin for any angle other than 0, a linear interpolation with lamination angle between the extreme values is not appropriate. However, relying on observed data scatter, it is safe to say that the 20-degree specimens lie closer to the 0-degree limit, whereas the 45-degree specimens lie closer to the 90-degree limit.

A summary of assigned accuracy and precision limits for all specimens measured in this program is given in section IX.

APPENDIX B

CORRELATION OF THERMAL CONDUCTIVITY AND POROSITY

Char zones III, II, and that portion of zone I wherein the data indicate that radiant energy transport across pores is negligible are considered in this correlation. A porosity correlation could not be expected between zones where significant "graphitization" occurred in the higher-temperature-zone specimen. Indeed, the porosity correlation proves of value in determining the significance of the effects of "graphitization" on the thermal conductivity.

Many theories exist which give the effective conductivity of a multiphase system in terms of the conductivities of the constituent "pure" phases. The Maxwell-Eucken relation, as developed by Bellie, et al [10], is used here to relate the effective conductivity of the char to those of the solid and void phases comprising the char. In a vacuum or argon gas environment and at low temperatures, the conductivity attributed to the pore itself is negligible compared to that of the solid matrix surrounding the pore. In this case, which was met in the present measurements in zones III, II and the low-temperature portion of zone I, the porosity relation is in the form given in Equation (1)

$$K = K_s \frac{(1 - \xi)}{(1 + \beta \xi)} \tag{1}$$

where β = pore shape factor $= \left(\frac{\frac{1}{x}}{\frac{1}{y} + \frac{1}{z}}\right) R$ (2)

K = conductivity of porous material

K_s = conductivity of dense material

ξ = volume pore fraction (porosity)

x = axis of ellipsoidal pores parallel to the heat flow through the porous material

y, z = other two axes of ellipsoid

R = "roughness factor" for pore which represents the extent of departure of the pore from an ellipsoidal shape. R is greater than one.

The study of char porosity through the use of photomicrographs indicated that the large pores (inter-yarn size) have a tendency to form along the yarns and with about a 4:1 dimension ratio, the long dimension being along the yarn direction. Assuming that these pores are largely responsible for the deviations of the thermal conductivity of the porous specimens from that of the theoretically dense material, and that they are ellipsoidal in shape, (R = 1), the following values of β are obtained for heat flow parallel and normal to the pores.

$$\beta = 4/5 \text{ for heat flow normal to the long axis of the ellipsoidal pores distributed throughout the material.} \quad (3)$$

$$\beta = 1/8 \text{ for heat flow parallel to the long axis of the ellipsoidal pores distributed throughout the material.} \quad (4)$$

A simplified picture of the reinforcement fabrics as seen by the applied heat flow shows two extreme views for the cases of 0-degree and 90-degree angles of the reinforcing yarns to the surface of the specimen. In the 0-degree case the applied heat flux sees all of the yarns of the fabrics essentially as cross-hatched cylinders, the axes of the "cylinders" being normal to the applied heat flux. Since the pores are assumed to be aligned along the yarns, this case represents the flow of heat normal to the long axis of ellipsoidal pores for which the pore shape factor is given in Equation (3). In the 90-degree case, applied heat flux sees the equivalent of about one-half the yarns aligned parallel to the direction of heat flux and about one-half of the yarns aligned normal to the heat flux. Thus, the pore shape factor for the 90-degree lamination specimens is a linear combination of those given by Equations (3) and (4). Since the ratios required in the porosity correlation varied little from the use of Equation (4) in place of an appropriate combination of (3) and (4) for the 90-degree case, Equation (4) was used for the shape factor.

The conductivities of the theoretically dense material in Equation (1) must be different in the 0- and 90-degree specimens since these two cases actually approximate the orientation of the principle conductivity axes for the laminate materials.

Using Equations (3) and (4) in Equation (1) gives the required equations describing porosity effects in the thermal conductivities for the 0- and 90-degree lamination materials.

$$K_0 = K_s^0 \frac{(1 - \xi)}{(1 + \frac{4}{5}\xi)} \quad (5)$$

$$K_{90} = K_s^{90} \frac{(1 - \xi)}{(1 + \frac{1}{8}\xi)} \quad (6)$$

If it is assumed that the changes in thermal conductivity between zones III, II and I are due only to changes in porosity, K_s in Equations (5) and (6) will be the same for each zone and only ξ will change. This gives three equations each for the 0- and 90-degree lamination specimens.

$$K_0^{\,i} = K_s^{\,0} \frac{(1 - \xi_i)}{(1 + \frac{4}{5} \xi_i)} \tag{7}$$

$$K_{90}^{\,i} = K_s^{\,90} \frac{(1 - \xi_i)}{(1 + \frac{1}{8} \xi_i)} \tag{8}$$

where $i = 3, 2, 1$ for zones III, II and I.

From Equations (7) and (8) it follows that the slopes of the conductivities from one zone to another will be related in the same ratio as the conductivities.

$$\frac{K_0^{\,i}}{K_0^{\,j}} = \frac{dK_0^{\,i}/dT}{dK_0^{\,j}/dT} \tag{9}$$

The same is true for $K_{90}^{\,i}$.

Porosity correlations for the two materials studied in this program will now be discussed separately.

FM-5014 Material

As discussed in Section XIII, open porosities were measured for duplicates of all of the conductivity specimens tested (taken from the same furnace slab char), and apparent solid density was calculated from the open porosity and the measured apparent density. Also, solid and apparent densities and total porosities were directly determined on the six FM-5014 thermal conductivity specimens after completion of the thermal conductivity measurements. Significant differences were observed between open (connected porosities) and total porosities.

Use of Equations (7) and (8), with the values for open porosity and for total porosity obtained after test on conductivity specimens, gives the following relations between the conductivities of the porous and theoretically dense materials.

TABLE B-1 RELATIONS BETWEEN POROUS AND THEORETICALLY DENSE THERMAL CONDUCTIVITIES FOR 0- AND 90-DEGREE LAMINATION SPECIMENS OF FM-5014

Using Total Porosity (ϵ_t) of Conductivity Specimen	Using Open Porosity (ϵ_o) of Duplicate Specimen
$K_0^3 = 0.724\ K_s^0$	$K_0^3 = 0.717\ K_s^0$
$K_0^2 = 0.512\ K_s^0$	$K_0^2 = 0.588\ K_s^0$
$K_0^1 = 0.707\ K_s^0$	$K_0^1 = 0.663\ K_s^0$
$K_{90}^3 = 0.752\ K_s^{90}$	$K_{90}^3 = 0.791\ K_s^{90}$
$K_{90}^2 = 0.663\ K_s^{90}$	$K_{90}^2 = 0.696\ K_s^{90}$
$K_{90}^1 = 0.775\ K_s^{90}$	$K_{90}^1 = 0.802\ K_s^{90}$

The ratios of conductivities across zones as predicted by the porosity formulae may be compared with the measured conductivity data. The group of conductivity relations of Table B-1 give the following ratios:

Based on Total Porosities	Based on Open Porosities
$K_0^3/K_0^2 = \frac{0.724}{0.512} = 1.414$	$K_0^3/K_0^2 = \frac{0.717}{0.588} = 1.219$
$K_0^2/K_0^1 = \frac{0.512}{0.707} = 0.724$	$K_0^2/K_0^1 = \frac{0.588}{0.663} = 0.887$
$K_{90}^3/K_{90}^2 = \frac{0.752}{0.663} = 1.134$	$K_{90}^3/K_{90}^2 = \frac{0.791}{0.696} = 1.136$
$K_{90}^2/K_{90}^1 = \frac{0.663}{0.775} = 0.855$	$K_{90}^2/K_{90}^1 = \frac{0.696}{0.802} = 0.868$

A remark is in order at this point to indicate the manner in which the porosity correlation influenced the fitting of the final curves to the experimental data for the FM-5014 material.

In fitting curves to the data, a preliminary curve was first drawn through the data points. For zones III, II and the low-temperature part of zone I, a straight line appeared to be an accurate representation of the data. Then the ratios of conductivities across the zones which are given above were utilized to supply the porosity-predicted values of conductivity in the higher zone using the experimental value of conductivity obtained for the lower zone appearing in the ratio. The porosity-predicted conductivities for the higher zone were calculated from the lower zone data at temperatures where the data for the two zones overlapped. The slope of the higher temperature zone was also calculated from that of the lower zone through Equation (9), again using the conductivity ratio as given by the porosity change from the lower to the higher zone. If the porosity-predicted value and slope for the higher zone fell within the error band of the measured values, the preliminary conductivity curve for the higher zone was weighted toward these values. The fact that the conductivity curves were essentially straight until the temperatures in zone I were reached made this procedure simple. The most precise thermal conductivity data were obtained for zone III. These data had little scatter and gave good definition. Therefore, the procedure described above was started in zone III and used to weight the data curve fit to the zone II data. Then the final zone II curve was used in the same way to estimate the level and slope of the initial, low-temperature section of the zone I curve. As it turned out, the preliminary curves fitted to the data for zone II and the low-temperature portion of zone I were very close to those predicted by the porosity changes utilizing the well defined zone III data. Only very slight changes, well within the experimental error, were required to bring the curves into good agreement with the porosity change predictions except in two cases discussed below where the porosity correlation gave conductivities and slopes which were outside of the error limits associated with the data.

Table B-2 compares the conductivity ratios across zones as given by the measured porosities and the actual data. The data were taken at the temperatures indicated in Table B-2 from the curves fitted to the data as given in Figures 75, 76, 77, 78, 79 and 80.

TABLE B-2 THERMAL CONDUCTIVITY-POROSITY CORRELATIONS FOR FM-5014 MATERIAL, ZONES III, II AND I

	Zones III to II Correlations, 0-Degree Laminations				
Temperature (R)	K_0^3	K_0^2	$K_0^3/K_0^{2(a)}$	$K_0^3/K_0^{2(b)}$	$K_0^3/K_0^{2(c)}$
1200	5.71	4.1	1.39	1.41	1.22
1400	6.20	4.4	1.41	1.41	1.22
1500[d]	6.45	4.6	1.40	1.41	1.22
1600	6.70	4.7	1.42	1.41	1.22

TABLE B-2 (CONTINUED)

Zones II to I Correlations, 0-Degree Laminations

Temperature (R)	K_0^2	K_0^1	$K_0^2/K_0^{1(a)}$	$K_0^2/K_0^{1(b)}$	$K_0^2/K_0^{1(c)}$
2200	5.8	14.6	0.40	0.72	0.89
2400	6.1	14.8	0.41	0.72	0.89
2600[d]	6.5	15.0	0.43	0.72	0.89

Zones III to II Correlations, 90-Degree Laminations

Temperature (R)	K_{90}^3	K_{90}^2	$K_{90}^3/K_{90}^{2(a)}$	$K_{90}^3/K_{90}^{2(b)}$	$K_{90}^3/K_{90}^{2(c)}$
1000	24.7	21.5	1.15	1.13	1.14
1200	26.1	22.8	1.14	1.13	1.14
1400[d]	27.4	23.9	1.15	1.13	1.14
1600	28.7	25.2	1.14	1.13	1.14

Zones II to I Correlations, 90-Degree Laminations

Temperature (R)	K_{90}^2	K_{90}^1	$K_{90}^2/K_{90}^{1(a)}$	$K_{90}^2/K_{90}^{1(b)}$	$K_{90}^2/K_{90}^{1(c)}$
2000	27.3	27.3	1.00	0.85	0.87
2100[d]	27.9	27.8	1.00	0.85	0.87
2300[d]	29.3	28.8	1.02	0.85	0.87
2400[d]	30.2	30.3	1.00	0.85	0.87

(a) Value from the curve fit to the measured conductivity data.

(b) Value calculated from the total porosity change across zones.

(c) Value calculated from the open porosity change across zones.

(d) Temperature at which the experimental data for the two zones overlapped.

The agreement between the porosity-predicted and experimentally obtained conductivity ratios across the char zones in Table B-2 shows that a correlation is apparent between the change in thermal conductivity from one char zone to another and the corresponding change in porosity between the chars, except for the 0- and 90-degree laminations, zone I specimen. The fact that the measured conductivity ratio between zones II and I for the 0-degree case is a factor of 1.8 smaller than the ratio predicted by the difference in porosity between the two specimens can be interpreted as an indication that the solid

matrix conductivity of the zone I char was increased by the "graphitization" which occurred in the high temperature char. In the zone II to zone I, 90-degree case, the experimentally determined ratio is a factor of 1.1 to 1.2 larger than the ratio as given by the difference in specimen porosities. Attributing this to a "graphitization" effect on the solid matrix conductivity, it appears that in the 90-degree case, the solid matrix conductivity was decreased by the "graphitization" which occurred in the high temperature, zone I char. The significant increase in solid matrix conductivity for the 0-degree, zone I case could not be accounted for by experimental error; the effect of "graphitization" is apparent. However, the decrease in solid matrix conductivity noted for the 90-degree case is relatively small and could possibly be attributed to experimental error.

The relative effects of "graphitization" on the 0- and 90-degree specimens can be interpreted in relation to the influence of the reinforcement cloth on the phonon conduction process in the material. In the 90-degree specimen, up to half of the cloth yarns were aligned nearly parallel to the applied heat flux. These yarns tended to dominate the conduction process, and since the reinforcement cloth was originally graphitized, the further "graphitization" which occurred in the zone I char had relatively little effect. However, in the 0-degree specimen the axes of the yarns were normal to the applied flux. In this case, crystalline growth occurring at pore sites located around the cloth fibers could significantly improve the conduction path through the cloth, thus increasing the solid matrix conductivity.

The success of the porosity correlation in zones III and II indicates that the pyrolysis process occurring through zones III and II principally affects the porosity of the specimen; concurrent chemical changes which occur during pyrolysis appear to exert only minor influence on the thermal conductivity.

MX-4926 Material

The same procedure as in the case of the FM-5014 material was followed to investigate the possibility of correlating the observed changes in thermal conductivity between zones with corresponding changes in specimen porosity. As discussed in section VIII, open porosities were measured on the furnace slab samples, and the total porosities for four of the six 0- and 90-degree conductivity measurements were completed. Table B-3 gives the relations between the porous and theoretically dense conductivities obtained from Equations (7) and (8) using total and open porosities. The porosity-predicted thermal conductivity ratios across zones III to II, and zones II to I for the 0- and 90-degree lamination specimens are then compared with the ratios obtained from the reported data curves in Table B-4. Finally, the results of the comparison are discussed below under the assumption that the porosity formulae correctly account for porosity effects on the thermal conductivity.

TABLE B-3 RELATIONS BETWEEN POROUS AND THEORETICALLY DENSE THERMAL CONDUCTIVITIES FOR 0- AND 90-DEGREE LAMINATION SPECIMENS OF MX-4926

Using Total Porosity (ξ_t) of Conductivity Specimen	Using Open Porosity (ξ_o) of Duplicate Specimen
$K_0^3 = 0.394\ K_s^0$	$K_0^3 = 0.564\ K_s^0$
▷1 $K_0^2 = 0.378\ K_s^0$	$K_0^2 = 0.497\ K_s^0$
▷1 $K_0^2 = 0.433\ K_s^0$	- - - - - - -
$K_0^1 = 0.650\ K_s^0$	$K_0^1 = 0.676\ K_s^0$
$K_{90}^3 = 0.718\ K_s^{90}$	$K_{90}^3 = 0.717\ K_s^{90}$
$K_{90}^2 = 0.619\ K_s^{90}$	$K_{90}^2 = 0.675\ K_s^{90}$
$K_{90}^1 = 0.806\ K_s^{90}$	$K_{90}^1 = 0.834\ K_s^{90}$

▷1 Values for total porosity were measured on two samples of the PC-11-0 conductivity specimen. Material other than specimen material (thermocouple material) was probably present in one of the samples. Both values are carried through the calculations which follow.

The group of conductivity relations of Table B-3 give the results below:

Based on Total Porosities	Based on Open Porosities
$K_0^3/K_0^2 = \frac{0.394}{0.378} = 1.042$	$K_0^3/K_0^2 = \frac{0.564}{0.497} = 1.135$
$K_0^3/K_0^2 = \frac{0.394}{0.433} = 0.910$	- - - - - - - - - - -
$K_0^2/K_0^1 = \frac{0.378}{0.650} = 0.581$	$K_0^2/K_0^1 = \frac{0.497}{0.676} = 0.735$
$K_0^2/K_0^1 = \frac{0.433}{0.650} = 0.666$	- - - - - - - - - - -
$K_{90}^3/K_{90}^2 = \frac{0.718}{0.619} = 1.160$	$K_{90}^3/K_{90}^2 = \frac{0.717}{0.675} = 1.062$
$K_{90}^2/K_{90}^1 = \frac{0.619}{0.806} = 0.768$	$K_{90}^2/K_{90}^1 = \frac{0.675}{0.834} = 0.809$

The data curves for the above MX-4926 specimens were used to give the values of thermal conductivity presented in Table B-4 below for comparison with the ratios predicted by the porosity formulae. No adjustment to the data curves was made to weight them toward the porosity predicted values as was done for the FM-5014 material. In the MX-4926 material case, the 0-degree lamination curves were well defined by the data, the 90-degree lamination data were less well defined. The data of Table B-4 allow the changes in conductivity through zones III, II and I to be interpreted. As in the case of the FM-5014 material, the agreement between conductivity ratios based on total and open porosities is generally good.

Consider the 0-degree lamination conductivities. The fact that the measured conductivity ratio from zones III to II is significantly greater (by a factor of about 1.8) than that which would be due only to the increase in porosity suggests that the solid matrix conductivity of the zone II material was decreased by some change in the character of the material. The x-ray diffraction intensity measurements at 3.37A on the duplicate to specimen PC-II-0 did indicate graphitic crystallization occurring in this zone, although the measured intensity was about half that of the corresponding zone II, FM-5014 specimen. If the change in conductivity from zone III to II in the MX material is attributed to partial "graphitization" of the filler material and/or reinforcing cloth fibers, then the crystals which formed may have been highly oriented with the axis of highest conductivity, the "a" axis, aligned along the fibers. Conductivity may also be affected by the tendency for the formation of continuous paths of "graphitized" pyrolysis deposits along fibers in this material. This could account for the large increase observed in the thermal conductivity parallel to the laminations (the 90-degree specimens), in zone II. The surprising result deduced from the porosity formulation is that the "graphitization" had the effect of decreasing the solid matrix conductivity normal to the laminate in zone II in relation to that of zone III. This is in opposition to the effect of "graphitization" deduced from the porosity correlation on the zone I 0-degree lamination FM-5014 material. This decrease in conductivity is not believed due to advanced pyrolysis of the resin in zone II because the success of the porosity correlation between zones III and II for the FM-5014 material indicated that the main effect of pyrolysis was to change the porosity of the specimens. It is also surprising that the relatively slight degree of "graphitization" which is attributed to the zone II specimens could have exerted the large effects on the conductivity which were observed in the 90-degree specimens.

In considering the 90-degree lamination specimens, Table B-4 shows that the difference between predicted and measured conductivity ratios in the zone II to I case is about 1/7 that in the zone III to II case. This could mean that the effects of "graphitization" on the solid matrix thermal conductivity normal to the laminates is largely complete at the zone II temperature level, the increase in measured conductivity from zones II to I being essentially due to the corresponding decrease in porosity.

TABLE B-4 THERMAL CONDUCTIVITY-POROSITY CORRELATION FOR MX-4926 MATERIAL ZONES III, II, AND I

	Zones III to II Correlation, 0-Degree Laminations				
Temperature (R)	K_0^3	K_0^2	$K_0^3/K_0^{2(a)}$	$K_0^3/K_0^{2(b)}$	$K_0^3/K_0^{2(c)}$
1000	3.08	1.85	1.66	1.04, 0.91(e)	1.14
1200(d)	3.62	2.00	1.81	1.04, 0.91(e)	1.14
1400(d)	4.15	2.15	1.93	1.04, 0.91(e)	1.14

	Zones II to I Correlation, 0-Degree Laminations				
Temperature (R)	K_0^2	K_0^1	$K_0^2/K_0^{1(a)}$	$K_0^2/K_0^{1(b)}$	$K_0^2/K_0^{1(c)}$
2000(d)	2.56	3.0	0.85	0.58, 0.67 (e)	0.74
2200(d)	2.71	3.2	0.85	0.58, 0.67 (e)	0.74
2400(d)	2.86	3.4	0.84	0.58, 0.67 (e)	0.74
2600(d)	3.01	3.6	0.84	0.58, 0.67 (e)	0.74
2800	3.16	3.9	0.81	0.58, 0.67 (e)	0.74

	Zones III to II Correlation, 90-Degree Laminations				
Temperature (R)	K_{90}^3	K_{90}^2	$K_{90}^3/K_{90}^{2(a)}$	$K_{90}^3/K_{90}^{2(b)}$	$K_{90}^3/K_{90}^{2(c)}$
1200	10.4	28.7	0.36	1.16	1.06
1300(d)	10.9	29.0	0.37	1.16	1.06
1400(d)	11.4	29.3	0.39	1.16	1.06

	Zones II to I Correlation, 90-Degree Laminations				
Temperature (R)	K_{90}^2	K_{90}^1	$K_{90}^2/K_{90}^{1(a)}$	$K_{90}^2/K_{90}^{1(b)}$	$K_{90}^2/K_{90}^{1(c)}$
1800	30.9	54.0	0.57	0.77	0.81
2000(d)	31.4	56.7	0.55	0.77	0.81
2200(d)	31.9	59.4	0.54	0.77	0.81
2400	32.4	62.1	0.52	0.77	0.81
2600	32.9	64.8	0.51	0.77	0.81

(a) Value from the curve fit to the measured conductivity data
(b) Value calculated from the total porosity change across zones
(c) Value calculated from the open porosity change across zones
(d) Temperatures at which the experimental data for the two zones overlapped
(e) Two values from the two total porosities measured on specimen PC-II-0.

In considering the 90-degree lamination results in Table B-4 it is obvious that even the relatively slight "graphitization" occurring in zone II had a major effect on the thermal conductivity parallel to the laminations. In the zone III to II case, the porosity increase between zones III and II indicates that the conductivity in zone II should be less than, or at least the same as, that of zone III. In fact, the measured zone II conductivity is almost three times as great as that of zone III. As in the 0-degree case, the difference between porosity-predicted and measured conductivity ratios between zones II and I is not as great as in the zone III to II case, although the increased "graphitization" in zone I did increase the conductivity to a greater extent than the decrease in porosity from zone II to I could account for. Thus, continued "graphitization" steadily increases the solid matrix conductivity in the direction parallel to the reinforcing cloth laminates.

APPENDIX C

EFFECT OF LAYUP ANGLE ON THERMAL CONDUCTIVITY

In the self-guarding disc conductivity measurement technique, the ideal situation (i.e., no radial heat flux, and true one-dimensional axial flow in isotropic specimens) produces isotherms in the specimens which are normal to the centerline of the disc specimen. In isotropic specimens, the presence of radial heat flux distorts the isotherms near the edge of the specimen, but the boundary conditions on the specimen are adjusted such that the isotherms become normal to the centerline within the one-inch-diameter test volume of the specimen. In anisotropic materials, the experimental arrangement still produces isotherms normal to the specimen centerline, but the heat flux vector through the specimen is no longer necessarily normal to the isotherms. The component of the heat flux normal to the isotherms is the heat flux measured by the heat flow meter so that it is the thermal conductivity normal to the isotherms (denoted by subcript n) and normal to the disk specimen faces which is actually measured. Since the specimen isotherms are at an angle θ, the lamination angle measured from the diameter of the specimen, to the principal conductivity axis along the cloth layers, then the conductivity through specimens of lamination angle θ is related to the principal conductivities as in equation (1); given in another form in Carslaw and Jaeger [20].

$$K_n(\theta) = K_3 \left[1 + \left(\frac{K_1}{K_3} - 1 \right) \sin^2 \theta \right] \qquad (1)$$

The principal conductivity, K_1, is that measured along the cloth layers (the 90° lamination specimens; $K_1 = K_{90}$ in body of report), and K_3 is the conductivity measured normal to the layers (the 0° lamination specimens; $K_3 = K_0$ in body of report). Equation (1) was derived on the basis that the conductivity K_1 in any direction in the cloth layer was the same. This is believed to be a valid assumption for the materials on this program; in any case any minor variations would be averaged out by the orientation in the conductivity samples. All actual measurements of K_1 or $K_n(\theta)$ were made on samples with the lamination angle measured in the cloth layer bias direction in MX-4926, and in randomly oriented cloth layers in FM-5014.

A variation of Equation (1) was suggested by Schaefer and Dahm [21] to describe the influence of lamination angle. This relation differs from Equation (1) in assigning less influence to the angle.

$$K_n(\theta) = K_3 \left[1 + \left(\frac{K_1}{K_3} - 1 \right) \sin \theta \right] \qquad (2)$$

The data for the MX-4926 material were used to investigate the validity of Equations (1) or (2) in predicting the effect of lamination angle on the thermal conductivity. In the zone III measurements, the data for specimen PC-III-0 and specimen PC-III-45

were the best defined so that these two sets of data were used in Equations (1) and (2) to calculate the principal conductivity, K_1, corresponding to the 90 degree lamination specimen, PC-III-90. The two curves resulting from Equations (1) and (2) are shown in Figure C-1. Values for K_1 were then taken from the two curves of Figure C-1 and used in conjunction with K_3 from PC-III-0 to calculate K_n (20° 15')* which corresponded to specimen PC-III-20.

The two curves corresponding to Equations (1) and (2) for the 20 degree specimen are shown in Figure C-1 along with the actual data. Figures C-1 and C-2 show that the sin θ relation of Equation (2) better fits the data for PC-III-90 and PC-III-20 than the $\sin^2 \theta$ relation of Equation (1).

For zone II, the data curves for specimens PC-II-90 and PC-II-0 were used to give K_1 and K_3 for use in Equations (1) and (2), and K_n(21°) corresponding to specimen PC-II-20 were then calculated. (Again the exact lamination angles for PC-II-20 and PC-I-20 were measured from appropriate specimen sections and found to be 21°.) The results are given in Table C-1 for a range of temperatures in order to allow easy comparison. It is seen that the $\sin^2 \theta$ relation of Equation (1) is definitely preferred in this case. The percent deviation between the conductivity calculated from Equation (1) and the measured conductivity is given in the last column in the table. It is seen that adjustment in the slope of the conductivity curve for specimen PC-II-90 could produce a consistent deviation with temperature; however, the percent deviation would still be significant. It should be noted here that the data curve for specimen PC-II-90 has the highest uncertainty of all the measurements. Therefore, although the angular correlation given by Equation (1) can be considered as approximately correct, its true validity in the case of zone II specimens has not been conclusively established.

For zone I, the data curves for specimen PC-I-90 and PC-I-0 were used to give K_1 and K_3 for use in Equations (1) and (2) from which K_n(21°) corresponding to specimen PC-I-20 were calculated. The results also appear in Table C-1. Again Equation (1) proved more accurate in predicting the effect of lamination angle on thermal conductivity. The deviation of calculated and measured K_n(21°) is consistent with temperature at about 29 percent. Since the deviation is consistent with temperature, the slopes of the data curves for K_1, PC-I-90, and K_3, PC-I-0, seem to be in the proper proportions to satisfy the predictions of lamination angle

---

* The lamination angles for the nominally 20 and 45 degree specimens were measured with a vernier protractor from appropriate sections of the samples after the specimens were sectioned for thermocouple location remeasurement. The angles were found to be 20° 15' and 43° 20', respectively, on the average.

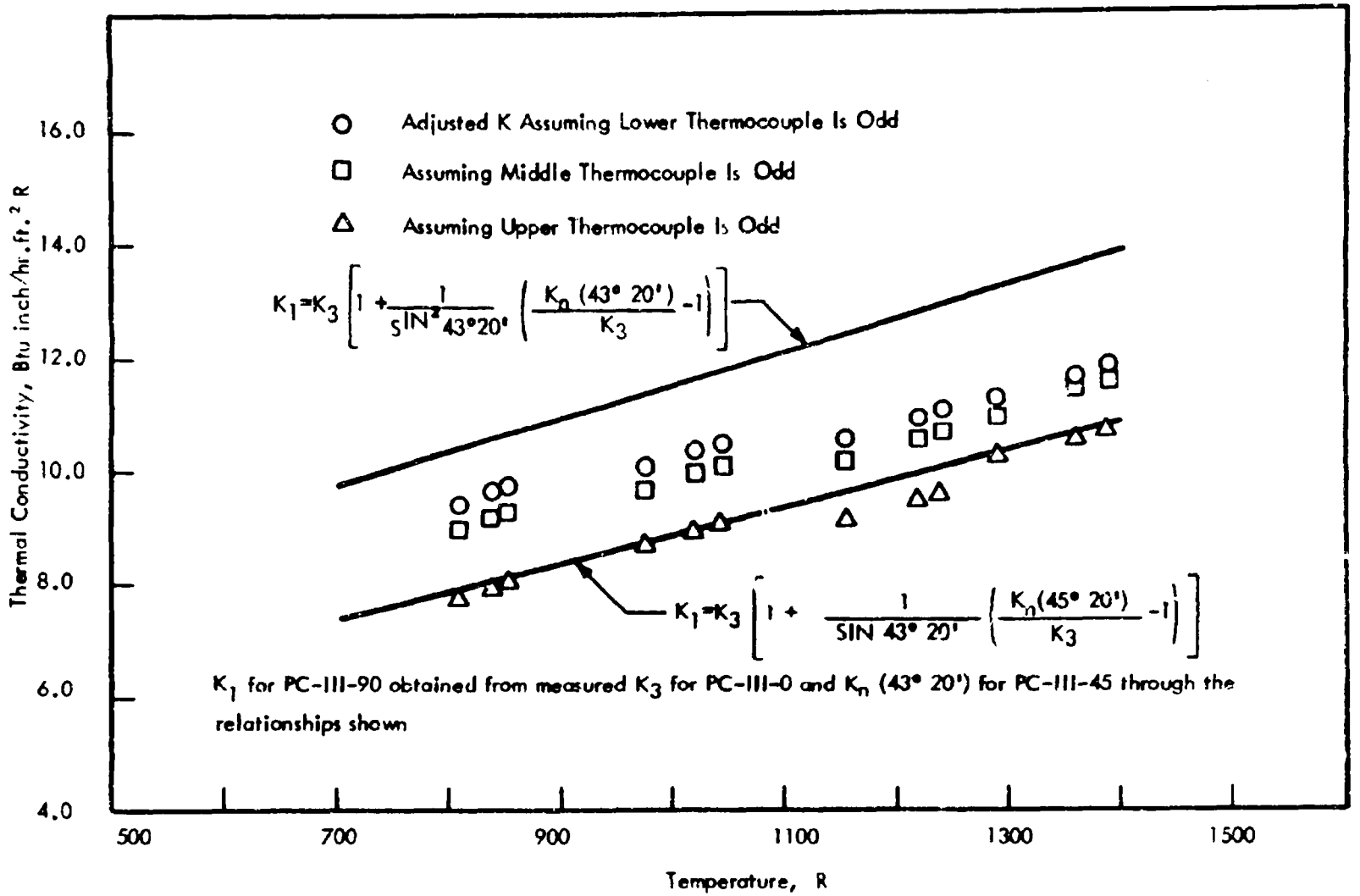

FIGURE C-1 LAMINATION ANGLE CORRELATION AND "ODD THERMOCOUPLE" ADJUSTMENT OF THE THERMAL CONDUCTIVITY DATA OF SPECIMEN PC-III-90 (MX-4926)

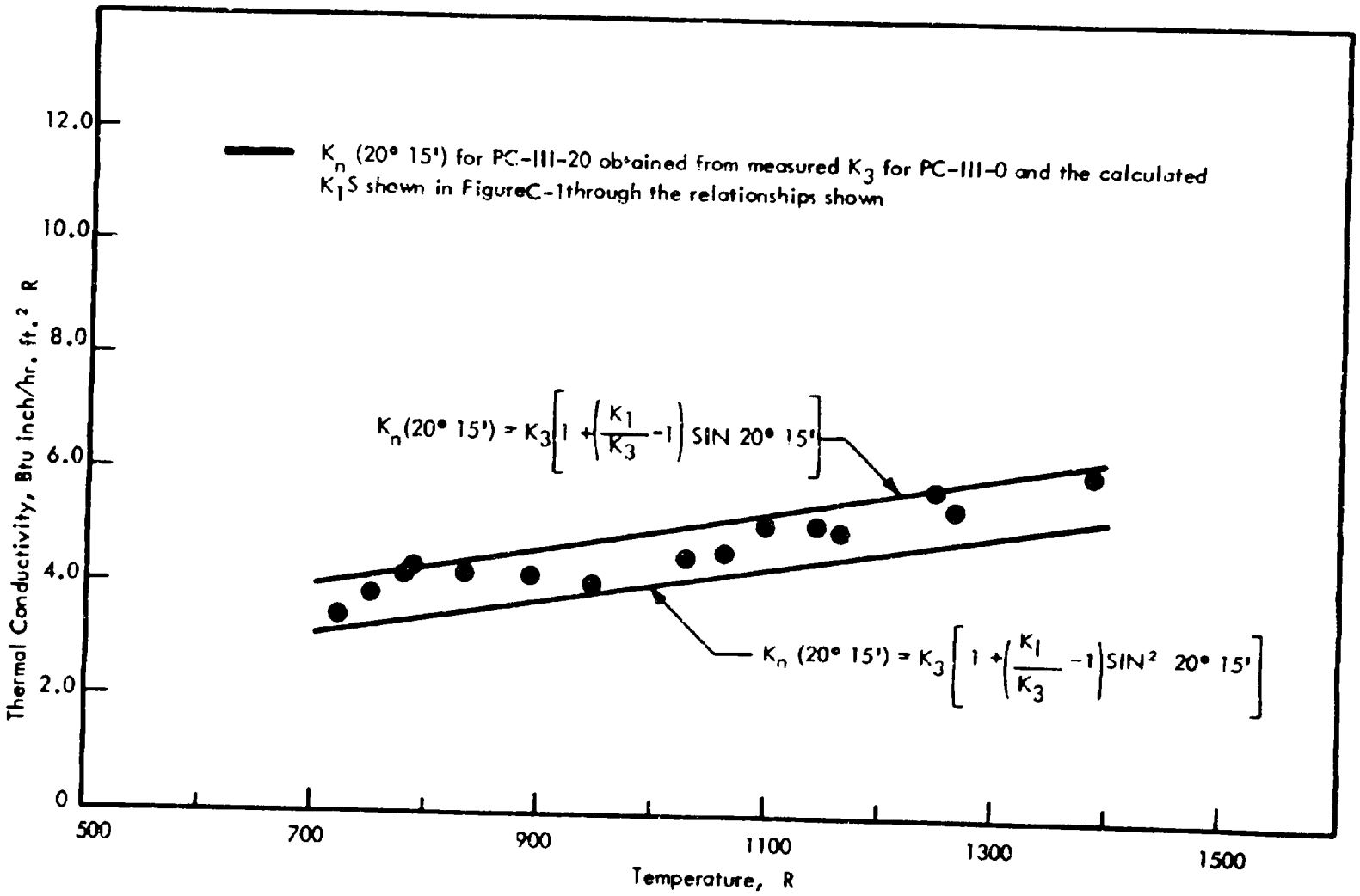

FIGURE C-2 LAMINATION ANGLE CORRELATION TO DATA FOR THE THERMAL CONDUCTIVITY OF SPECIMEN PC-III-20 (MX-4926).

TABLE C-1 COMPARISON OF MEASURED AND PREDICTED THERMAL CONDUCTIVITIES FOR THE MX-4926 20 DEGREE LAMINATION SPECIMENS OF ZONES II AND I

T (R)	K_1 [a]	K_3 [b]	Kn(21°) [c]	Kn(21°) [d]	Kn (21°) [e]	D(Percent) [f]
Zone II						
1300	28.8	2.06	11.6	5.5	4.3	-28
1600	29.7	2.27	12.1	5.8	4.6	-26
2400	32.0	2.87	13.3	6.6	5.8	-14
2700	32.9	3.08	13.8	6.9	6.3	-10
Zone I						
2000	56.3	3.0	22.1	9.8	14.0	+30
2400	61.7	3.4	24.3	10.9	15.1	+28
2800	67.3	3.9	26.6	12.0	16.4	+27
3600	95.0	5.8	37.7	17.2	23.0	+25

(a) Values taken from the curve of Figure 62 for Zone II, and the curve of Figure 72 for Zone I.
(b) Values taken from the curve of Figure 67 for Zone II, and the curve of Figure 70 for Zone I.
(c) Values calculated from Equation (2), ($\sin 2\theta$), using K_1 and K_3.
(d) Value calculated from Equation (1), ($\sin^2\theta$), using K_1 and K_3.
(e) Value taken from the curve of Figure 63 for Zone II, and from the curve of Figure 71 for Zone I.
(f) Percent deviation between the conductivity as calculated from Equation (1), ($\sin^2\theta$), and the measured conductivity.

effect as given by Equation (1), but the predicted value of $K_n(21°)$ is consistently low. Noting that the data curve for specimen PC-I-90 along with that for PC-II-90 used above had the highest assigned uncertainty of all the specimens measured, it is seen that the deviation of calculated and measured conductivities for PC-I-20 is within the combined error of measurements on specimens PC-I-90 and PC-I-20. Thus, the applicability of the angular correlation as given in Equation (1) can only be considered as inconclusively demonstrated in the zone I materials.

Porosity effects were not considered in the above calculations. The porosity was not the same for each specimen involved in the calculations. The proper way to test Equations (1) and (2) would be to calculate the conductivities of the theoretically dense materials corresponding to the principal conductivities (see the porosity correlation in section IX and Appendix B), and then use these values in Equations (1) and (2) to obtain the predicted dense material conductivity at the 20 degree lamination angle. These values should then be compared to the dense material conductivity as obtained from the measured, porous 20 degree specimen. Since total porosity fractions were not obtained on all of the MX-4926 specimens actually measured in this program, some values for tested specimens and some for duplicates to the tested specimens (cut from the same char block) were used to make the porosity corrections according to the porosity correlation procedure discussed in section IX. Comparison of the porosity-corrected measured values gives the same results as those indicated in Table C-1. For the sake of comparison, deviations in zone II ranged from 15 to 30 percent, while the range in zone I was from 20 to 23 percent. The conclusion is that porosity effects did not significantly contribute to the deviation between the predicted and measured thermal conductivities as given in Table C-1.

APPENDIX D

THERMAL CONDUCTIVITY DATA SCATTER AND ADJUSTMENTS

This appendix discusses data scatter which resulted from inhomogeneity and anisotropy in the materials. It points out that scatter can be caused by local temperature perturbations in such materials and suggests, through a simple analysis, the possible magnitude of scatter.

In addition, this appendix points out the difficulty of establishing symmetric temperature profiles and gradients for steady-state measurements in anisotropic materials. Results of an experiment to investigate the extent of scatter due to this factor are presented.

MATERIAL INHOMOGENEITY

A possible cause for data scatter lies in the relation between the size of the temperature sensing thermocouple bead and the thickness of the reinforcing cloth layers present in the specimen. In the virgin, zone III, and several of the zone II specimens, unsheathed thermocouples were used which had beads on the order of 0.02-inch diameter. Microscopic examination of sectioned specimens in this group revealed that the thermocouple bead diameter was only about 1/3 larger than the thickness of the cloth layers. It appeared that most of a thermocouple bead could lie with equal probability either in a warp or in a fill yarn. In the 0-degree lamination specimens, a simplified picture of the cloth structure shows that the heat flux applied to the specimen during the conductivity measurement sees the warp and fill yarns essentially as cross-hatched cylinders; the applied heat flux vector being normal to the long axes of the cylinders. Symmetry suggests that in this case there will be no local temperature fluctuations from fill to warp yarns. However, in the 90-degree lamination specimens, asymmetry in the local heat flux at the thermocouple bead may occur in two ways. For MX-4926, where all yarns are on the bias at 45 degrees to the heat flow path, local asymmetry could occur due to the different counts of fill and warp yarns. The higher count in the warp direction would cause distortion of the heat flow path toward the direction of warp yarns, giving an anisotropic effect due to material inhomogeneity. For FM-5014, where laminate orientations were random, many of the yarns will be nearly parallel and many normal to the applied heat flux vector. Due to this asymmetry, it is likely that there were local temperature gradients between warp and fill yarns in the 90-degree lamination specimen. Since most of any thermocouple bead

could be in a warp or fill yarn, it may have happened that two of the three specimen thermocouple beads were primarily in a fill yarn while the third was primarily in a warp yarn. In this event, the temperature differences used to calculate the thermal conductivity of the specimen would be perturbed by the local temperature difference between the warp yarn, which most influenced the "odd" (in a medium of different conductivity from the other two) thermocouple bead, and the fill yarn adjacent to the odd bead. This would give rise to scatter in the three thermal conductivity values calculated from the three specimen thermocouple readings at each equilibrium. It is to be noted that the 90-degree lamination specimens were, in fact, the most difficult to measure; they showed the greatest data scatter.

In order to define better the possible effect of material inhomogeneity on the thermocouple readings in the thermal conductivity measurements, the data for specimen PC-111-90, MX-4926, were reconsidered, assuming that data from one of the three specimen thermocouples was odd from the other two, i.e., one thermocouple was reading a temperature of material of different conductivity than that of the other two thermocouples. With this assumption, the deviation of each set of values of conductivity obtained for each equilibrium point in the experiment could be used to reduce the data scatter as follows:

A deviation for two of the three thermal conductivity values obtained at an equilibrium in the conductivity measurements may be defined. The two independent conductivity values are calculated from the temperature differences between the hot zone and middle thermocouples, and the temperature difference between the middle and cold zone thermocouples:

$$\frac{K_1 - K_2}{K_1 + K_2} = P = \text{percent deviation} \qquad (1)$$

In order to allow for the natural variation of K with T, a straight line approximation was used to give a K (T) slope. From the PC-111-90 data, the following slope was obtained.

$$K^1(T) = \frac{1}{200} \frac{\text{Btu inch}}{\text{hr ft}^2\,\text{R}}/\text{R}$$

If K_2 refers to the conductivity value measured at the lower mean temperature attained at an equilibrium, and K_1 is the conductivity value obtained at the higher mean temperature of the same equilibrium, then the linear approximation gives the following equation:

$$K_1 = K_2 + \frac{\Delta T}{200}$$

The following quantity, P^t, based on the linear K(T) approximation, is defined as follows:

$$P^t = \frac{K_1 - K_2}{K_1 + K_2} = \frac{1}{\left[400\left(\frac{K_2}{\Delta\bar{T}}\right) + 1\right]} \qquad (2)$$

where: $\Delta\bar{T}$ = temperature difference between the mean temperatures at which K_1 and K_2 are evaluated.

Using the measured value of K_2, taken in this calculation as the K calculated between the middle and cold zone thermocouples in the specimen, to calculate P^t in Equation (2), one can then approximately bring the natural temperature dependence of K into the percent deviation by using the more general definition of deviation given in Equation (3).

$$P(K) = P - P^t \qquad (3)$$

As defined in Equation (1), P accounts for the measured data scatter, and P^t preserves the natural temperature dependence of K on temperature. If P^t were not included, the three data points for K at each equilibrium point would be adjusted into one single value and the temperature dependence of K within the group of three entirely lost.

Using the one-dimensional heat flow equation, $\frac{Q}{A} = K\frac{\Delta T}{d}$ for K, remembering that $\frac{Q}{A}$ is the same for all three specimen thermocouples, one obtains the following equation for P(K) independent of Equation (3) above:

$$P(K) = \frac{K_1 - K_2}{K_1 + K_2} = \frac{\frac{d_{1-2}}{\Delta T_{1-2}} - \frac{d_{2-3}}{\Delta T_{2-3}}}{\frac{d_{1-2}}{\Delta T_{1-2}} + \frac{d_{2-3}}{\Delta T_{2-3}}} \qquad (4)$$

In Equation (4), d_{1-2} and d_{2-3} are the distances between the hot zone and middle thermocouple beads, and middle and cold zone thermocouple beads, respectively, and ΔT_{1-2}, ΔT_{2-3} are the corresponding temperature differences.

Equation (4) can be rearranged into Equation (5) below to relate the temperature gradient between the middle and cold zone thermocouple beads to the temperature gradient between the hot zone and middle thermocouple beads.

$$\frac{T_2 - T_3}{d_{2-3}} = \bar{P}(K) \frac{T_1 - T_2}{d_{1-2}} \tag{5}$$

In Equation (5), $\bar{P}(K)$ is defined by Equation (6).

$$\bar{P}(K) = \frac{1 + P(K)}{1 - P(K)} \tag{6}$$

The generalized deviation, P(K), of Equation (6) is now considered defined by Equation (3).

Assuming that the hot zone thermocouple is odd, a temperature T_1' should exist such that $\bar{P}(K) = 1$. In other words, T_1' is a hypothetical hot zone temperature, which, if actually attained by the hot zone thermocouple, would have reduced the variation in thermal conductivity with temperature to the assumed linear relation, thus eliminating the data scatter among the three values of conductivity obtained at an equilibrium. This corresponds physically to the case where all three specimen thermocouples would have been in the same local environment. Equations (5), with $\bar{P}(K) = 1$, defines T_1' as in Equation (7).

$$\frac{T_1' - T_2}{d_{1-2}} = \frac{T_2 - T_3}{d_{2-3}} \tag{7}$$

Equations (5) and (7) can be combined to give T_1' in terms of the quantities, $\bar{P}(K)$, T_1, and T_2 which are known from the conductivity measurements.

$$T_1' - T_1 = (\bar{P}(K) - 1)(T_1 - T_2) \tag{8}$$

The calculation of T_1' is accomplished by using the measured conductivity at the mean temperature between the hot zone and middle thermocouples, K_1, and that at the mean temperature between the middle and cold zone thermocouples, K_2, in Equation (1) to calculate P, the percent deviation of K_1, K_2. Then, the temperature dependence of the conductivity which must separate the value of K_1 from K_2 is accounted for by calculation of P^t by means of Equation (2). The generalized deviation, P(K), is then calculated from Equation (3) and used in Equation (6) to give $\bar{P}(K)$. The actual value of the measured temperature at the hot zone thermocouple,

T_1, and that at the middle thermocouple, T2, are used with $\bar{P}(K)$ in Equation (8) to give the hypothetical temperature T_1'. This temperature is then used in place of the measured hot zone temperature to adjust the three values of conductivity obtained from the original hot zone, middle, and cold zone measured temperatures. Since the hot zone thermocouple was assumed at fault, the value of the measured conductivity obtained from the temperature difference between the middle and cold zone thermocouples remains unchanged. The conductivities calculated from the temperature differences between the hot zone and middle, and hot zone and cold zone thermocouples are changed in such a way as to align them with the unchanged conductivity . The results of these calculations appear as the lower set of points in Figure C-1. The perturbation temperatures, $(T_1' - T_1)$ required to affect this data adjustment for the four data points presented in Figure C-1 in this case where the hot zone thermocouple was presumed odd, varied from 14 to 20 degrees R.

The same procedure was applied assuming successively that the middle thermocouple and then the cold zone thermocouple were odd. In the above calculations only the final Equation (8) changes. If the middle thermocouple is odd, Equation (8) is replaced by (9).

$$(T_2 - T_2') \approx (T_1 - T_2) \frac{\bar{P}(K) - 1}{1 + \frac{d_{1-2}}{d_{2-3}}} \qquad (9)$$

The adjusted conductivities arising from Equation (9) are the middle set of points in Figure C-1 , the original conductivity calculated between the hot and cold zone thermocouples remaining unchanged. The perturbation temperatures, (T_2-T_2'), required to affect this data adjustment for the four data points ranged from 3.4 to 4.9 degrees R.

If the cold zone thermocouple is assumed to be the odd one, Equation (8) is replaced by Equation (10) in the calculations.

$$(T_3' - T_3) \approx \frac{d_{2-3}}{d_{1-2}} (\bar{P}(K) - 1)(T_1 - T_2) \qquad (10)$$

The adjusted conductivities arising from Equation (10) appear as the upper set of points in Figure C-1, the original conductivity calculated between the hot zone and middle thermocouples remaining unchanged. The perturbation temperatures $(T_3' - T_3)$, required to effect the adjustment for the four data points, ranged from 4.5 to 6.5 degrees R.

The preceding calculations were made only to illustrate that material inhomogeneity could have contributed to the observed data scatter; the perturbation temperatures required to account for the scatter are not unreasonably high. However, the fraction, if any, of the scatter which could be directly attributed to material inhomogeneity could not be determined. Therefore, no corrections could be made to the data to account for this effect.

MATERIAL ANISOTROPY

The anisotropy of the specimens also limited the precision of data in another way. The three specimen thermocouples yielding the thermal conductivity values for the specimen were placed nominally at 1/4 inch from the centerline of the specimens at appropriate distances apart. By necessity, the three thermocouple holes had to be drilled some angular distances apart from each other around the circumference of the specimens.

Consider the 90-degree lamination specimens. Viewed from the flat surfaces, the laminations all run in the same direction. To a fair approximation, the directions parallel and normal to the laminations represent the directions of the principal conductivity axes. Thus, it is obvious that in the experimental apparatus where some radial heat flux is bound to occur, the temperature in a plane normal to the specimen centerline has angular as well as radial dependence. Since the thermocouples enter at different angles to the lamination direction as viewed from a flat surface, and lie at equal radial distances from the specimen centerline, it is apparent that the temperature at each thermocouple bead location is perturbed from the average in its axial plane by a different amount, depending on the angle between the radius vector to the bead and the direction of the laminations. Although the radial flux may not be great enough to cause significant error in the average level of the measured thermal conductivity, as determined by an appropriate weighted average between the three conductivities calculated at each equilibrium, it may still be great enough to cause the three conductivities to scatter rather than fall on a smooth curve as is desired. Since the temperature differences measured in the 90-degree specimens were generally low as compared to those in the 0-degree specimens, small temperature perturbations of the order of a degree could account for the observed data scatter. Due to their lamination symmetry, the 0-degree specimens should not have shown this effect and, in fact, the data scatter for the 0-degree specimens were generally small compared to the other cases where the laminations were at any other angle than zero; the 90-degree lamination specimens showed most scatter.

Specimen PC-II-90, MX-4926, was instrumented to study asymmetry in the temperature distribution. Figure D-1 shows the location of the three specimen thermocouples used in the thermal conductivity measurements, plus the six additional thermocouples aligned along the normal to the laminations as viewed from a flat surface. Two thermocouples were flash-welded to the tantalum pellet insulation surrounding the curved surface of the specimen at points close to the edge thermocouples in the specimen and at approximately the mid-plane of the specimen to indicate the temperature of the insulation. Also, the central thermocouples were drilled to 0.1 inch from the specimen center instead of the normal 1/4 inch in order to reduce the effect of any radial heat flux which may have been present. (The offset is used to minimize the distortion of the axial heat flow pattern through the one-inch diameter test volume of the specimen.)

Table D-1 gives results of the measurements corresponding to those data points which appear in the thermal conductivity curve for specimen PC-II-90. The asymmetrical temperature variation is clearly evident in the signs and magnitudes of the radial temperature differences between the 3/4-inch and 1 3/8-inch temperatures, and the temperature differences between the appropriate insulation temperature and corresponding 1-3/8 and 3/4-inch thermocouples. These values all show a highly asymmetric heat flow in the specimen during measurement. The $\Delta T_{3/4-1-3/8}$ values of Table D-1 indicate a radial heat flow out of the one-inch-diameter test volume both parallel and normal to the laminates. However, the $\Delta T_{1-3/8-I}$ indicate a heat flow from the insulation into the specimen along the laminates and heat flow from the specimen into the insulation normal to the laminates. The $\Delta T_{3/4-I}$ values parallel to the laminates are inconsistent, indicating that the axial location of the insulation thermocouple relative to the axial location of the specimen thermocouple was not known with precision, although the directions of radial heat flow from specimen to insulation as indicated by the $T_{1-3/8-I}$ values are of high enough magnifude and consistency to be considered qualitatively correct.

The data of Table D-1 indicate that the specimen isotherms are saddle-shaped to a degree depending on the axial location within the specimen. These complex flow patterns can easily be a major contributor to the observed data scatter in all non-zero-degree lamination specimens. As stated above, the thermocouples utilized in the thermal conductivity measurement are offset 1/4 inch from the specimen centerline. In the case of PC-II-90 the three thermocouples were drilled to within 1/10 inch of the centerline. Even in this case, however, the measurements in Table D-1 indicate the asymmetrical temperature perturbations of the order of one degree could have been possible within a 1/10-inch radial distance.

Corresponding to Table D-1 and the case of 20 degrees temperature difference between two of the three specimen thermocouples, a one degree temperature perturbation could lead to fluctuations of 5 percent between the values of

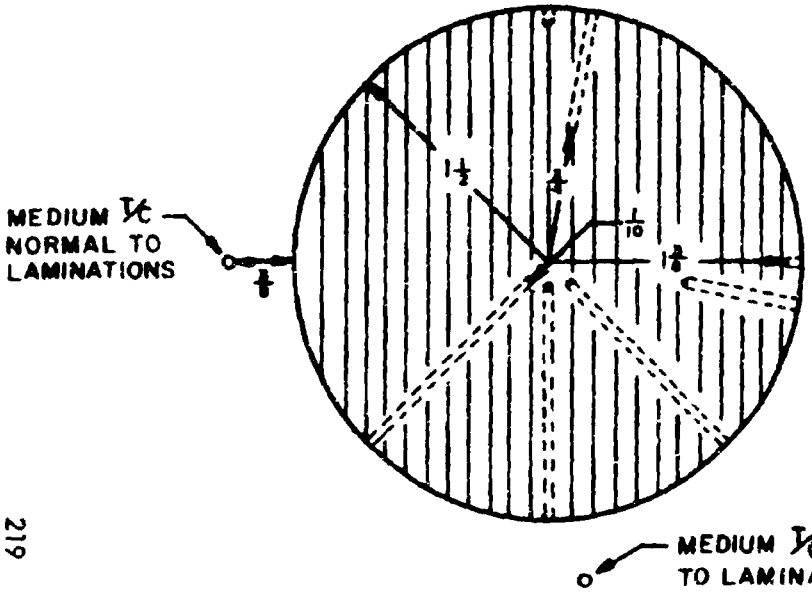

SPECIMEN VIEWED FROM HOT FACE SHOWING ALL SPECIMEN THERMOCOUPLE LOCATIONS AND DIRECTION OF SPECIMEN LAMINATIONS

VIEW PARALLEL TO LAMINATIONS SHOWING LOCATION OF THERMOCOUPLES USED IN THERMAL CONDUCTIVITY MEASUREMENTS

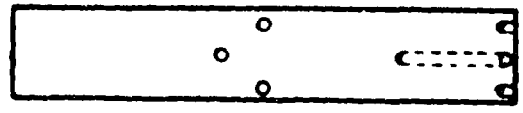

VIEW NORMAL TO LAMINATIONS SHOWING RADIAL THERMOCOUPLE LOCATIONS

FIGURE D-1 INSTRUMENTATION OF SPECIMEN PC-II-90 USED IN DEMONSTRATING ANISOTROPY EFFECTS

TABLE D-1 RESULTS OF TEMPERATURE PROFILE MEASUREMENTS PERFORMED ON SPECIMEN PC-II-90

T_A(R)	ΔT(R)	$\Delta T^{II}_{3/4 - 1-3/8}$	$\Delta T^{\underline{I}}_{3/4 - 1-3/8}$	$\Delta T^{II}_{1-3/8 - 1}$	$\Delta T^{\underline{I}}_{1-3/8 - 1}$	$\Delta T^{II}_{3/4 - 1}$	$\Delta T^{\underline{I}}_{3/4 - 1}$	T^{II}_1	$T^{\underline{I}}_1$
1802	50	+7.0	+10.1	-14.8	+ 47.0	- 7.7	+ 57.1	1798.6	1747.1
2049	82	+8.6	+23.9	+ 1.4	+46.3	+10.1	+ 70.2	1989.4	1944.6
2873	208	+10.6	+35.5	-24.5	+30.1	-14.4	+ 65.5	2797.1	2286.7

T_A Average specimen temperature as determined from extrapolated central specimen thermocouple values.

ΔT Temperature difference across flat surfaces of specimen; extrapolated as in T_A determination.

ΔT_{i-j} Temperature difference between the thermocouple at the distance, i, in inches from the center of the specimen, to that at distance j from the center of the specimen ($T_i - T_j$). Subscript 1 refers to the insulation around the curved surface of the specimen. Superscript II denotes the direction along laminates as viewed from a flat surface; superscript $\underline{I}$ denotes the direction normal to the laminates. See Figure D-1 for the thermocouple layout. The temperatures $T_{1-3/8}$ were obtained at the $T_{3/4}$ axial location by linear interpolation between the two 1-3/8 thermocouples stacked axially as shown in Figure D-1.

T_1 Temperature of insulation at about the specimen half-plane; superscript explained above.

conductivity calculated from the three sets of temperature differences obtained from the three specimen thermocouples. Since the temperature differences between specimen thermocouples were higher for the specimens with laminations n less than 90 degrees, the effects of the asymmetrical temperature perturbations were correspondingly less for these specimens; however, the strength of the anisotropy effect is such that each specimen requires individual attention.

APPENDIX E

ENTHALPY VERSUS TEMPERATURE DATA

VIRGIN MATERIALS - SEALED VERSUS VENTED SPECIMENS

Preliminary heat content measurements on the three virgin state materials showed a discontinuity in the enthalpy-temperature curve in the range 600-700 R. These specimens were sealed in type 347 stainless steel capsules under a helium atmosphere. Results of these measurements are illustrated in Figures E-1 , E-2 , and E-3 . In each case, the data points for the sealed specimens are numbered in the order taken. When the MX-4926 (Figure E-1) specimen was removed from its capsule following the measurements, there was no noticeable change in its appearance, by microscopic examination, and its capsule inner wall surfaces were clean. However, there was a one percent weight loss by the specimen.

A second measurement of this material resulted in a weight loss of 2.1 percent when the capsule was vented to permit escape of vapors. When plotted in Figure E-1 the data show a change in enthalpy due to vaporization of around 5.5 to 6.5 calories per gram. Therefore, the latent heat of vaporization of the material vaporized is about 260 to 310 cal/g. The figures show that the vaporization temperature lies somewhere between 60 and 93 C (600 and 660 R). It is interesting to note that alcohol (methyl) fits into this range of vaporization temperature and latent heat of vaporization, whereas water does not.

On the other hand, the scatter data for the sealed-capsule case suggests the possibility of vaporization by more than one component. If a smooth curve is drawn through all the data points for this case, inflection points (phase changes) are indicated in the region 610 to 670 R. Comparison of the slope of this curve with that for the vented-capsule case shows unequal slopes until about 800 R. This can be interpreted as being caused by vaporization proceeding at a finite rate within the specimen, the vaporization apparently being completed at about 800 R.

CHAR MATERIALS

The enthalpy-temperature relations for the three zone I char materials are shown in Figure E-4 and E-5.

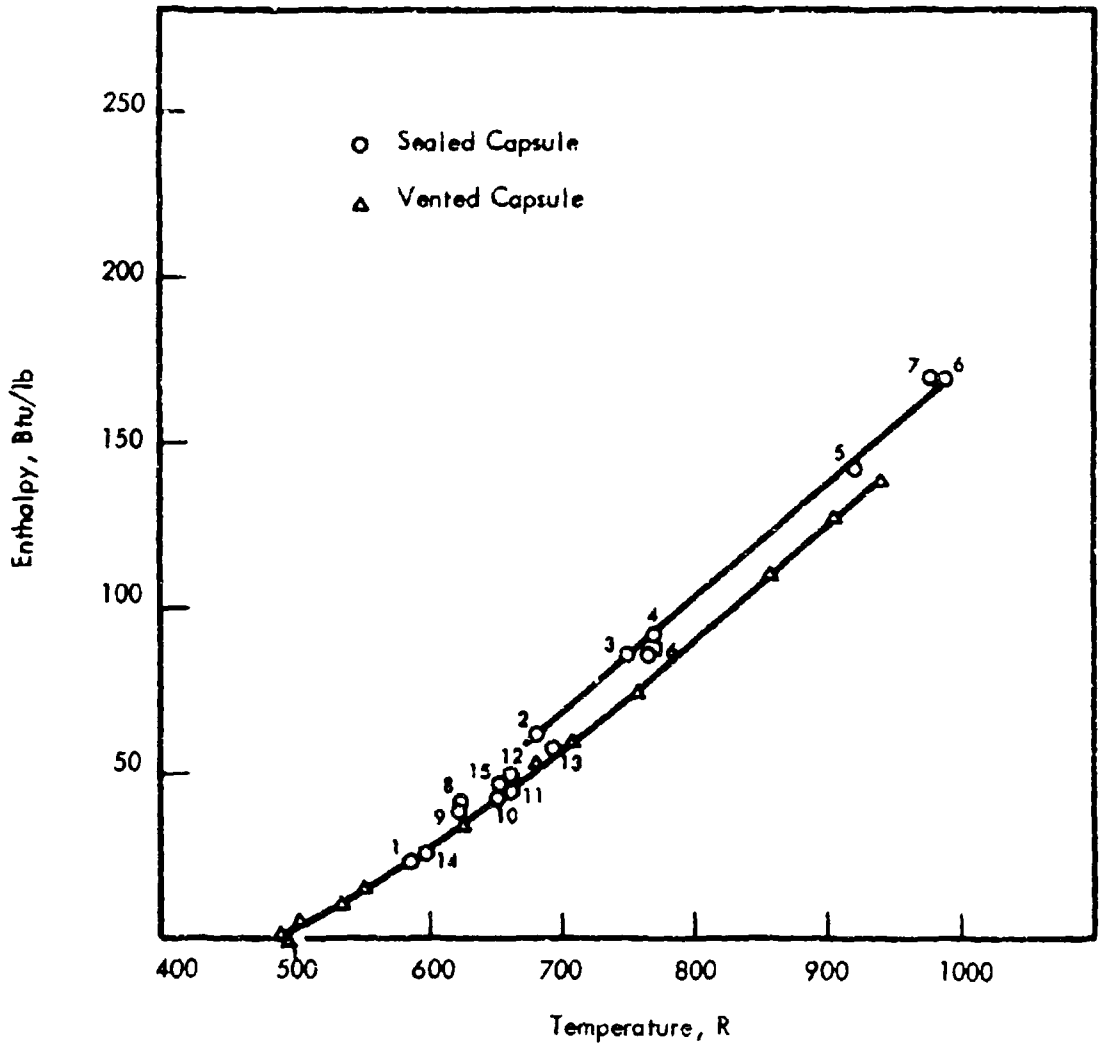

FIGURE E-1 ENTHALPY OF MX-4926 VIRGIN MATERIAL (SEALED AND VENTED CAPSULE)

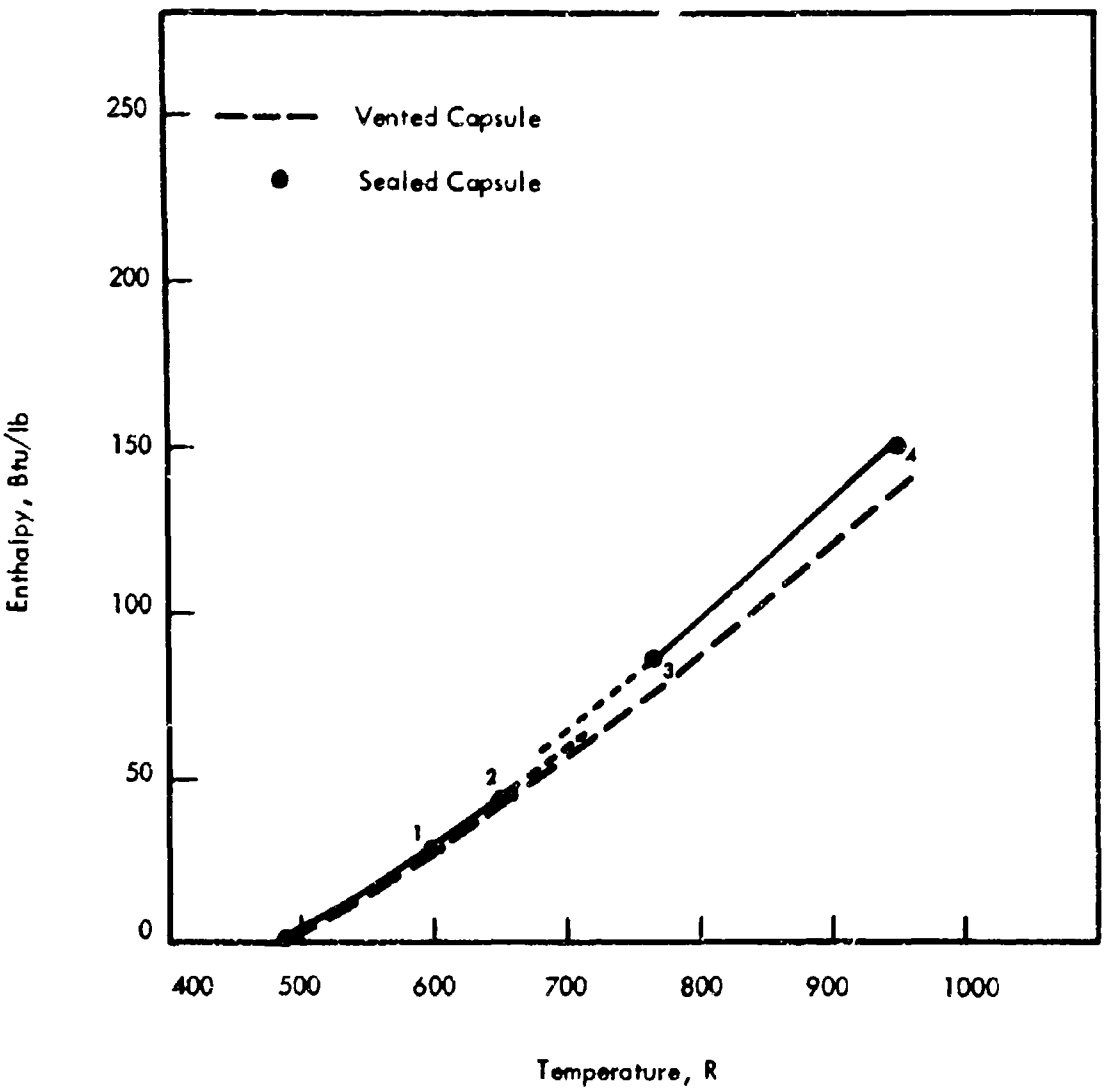

FIGURE E-2 ENTHALPY OF MX-4926 (NOZZLE "A") VIRGIN MATERIAL (SEALED AND VENTED CAPSULE)

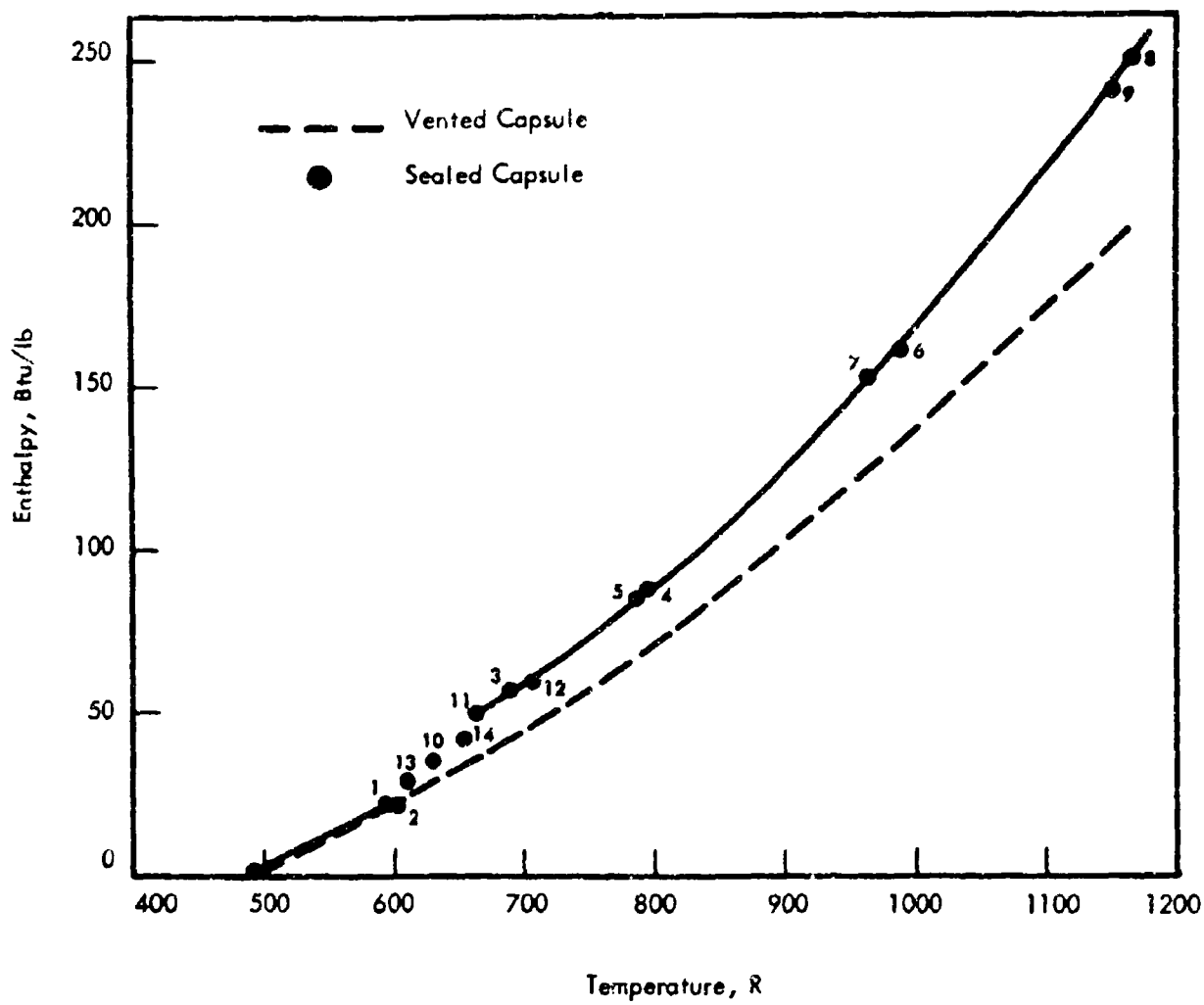

FIGURE E-3 ENTHALPY OF FM-5014 VIRGIN MATERIAL (SEALED AND VENTED CAPSULE)

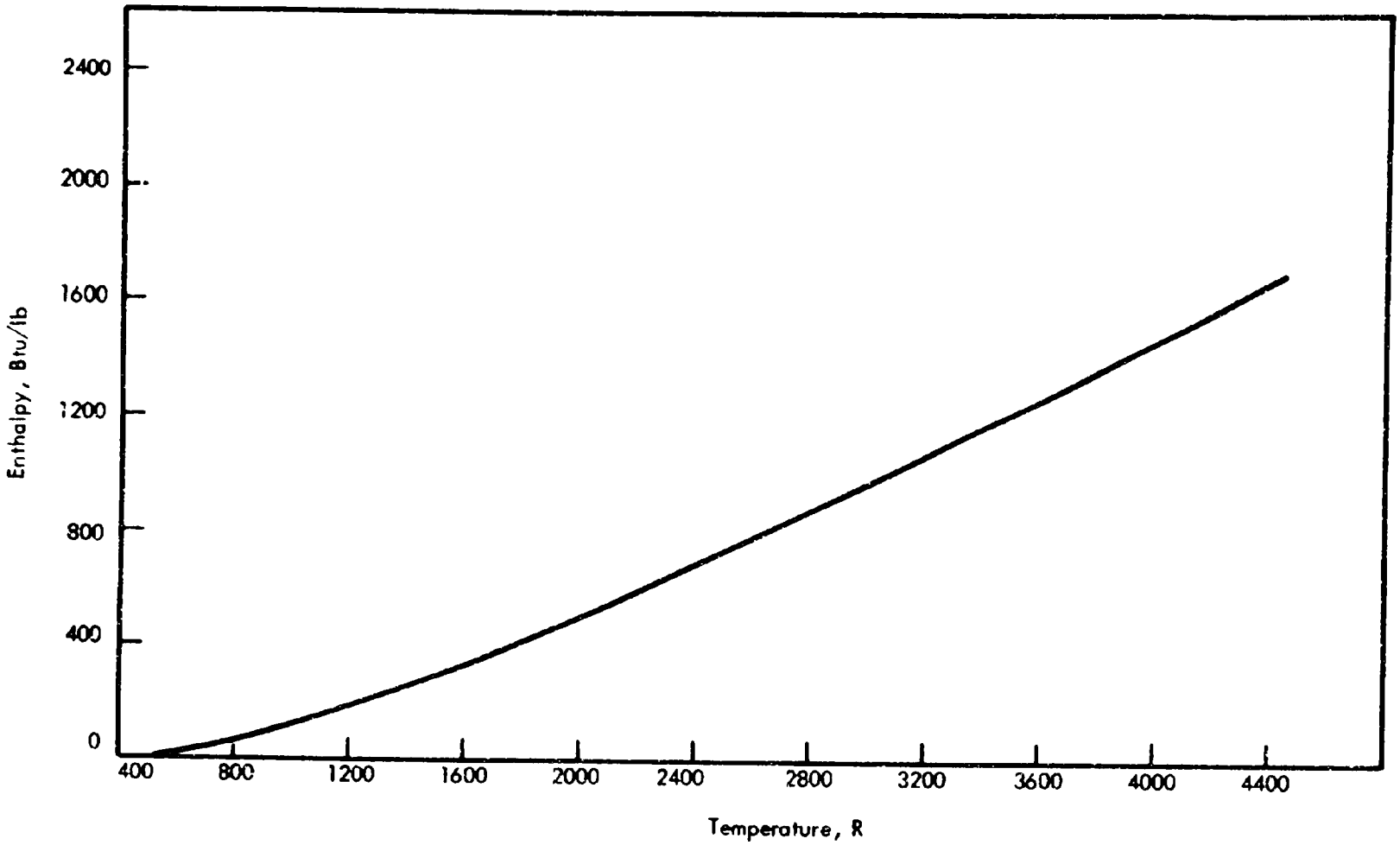

FIGURE E-4 ENTHALPY OF MX-4926 (ZONE I) CHAR MATERIAL (LABORATORY CHAR AND NOZZLE CHAR)

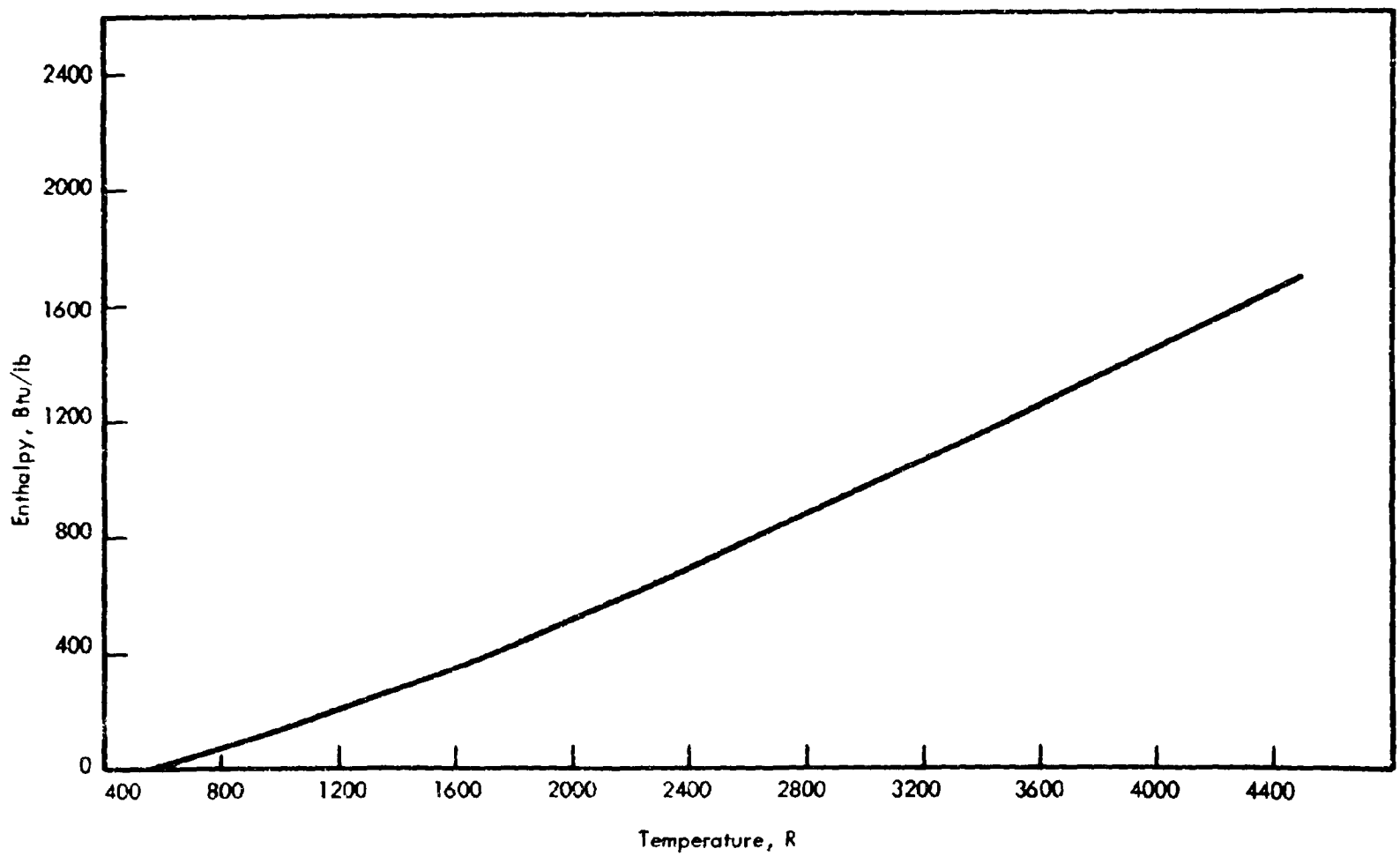

FIGURE E-5 ENTHALPY OF FM-5014 (ZONE I) CHAR MATERIAL (SPEC N-I-CIA)

REFERENCES

1. Ginnings, D.C., and Corruccini, R.J., "An Improved Calorimeter - The Determination of Its Calibration Factor and Density of Ice at 0 C." Journal of Research, National Bureau of Standards, 38 , 583-591 (1947).

2. Deem, H.W., and Lucks, C.F., "An Improved All-Metal Bunsen-Type Ice Calorimeter," Instrument Society of America, PPt-4, 1-9 (1958).

3. Ginnings, D.C., Douglas, T.B., and Ball, A.F., "Heat Capacity of Sodium Between 0 to 900 C, the Triple Point and Heat of Fusion," Journal of Research, National Bureau of Standards, 45 , 23-33, RP 2110 (1950).

4. Ginnings, D.C., and Corruccini, R.J., "Enthalpy, Specific Heat, and Entropy of Aluminum Oxide from 0 to 900 C," Journal of Research, National Bureau of Standards, 38, 593-600, RP 1797 (1949).

5. Ginnings, D.C., and Furukawa, G.T., "Heat Capacity Standards for the Range 14 to 1200K," Journal of American Chemical Society, 75, 525 (1953).

6. Pears, C.D., Engelke, W.T., and Thornburg, J.D., "Ther Thermal and Mechanical Properties of Five Ablative Reinforced Plastics from Room Temperature to 750°F," Technical Report No. AFML-TR-65-133, (April 1965).

7. Rasor, N.S., and McClelland, J.D., "Thermal Properties of Materials, Part I Properties of Graphite, Molybdenum and Tantalum to Their Destruction Temperatures," WADC-TR-56-400, ASTIA Document No. AD 118144 (March 1957).

8. Lucks, C.F., and Deem, H.W., "Thermal Properties of Thirteen Metals," American Society for Testing Materials, 227 , (1958).

9. Touloukian, Y. S., Editor, "Thermophysical Properties of High Temperature Solid Materials," Thermophysical Properties Research Center, Purdue University (1967).

10. Belle, J., Berman, R.M., Bourgeois, W.F., Cohen, I., Daniel, R.C., "Thermal Conductivity of Bulk Oxide Fuels," AEC Research and Development Report, WAPD-TM-686 (February 1967).

11. Viskanta, R., "Influence of Internal Thermal Radiation on Heat Transfer in UO_2 Fuel Elements," Nuclear Science and Engineering, 21, 13-19 (1965).

12. Bates, J.L., "Thermal Conductivity of UO_2 Improves at High Temperatures," Nucleonics, 19, (June 1961).

13. Kingery, W.D., "Thermal Conductivity: XII, Temperature Dependence of Conductivity for Single-Phase-Ceramics," Journal of American Ceramic Society, 38, 251-255 (July 1955).

14. Kasper, J., "Thermal Propagation In Carbons and Graphites at Very Hig Temperatures", Aerospace Corporation, Report SSD-TR-67-5, Contract AF04(695)-1001, (March 1967)

15. Kellett, B.S., "The Steady Flow of Heat Through Hot Glass," Journal of Opt. Society of America, 42, 339-343 (May 1952).

16. Loeb, A.L., "Thermal Conductivity: VIII, A Theory of Thermal Conductivity of Porous Materials," Journal of American Ceramic Society," 37, 96-99 (February 1964).

17. Larkin, B., and Churchill, S.W., "Heat Transfer by Radiation Through Porous Insulations," American Institute of Chemical Engineers Journal, 5, 467-474, (December 1959).

18. Francl, J., and Kingery, W.D., "Thermal Conductivity" IX, Experimental Investigation of Effect of Porosity on Thermal Conductivity," Journal of American Ceramic Society," 37, 99-107 (February 1954).

19. Englemann, F., and Schmidt, H.E., "Heat Transfer by Radiation in Solids," Nuclear Science and Engineering, 24, 317-321 (1966).

20. Carslaw, H.W., and Jaeger, J.C., "Conduction of Heat in Solids," Oxford, Clarendon Press, Second Edition, 46-48, 426 (1959).

21. Schaefer, J.W., and Dahm, T.J., "Studies of Nozzle Ablative Material Performance for Large Solid Boosters," NASA CR-72080, Aerotherm Report No. 66-2 (December 1966).

22. Grindle, S.L., Christensen, D.S., and Marvin, W.S., "Evaluation of Thermal Protection Materials for Lifting and Ballistic Re-entry Heat Shield Materials," AFML-TR-67-22 (July 1967).

Unclassified

Security Classification

DOCUMENT CONTROL DATA - R&D

(Security classification of title, body of abstract and indexing annotation must be entered when the overall report is classified)

1 ORIGINATING ACTIVITY (Corporate author)
The Boeing Company, Aerospace Group
P.O. Box 3868
Seattle, Washington 98124

2a REPORT SECURITY CLASSIFICATION
Unclassified

2b GROUP

3 REPORT TITLE
Thermal Properties of Ablative Chars

4 DESCRIPTIVE NOTES (Type of report and inclusive dates)
Final Report

5 AUTHOR(S) (Last name, first name, initial)
Clayton, Wilson A., Kennedy, Paul B., Evans, Robert J., et. al.

6 REPORT DATE	7a TOTAL NO. OF PAGES	7b NO. OF REFS
January 1968	254	22

8a CONTRACT OR GRANT NO.	9a ORIGINATOR'S REPORT NUMBER(S)
AF 33(615)-3804	None
b PROJECT NO. 7381	
c Task No. 738106	9b OTHER REPORT NO(S) (Any other numbers that may be assigned this report) AFML-TR-67-413
d	

10 AVAILABILITY/LIMITATION NOTICES
This document has been approved for public release and sale, its distribution is unlimited.

11 SUPPLEMENTARY NOTES	12 SPONSORING MILITARY ACTIVITY
None	Air Force Materials Laboratory Wright-Patterson AFB, Ohio 45433

13 ABSTRACT

Thermal conductivity, specific heat, thermal expansion, and a complete microstructural and chemical compositional characterization were established from room temperature to 5000°F for MX-4926 phenolic-carbon and FM-5014 phenolic-graphite nozzle throat chars recovered from fired 120- inch solid boosters. Characterization of FM-5055A ablative chars from plasma tests simulating reentry was also completed. Characterization, versus depth from the char surface, included determination of apparent and solid density, total porosity, open porosity size distribution, microstructural characteristics, elemental composition, thermal stability, and extent and nature of char "graphitization." Computer predicted internal density and temperature histories related post-test ablative char characteristics to temperature during prior ablation. Thermophysical properties were measured as a function of layup angle on virgin material and on furnace charred samples duplicating three distinct char zones found in the nozzle chars. Thermophysical properties were correlated with sample characterization and heat transport theory to predict properties applicable during ablation. Thermal conductivity, obtained by the steady state, unidirectional comparative disk method, depended on the rate controlled pyrolysis generation of porosity and on temperature dependent "graphitization" so that data for any application must be extrapolated from values measured on after test chars. Low lamination angles relative to the heat flow path gave substantially lower conductivity for all states of ablating material. Specific heat, obtained from Bunsen ice calorimeter enthalpy measurements, was established as a function of temperature in third order equations for all states of ablating material. Linear thermal expansion did not behave systematically and permanent dimensional changes were obtained on all samples. Crossply shrinkage during pyrolysis was the largest dimensional change resulting from ablation heating.

DD FORM 1 JAN 64 1473
U3 4802 1030 REV. 4/65
PART 1 OF 2

Unclassified

Security Classification

14 KEY WORDS	LINK A		LINK B		LINK C	
	ROLE	WT	ROLE	WT	ROLE	WT
Ablation Char Thermal Properties						

INSTRUCTIONS

1. ORIGINATING ACTIVITY: Enter the name and address of the contractor, subcontractor, grantee, Department of Defense activity or other organization (corporate author) issuing the report.

2a. REPORT SECURITY CLASSIFICATION: Enter the overall security classification of the report. Indicate whether "Restricted Data" is included. Marking is to be in accordance with appropriate security regulations.

2b. GROUP: Automatic downgrading is specified in DoD Directive 5200.10 and Armed Forces Industrial Manual. Enter the group number. Also, when applicable, show that optional markings have been used for Group 3 and Group 4 as authorized.

3. REPORT TITLE: Enter the complete report title in all capital letters. Titles in all cases should be unclassified. If a meaningful title cannot be selected without classification, show title classification in all capitals in parenthesis immediately following the title.

4. DESCRIPTIVE NOTES: If appropriate, enter the type of report, e.g., interim, progress, summary, annual, or final. Give the inclusive dates when a specific reporting period is covered.

5. AUTHOR(S): Enter the name(s) of author(s) as shown on or in the report. Enter last name, first name, middle initial. If military, show rank and branch of service. The name of the principal author is an absolute minimum requirement.

6. REPORT DATE: Enter the date of the report as day, month, year, or month, year. If more than one date appears on the report, use date of publication.

7. TOTAL NUMBER OF PAGES: The total page count should follow normal pagination procedures, i.e., enter the number of pages containing information.

7b. NUMBER OF REFERENCES: Enter the total number of references cited in the report.

8a. CONTRACT OR GRANT NUMBER: If appropriate, enter the applicable number of the contract or grant under which the report was written.

8b, 8c, & 8d. PROJECT NUMBER: Enter the appropriate military department identification, such as project number, subproject number, system numbers, task number, etc.

9a. ORIGINATOR'S REPORT NUMBER(S): Enter the official report number by which the document will be identified and controlled by the originating activity. This number must be unique to this report.

9b. OTHER REPORT NUMBER(S): If the report has been assigned any other report numbers (either by the originator or by the sponsor), also enter this number(s).

10. AVAILABILITY/LIMITATION NOTICES: Enter any limitations on further dissemination of the report, other than those imposed by security classification, using standard statements such as:

(1) "Qualified requesters may obtain copies of this report from DDC."

(2) "Foreign announcement and dissemination of this report by DDC is not authorized."

(3) "U.S. Government agencies may obtain copies of this report directly from DDC. Other qualified DDC users shall request through _____."

(4) "U.S. military agencies may obtain copies of this report directly from DDC. Other qualified users shall request through _____."

(5) "All distribution of this report is controlled. Qualified DDC users shall request through _____."

If the report has been furnished to the Office of Technical Services, Department of Commerce, for sale to the public, indicate this fact and enter the price, if known.

11. SUPPLEMENTARY NOTES: Use for additional explanatory notes.

12. SPONSORING MILITARY ACTIVITY: Enter the name of the departmental project office or laboratory sponsoring (paying for) the research and development. Include address.

13. ABSTRACT. Enter an abstract giving a brief and factual summary of the document indicative of the report, even though it may also appear elsewhere in the body of the technical report. If additional space is required, a continuation sheet shall be attached.

It is highly desirable that the abstract of classified reports be unclassified. Each paragraph of the abstract shall end with an indication of the military security classification of the information in the paragraph, represented as (TS), (S), (C), or (U).

There is no limitation on the length of the abstract. However, the suggested length is from 150 to 225 words.

14. KEY WORDS: Key words are technically meaningful terms or short phrases that characterize a report and may be used as index entries for cataloging the report. Key words must be selected so that no security classification is required. Identifiers, such as equipment model designation, trade name, military project code name, geographic location, may be used as key words but will be followed by an indication of technical context. The assignment of links, roles, and weights is optional.